Influence of the step properties on submonolayer growth of Ge and Si at the Si(111) surface

Von der Fakultät für Mathematik, Informatik und Naturwissenschaften der Rheinisch-Westfälischen Technischen Hochschule Aachen zur Erlangung des akademischen Grades eines Doktors der Naturwissenschaften genehmigte Dissertation

vorgelegt von

Konstantin Romanyuk, M.Sc.

aus Petrovka, Russische Föderation

Berichter: apl. Prof. Dr. Bert Voigtländer

Univ.- Prof. Dr. Stefan Tautz

Tag der mündlichen Prüfung: 21. Oktober 2009

Diese Dissertation ist auf den Internetseiten der Hochschulbibliothek online verfügbar.

ABSTRACT

The present work describes an experimental investigation of the influence of the step properties on the submonolayer growth at the Si(111) surface. In particular the influence of step properties on the morphology, shape and structural stability of 2D Si/Ge nanostructures was explored. Visualization, morphology and composition measurements of the 2D SiGe nanostructures were carried out by scanning tunneling microscopy (STM).

The formation of Ge nanowire arrays on highly ordered kink-free Si stepped surfaces is demonstrated. The crystalline nanowires with minimal kink densities were grown using Bi surfactant mediated epitaxy. The nanowires extend over lengths larger than 1 µm have a width of 4 nm. To achieve the desired growth conditions for the formation of such nanowire arrays, a modified variant of surfactant mediated epitaxy was explored. It was shown that controlling the surfactant coverage at the surface and/or at step edges modifies the growth properties of surface steps in a decisive way. The surfactant coverage at step edges can be associated with Bi passivation of the step edges. The analysis of island size distributions showed that the step edge passivation can be tuned independently by substrate temperature and by Bi rate deposition. The measurements of the island size distributions for Si and Ge in surfactant mediated growth reveal different scaling functions for different Bi deposition rates on Bi terminated Si(111) surface. The scaling function changes also with temperature. The main mechanism, which results in the difference of the scaling functions can be revealed with data of Kinetic Monte-Carlo simulations. According to the data of the Si island size distributions at different growth temperatures and different Bi deposition rates the change of SiGe island shape and preferred step directions were attributed to the change of the step edge passivation. It was shown that the change of the step edge passivation is followed by a change of the preferred steps direction resulting into different islands shapes.

The symmetry of the properties of the different step directions can determine the symmetry of the 2D islands. The growth shape of reconstructed 2D islands (nanostructures) on reconstructed surfaces can deviate from the internal symmetry of the substrate and the island. An analysis of the symmetry of the combined system of reconstructed substrate and island can deduce predictions for the island growth shape. It was found experimentally that the shape of two-dimensional (2D) Si or Ge islands has a lower symmetry than the threefold symmetry of the underlying Si(111) substrate if Bi is used as a surfactant during growth. Arrow-shaped or rhomb-shaped 2D islands were observed by scanning tunneling microscopy. This symmetry breaking was explained by a mutual shift between the surface reconstructions present on the substrate and on the islands. The mutual shift results into different step structure for initially symmetry related step directions. Using the kinematic Wulff construction the growth velocities of the steps could be determined from the island shape if the nucleation center had been located by a marker technique.

The structural stability of 2D SiGe nanostructures was studied by scanning tunneling microscopy (STM). The formation of pits with a diameter of 2-30 nm in one atomic layer thick Ge stripes was observed. The unanticipated pit formation occurs due to an energetically driven motion of the Ge atoms out of the Ge stripe towards the Si terminated step edge followed by an entropy driven GeSi intermixing at the step edge.

The pit formation can be also used for nanostructuring. Using conditions at which pit formation is enhanced the fabrication of freestanding GeSi stipes with single digit nanometer

width is possible. Continuous ~ 8 nm wide freestanding GeSi wires have been fabricated by pit coalescence.

Contents

Abstract 1 Introduction	
2.1 Elementary processes at surface	8
2.1.1 Adsorption and desorption2.1.2 Diffusion2.1.3 Surface electromigration	8 11 13
2.2 Thin film growth	14
2.2.1 Growth modes2.2.2 Nucleation and growth of islands	14 16
2.3 Surfactant mediated epitaxy	23
3 Step properties	25
3.1 Step classification and symmetry of the subst3.2 Growth properties of steps	rate 25 32
3.2.1 Energy of steps3.2.2 Kinetic processes at steps3.2.3 Transparent steps	32 34 36
3.3. Exchange intermixing at step edges	38
4 Preparation of highly ordered Si(111) templates	40
4.1 Precise misscut angle of sample plus annealing4.2 Mesa structures4.3 Step ordering by kink bunching	ng procedure 40 43 46
5 Experimental techniques	48
5.1 Molecular beam epitaxy system5.2 Sample preparation5.3 Sample heating and temperature measuremen	49 51 st 52

6 Growth of Ge nanowires on a Bi-terminated Si(111) template	
6.1 Preparation of Ge nanowire arrays by step flow growth	53
6.2 Preparation of a highly ordered Si(111)-7x7 template	55
6.3 Maintaining good step ordering during Bi termination	58
6.4 Modified surfactant-mediated epitaxy	66
7 Symmetry breaking in the growth of two-dimensional islands on Si(111)	70
8 Step edge passivation during SiGe epitaxy	88
9 Influence of entropy and energy on pit formation in 2D Ge layer	98
10 Summary	105
11 Appendix	106
12 Acknowledgments	161
Bibliography	162
Curriculum Vitae	167

1 Introduction

The enormous interest in the development of the methods for fabrication of smaller and higher density nanostructures is triggered by both: new demands for micro/nano-electronics and also interests in the physics of these structures. One of the effective strategies in the nanostructure synthesis is the bottom-up strategy, in comparison with the top-down the bottom-up strategy is not limited by lithography. The bottom-up methods enable to create structures in the single-digit nanometer range, such small structures can be also interesting for subsequent investigations of their electronic properties. Bottom-up methods can follow two different approaches: one is the direct atom manipulation by the tip of the scanning tunneling microscope (STM) and other is self-assembly or self-organization. The first is ultimate in terms of size of the nanostructures but a very slow and sophisticated method, the second is a parallel method which enables to form billions of nanostructures in parallel. However, this method is limited in the degree of uniformity and size control which can be achieved. Both methods can be complementary to each other. The processes based on self-assembly have the key advantage that they can be easily used for fabrication of electronic devices. One approach for the self-assembly synthesis of nanostructures is epitaxial growth. In the last decades several epitaxial growth techniques have been developed: chemical vapor deposition (CVD), molecular beam epitaxy (MBE) and surfactant mediated epitaxy (SME). More advanced methods like CVD and SME are more complicated but those offer the opportunity to fabricate structures which can't be created by standard MBE.

Surfactant Mediate Epitaxy (SME) is a powerful method with the following modification of the standard Molecular Beam Epitaxy (MBE). Using a third element named surfactant in SME allows to change (modify) kinetics and energetic of elementary processes on the surface during epitaxy. A striking example is Si/Ge Bi-SME on the Si(111) surface. Using Bi as surfactant suppresses Si/Ge exchange intermixing and allows to achieve layer-by-layer growth of Ge on Si. Due to that Bi-SME allows to form different 1 ML high 2D Si/Ge nanostructures. This beneficial growth behavior is explained by strong Bi passivation of the Si(111) surface and surface steps resulting in suppression of Si/Ge exchange intermixing and 3D island formation during growth.

The 2D Si/Ge nanostructures, nanowires and nanorings, can be used as a template for the following applications, for example: selective adsorption of foreign chemical elements, organic molecules or fullerenes. Ge and Si are essential for the technology of semiconductor devices. Besides the technological importance, the Ge/Si Bi-SME system can serve as a model system for the study of elementary processes at the surface by means of Scanning Tunneling Microscopy (STM). STM is usually a topographic method since it has no chemical sensitivity. The use of Bi as surfactant gives an unique ability to control SiGe composition on the surface. Due to different electronic structure of the Bi terminated Si and Ge surfaces an apparent height difference between Ge and Si is observed in STM images. The Ge area appears in STM images about 0.1 nm higher than the apparent height of Si. The apparent height difference in comparison with pure Si(Ge) is proportional to the local Ge concentration in SiGe composition of the surface layer. This allows to determine the SiGe composition on the nanoscale via the measured height contrast and introduces a powerful method for studying of the atomic diffusion processes at the surface and at the surface steps.

In the growth of 2D nanostructures the step properties are very important since the step is the structural key element in 2D growth which determines the incorporation of growing material into the crystal. Specifically the step properties influence the morphology, shape and the structural stability of the 2D nanostructures. The influence of the step properties is particularly important for the growth of 1 ML high 2D structures.

The present work describes an experimental investigation of the influence of the step properties on submonolayer growth at the Si(111) surface. The results of investigations allow to synthesize new nanostructures (free standing SiGe stripes, chapter 9) and find an optimized procedure for the preparation of highly ordered Ge nanowire arrays on the Si(111) surface (chapter 6). The thesis includes a description of the following phenomena:

- different preferable step directions during Ge Bi-SME on Si(111) surface at different Bi vapor pressure (Modified surfactant mediated epitaxy, chapter 6, 8).
 - symmetry breaking in the growth of 2D structures on Si(111) surface (chapter 7).
 - pit formation at 2D Ge layer on Si (chapter 9).

The present phenomena were investigated theoretically and experimentally and were explained as result of different processes at the step edges.

2 Fundamentals of epitaxial growth

2.1 Elementary processes at surface

2.1.1 Adsorption and desorption

Adsorption

According to kinetic theory of gases the flux of atoms I coming from a vapor phase on the surface is described by expression:

$$I = \frac{p}{\sqrt{2\pi m k_B T}},\tag{2.1}$$

where p is a partial pressure of gas of adsorbate, m is a molecular (atomic) mass, k_B is the Boltzmann constant (8.617 343×10⁻⁵ eV/°K), T is a temperature.

However, only a fraction of atoms adsorbs on the surface. The ratio of adsorption rate to the coming flux is a sticking coefficient or sticking probability s. Thereby the rate of adsorption r_a is:

$$r_a = sI. (2.2)$$

General formula for sticking coefficient reads:

$$s = \sigma f(\theta) \exp(-E_{act}/k_B T), \tag{2.3}$$

where σ is a condensing coefficient, takes orientation effects into account (steric factor) and for energy transmission of adsorbed atoms (molecules); $f(\theta)$ is a function depending on coverage describes probability of atom to find an adsorption state; E_{act} is an energy activation of adsorption. In simple case of Langmuir adsorption model [1,2] nondissociative $f(\theta)$ takes the form:

$$f(\theta) = 1 - \theta \,, \tag{2.4}$$

and kinetics of Langmuir adsorption is given by:

$$\frac{d\theta}{dt} = s_0 I(1 - \theta),\tag{2.5}$$

where s_0 is a sticking probability at zero coverage. For dissociative adsorption when a fallen molecule dissociates on n atoms which occupy the adsorption sites:

$$f(\theta) = (1 - \theta)^n. \tag{2.6}$$

Usually chemisorption is going through intermediate state named as precursor state. In the precursor state an atom can diffuse over the surface until it reaches a position with a higher energy (chemisorbed state). The case with one potential well for simple chemisorption is shown on **Figure 2.1** (a).

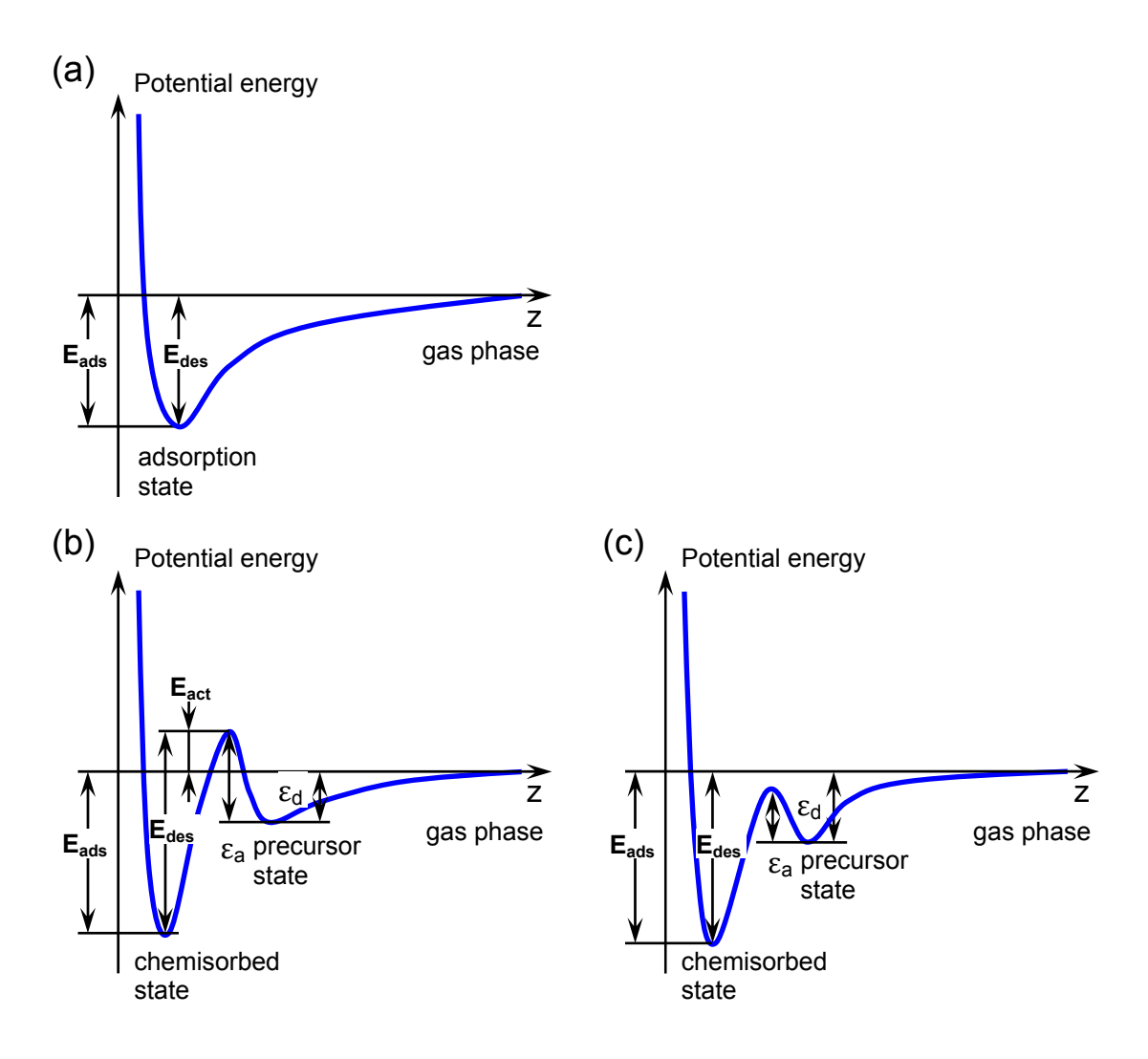


Figure 2. 1. Potential curves of chemisorption as functions of distance z between an adsorbed atom and the surface. (a) - presents the case of simple not activated adsorption. (b), (c) - potential curves for precursor chemisorption; (b) - the case of activation chemisorption with energy activation $E_{act} = \mathcal{E}_a - \mathcal{E}_d$, (c) - not activated chemisorption when $\mathcal{E}_a < \mathcal{E}_d$, E_{ads} - bonding energy of chemisorbed state, E_{des} - energy barrier for desorption from the chemisorbed state, \mathcal{E}_a and \mathcal{E}_d - energy barriers for adsorption and desorption from the precursor state, respectively.

Precursor adsorption diagram consists of two wells: a small well for a physisorbed precursor state and a deep well for the final chemisorbed state Figure 2. 1 (b), (c).

An atom in the precursor state can desorb into the gas phase or adsorb into the chemisorbed state. The rate of desorption k_d and adsorption k_a from the precursor state can be written as:

$$k_d = \theta_p V_d \exp(-\varepsilon_d/k_B T), \tag{2.7}$$

$$k_a = \theta_p v_a \exp(-\varepsilon_a/k_B T), \tag{2.8}$$

where v_d and v_a are attempt frequencies, θ_p is a coverage in the precursor state. The sticking coefficient (from precursor to chemisorbed state) can be written correspondingly:

$$s_0 = \frac{k_a}{k_a + k_d} = \left[1 + \frac{v_d}{v_a} \exp\left(-\frac{\varepsilon_d - \varepsilon_a}{k_B T}\right) \right]^{-1}, \tag{2.9}$$

• Desorption

The kinetics of desorption is described in terms of the rate of desorption r_{des} which is equal to the number of particles desorbing from a unit area of the surface per unit time. In a general form the rate of desorption is an expression of the form:

$$r_{doc} = \sigma^* f^*(\theta) \cdot \exp(-E_{doc}/k_B T), \tag{2.10}$$

where $f^*(\theta)$ describes dependence on coverage, and σ^* is a steric coefficient of desorption.

In assumption that all adsorbed atoms or molecules occupy identical states and no interaction between each another, the rate of desorption can be expressed as:

$$r_{des} = -\frac{d\theta}{dt} = k_n \theta^n = k_n^0 \theta^n \exp(-E_{des}/k_B T), \tag{2.11}$$

where E_{des} is energy activation of desorption, n is the order of desorption kinetics, and k_n is an attempt frequency of desorption.

In first order kinetics (n = 1) the rate of desorption is proportional to the coverage θ . That corresponds to the most simple case when atoms desorb independently on adsorption sites. In the case of desorption of molecules consisting of n atoms the kinetic of desorption is proportional to θ^n [2].

2.1.2 Diffusion

On the atomic scale the surface can be considered as a periodic potential landscape with adsorption places which correspond to energy minima **Figure 2. 2**. Because of thermal excitation the atoms can jump from one neighbor adsorbed place to another. The change of atom position on defect free surface can be described by a random walk model. It can be shown that after n jumps of length a the atom will have moved, on average, a distance of:

$$\sqrt{\left\langle \Delta r^2 \right\rangle} = a\sqrt{n} = a\sqrt{v \cdot t} \,\,\,\,(2.12)$$

where a is a distance between adsorption places, and v is the jump or hopping rate. The relation (2. 13) can be written as:

$$\sqrt{\left\langle \Delta r^2 \right\rangle} = \sqrt{D \cdot t} \;, \tag{2.13}$$

where the diffusion coefficient D is given by relation:

$$D = \frac{\left\langle \Delta r^2 \right\rangle}{zt} = \frac{v \cdot a^2}{z} \,, \tag{2.14}$$

where z is a number of neighbor states, z = 2 for the 1D diffusion, z = 4 for a diffusion on square lattice and z = 6 for a diffusion on hexagon lattice. A jumping of adsorbed atom from one state to another needs for thermal activation energy which must be higher than energy activation for diffusion E_{diff} , then frequency of successful jumps can be present:

$$v = v_0 \exp\left(\frac{-E_{diff}}{k_B T}\right),\tag{2.15}$$

where v_0 is an attempt frequency. Energy activation of diffusion E_{diff} is a difference of potential energy in adsorbed state (position 1) and potential energy in transient state (position 2) **Figure 2. 2**. E_{diff} is much less than desorption energy E_{des} , usually E_{diff} is about 5-20% from E_{des} [2]. For chemisorbed particles $E_{diff} >> k_B T$ and we have a *hopping diffusion* mechanism. If $E_{diff} < k_B T$, then we have a *mobile diffusion* mechanism.

In the presence gradient of concentration of atoms we have an averaged migration flux from area with higher concentration to area with lower concentration of atoms. The diffusion flux J is proportional to gradient of concentration ∇c and described by Fick's first law:

$$J = -D \cdot \nabla c \,, \tag{2.16}$$

For one dimensional diffusion:

$$J = -D\frac{\partial c}{\partial x}. ag{2.17}$$

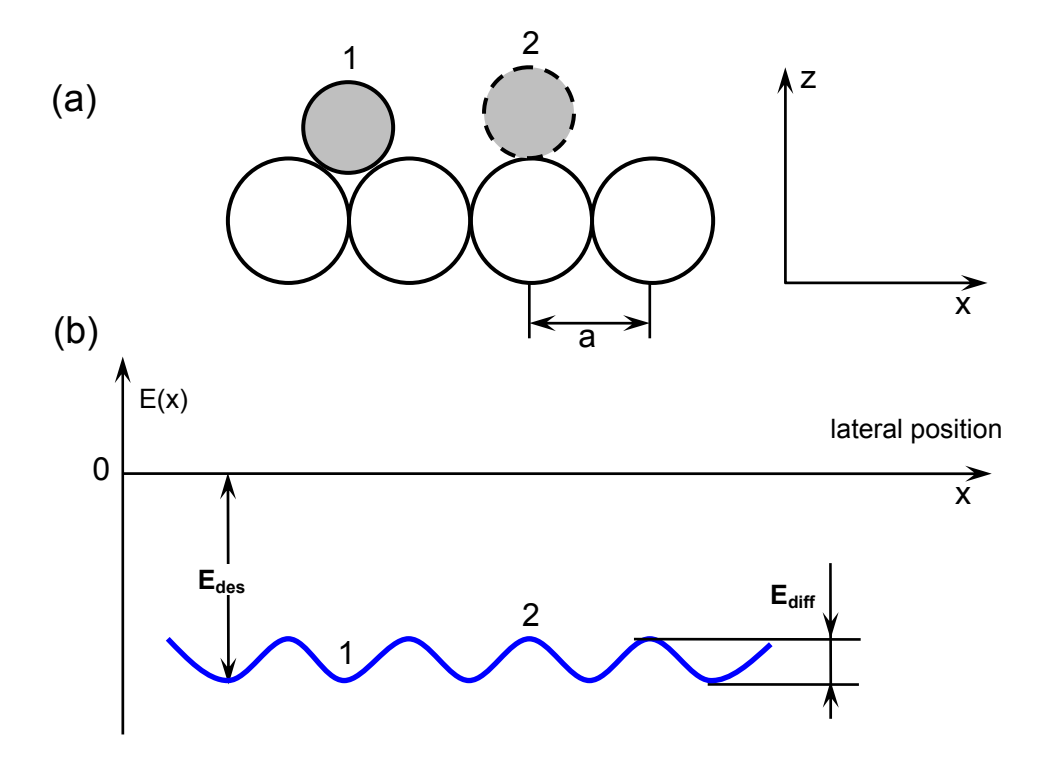


Figure 2. 2. The one dimensional schematic diagram representing, (a) – substrate (white balls) and an adatom (dark ball). The adsorbed state of adatom is marked by "1" and transition state of atom is marked by "2". Z – is the distance from the surface, and x – is the lateral position on the surface. (b) schematic diagram of potential energy of an adatom on the surface. E_{diff} - activation energy for surface diffusion.

Fick's second law describes a nonstationary case when diffusion flux and concentration are changing in time. For one dimension case it can be written as:

$$\frac{\partial c}{\partial t} = \frac{\partial}{\partial x} \left(D \frac{\partial c}{\partial x} \right). \tag{2.18}$$

There are two types of diffusion:

- tracer diffusion is observed at low concentrations when particles have no interaction between each other,
- and chemical diffusion observed at high concentrations when an interaction between particles is significant.

At high coverage when an interaction between particles is significant, Fick's first low must be written in more general form:

$$J = -L\frac{\partial \mu}{\partial x} = -L\frac{\partial \mu}{\partial \theta}\frac{\partial \theta}{\partial x} = -D_c(\theta)\frac{\partial \theta}{\partial x},$$
(2. 19)

where μ is a chemical potential of diffusing particles, L is a transport coefficient, D_c is a chemical diffusion coefficient depending on coverage θ .

2.1.2 Surface electromigration

An external force can have a strong influence on the diffusion process. Drift of atoms along direct current on the surface is named as surface electromigration. The effective force acting on migrating atom is proportional to the electric field E and can be written as sum of two components [2,3,4]:

$$F = F_d + F_w = e(Z_d + Z_w)E = eZE,$$
 (2. 20)

where $Z = Z_d + Z_w$ is a sum of effective charges of an atom. F_d presents a direct force acting on an atom by electric field. F_w is a force of electron wind induced by impulse pass from the current electrons scattered on the atom.

2.2 Thin film growth

2.2.1 Growth modes

The thin film growth can proceed by one of three essential types of growth modes [2,5,6] **Figure 2. 3**:

- Layer-by-layer growth (2D) or *Frank-van der Merwe* growth mode.
- Island growth (3D) or *Vollmer-Weber* growth mode.
- Layer by layer plus island growth or *Stranski-Krastanov* growth mode.

In terms of wetting – not wetting the two first modes can be classified by relations between surface energies of substrate γ_s , film γ_f , and the interface energy γ_{sf} . In the case of wetting (*Frank-van der Merwe*) the surface energy of substrate is larger than a sum of energies of film surface and interface surface:

$$\gamma_s > \gamma_f + \gamma_{sf}$$
,

a nucleation and a growth of subsequent layer start after the completion of the preceding layer. This kind of growth realizes when atoms of film are stronger bonded to substrate than to each other. In the case of not wetting (*Vollmer-Weber*) the surface energy of substrate is lower than a sum of energies of film surface and interface surface:

$$\gamma_s < \gamma_f + \gamma_{sf}$$
,

a nucleation of subsequent layer starts before the completion of the preceding layer. *Vollmer-Weber* growth mode corresponds to the case when film atoms more strongly bound to each other than to the substrate. An intermediate case when layer by layer growth is followed by 3D islands growth is named as *Stranski-Krastanov* (SK) growth mode. The SK growth mode usually observed for mismatched materials for example such as Si and Ge.

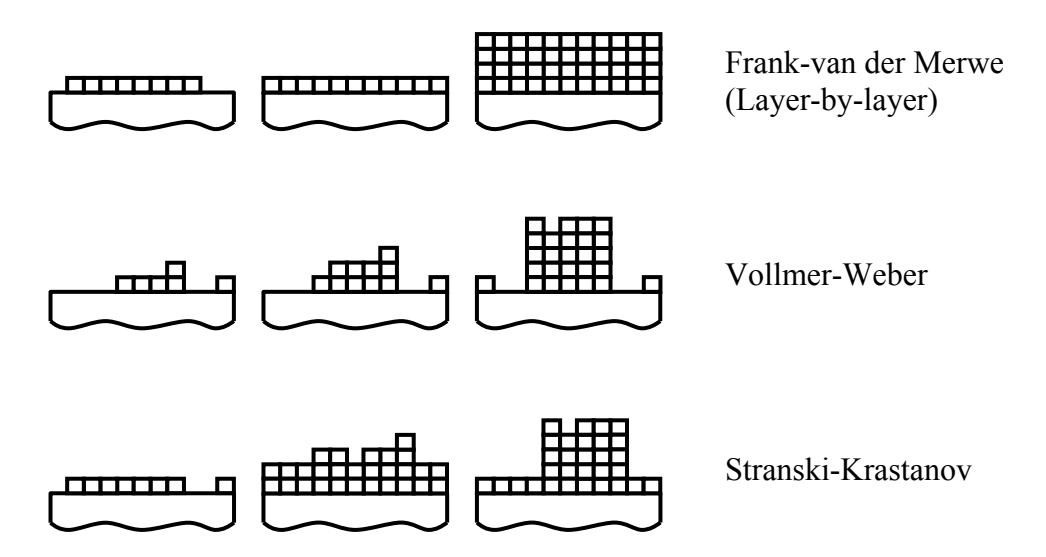


Figure 2. 3. The three classical growth modes.

Frank-van der Merwe growth mode can be divided on two-dimensional island growth and step-flow growth.

In two-dimensional island growth the formation of epitaxial layer starts with nucleation of 2D islands with the following lateral growth of the islands until coalescence. After complete coalescence of the islands the next layer starts growth with nucleation of 2D islands on top of the previous layer.

In the presence of preexisting steps the layer-by-layer growth can be realized by step propagation **Figure 2. 4**. No nucleation of 2D islands is expected because the diffusing adatoms reach the step edges and are incorporated there before nucleation of 2D islands occurs. Due to the incorporation at step edges, the steps move and this growth mode is called step-flow growth or growth by step propagation. Depending on the growth conditions (temperature and growth rate) intermediate growth modes with partial growth at the step edges and simultaneous nucleation of islands on terraces are also possible [7].

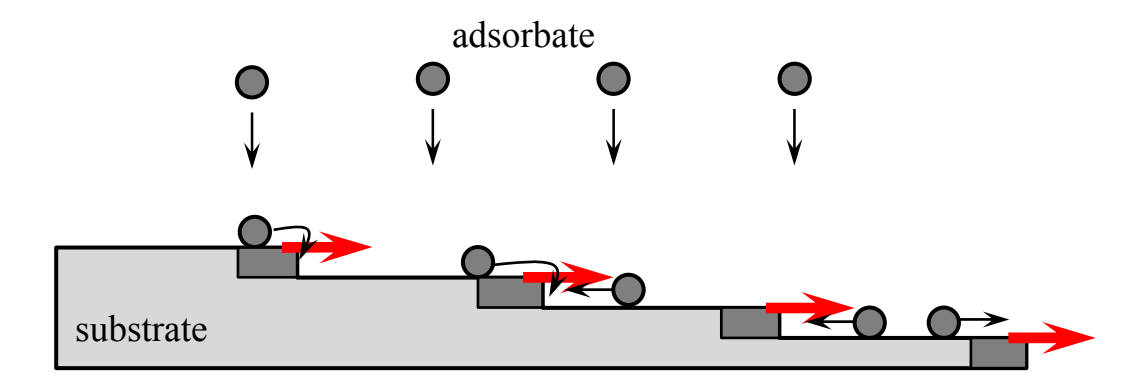


Figure 2. 4. Step-flow growth or growth by step propagation. Red arrows show a direction of the step propagation during growth.

The step-flow growth is usually realized on vicinal surfaces and can be a useful method for nanowire fabrication on single digit nanometer scale.

2.2.2 Nucleation and growth of islands

• Nucleation and growth

Elementary processes on the surface during growth of islands are shown on **Figure 2.5**. Atoms arrive on the surface from vapor phase with rate of adsorption R and bond to the surface with energy E_{ads} . Adsorbed adatoms diffuse on the surface until one of the reactions occurs:

- 1. the atoms can re-evaporate in time of desorption $\tau_{ads} = v^{-1} \exp(E_{ads}/k_B T)$,
- 2. the atoms can be captured by existing islands or steps,
- 3. the atom can meet another atom and form island.

The small islands are not stable and can decay into single atoms. However, during growth, the islands become larger and more stable. If the island size of i after attachment of one atom becomes stable, then i is a critical size of the island.

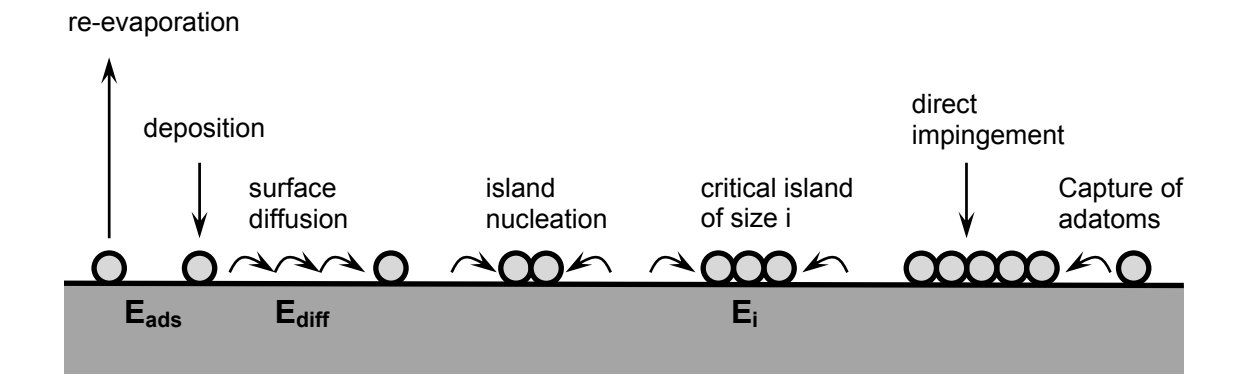


Figure 2. 5. Schematic diagram showing atomic processes of nucleation and growth of islands on the surface.

Atomic processes can be quantitatively described in term of kinetic rate equations. The description is based on estimation of nucleation rate and decay rate of the islands. The fluxes defining concentration n_j of metastable island size of j < i, where i is a size of critical island are shown on **Figure 2. 6**.

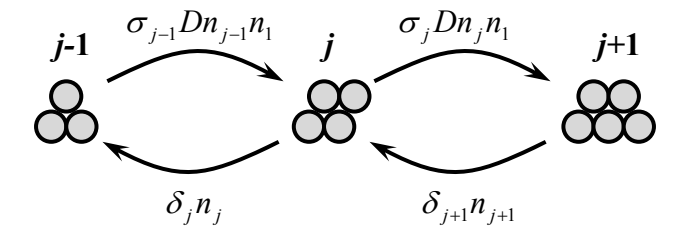


Figure 2. 6. Schematic diagram showing fluxes which fix concentration of the cluster size of *j*.

Four processes give contribution into concentration n_i of island size of j.

- Capture of adatom by island size of j-1 increases number of the island size of j with rate of $\sigma_{j-1}Dn_{j-1}n_1$.
 - Detachment of atom from island size of j + 1 gives a rate of $\delta_{i+1}n_{i+1}$.
- Capture of adatom by island size of j decreases number of the island size of j with a rate of $\sigma_i Dn_i n_1$.
 - Detachment of atom from island size of j gives a rate of decay $\delta_j n_j$.

Here n_1 is an adatom concentration, D is a diffusion coefficient, σ is referred to as a capture number, $\delta_{j+1} \sim \exp(-\Delta E_j^{j+1}/k_B T)$ is a rate of decay, where ΔE_j^{j+1} is the energy difference between island size of (j+1) and island size of j. Description and solution of kinetic equations were made by J. Venables [8,9,10]. In assumption of local equilibrium (steady-state concentration) for 1 < j < i+1, where i is a size of critical island, the solution of equations gives island density expression type of:

$$N \propto \left(\frac{R}{\nu_0}\right)^p \exp\left(\frac{E}{k_B T}\right),$$
 (2.21)

where v_0 is an attempt frequency, R is a rate of adsorption, the expressions for p and E depend on regime of condensation and can be found in [10].

• Island size distribution

The study of island size distribution can give quantitative information about a size of critical island and qualitative information about mechanisms of growth. A function of island size distribution N_s shows island concentration of size s (s – number of atoms in island). Thus, complete number of stable islands N and coverage θ can be written as:

$$N = \sum_{S>i} N_S \text{ and } \theta = \sum_{S\geq i} s \cdot N_S.$$
 (2.22)

Then mean island size can be written as:

$$\langle s \rangle = \frac{\sum_{S>i} s \cdot N_S}{\sum_{S>i} N_S} = \frac{\theta - \sum_{S \le i} s \cdot N_S}{N}. \tag{2.23}$$

For small sizes of critical island, i = 1,

$$\langle s \rangle = \frac{\theta - N_1}{N} \approx \frac{\theta}{N}.$$
 (2. 24)

In these assumptions the *scaling theory* [11] gives relation:

$$N_S = \theta \cdot \langle s \rangle^{-2} f_i(s/\langle s \rangle), \tag{2.25}$$

where $f_i(s/\langle s \rangle)$ is a scaling function of island size distribution at critical island size of *i*. Comparison of calculated scaling function with experimental scaling function can be used for estimation of critical island size. Observation of deviation of the experimental function from the standard one also gives qualitative information about mechanisms of growth.

• Shape of islands

The observation of the island shape provides a direct access to step edge energetics and to the symmetry of the bulk lattice of the crystal. The shape of 2D islands can be classified by growth conditions into growth shape and equilibrium shape. The shape of islands observed during growth (noneguilibrium conditions) is called a growth shaped. The shape of islands being in equilibrium with vapour or liquid phase is called an equilibrium shape. The 2D equilibrium shape of an island is defined by the minimum of the total *step free energy* for an island of fixed particle number and area [12]:

$$\int_{L} \gamma(\phi) dl = \min. \tag{2.26}$$

Here $\gamma(\phi)$ is the step free energy per unit length, and the integral is taken over the entire edge length L.

The two dimensional compact island shape problem is the 2D analog to the (3D) crystal growth problem. In both cases the crystal grows by the transport of particles from the surrounding phase, which is driven by concentration gradient around the crystal. The crystal shapes reflect the symmetry of 2D or 3D crystal lattice and the resulting energetic at the phase boundaries (1D steps or 2D surfaces).

For small islands and under conditions allowing sufficient material transport the equilibrium shape may be reached experimentally [13,14,15,16]. According to the 2D Wulff

theorem the step free energy ratio $\frac{\gamma_B}{\gamma_A}$ for the specific directions (**Figure 2. 7 (a)**) is the ratio

of the distances r_A and r_B measured from the symmetry centre "O" of the island to the step edges:

$$\frac{r_B}{r_A} = \frac{\gamma_B}{\gamma_A} \,. \tag{2.27}$$

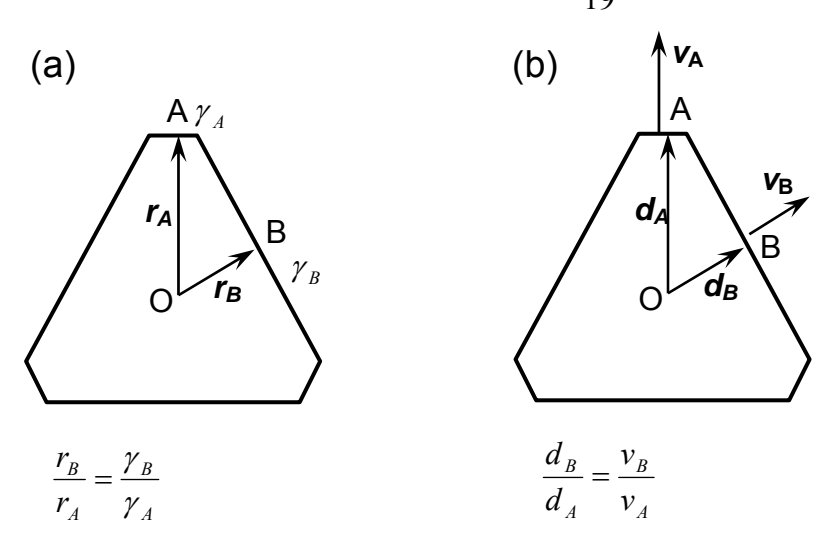


Figure 2. 7. Schematic diagram showing the Wulff theorem for 2D compact islands. (a) equilibrium shape of the island. (b) growth shape of the island as a result of step speed propagation.

The chemical potential which is a free energy per atom is a useful concept, since it is the same everywhere at equilibrium. If the shape of the solid does not conform to the equilibrium form, it must be the case that a chemical potential gradient exists which (some form of Fick's law) drives mass transport until a morphological equilibrium is attained. As example, let's consider an island in the shape of a rectangle **Figure 2. 8**. An attachment of a particle of the volume Ω to A or B sides changes the proportions of a rectangle as shown by dashed lines on **Figure 2. 8**. The change of the rectangle shape is resulting in a change of the system energy which includes bulk energy and step energy. For the geometry of **Figure 2. 8** the resulting chemical potential can be written as:

$$\mu_{A} = \mu_{c} + 2\gamma_{B} \cdot \frac{\Omega}{l_{A}},$$

$$\mu_{B} = \mu_{c} + 2\gamma_{A} \cdot \frac{\Omega}{l_{B}},$$
(2. 28)

where μ_c is the chemical potential of the bulk and Ω is the volume of a particle. The gradient noted above exists because $\mu_A \neq \mu_B$ unless the linear dimensions l_A and l_B attain their equilibrium values \widetilde{l}_A and \widetilde{l}_B . At the equilibrium $\mu_A = \mu_B$:

$$\frac{\gamma_B}{\widetilde{l}_A} = \frac{\gamma_A}{\widetilde{l}_B} \,. \tag{2.29}$$

the linear dimensions \widetilde{l}_A and \widetilde{l}_B can be written as $\widetilde{l}_A = 2\widetilde{r}_B$ and $\widetilde{l}_B = 2\widetilde{r}_A$ Figure 2. 8, then (2. 29) takes the form:

$$\frac{\widetilde{r}_B}{\widetilde{r}_A} = \frac{\gamma_B}{\gamma_A} \ .$$

This is the 2D Wulff theorem (2. 27) followed from the equilibrium conditions $\mu_A = \mu_B$ at the facets of a rectangle.

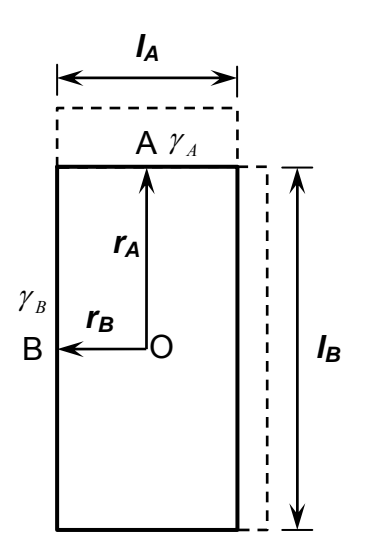


Figure 2. 8. The island of a rectangular shape.

The same relations can be found for 3D case with a crystal in the shape of a parallelepiped [17].

More general 2D case can be considered for a cyclic polygon which is the hexagon in **Figure 2. 7**. The corner of a cyclic polygon is shown on **Figure 2. 9**. An attachment of a particle of the volume Ω to A or B sides changes the proportions of a polygon as shown by dashed line on **Figure 2. 9**. The corresponding change of the step energy can be written as:

$$\Delta E_A = h_A \left(\gamma_B \frac{1}{\sin \theta} - \gamma_A \frac{1}{\tan \theta} \right)$$
$$\Delta E_B = h_B \left(\gamma_A \frac{1}{\sin \theta} - \gamma_B \frac{1}{\tan \theta} \right)^*$$

where ΔE_A and ΔE_B are changes of the step energy of the system after attachment a particle to A and B sides, respectively, angle $\theta = \alpha + \beta$, height $h_{A,B} = \frac{\Omega}{l_{A,B}}$ (**Figure 2. 9**), and Ω is the volume of a particle. The relations for chemical potential can be written as:

$$\mu_{A} = \mu_{c} + \frac{\Omega}{l_{A}} \left(\gamma_{B} \frac{1}{\sin \theta} - \gamma_{A} \frac{1}{\tan \theta} \right)$$

$$\mu_{B} = \mu_{c} + \frac{\Omega}{l_{B}} \left(\gamma_{A} \frac{1}{\sin \theta} - \gamma_{B} \frac{1}{\tan \theta} \right)^{2}$$
(2. 30)

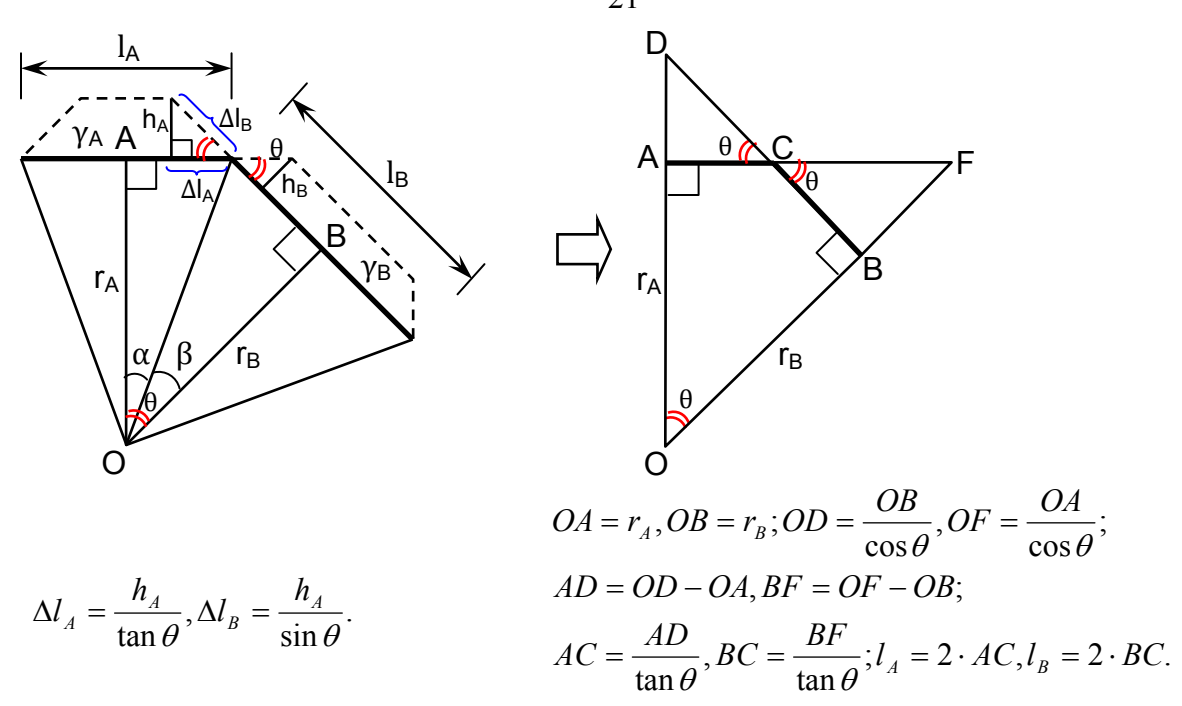


Figure 2. 9. Corner of a cyclic polygon.

where μ_c is the chemical potential of the bulk, the lengths of facets l_A and l_B can be expressed as (**Figure 2. 9**):

$$l_{A} = 2\left(\frac{r_{B}}{\cos\theta} - r_{A}\right) \frac{1}{\tan\theta}$$

$$l_{B} = 2\left(\frac{r_{A}}{\cos\theta} - r_{B}\right) \frac{1}{\tan\theta}$$
(2. 31)

At the equilibrium $\mu_A = \mu_B$:

$$l_{B}\left(\gamma_{B} \frac{1}{\sin \theta} - \gamma_{A} \frac{1}{\tan \theta}\right) = l_{A}\left(\gamma_{A} \frac{1}{\sin \theta} - \gamma_{B} \frac{1}{\tan \theta}\right) \Rightarrow$$

$$\gamma_{B}\left(\frac{l_{B}}{\sin \theta} + \frac{l_{A}}{\tan \theta}\right) = \gamma_{A}\left(\frac{l_{A}}{\sin \theta} + \frac{l_{B}}{\tan \theta}\right)$$
(2. 32)

After substitution of (2. 31) into (2. 32) the relation of equilibrium takes the form:

$$\begin{split} \gamma_{B} & \left(\frac{1}{\sin \theta} \left(\frac{r_{A}}{\cos \theta} - r_{B} \right) + \frac{1}{\tan \theta} \left(\frac{r_{B}}{\cos \theta} - r_{A} \right) \right) = \gamma_{A} \left(\frac{1}{\sin \theta} \left(\frac{r_{B}}{\cos \theta} - r_{A} \right) + \frac{1}{\tan \theta} \left(\frac{r_{A}}{\cos \theta} - r_{B} \right) \right) \Rightarrow \\ \gamma_{B} r_{A} & \left(\frac{1}{\cos \theta \sin \theta} - \frac{1}{\tan \theta} \right) = \gamma_{A} r_{B} \left(\frac{1}{\cos \theta \sin \theta} - \frac{1}{\tan \theta} \right) \Rightarrow \\ & \frac{r_{B}}{r_{A}} = \frac{\gamma_{B}}{\gamma_{A}} \end{split}$$

This relation of the 2D Wulff theorem (2. 27) is followed from the equilibrium conditions $\mu_A = \mu_B$ at the neighbor facets of a corner of cyclic polygon.

Originally the islands are nucleated and grown in substantially nonequilibrium conditions. The shape of the growth islands is named growth shape. In order to understand the growth shape of islands, it is useful to define the advancement speed v of a step normal to itself. During growth the steps of the island propagate on distances d measured from the center of nucleation. The distances d are proportional to the step speeds v Figure 2. 7 (b),

i. e.
$$d_{A,B} = \int_{0}^{t} v_{A,B}(t') \cdot dt'$$
. For a growth regime (isotropic growth conditions) in which the

incorporation into the steps is limited by attachment and the adatom concentration n on the surface is constant (due to large incorporation barrier) the expression for $d_{A,B}$ can be written

as:
$$d_{A,B} = \int_0^t v_{A,B}(t^{\prime}) \cdot dt^{\prime} \propto \int_0^t k_{A,B} \cdot n(t^{\prime}) \cdot dt^{\prime}$$
, where $k_{A,B} = v \exp\left(\frac{-E_{A,B}}{k_B T}\right)$ is a frequency of

attachment of adatoms to the step edges (T = const), $n(t^{\prime})$ is an adatom concentration, and t is a time of growth. The shape is evidently characterized by:

$$\frac{d_B}{d_A} = \frac{\overline{V}_B}{\overline{V}_A} \,. \tag{2.33}$$

Here $\overline{v}_{A,B} = \frac{1}{t} \int_{0}^{t} v_{A,B}(t') \cdot dt'$ are average step speeds. At constant frequencies of attachment

 k_{AB} during growth the ratio (2. 33) can be written as:

$$\frac{d_B}{d_A} = \frac{v_B(t)}{v_A(t)} \propto \frac{k_B}{k_A} \,. \tag{2.34}$$

This is the kinetic analog of the relation (2.27) derived from the Wulff construction for equilibrium shapes.

The growth shape of the islands can differ with different growth conditions and can be also classified by type of the shape into two big classes:

- Ramified islands or fractal islands.
- Compact islands.

Ramified islands are usually formed at low temperatures when diffusion along step edges is negligible. In the limiting case called "hit-and stick", adatoms incorporate into steps of the islands and are immobilized immediately. This case is described by the diffusion limited aggregation (DLA) model [18,12]. The model predicts a formation of fractal islands with an average branch thickness of about one atom independent on the geometry of the bulk lattice.

The shape of compact islands, as considered above, can obey the symmetry of bulk lattice of substrate and contains quantitative data on step (facet) energies.

2.3. Surfactant mediated epitaxy

The presence of atoms of a foreign element on the surface, different from both the growing film and the substrate, introduces additional mechanisms into the behavior of the film growth. Such foreign elements are named surfactants if the atoms of the elements float on top of the surface during growth without incorporation into growing film. The presence of a surfactant on top of the film changes the surface properties such as surface diffusion and adsorption energy. Generally the surfactants passivate the surface, saturate the surface dandling bonds and decrease the surface energy [19,20,21,22,23].

The standard surfactant mediated epitaxy (SME) starts by termination of the surface with some amount of the surfactant. The termination procedure includes covering the substrate surface by surfactant that is followed with change of the surface reconstruction. The change of the surface reconstruction on substrate usually induces a mass transport of the substrate atoms since different surface reconstructions have often a different density of surface atoms. During growth the surfactant can evaporate from the surface. Therefore a simultaneous codeposition of the surfactant during film growth is used to maintain the required amount of the surfactant on the surface. The deposited atoms of the growing film adsorb first on top of the surfactant layer and diffuse over the surface until they incorporate into a step edge or nucleate a new island **Figure 2. 10**. The atoms diffuse over the surfactant layer in a physisorbed precursor state. When the atoms reach the step edges thermal activation energy is needed to proceed into the chemisorbed state with higher energy. During growth the surfactants suppress Si-Ge intermixing.

In the case of Si and Ge SME growth on Si substrate the surfactant elements of 3 and 5 groups of the Periodic Table of the Elements are usually used: Sb, As, Bi, In, Ga [19]. The use of Bi as a surfactant effectively suppresses Si-Ge intermixing during growth on the Si(111) surface as well as other surfactants. Due to different electronic structure of the Bi terminated Si and Ge surfaces the apparent height difference between Ge and Si is observed in STM images. The Ge area appears in STM image about 0.1 nm higher than the apparent height of Si. The apparent height difference in comparison with pure Si(Ge) is proportional to the local Ge concentration in SiGe composition of the surface layer [24].

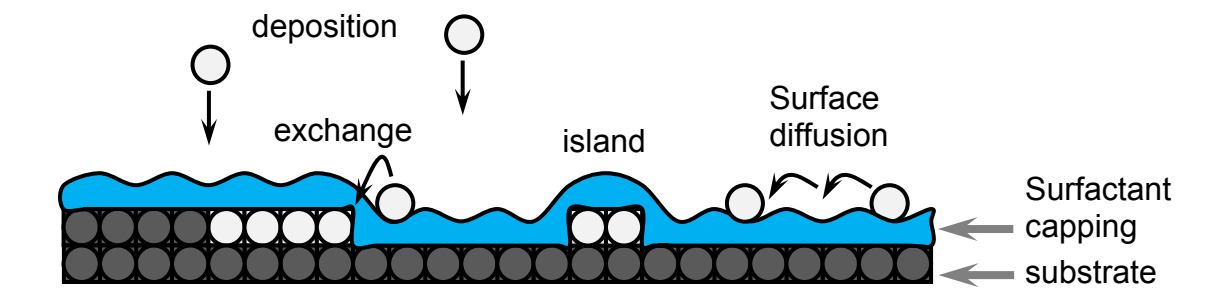


Figure 2. 10. The schematic view of processes during SME growth. Adsorbed atoms on top of the surfactant layer can diffuse over the surface. To incorporate into step edge the adatoms need to proceed through the surfactant capping layer.

This allows to determine the SiGe composition on the nanoscale via the measured height contrast and introduces a powerful method for studying of the atomic diffusion processes at the surface and at the surface steps.

3. Step properties

3.1 Step classification and symmetry of the substrate

In tendency to order our knowledge about matter we are looking for the laws which can arrange diversity of the states of the matter structures. The laws are beginning from fundamental feature of all structures we have described is symmetry invariance. A crystal is a self-assembled state of a matter with high symmetry of atomic structure. The transformations which a perfect crystal may undergo and remain unchanged are the symmetry group of transformations. The symmetry of a crystal is characterized by two symmetry groups: a translation group and a point group. The result of combination of translational symmetry and the point group symmetry is the space group. The space group contains all symmetry operations which takes crystal into itself.

The translational symmetry means that there are a large number of translations which remain crystal unchanged. This, of course, moves the boundaries, but we are interested in the behavior in the interior of the crystal.

Translation symmetry in 2D is characterized by two unit shift vectors \mathbf{a} and \mathbf{b} . Every equivalent point on the lattice can be reached by a lattice vector of the form

$$r_n = n_1 a + n_2 b$$

where n_1 and n_2 are integers.

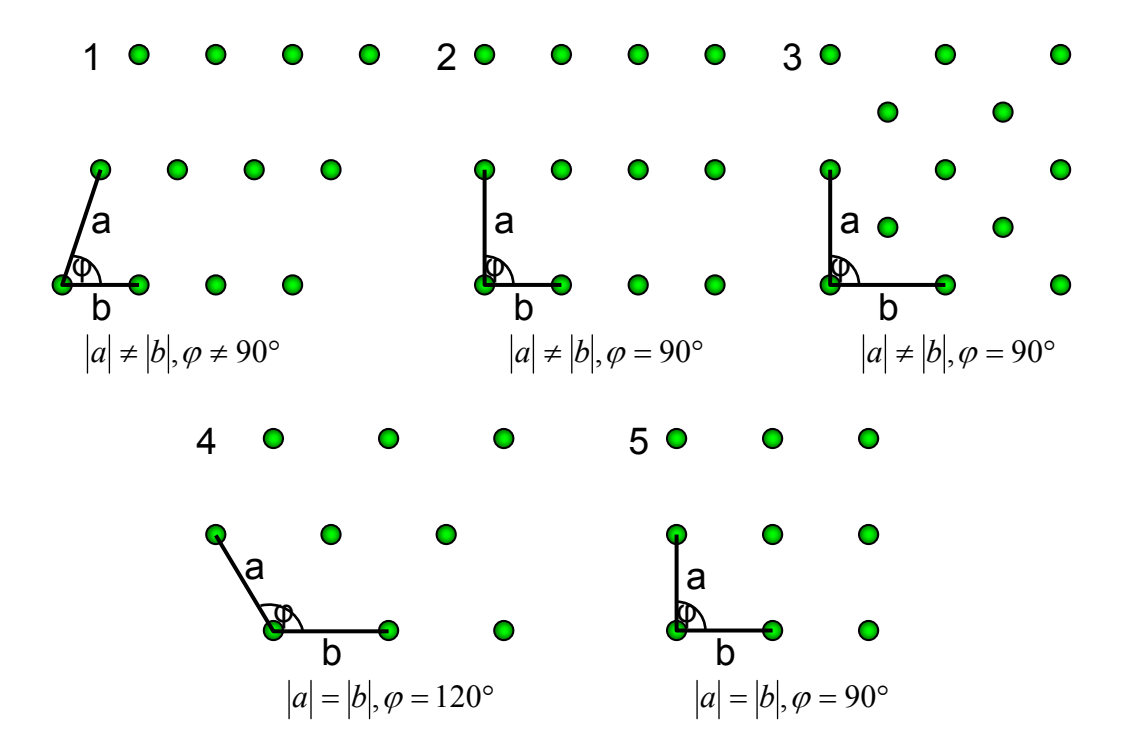


Figure 3. 1. The five fundamental two-dimensional Bravais lattices: 1 oblique, 2 rectangular, 3 centered rectangular, 4 hexagonal, and 5 square.

Figure 3. 1 presents five fundamental two-dimensional Bravais lattices. The minimal shift vectors \boldsymbol{a} and \boldsymbol{b} are called the basis vectors of the lattice.

The operations which have common (unmovable) points: rotations, reflections, inversions, rotary reflections are called point symmetry group operations. The possible different point groups which are allowed in a crystal are greatly reduced from those which might be allowed in a molecule because of the translational symmetry. Thus, only rotations of 60°, 90°, or multiples to these are possible in a crystal.

The principles of 2D lattice can be extended to lattice in 3D. In 3D lattice a translation symmetry is characterized by three shift vectors **a**, **b** and **c** Figure 3. 2.

$$r_n = n_1 a + n_2 b + n_3 c$$

where n_1 , n_2 and n_3 are integers. Instead of five possible sets of basis vectors in plane, 3D case has seven possibilities **Table 3.1**.

Table 3. 1. The seven different basis-vector systems or crystal system

Tuble 6. 1. The bevon different busis vector by stems of crystal by stems.		
Basis vector/crystal	Angles	Crystal system
axes		
$a \neq b \neq c$	$\alpha \neq \beta \neq \gamma \neq 90^{\circ}$	triclinic
$a \neq b \neq c$	$\alpha = \gamma = 90^{\circ}; \beta \neq 90^{\circ}$	monoclinic
$a \neq b \neq c$	$\alpha = \beta = \gamma = 90^{\circ}$	orthorhombic
$a = b \neq c$	$\alpha = \beta = \gamma = 90^{\circ}$	tetragonal
$a = b \neq c$	$\alpha = \beta = 90^{\circ}; \gamma = 120^{\circ}$	hexagonal
a = b = c	$\alpha = \beta = \gamma \neq 90^{\circ}$	rhombohedral
a = b = c	$\alpha = \beta = \gamma = 90^{\circ}$	cubic

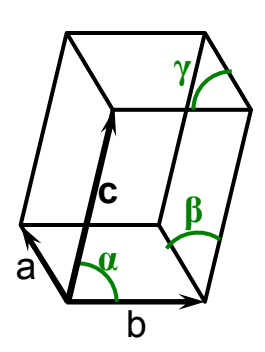


Figure 3. 2. Three basis vectors of primitive 3D lattice cell a, b and c with angles α , β and γ relative to each other.

Most elements crystallize in a cubic or hexagonal structure. For this reason and also because of their high symmetry, the cubic and hexagonal systems are particularly important. Different simple crystal structures and symmetry aspects of these structures can be found in [25]. In the following we will focus on principles of classification of the steps on surfaces.

The unit shift vectors **a**, **b**, **c** Figure 3. 1. form the basis of the lattice. In that basis we can determine crystallographic directions.

• The notation [l m n] denotes a direction in the basis of the direct lattice vectors, where three integers l, m and n are Miller indices.

- The notation $\langle l m n \rangle$ denotes all directions which are equivalent to [l m n] by symmetry of the crystal.
- The notation $(l \ m \ n)$ denotes planes orthogonal to a [l, m, n] direction in the basis of reciprocal lattice vectors.
- The notation $\{l \ m \ n\}$ denotes all planes which are equivalent to $(l \ m \ n)$ by the symmetry of the crystal.

To denote surfaces of a crystal the notation for a plane is used. Besides directions, the surfaces of a crystal can differ by reconstructions. To denote steps on a surface the $[l\ m\ n]$ notation is used. That means a step perpendicular to the $[l\ m\ n]$ direction. The notation $< l\ m$ n> denotes all step directions which are equivalent to $[l\ m\ n]$ by symmetry of the crystal.

The step definition is more complicated since lateral phase shift between surface reconstructions on adjacent terraces at step edge influences on the step structure. The surface reconstruction decrease the translation symmetry, the surface reconstructed unit cell has a larger size relative to underlying bulk structure. Due to that steps can differ by mutual lateral shift of surface reconstruction on lower and upper terraces at the step edge. That shift is a multiple of the bulk unit cell.

For instance we will describe the step classification on the Si(111) surface. To do that we will look into bulk structure of Si. Bulk of Si has a diamond structure. This structure can be presented as a sum of two face-centered cubic (fcc) structures, one of them is rotated on 90° and shifted on ¼ along its long diagonal relative to another Figure 3.3. This combination decreases a C₄ rotation symmetry for the (100) plane down to a C₂ rotation symmetry. That representation of a diamond structure can be useful for analysis of different surface structures. In the (111) plane the diamond structure and unreconstructed Si(111) surface still have the C_{3v} symmetry. At temperature lower than 870°C the Si(111) surface usually has the 7x7 reconstruction. The 7x7 is a structure well studied by different authors. Takanagi et al. [26] propose the dimmer-adatom-staking-fault (DAS) model of this reconstruction. The 7x7 structure is one of a family of DAS structures of the form (2n+1)(2n+1). The unit cell (UC) of the 7x7 reconstruction is shown in Figure 3.4. by coloured area. The structure has two triangular half-unit cells (HUCs). The green HUC is stacked with a normal sequence, see cross-sectional view **Figure 3. 4. b)** left of the image, and is called unfaulted halves. The pink HUC is stacked with a faulted sequence - bonds of the upper layer rotated by 180°, cf. a cross-sectional view in Figure 3. 4. b) right of the image, and is called faulted halves. It may be also said that the upper layer of faulted halves is mirror reflected to upper layer of unfaulted halves. The 7x7 including two half have 3 mirror planes $(01\overline{1})$, $(\overline{1}10)$ and $(10\overline{1})$ that corresponds to the initial C_{3v} symmetry of underlying substrate in a (111) plane. This means that the step directions are symmetry equivalent on the Si(111)7x7 surface and can be found by C_{3v} symmetry transformations applied to each direction. The Si(111)-7x7 surface reconstruction has $7 \times 7 = 49$ times larger area than an unreconstructed 1x1. Thus, 49 different phase positions of 7x7 on lower and upper terraces relative to each other are possible. To denote $|\overline{1} \ \overline{1} \ 2|$ and $|11\overline{2}|$ -type steps on the Si(111) surface a short notation can be used as U and F steps, respectively [13,27,28]. The U steps represent the ones terminated by unfaulted halves of 7x7 on the upper terrace at step edge, while the F steps are terminated by faulted halves on the upper terrace at step edge Figure 3.5. U(0,0) step is a step terminated at the boundaries of 7x7 unit meshes on both upper and lower terraces with zero phase shift between 7x7 structures on upper and lower terraces.

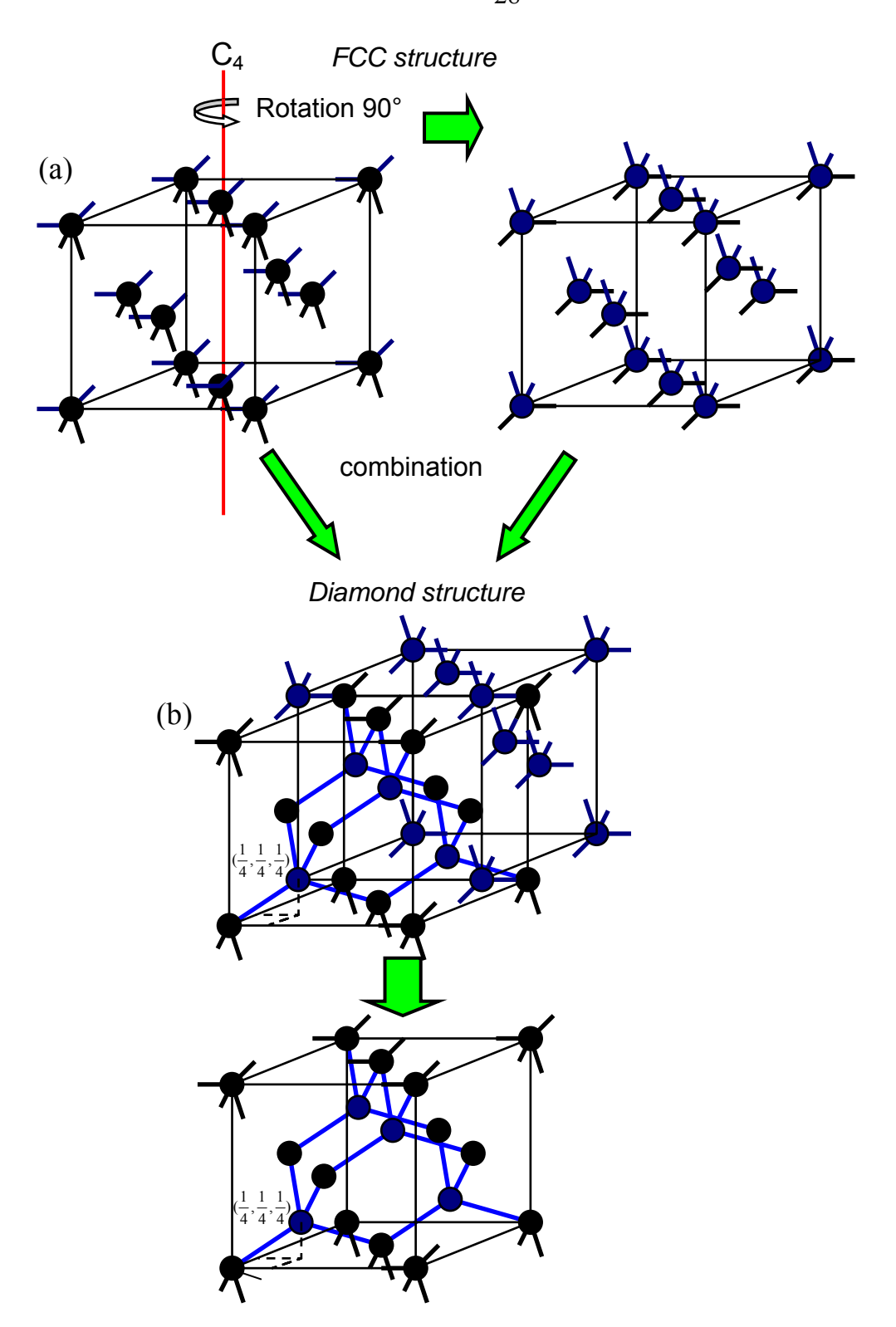


Figure 3.3. The diamond structure (b) consists of two inter-penetrating fcc lattices (a). This interembedding can be done as follows:

^{1.} one of fcc structures, with atom bonds orientation as shown in figure (a), is rotated relative to another by 90° around C_4 axes of the cube (a)

^{2.} a combination of two fcc structures which are displaced relative to one another by $\frac{1}{4}$ of the long diagonal of the cube (b).

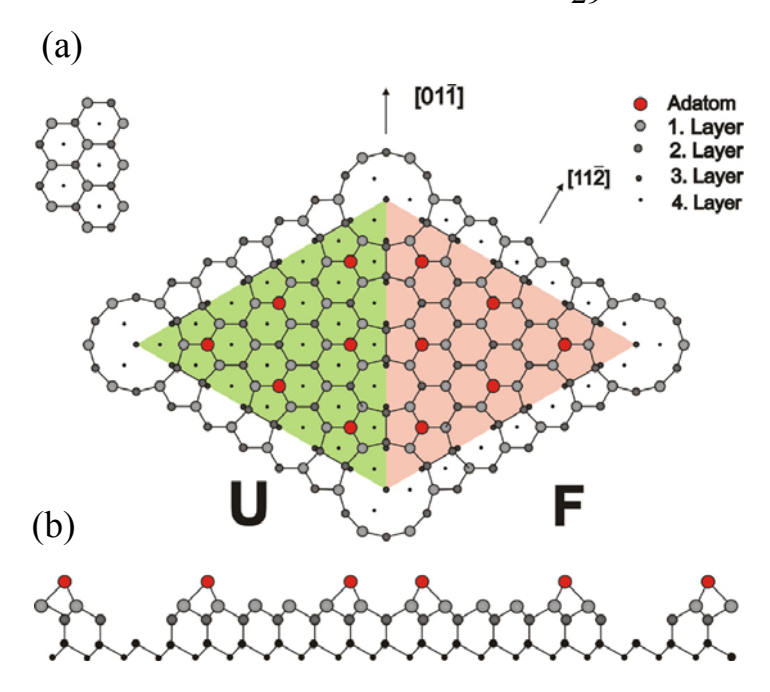


Figure 3. 4. (a) Top view of the unit cell of the DAS structure on the Si(111)7x7 surface. **(b)** Cross-sectional view along two arrows shown in (a).

To denote a step with shift of n position perpendicular to step edge and m position parallel to step edge, the notations U(n,m) and F(n,m) are used. Figure 3. 5. shows seven different positions in the direction perpendicular to step edge for both types of steps $[\overline{1} \ \overline{1} \ 2]$ and $[11\overline{2}]$, (U and F, respectively).

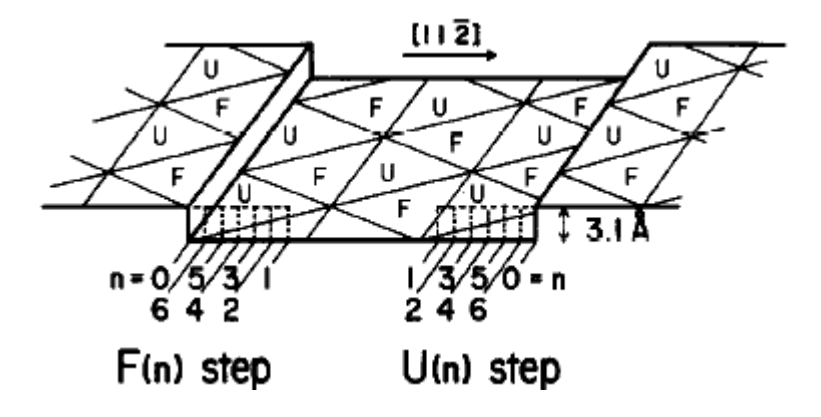
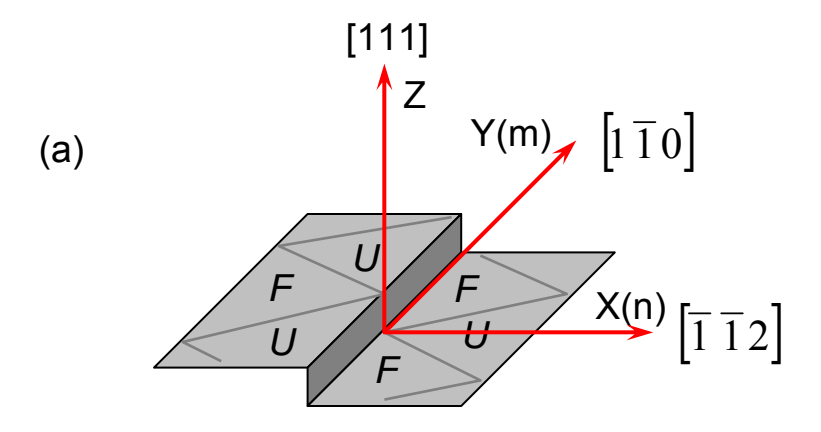


Figure 3. 5. Seven different positions of steps in the direction perpendicular to step edges are shown, the position of each step is indicated by n, where n is an integer of $0 \le n \le 6$. U and F denote the unfaulted and faulted halves of the (7x7) DAS structure, respectively.



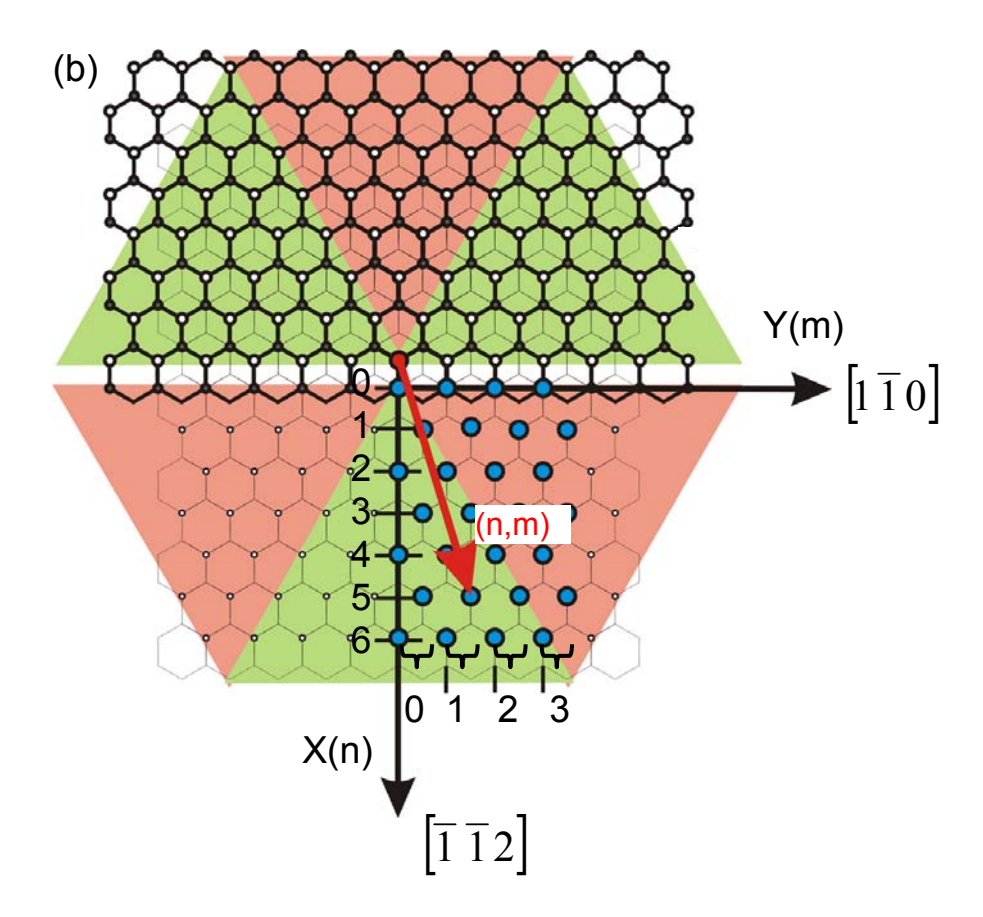


Figure 3. 6. (a) Basis vectors at the step; (b) – top view of the Si(111) surface at $[\overline{1}\ \overline{1}\ 2]$ step edge, 28 different phase positions of 7x7 unit cell on upper terrace relative to 7x7 unit cell on lower terrace shown by blue balls, (n,m) is a shift vector in the X-Y basis of the $[\overline{1}\ \overline{1}\ 2]$ step direction (a).

The number of different atomic positions along the step edges is reduced from 7 to 4 due to a mirror $(1\overline{1}0)$ plane symmetry of DAS structure **Figure 3.** 6. (b). Thus, we have 28 different positions **Figure 3.** 6. (b). instead of 49 allowed.

The notation of steps is generally like "surf. + surf. rec." + [l, m, n] (i, k) for one step direction or "surf. + surf. rec." + [l, m, n] [l, k] for the steps equivalent by symmetry of a crystal, where all [l, m, n] are integers, [l, k] are numbers of [l, k] unit cells indicating the phase shift vector in the basis of the step direction Figure 3. 5. a, and "surf. + surf. rec." is a notation of the surface with the surface reconstruction. For the steps on [l, k] mentioned above, [l, k] and [l, k] steps are [l, k] and [l, k] and [l, k] steps, respectively. The surfaces with different reconstructions have different families of the steps.

3.2. Growth properties of steps

3.2.1 Energy of steps

The thermodynamic properties of a single step are defined by the step free energy per unit length γ which, because of the underlying crystal structure, is generally a function $\gamma(\theta)$ of the in-plane step orientation angle θ (see **Figure 3.** 7) [29].

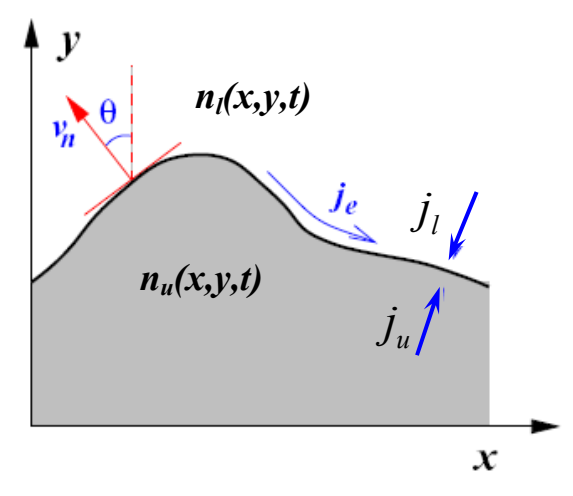


Figure 3. 7. The local step orientation is described by the angle θ between the step normal and the y-axis. The step moves at speed v_n in the normal direction. The adatom diffusion field n(x, y, t) is defined on both the upper and lower terrace. Step atoms contribute to the step edge current j_e , while terrace adatoms attaching to, detaching from, or crossing the step are included in the mass currents j_u and j_l

The free energy F of an arbitrary step configuration y(x) is obtained by integrating along the step,

$$F = \int ds \cdot \gamma(\theta(s)) = \int dx \sqrt{1 + (dy/dx)^2} \gamma(\theta(x)), \qquad (3.1)$$

where s denotes the arc length along the step and $\theta(x) = \arctan(dy/dx)$. From (3. 1) the step chemical potential, i.e. the free energy change upon adding an atom to the step, can be derived by functional differentiation [30]. This yields the expression

$$\mu = \Omega \frac{\delta F}{\delta y} = \Omega \widetilde{\gamma} k , \qquad (3.2)$$

where Ω denotes the area occupied by a surface atom, κ is the step curvature, and the quantity $\tilde{\gamma} = \gamma + d^2 \gamma / d\theta^2$ is known as the stiffness of the step. The step stiffness appears in a local version of the Wulff construction, which relates the step free energy to the equilibrium shape of two-dimensional islands [31,32]. In this formulation the equilibrium condition reads simply

$$\widetilde{\gamma}k = const.$$
, (3.3)

i.e. the local curvature of the equilibrium shape is inversely proportional to the local step stiffness.

The equilibrium shape of the 2D islands can be also found as the shape at which (3.1) reach the minimum at fixed area of island. This is analog of equilibrium shape of 3d crystal. If the temperature is lower than temperature of roughening transition we can speak about energy of steps. From equilibrium shape of the islands the step energy can be found by 2d Wullf construction [33]. The geometric interpretation of the Wulff theorem is the Wulff construction, which is defined as follows: At each point of the polar plot of the free step energy $\gamma(\theta)$ Figure 3. 8, a straight line perpendicular to radius vector to that point is drown; the inner envelope of the resulting family of lines is then geometrically similar to the equilibrium shape [31]. The step energy minima "A" and "B" on the energy plot diagram Figure 3. 8 correspond to the preferred step orientations with front perpendicular to \overline{OA} and \overline{OB} vectors.

Usually the steps with a high density of atom packing at the step edges are observed on the surface. The low index step directions: $\langle \overline{1} \ \overline{1} 2 \rangle$, $\langle 11\overline{2} \rangle$ and $\langle 1\overline{1} 0 \rangle$ are observed on the Si(111)-7x7 surface. Step directions which usually occur during growth or annealing will be called as preferred step directions. The $\langle \overline{1} \ \overline{1} 2 \rangle$ steps with front parallel to the 7x7 boundaries is the most stable steps on the Si(111)-7x7 surface. The $\langle \overline{1} \ \overline{1} 2 \rangle$ steps are found to occur during Si on Si(111) epitaxy [34]. The preferred step directions can be changed with a modification of the surface structure by adsorption of a foreign element. So, Bi terminated Si(111) $\sqrt{3}$ x $\sqrt{3}$ -R30° surface has a 30° rotated structure. The $\langle \overline{1} \ \overline{1} \ 0 \rangle$ steps with front parallel to the $\sqrt{3}$ x $\sqrt{3}$ -R30° cell boundaries were found as preferred steps on the Si(111)-Bi- $\sqrt{3}$ x $\sqrt{3}$ surface [35,36].

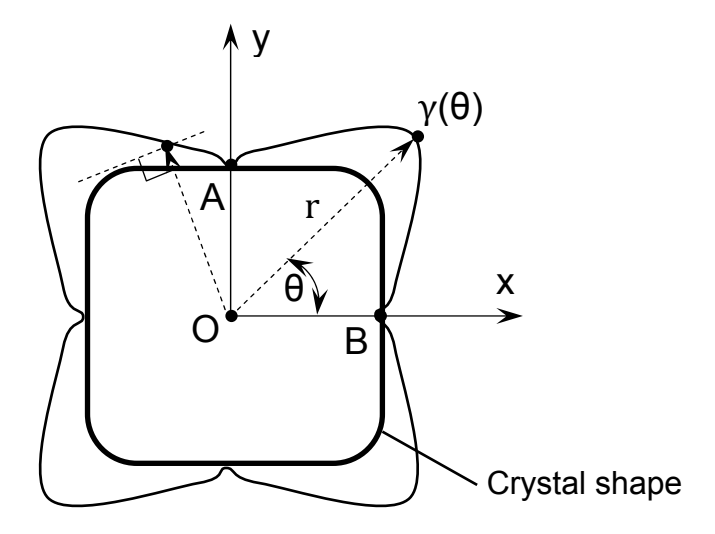


Figure 3. 8. Energy Wulff diagram of the steps on the surface.

The step energy and activation energy for attachment as well as preferred step directions are also depend on mutual shift of the surface reconstructions on upper and lower terraces at the step edges [36].

3.2.2 Kinetic processes at steps

Kinetic processes at steps (Figure 3. 9 (b)) include:

- Attachment and detachment **Figure 3. 9 (b)** (1), (2). These processes actually consist of two stages: When attaching to the step, an adatom first attaches to a straight step segment and then moves along the segment (**Figure 3. 9 (b)** (5)) until it reaches a kink, where it is incorporated (**Figure 3. 9 (b)** (3), (4)); similarly a detachment event requires first that an atom detaches from a kink to the straight step and subsequently detaches from the step segment to the terrace.
 - Diffusion along the step edge Figure 3. 9 (b) (5).
- Step crossing Figure 3. 9 (b) (7). An atom may also cross a step without attaching to a kink; this happens if the kink concentration is low and the binding to the straight step is weak, so the step atom detaches from the straight step before a kink is encountered.
- One-dimensional nucleation **Figure 3. 9 (b)** (8) [37]. If two step atoms are present simultaneously on a straight segment of the step, they can meet and form a step dimer, which is essentially a pair of kinks of opposite sign. This provides a nonequilibrium mechanism for the creation of kinks, in addition to the thermally excited kinks that are present in equilibrium. If step atoms cannot detach to the terrace, the typical distance between kinks created by one-dimensional nucleation is

$$l_{1d} \sim \left(\frac{D_e}{F_{1d}}\right)^{1/4} = \left(\frac{\exp\left(\frac{-E_d}{k_B T}\right)}{F_{1d}}\right)^{1/4},\tag{3.4}$$

where $D_e = a v \exp\left(\frac{-E_d}{k_B T}\right)$ is the diffusion coefficient of a step atom along a straight step

segment, and F_{1d} is the one-dimensional flux impinging onto the step from the terrace [38,39]. Generalizations of (3. 4) to other conditions can be found in [40,37,41]. The typical distance between equilibrium kinks is [42]

$$\tilde{l}_{1d} \sim \frac{a}{2} \exp\left(\frac{E_k}{k_B T}\right),$$
(3.5)

where E_k is the kink formation energy, and a is an interatomic distance.

• Diffusion along a rough step. Since steps always contain a finite concentration of kinks (of equilibrium or nonequilibrium origin), mass transport by step edge diffusion requires that step atoms are able to cross kinks and corners. The diffusion along a rough step is therefore considerably slower than the diffusion along a straight step segment. As indicated in **Figure 3. 9 (b)** (6), a step atom crossing a kink "from above" first has to round the kink

and then detach from it onto the step. Kink rounding is often associated with an additional energy barrier [43,44,45].

The attachment rates $k_+^{u,l}$ for adatoms from upper and lower terraces into step edge were introduced by Schwoebel in his paper [46]. Schwoebel and Shipsey were the first who explored the consequences of attachment asymmetry $(k_+^u \neq k_+^l)$ for the stability of growing stepped surfaces [46,47]. There are differ *normal Ehrlich-Schwoebel (ES) effect* $k_+^u < k_+^l$ and *inverse E-S effect* $k_+^u > k_+^l$. These attachment asymmetries can be also considered for the kinks **Figure 3. 9 (b)** (3), (4).

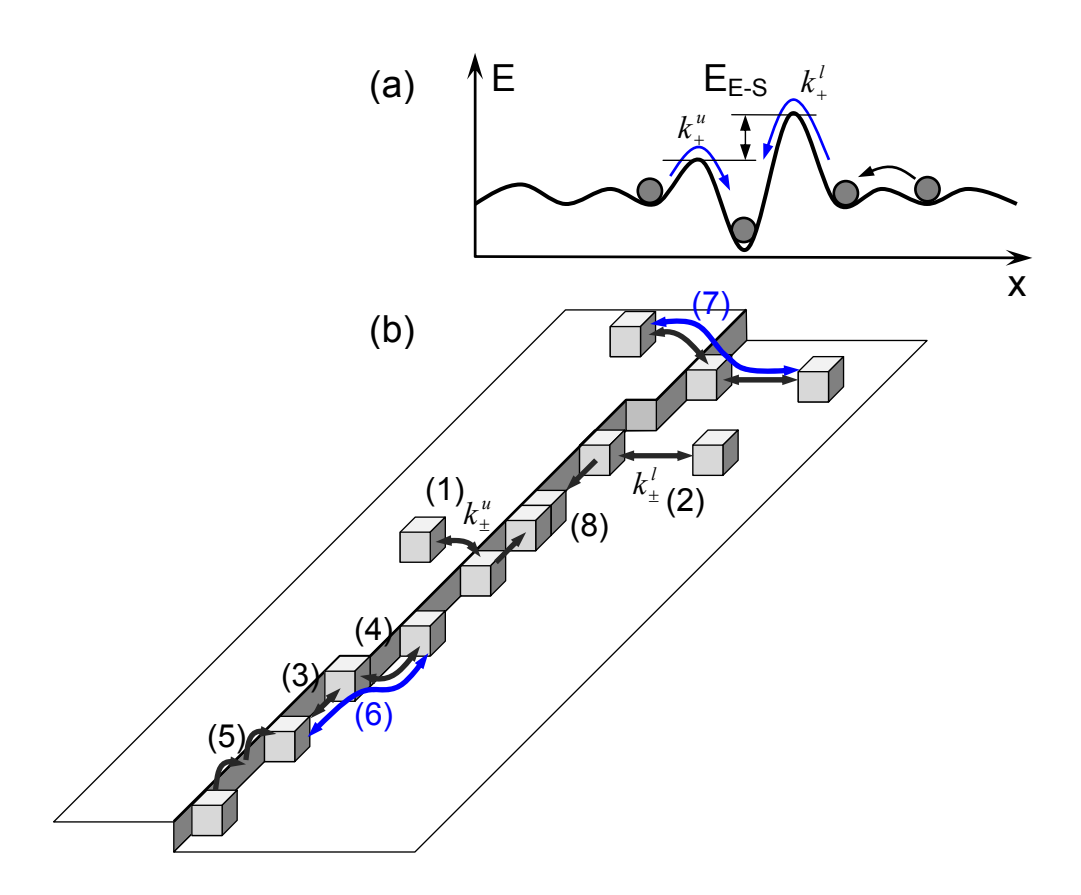


Figure 3. 9. The elementary processes at step edges (b): (1) – attachment-detachment from upper terrace k_+^u , (2) – attachment-detachment from lower terrace k_+^l , (3) – attachment –detachment into kink from left, (4) – attachment detachment into kink from right, (5) – atom diffusion along a step edge, (6) – kink crossing, (7) – step crossing, (8) – 1D island nucleation. Attachment-detachment from upper and lower terraces can differ by the activation energy E_{E-S} ($k_+^u \neq k_+^l$), this difference is named Echrilich-Schwoebel barrier at a step edges (a).

3.2.3 Transparent steps

The step crossing effect (Figure 3. 10) was first considered as so-called step *permeability* or *transparency* phenomenon in [48, 49]. At the atomic scale, this phenomenon results from the ability of an adatom to cross the step edge without visiting the kink sites at the edge [2] Figure 3. 10. The downward or upward net flux of adatoms crossing the edge of the permeable step will take place given the non-zero difference of the concentrations of adatoms on the adjacent terraces.

Usually the step crossing flux j_{cros} as well as the fluxes of adatoms incorporating into the step from the lower (upper) terraces $j_{l(u)}$ are assumed to be proportional to the relevant driving forces: $j_{cros} = \beta_p(n_l - n_u)$ and $j_{l(u)} = \beta_{inc}^{l(u)}(n_{l(u)} - \tilde{n})$, where n_l and n_u are the concentrations of adatoms on the lower and upper terraces, respectively, and \tilde{n} is the equilibrium adatom concentration on the terrace. The step permeability coefficient β_p and the incorporation coefficients $\beta_{inc}^{l(u)}$ are commonly treated as phenomenological parameters. Such a phenomenological approach provides a relatively easy way to describe growth with the permeable steps. The kinetics of the second layer nucleation in the 3D growth of the islands was described with the step permeability effect in [50].

The balance equations for incorporation and climbing fluxes read:

$$\begin{split} &j_l = j_{inc}^l + j_{cros}^l = \beta_{inc}^l (n_l - \widetilde{n}) + \beta_p (n_l - n_u), \\ &j_u = j_{inc}^u + j_{cros}^u = \beta_{inc}^u (n_u - \widetilde{n}) + \beta_p (n_u - n_l), \text{ here } j_{cros}^l = -j_{cros}^u. \end{split}$$

In the symmetric case of the attachment barriers from lower and upper terraces the incorporation coefficients for attachment β_{inc}^l and β_{inc}^u have the same value: $\beta_{inc}^l = \beta_{inc}^u = \beta_{inc}$. Then sum of incorporation and crossing fluxes can be written as:

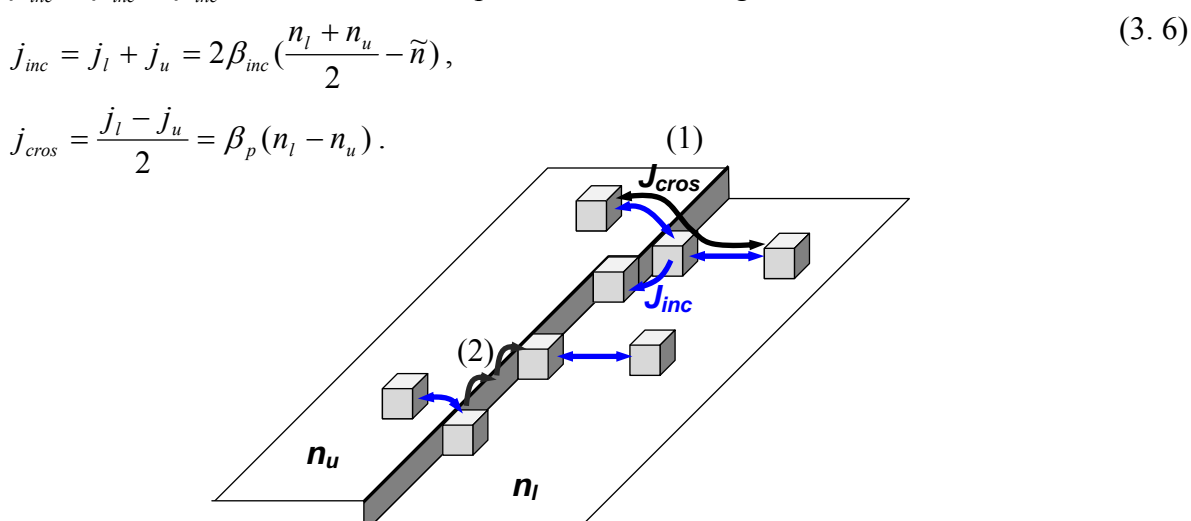


Figure 3. 10. The step crossing process (1) consists of an adatom attachment (detachment) to the step from lower terrace and detachment (attachment) to the step from upper terrace. Before detachment the adatom can diffuse along the step (2) without visiting the kinks.

The ratio of the crossing and incorporation fluxes is proportional to the ratio of the permeability and incorporation coefficient:

$$\frac{j_{cros}}{j_{inc}} \propto \frac{\beta_p}{\beta_{inc}} = \eta , \qquad (3.7)$$

The step is permeable if the ratio $\frac{\beta_p}{\beta_{inc}} = \eta >> 1$. And the step is impermeable if $\eta << 1$, that means that the edge adatom much more probably reaches the kink than detaches from the step.

3.5. Exchange intermixing at step edges

An adsorbed atom can have different positions on the surface with different activation energy for an exchange intermixing. **Figure 3. 11** shows six different positions of an atom at the surface. Position (1) corresponds to a single adatom on the terrace, (2) corresponds to a single adatom at the step edge, (3) – atom in the kink, (4) – atom in the step, (5) – atom in the upper surface layer, and (6) – atom in the bulk of a crystal. The activation energy for an exchange can be estimated qualitatively on a simple cubic model **Figure 3. 11** as a function of number of neighbors (neighbor atoms), $E_{exchange} = f(n,m) \propto (n+m-1) \cdot \Delta E(n,m)$. Where n is a number of neighbors for an adsorbed atom (purple cube), and m is a number of neighbors of an atom for exchange (can be any neighbor yellow cube), and (–1) to exclude double counting of common bonds. An atom adsorbed at position (1) have a minimal number of neighbors: 1 neighbor **Figure 3. 11**. The following adsorbed atoms have correspondingly: (2) -2, (3) -3, (4) -4, (5) -5, and (6) -6 neighbors.

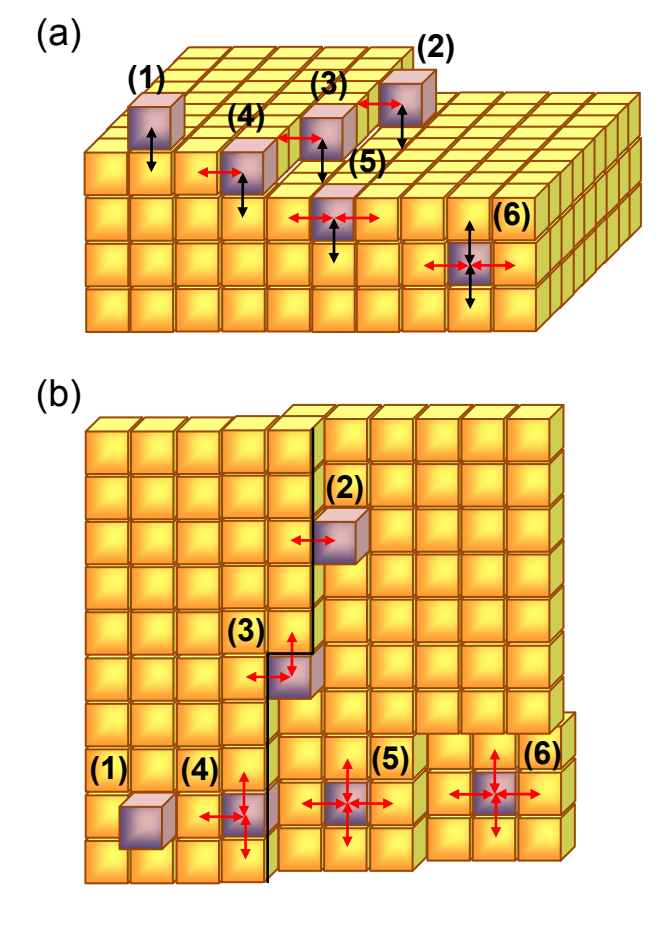


Figure 3.11. Side cross section view (a) and upper view (b) of the different positions (1) - (6) of adsorbed atom (purple coloured cube) with different number of neighbors (black arrows – vertical, neighbors and red arrows – lateral neighbors) at the surface.

The neighbor atoms at (1) position have a minimal number of neighbors for vertical exchange, upper (purple) atom has one neighbor below, and underlying neighbor atom has 6 neighbors in sum it will be (n+m-1)=6. The same (n+m-1)=6 number of neighbors can be found for lateral exchange perpendicular to the step edge for atom at position (2), and for lateral exchange along the step edge for atom at position (3). (n+m-1)=7 for vertical exchange at position (2), for lateral exchange perpendicular to the step edge at position (3) and for lateral exchange along step edge at position (4). (n+m-1)=8 for vertical exchange at position (3) and for lateral perpendicular to the step edge at position (4). (n+m-1)=9 for vertical exchange at position (4) and for lateral for position (5). (n+m-1)=10 for vertical exchange at position (5). And maximal (n+m-1)=11 can be found for the bulk diffusion, position (6).

In Bi-SME Ge on Si(111) the vertical exchange intermixing **Figure 3. 12** (position (1) **Figure 3. 11**) is suppressed by surfactant spacer between substrate and adatom adsorbed on the surface, $E_{Ge-Bi}^{ex} > E_{Ge-Si}^{ex}$. During growth Ge atoms attach to the step edges (E_{Ge-Bi}^{ex} is lower at step edges than on terrace) and take positions (2), (3) **Figure 3. 11**. Therefore the easiest intermixing is observed at the step edges at positions (2) and (3) **Figure 3. 11**. The lateral exchange intermixing (red arrows **Figure 3. 11**) is easier than vertical intermixing (black arrows **Figure 3. 11**) since the surface atoms in lateral intermixing have a less number of neighbors (**Figure 3. 11**). The process of vertical intermixing at the terrace during annealing and at the step edges of Bi terminated Si(111) $\sqrt{3}$ x $\sqrt{3}$ -R30° surface during growth were studied in [24]. The effective activation energy for vertical exchange intermixing at the step edges (positions (2), (3), (4) **Figure 3. 11**) is about 1.9 eV [24], the activation energy for vertical exchange intermixing between two upper layers (position (5) **Figure 3. 11**) is 2.2 eV, the activation energy for a bulk diffusion (position (6) **Figure 3. 11**) is 3.2 eV [51].

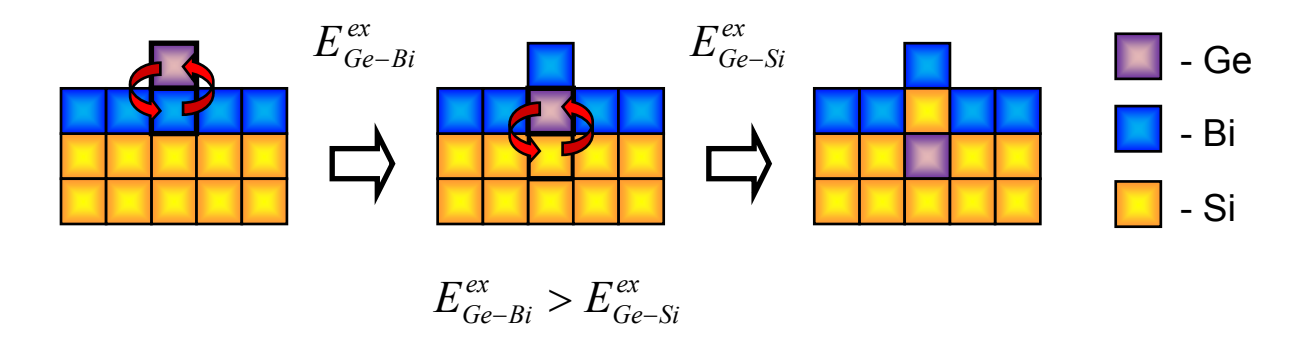


Figure 3. 12. Schematic side view of the vertical exchange of Ge atom on a terrace of Bi terminated Si(111) surface.

4. Preparation of highly ordered Si(111) templates

4.1. Precise misscut angle of sample plus annealing procedure

The standard way of the preparation of a template includes several stages. The first is an orientation of the wafer by X-ray diffraction. After appropriate orientation the wafer can be cut and polished in the desired direction. The polishing, which can be mechanical and chemical polishing, allows to achieve appropriate smoothness. The accuracy of the surface orientation in the standard procedure is not higher than 5 - 10 minutes. Such surface misorientation from the singular ((100), (111), (110)) orientations results in surfaces containing regular steps as shown on **Fig. 4.1** (a), where θ is the misscut angle from a singular orientation n_{θ} .

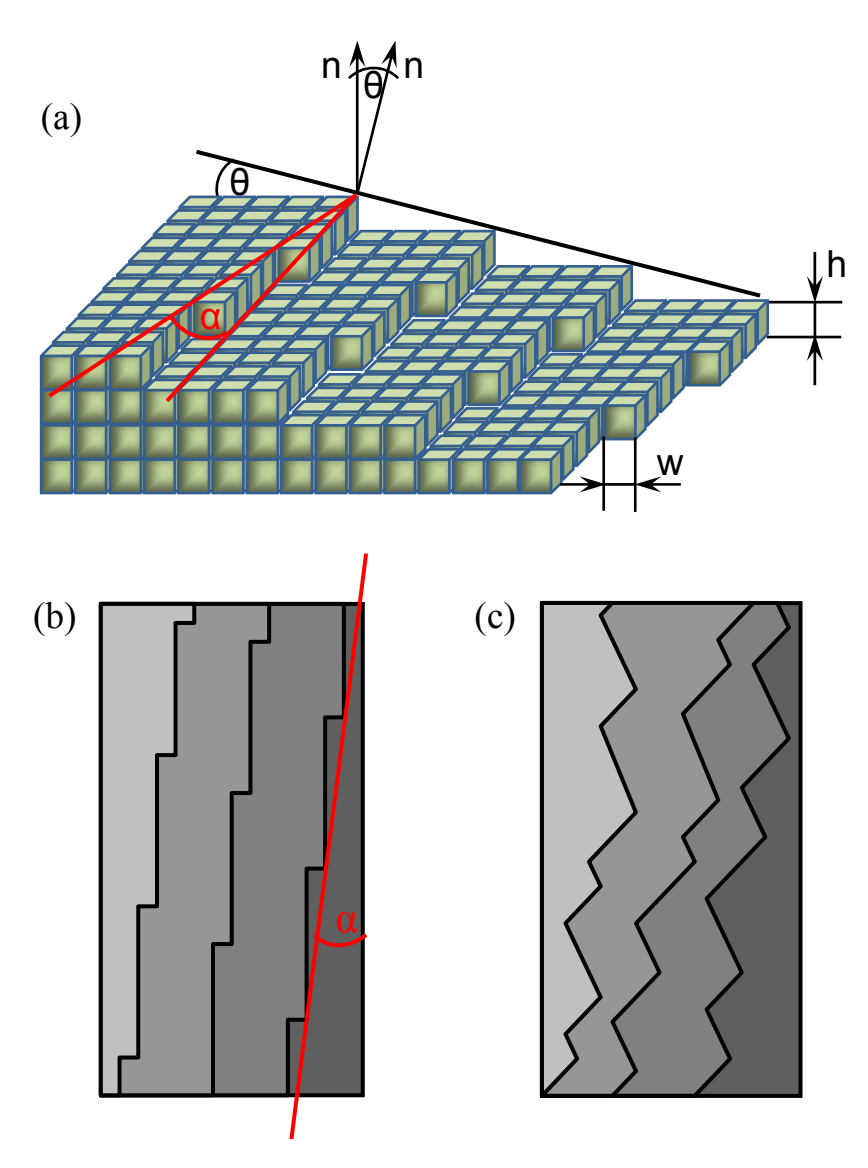


Fig. 4.1. a) Schematic 3D view of the stepped surface inclined from the singular (100) orientation on angle θ with azimuthal misorientation α ; b), c) top view of stepped surface, the facetted steps (c) or steps with regular kinks (b) are result of arbitrary azimuthal misorientation of a misscut angle α from the preferred step direction.

The average distance between steps d and height of the steps h are expressed by the relation

$$d = h/\tan(\theta). \tag{4.1}$$

Generally, the steps can contain kinks **Fig. 4.1 (b)** and facets **Fig. 4.1 (c)**. The straight segments of facets and straight segments between kinks are present by the stable steps with preferred directions. The regular kink density θ_k can be written as:

$$\theta_k = \tan(\alpha)/w, \tag{4.2}$$

where w – a height of the one kink, and α - the azimuthal misorientation from the preferred step direction. The highly ordered template with straight surface steps can be prepared by tilting toward azimuth of the preferred step direction. The template must be cut and polished with high accuracy, because of azimuthal misorientation α from the preferable step direction produces regular kinks (4. 2), **Fig. 4.1 (b)**. To have no more than one regular kink per one micrometer the accuracy for polar misscut angle α on the vicinal Si(111)7x7 surface must be $<\pm30$ sec. After polishing procedure the surface can have defects and contaminations. To clean and arrange the surface on atomic level an annealing procedure in UHV is used. Annealing at suitable high temperature is followed with desorption of the surface atoms, annealing also enhances the mass transport and adatom diffusion on the surface. The annealing starts from higher temperature and slowly goes down to the room temperature. That allows to clean and arrange the surface and reduce the concentration of surface defects to the equilibrium concentration at RT.

The periodicity of the surface structure has an influence on the step ordering on the surface. The preferred lateral positions of the steps are defined by the translation symmetry of the surface structure. The height w of the kinks **Fig. 4.1** (a) is usually equal to the size of the surface unit cell. The kinks with a larger size have a higher formation energy due to larger length w of the kinked step segment. Thereby, the surface with larger surface unit cell has a lower equilibrium concentration of the kinks - this is stabilization effect of the surface structure. The most stable steps on the Si(111)7x7 surface are the $\langle \overline{1} \ \overline{1} \ 2 \rangle$ and $\langle 11\overline{2} \rangle$ - steps. Because of the large size of the 7x7 unit cell and the high energy of kink formation the concentration of equilibrium kinks is low [52,53]. A similar stabilization effect of the surface structure has been observed for stepped metal surfaces with a large unit cell, such as Au(111) [54]. The stabilization effect of 7x7 structure can be observed at temperatures lower than 870°C (temperature of phase transition from 1x1 to 7x7 on Si(111) surface), therefore the annealing at the temperature lower than 870°C is the most important stage of the annealing procedure.

The method of preparation of highly ordered stepped Si(111)7x7 templates is described in [55,52,53]. Mainly, the preparation of a highly ordered stepped template faces the following problems: 1. problem of instability of the step arrangement induced by the current step bunching effect, 2. the tripling of the $\langle \overline{1} \ \overline{1} \ 2 \rangle$ steps [56] during phase transition from 1x1 to 7x7 structure and 3. the problem with the kinks induced by 7x7 domain boundaries at the step edges; the lateral phase shift between neighbour domains of the surface structure induces a kink at the step edge [52].

The first problem was solved by the orientation of the heating current parallel to the step direction. The problem of the tripling steps was solved by rapid quenching of the sample near the temperature of the phase transition from (1x1) to (7x7) $(880^{\circ}\text{C} - 860^{\circ}\text{C})$. The problem with the step kinks at domain boundary was solved by long time (1/2 - 1 h) of annealing at 850°C. The annealing at 850°C develops long-range 7x7 domains and reduces the density of domain boundaries and step kinks. The solution of the mentioned problems allows to form the straight steps without kinks over 8 µm length; actually, that distance was limited by accuracy of the surface orientation.

The requirement to a high accuracy of the surface orientation is not always achieved with standard procedure, in the following we consider an alternative method of preparation of highly ordered stepped template.

4.2. Mesa structures

Another way to produce an arranged stepped structure on the surface is step design on mesa structures. Mesa structures in micrometer range can be easy created on the surface in desired way. The mesas were used to fabricate large step-free regions on the surface [57]. The idea was to use the edges of the mesas to accumulate and localize atomic steps. In ideal case the steps are moving to the edges of the mesas during sublimation on bottom mesas or during deposition (step-flow growth) on top mesas, **Fig. 4.2**. New steps can be formed by nucleation of islands or vacancy islands at the center of flat mesa during adsorbate deposition or during sublimation, respectively. Therefore, the main requirement of the method consists in a preventing nucleation of islands at the center of flat mesas.

The question is: can the mesas be used to accumulate and localize atomic kinks in an analogous way, **Fig. 4.3**. It can be expected that this is more difficult problem because new kinks can be generated at the step edges by 1D nucleation. The 1D nucleation at step edge is easier than the nucleation of islands on the terrace. The most interested case with mesas perpendicular to $\langle \overline{1} \ \overline{1} \ 2 \rangle$ and $\langle 11\overline{2} \rangle$ steps on the Si(111) surface was studied in [6]. According to that work the ideal mechanism shown on **Fig. 4.3**. does not work so perfectly in case of Si(111) surface. But anyway, the authors found how the mesas can be used for the step arrangement.

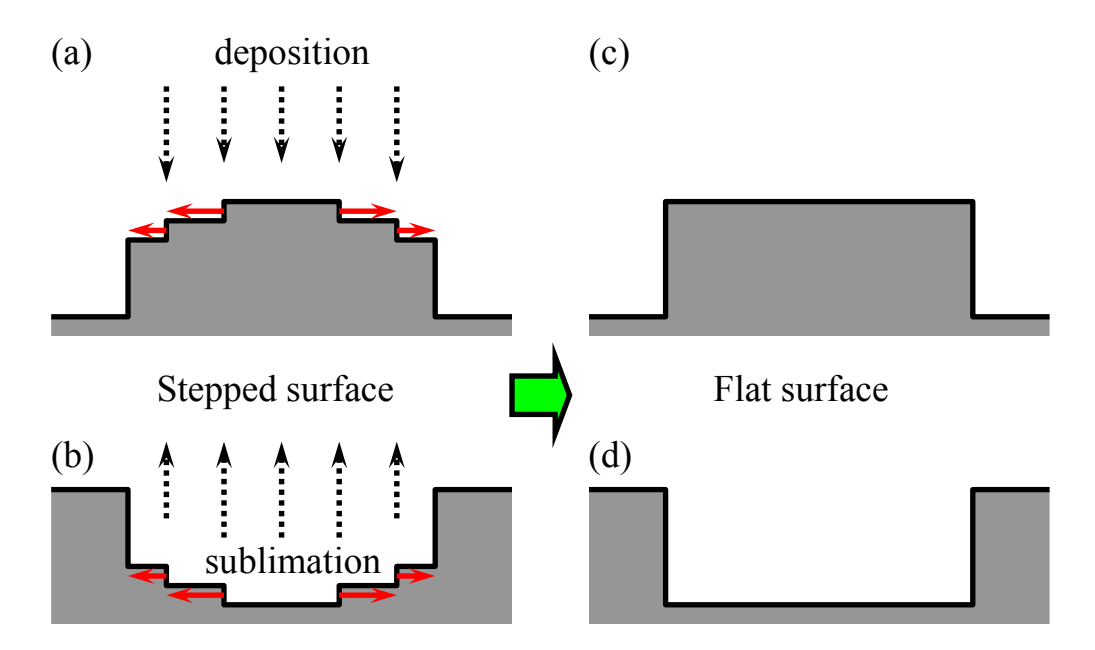


Fig. 4.2. Cross sectional view of stepped surface on top mesa (a) and bottom mesa (b); the steps moves in directions shown by red arrows from the center to the edge of mesas. The steps leave the mesas making them perfectly flat without steps (c), (d).

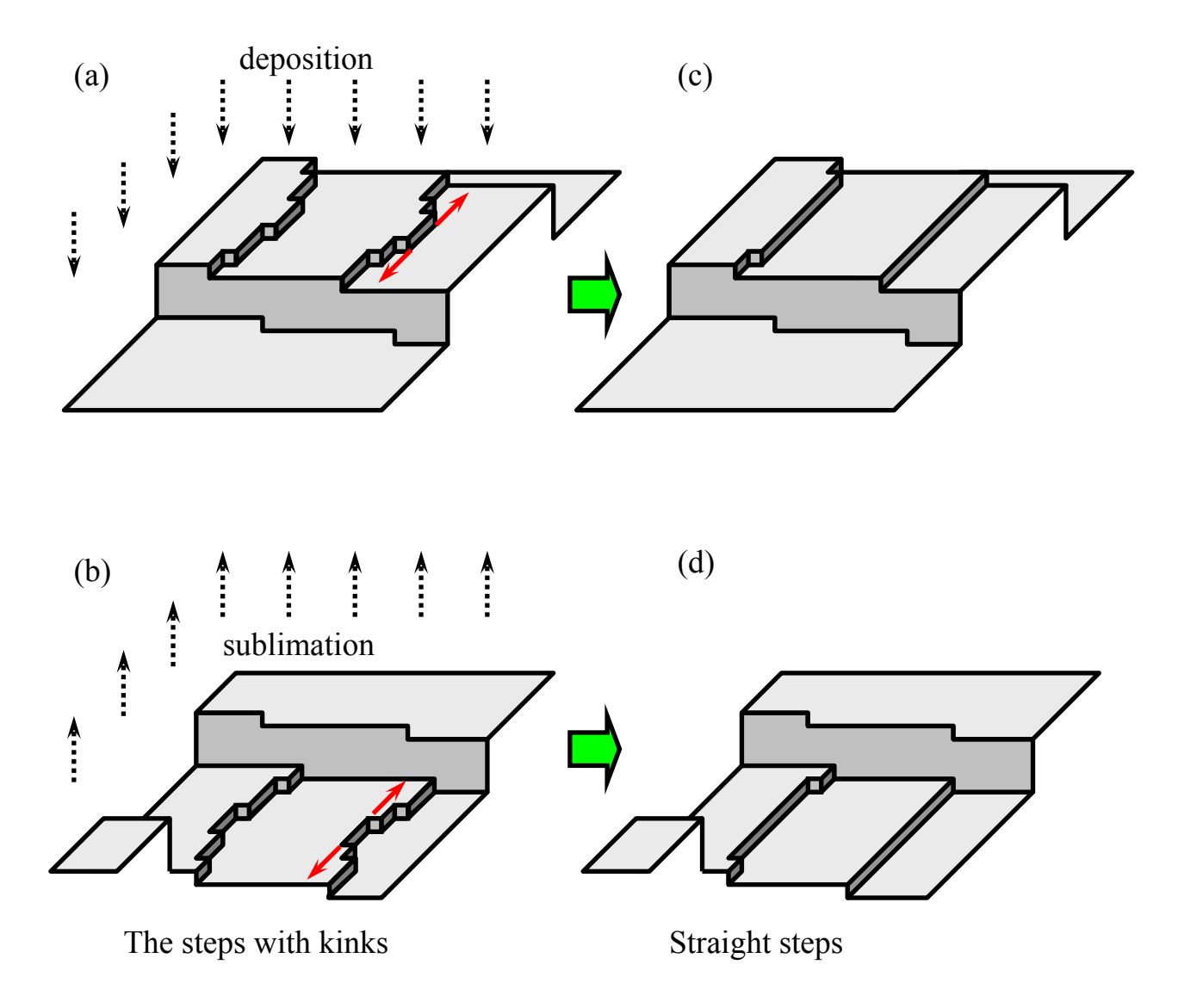


Fig. 4.3. The kinks are active place for attachment – detachment adatom process. Adsorption or desorption processes on the surface induce kinks movement. During deposition the kinks will move and accumulate at the edges on top mesa as shown by red arrows (a). During sublimation the kinks will move out on bottom mesa (b), the direction of kinks propagation also shown by red arrows. The straight steps can be formed when all kinks leave the steps and accumulate at the edges of mesas (c), (d). Curvature of the steps is opposite on top and bottom mesas according to geometry of these mesas (a), (b).

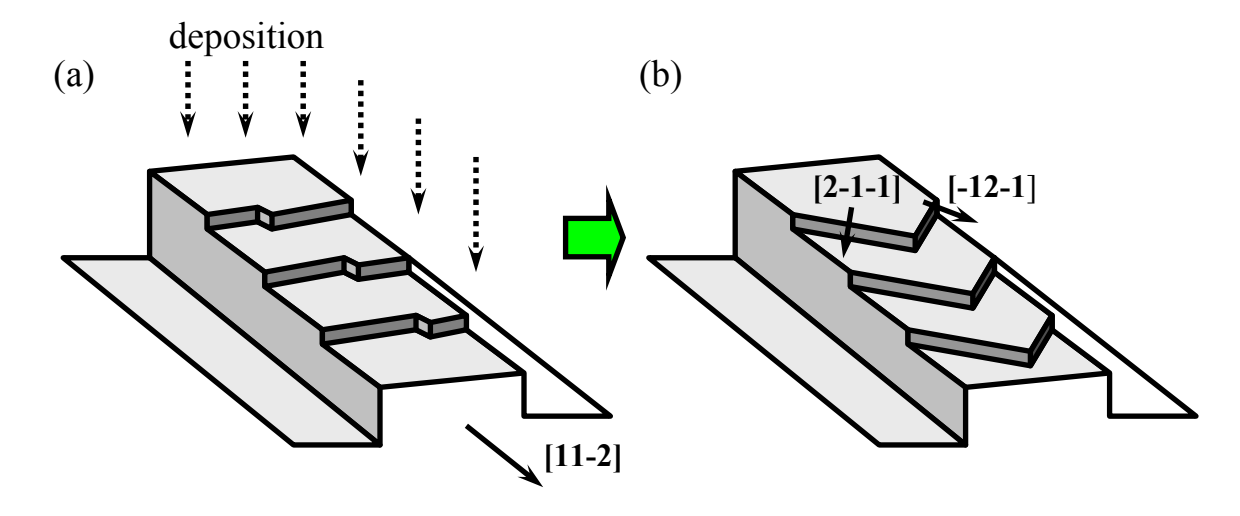


Fig. 4.4. During step-flow growth the [11-2] steps (a) transfer into more energetically preferable steps, i.e. $\langle \overline{1} \ \overline{1} \ 2 \rangle$ - type steps (b). The kinks on the $\langle \overline{1} \ \overline{1} \ 2 \rangle$ -type steps moved out by similar way as was shown on **Fig. 4.3.** (a).

An interesting behavior was found for 1- μ m-wide mesas perpendicular to $\langle 11\overline{2} \rangle$ steps [58]. During step flow growth the $\langle \overline{1} \overline{1} 2 \rangle$ steps were formed as shown on **Fig. 4.4.** It is known that the $\langle \overline{1} \overline{1} 2 \rangle$ -type step is energetically more stable than the $\langle 11\overline{2} \rangle$ -type steps [59,60]. It can be said that the step flow growth on 1 μ m-wide mesa top produces arrays of stable and straight steps. The macrokinks in the center on top the mesa were used in the next applications for positioning of nanostructures [61].

To exclude regular kinks produced by deviation of the missorientation the mesas perpendicular to $\langle \overline{1} \ \overline{1} \ 2 \rangle$ steps was used in [62]. The straight steps were formed only in the central area of the mesa due to a strong influence of the surface curvature on the surface energy at the edges of the mesas.

4.3. Step ordering by kink bunching

A new method of the step ordering was proposed in [63]. The method is based on the current induced kink bunching effect. To understand the current induced kink bunching effect we will start from the well known step bunching effect. The step bunching effect is well known as the result of step instability during growth or sublimation. **Fig. 4.5.** illustrates simple cases when stabilization and destabilization of the equidistant steps during growth and during sublimation are induced by normal *Ehrlich-Schwoebel (E-S) effect*. During growth an attachment process from the lower (leading) terrace stabilizes a configuration of equidistant, straight steps and attachment process from the upper (trailing) terrace destabilizes a configuration of equidistant, straight steps. In the symmetric case, when the kinetic conditions for attachment-detachment from upper and lower terraces are equal, the terrace width distribution stays unchanged.

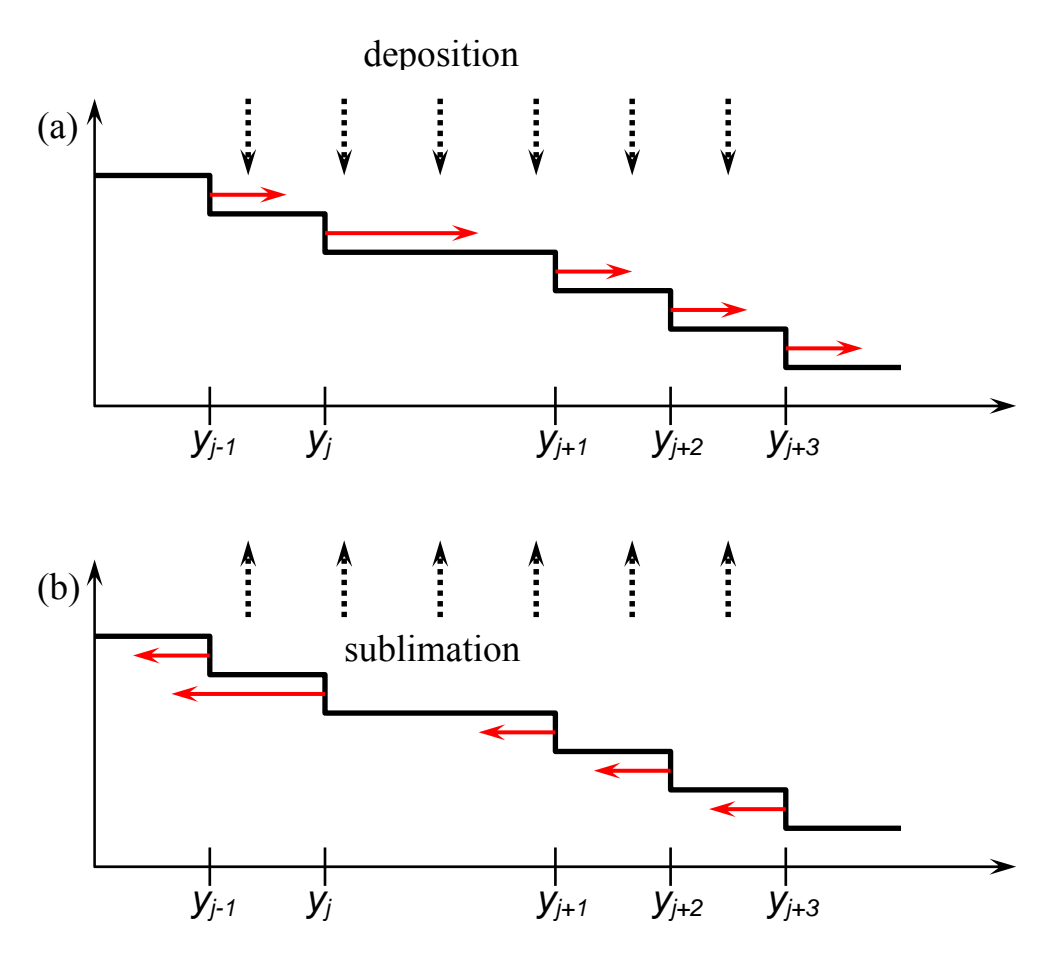
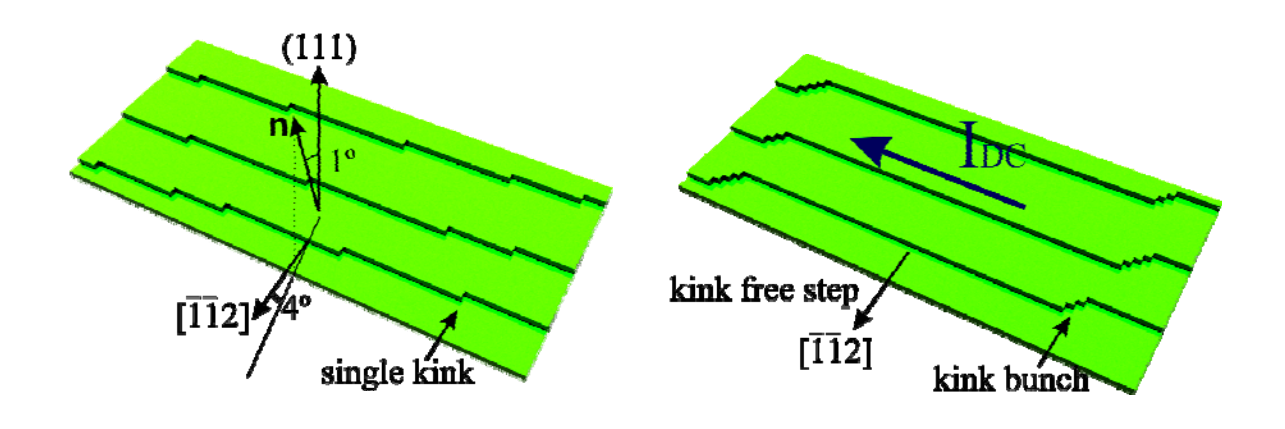


Fig. 4.5. Attachment process from lower terrace for the *normal E-S effect* stabilizes a configuration of equidistant straight steps during growth (a), the broader terrace $(y_{j+1} - y_j)$ adsorbs more atoms (proportional width of terrace) which incorporate into y_j step, the y_j step moves faster and due to that the distance between y_j and y_{j+1} steps decreases. So, stabilization (destabilization) effect will be found as decreasing (increasing) of width of broad terraces and increasing (decreasing) of width of short terraces. Sublimation process on the surface at the same *E-S effect* will destabilize a configuration of equidistant straight steps (b).

An asymmetry in the rate of attachment-detachment from the upper and lower terraces will stabilize or destabilize an equidistant configuration of the steps. *E-S effect* introduces asymmetry into that system. Normal and *inverse E-S effect* will give opposite effect on the step stabilization.

Another case of an asymmetry is electromigration of adatoms on the surface induced by direct current perpendicular to steps. Electromigration of adatoms on the surface perpendicular to step edges changes the symmetry of the attachment-detachment process from the lower and upper terraces. A current in step up and step down direction will give an opposite effect on the step instability [64,65]. The step bunching induced by current was reported for the first time by Latyshev [12]. The current induced step bunching can be used to form step free regions on the surface. The authors of ref. [11] used the electromigration effect to form straight $[\overline{1}\ \overline{1}\ 2]$ steps without kinks on the Si(111)7x7 surface. They found that the kink-up direction current at 800°C-830°C accumulates the kinks into bunches and leaves kink free regions about 1 µm length, **Fig. 4.6.**



Kink bunching → atomically straight steps

Fig. 4.6. The kink-up current forms the straight-step region which is 1 µm away in step length.

The temperature was chosen lower than the phase transition from $1x1 \rightarrow 7x7$ (870°) due to the importance of stabilization effect of the 7x7 reconstruction on the step edges. The appropriate misorientation of the substrate was 1° towards the $\left[\overline{1}\ \overline{1}\ 2\right]$ direction. In addition to the 1° polar misscut, an azimuthal misorientation of less than 3° from the $\left[\overline{1}\ \overline{1}\ 2\right]$ was intentionally introduced.

In the case of kinks at the steps the similar principles are working, the atoms attach to the step edge (2D - adsorb on the terrace) and diffuse along the step (2D - terrace) until reach the kink (2D - step). To describe the stabilization or destabilization of a configuration of the equidistant kinks we can interpret the **Fig. 4.5** as a top view of the step edges on the surface and step are transferred to kinks.

5 Experimental techniques

The experiments were performed in a homemade ultra-high vacuum (UHV) apparatus with base pressure $3\times10^{-11}-10^{-10}$ mbar. A schematic view of the system is shown in **Figure 5. 1**. The machine consists of a load-lock chamber, tip preparation chamber, STM chamber, MBE chamber, and a set of vacuum pumps. The load-lock chamber is used to introduce the samples from air to the UHV part of the system. The tip preparation chamber contains a tip thermal cleaning system.

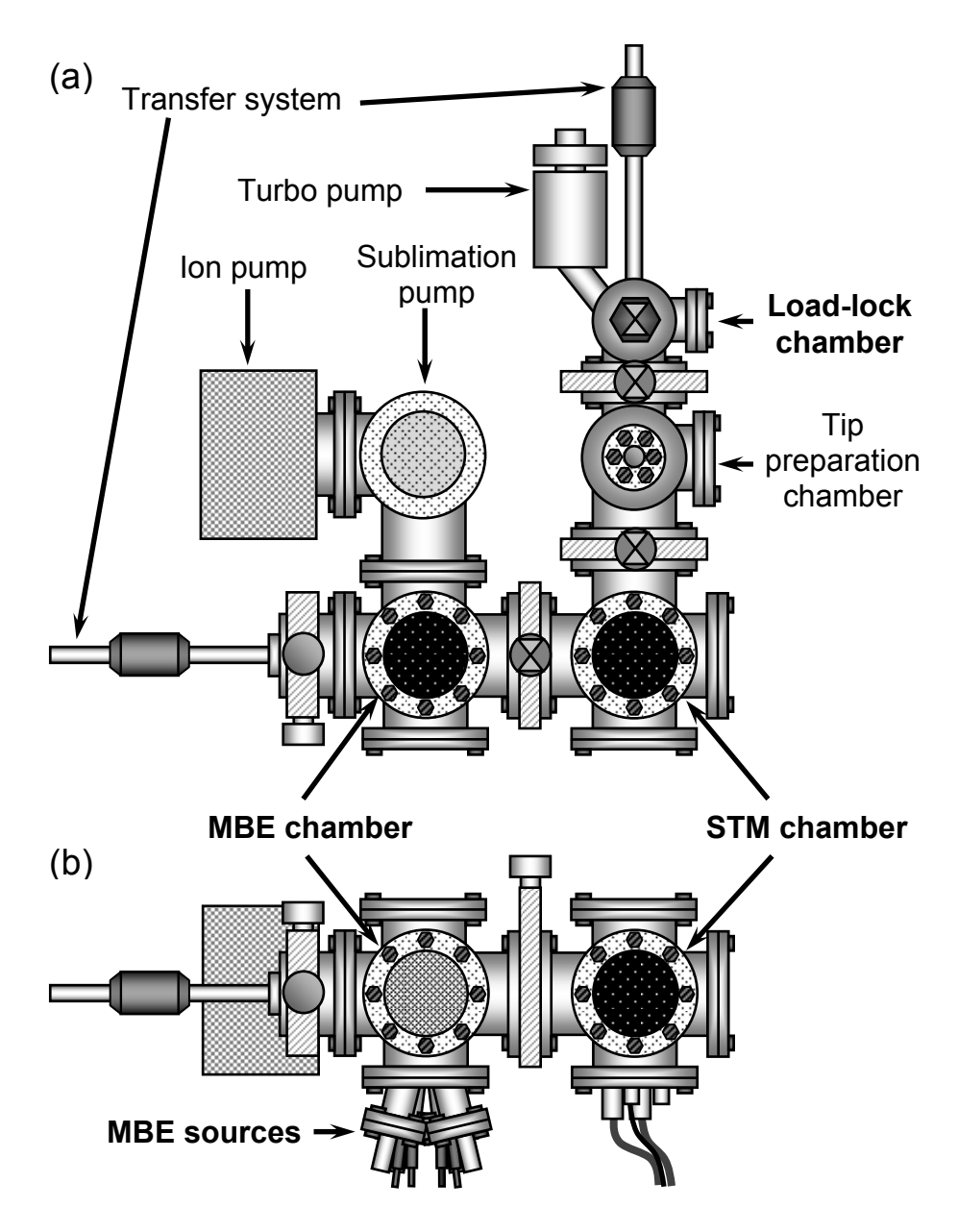


Figure 5. 1. Schematic top (a) and side (b) views of the experimental system.

The cleaning of the sample and deposition are carried out in the MBE chamber. The MBE chamber is equipped with Si and Ge electron beam evaporators, Bi and C_{60} evaporation cells, quartz-crystal monitor, infrared pyrometer, and sample transfer mechanism.

The design of the system allows to perform the subsequent and simultaneous deposition of materials and control a sample temperature and evaporation rates. After growth the sample can be transferred to the STM chamber for subsequent STM measurements.

5.1 Molecular beam epitaxy system

The MBE system consists of a UHV chamber equipped with four evaporators. A commercial W.A. Technology Ltd standard Knudsen cell with stabilized temperature controller (**Figure 5. 2**) was used for Bi and C_{60} evaporation.



Temperature controller



Figure 5. 2. W.A. technology Ltd standard Knudsen cell with stabilized temperature controller.

The schematic cross-sectional view of the Knudsen cell is shown in **Figure 5. 3**. The Knudsen cell consists of a W-heater fixed between two ceramic cylinders, water cooling system including water cooling jacket with water tubes, Ta heat shields between W-heater and water cooling jacket, thermocouple, and crucible. A pyrolytical boron nitride (PBN) crucible was used in the Bi evaporator and graphite crucible was used in the C_{60} evaporator. The rate of evaporation is determined by the temperature of the crucible. R(W)-type thermocouple was used to measure temperature of the crucible.

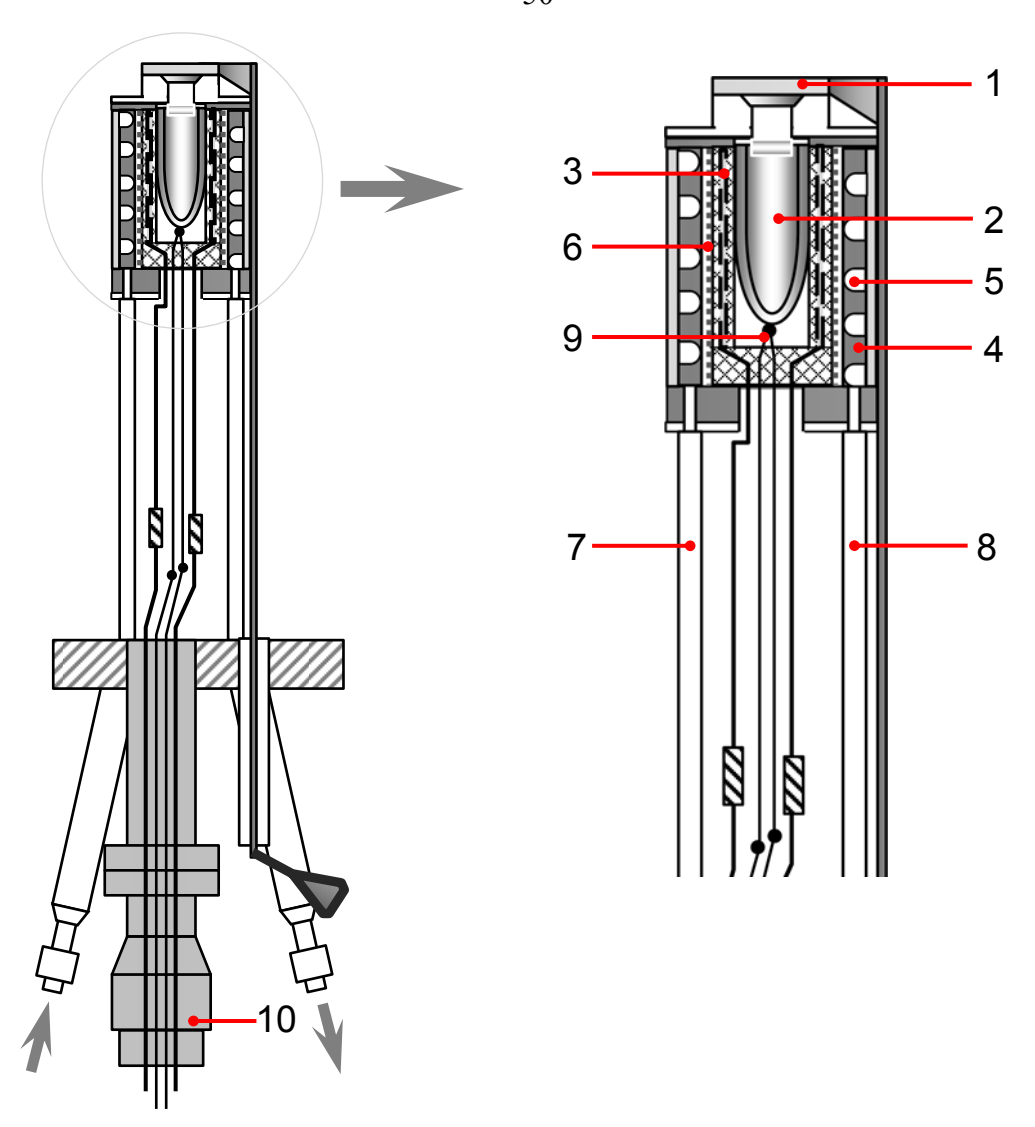


Figure 5. 3. Cross-sectional view of the Knudsen cell comprises a shutter (1), PBN or graphite crucible (2), W heater (3), water cooling jacket (4), water channels (5), Ta heat shields (6), water inlet (7) and outlet (8) tubes, thermocouple (9), electrical and thermocouple feedthrough (10).

A homemade electron beam evaporator was used to vaporize Ge and Si. Its schematic view is shown in **Figure 5.** 4. The central rod of the evaporator is connected to a high voltage source (2.5÷3 kV). Electrons are emitted from a glowing filament and are accelerated towards the central rod/crucible of the evaporator. A current of 10÷50 mA will flow to heat the crucible with Ge or Si. A Ta crucible and a graphite crucible are used in the Si evaporator and the Ge evaporator, respectively. The rate of evaporation is determined by a temperature of crucible which can be adjusted by emission current and by acceleration voltage.

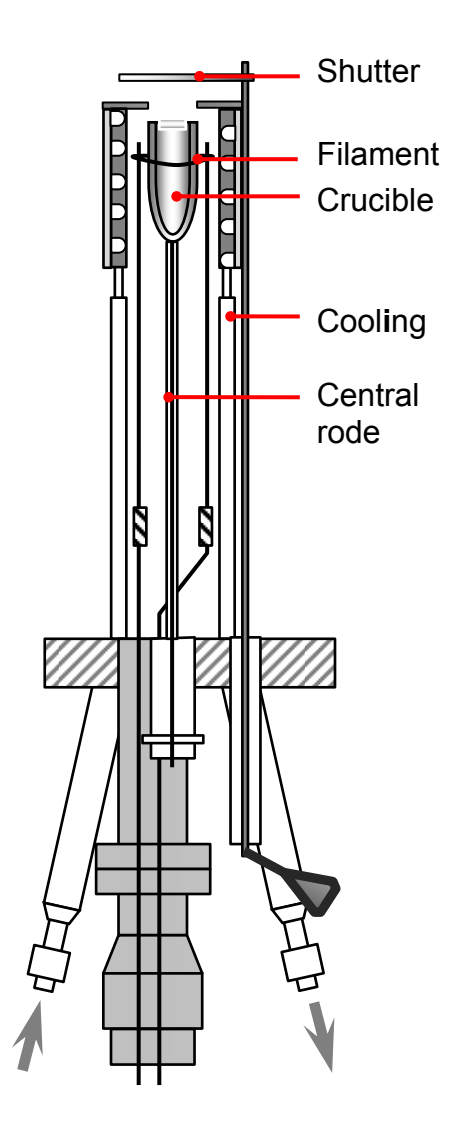


Figure 5. 4. Cross-sectional view of the electron beam evaporator used for Si and Ge evaporation.

The rate of deposition was measured with the commercial thin film deposition controller "Inficon XTC". The growth rate measurements are based on the effect of changing the resonance frequency of the quartz plate with a thickness of the film deposited on its surface.

5.2 Sample preparation

The samples were cut from Si(111) Sb-doped wafers with 1×10^{19} atom/cm doping and had a size of $\sim 8\times4\times0.5$ mm. The highly ordered stepped Si(111)-7×7 templates were prepared as described in [63]. The wafer was polished to 1° miscut (θ_m) toward the $[\overline{1}\ \overline{1}\ 2]$ direction with an intentional azimuthal misorientation ($\varphi_m = 4^\circ$) to orient all kinks at the surface steps in the same direction. Samples were cleaned in vacuum with flash heating to

1230°C and rapidly quenched. Then, samples were annealed at 800÷830°C for about 10 h with dc current flowing parallel to the steps in the "kink-up" direction [63] to extend the atomically straight step edges by surface electromigration of Si.

5.3 Sample heating and temperature measurement

All samples were heated by dc current. By changing the applied power the substrate temperature was varied from a room temperature (RT) to 1230°C. The temperature of the substrate was measured using the non-contact, infrared radiation pyrometer "Ircon Modline Plus". Its temperature range is $350\div1500$ °C. The pyrometer has an optic system with spot diameter about 6 mm, i.e. larger than a width of samples (~4 mm). An integral optic signal of the pyrometer from a 6 mm diameter spot consists of about 70% of sample irradiation and 30% of background signal corresponding to the room temperature. The temperatures above 500°C were calibrated with ~3 mm spot diameter pyrometer with temperature range of $500\div1500$ °C. A temperature deviation ΔT from the real temperature measured with "3 mm spot diameter" pyrometer was built up and extrapolated to RT **Figure 5.** 5. To control the substrate temperature below 350°C a power calibration was used. A temperature dependence on power was extrapolated from room temperature (RT) with zero power to temperatures higher than 350°C. The precision of temperature measurements was not worse than $\pm 2\%$.

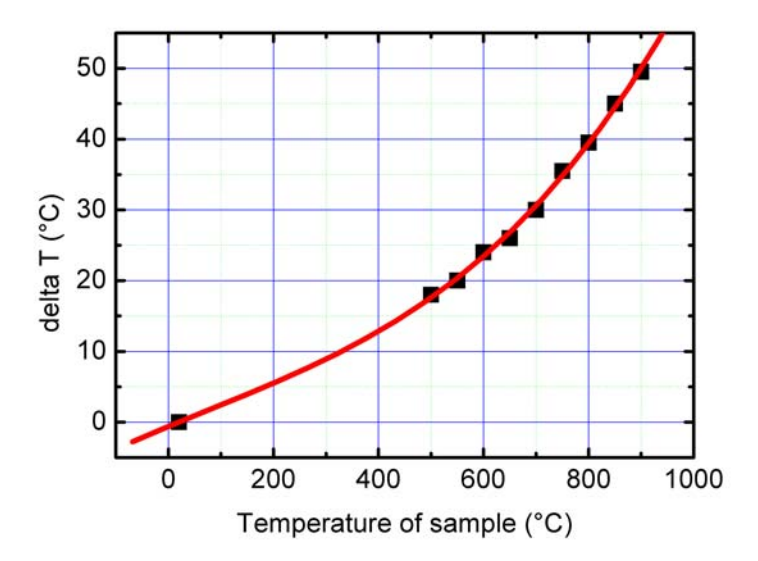


Figure 5. 5. The deviation ΔT of temperature measured with the "6 mm spot diameter" pyrometer from the real temperature of the sample.

6 Growth of Ge nanowires on a Bi-terminated Si(111) template

6.1 Preparation of a Ge nanowire arrays by step flow growth

In order to fabricate ever-smaller nanoscale device structures, there is an enormous interest in finding ways to build devices from the bottom up rather than fabricate from the top down. Using the bottom-up approach, the size of the structures is not limited by lithography; however, the uniformity and the ability for positioning of nanostructures are still a challenge. Specifically, nanowires are desirable as nanoscale interconnects [66]. One of the concepts followed in the bottom-up formation of nanowire arrays is to create a highly ordered atomic-step template on a vicinal single-crystal surface and to form the wires along the step edges, decorating the step edges with a selected material [67,68,69,70,71]. A suitable template is the vicinal surface of a Si(111) single crystal, since the structure of the step train on this surface can be controlled to a large extent [52,55,58,72,63]. Steps on Si(111) vicinal surfaces have been decorated by metals [70,73], semiconductors [62,71,74,75], and organic molecules [76]. The challenge is to improve the homogeneity of the nanowire array and the crystallinity and the aspect ratio of the wires.

The step flow growth mode is a useful method for fabrication of Si/Ge nanowires on stepped surfaces [71]. In the step flow growth mode adsorbed atoms diffuse over the surface until they reach a step edge **Figure 6. 1 (a)**. After attachment to the step edge Ge/Si atoms take a stable position and become a part of the Ge/Si stripe. The method is also useful for nanostructuring of alternating Si/Ge nanowires [71]. The alternating Si/Ge nanowires can be easy formed by alternating deposition of Ge and Si as shown on **Figure 6. 1 (b)**.

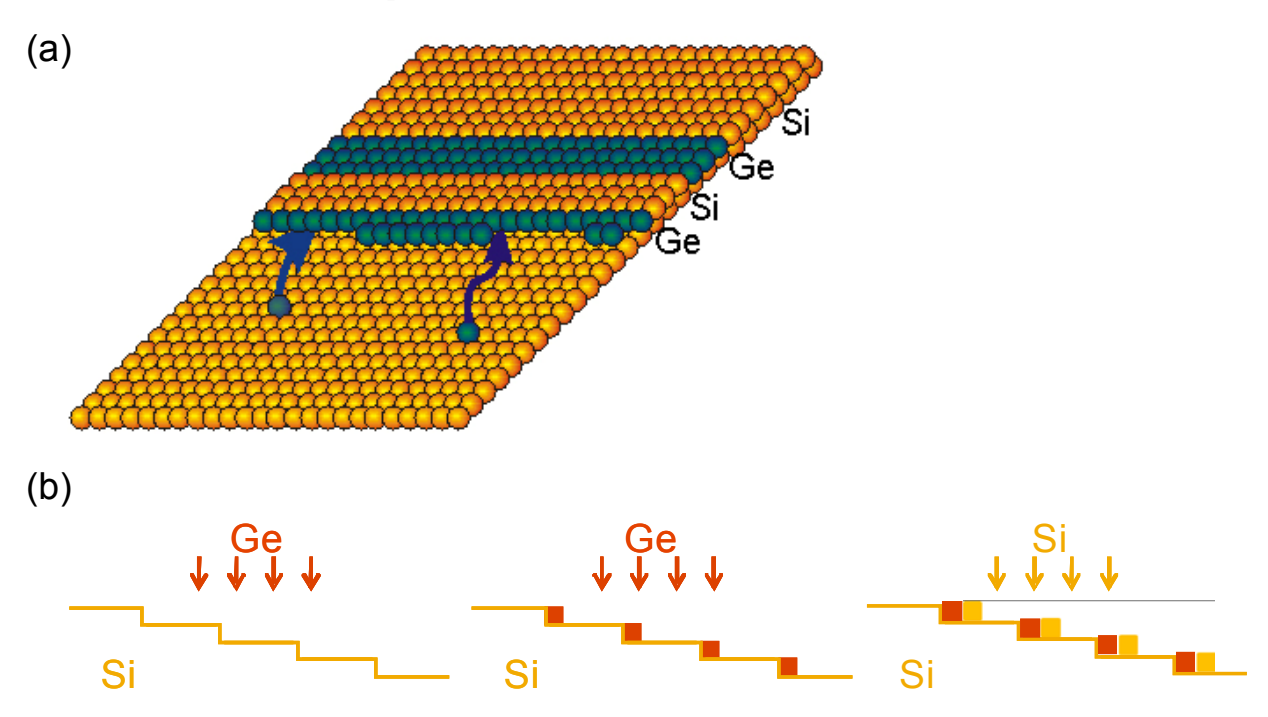


Figure 6. 1. In step flow growth mode adsorbed atoms diffuse over the surface before incorporation into a step (a). The system of alternating Si/Ge nanowires fabricated by Ge and Si deposition (b).

The average width of alternating Ge/Si wires is controlled by the time of Ge/Si deposition on the substrate. The shape and size uniformity of the wires are challenges. Initial step ordering of the substrate is important for the growth of good ordered nanowires, irregular step edges produce an irregular shape and an irregular width of the wires **Figure 6. 2 (a)**. Different preferable step direction on the clean substrate and on the substrate terminated by surfactant destroy the initial ordering of the steps. If the initial step direction of Si substrate is not equal to a preferable step direction of growing Ge layer, then the facetted Ge wires are formed as shown on **Figure 6. 2 (b)**. The initial step ordering of the substrate can be provided on a clean Si(111)-7x7 surface since it allows to form a straight step array over micrometer range [63]. The standard SME includes a termination of the surface by a surfactant. The termination process can destroy the initial ordering of the Si steps due to mass transport of additional Si atoms on the substrate. The additional Si atoms are induced by change of surface reconstruction. The important point is to conserve the long-range order of the initial Si template, which is usually lost during the nanowire preparation process using standard surfactant mediated epitaxy (as in [71]). **Figure 6. 2**

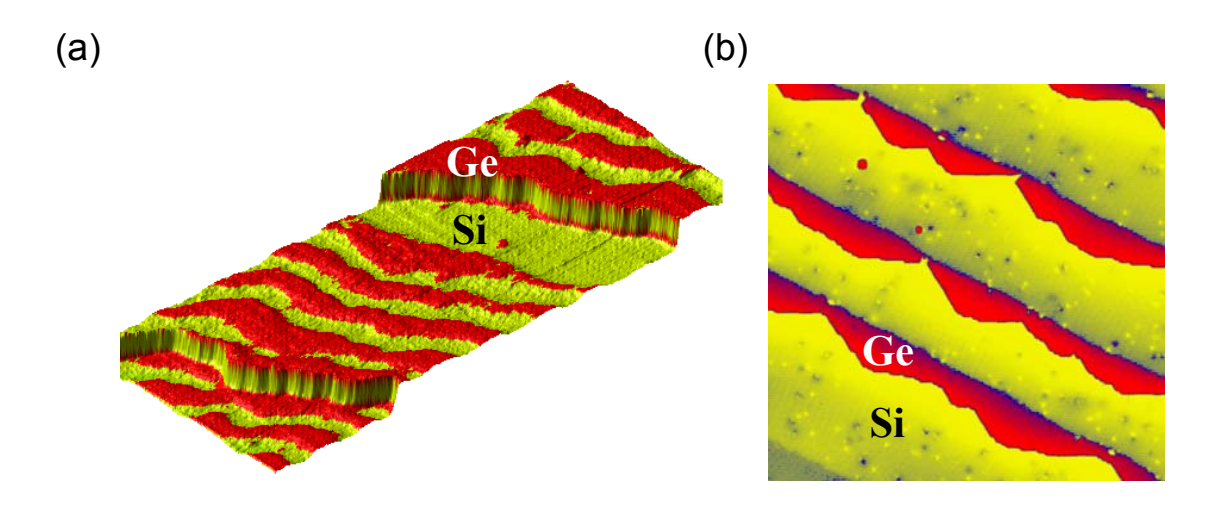


Figure 6. 2. (a) The irregular wires at irregular step edges of a substrate, (b) facetting of Ge wires by step direction different from step direction of preexisting steps.

The procedure of preparation of Ge nanowire array is divided into three stages: (1) preparation of the highly ordered Si(111) template, (2) termination of the template by 1 ML Bi, and (3) growth of Ge nanowires on the Bi-terminated template.

6.2 Preparation of a highly ordered Si(111)-7x7 template

The highly ordered Si(111)-7x7 template was prepared by a method described in [63] and in Chapter 4.§4.3 of the thesis. A Si(111) wafer was polished to 1° miscut (θ_m) toward the $[\overline{1}\ \overline{1}\ 2]$ direction with an intentional azimuthal misorientation $\varphi_m = 4^\circ$ to orient all kinks at the surface steps in the same direction. The samples were cleaned in vacuum with flash heating to 1300 °C and rapidly quenched.

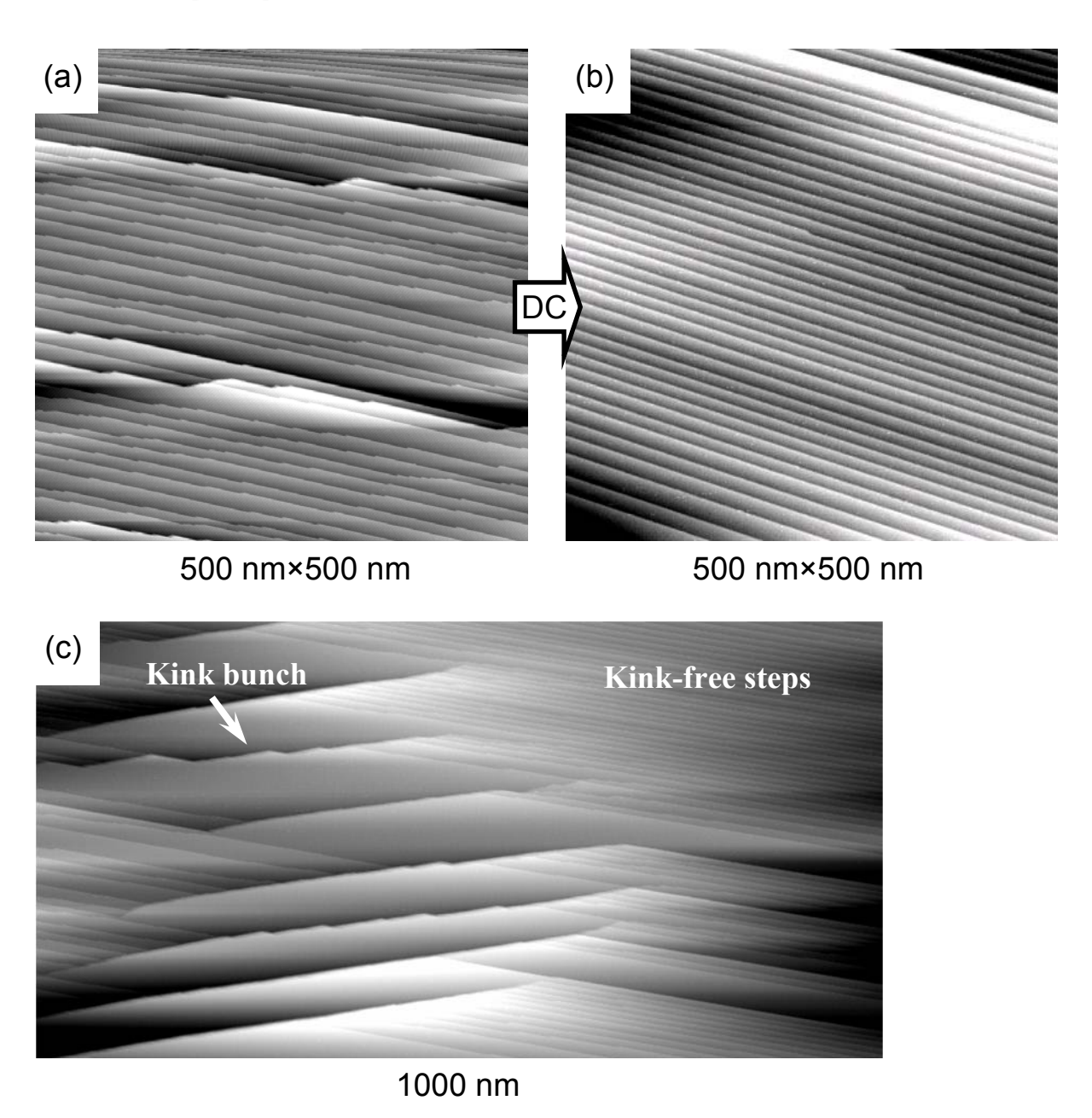


Figure 6. 3. (a) The initial surface contains kinks; a direct current heating in the kink-up direction extends a kink-free step region (b); (c) kink-free and kink bunch regions.

Afterward, the samples were annealed at 800–830 °C for about 10 h with dc current flowing parallel to the steps in the "kink-up" direction [63] to extend the atomically straight step edges by surface electromigration of Si **Figure 6. 3**. The resulting surface step structure is shown in **Figure 6. 4**, **Figure 6. 3** (b).

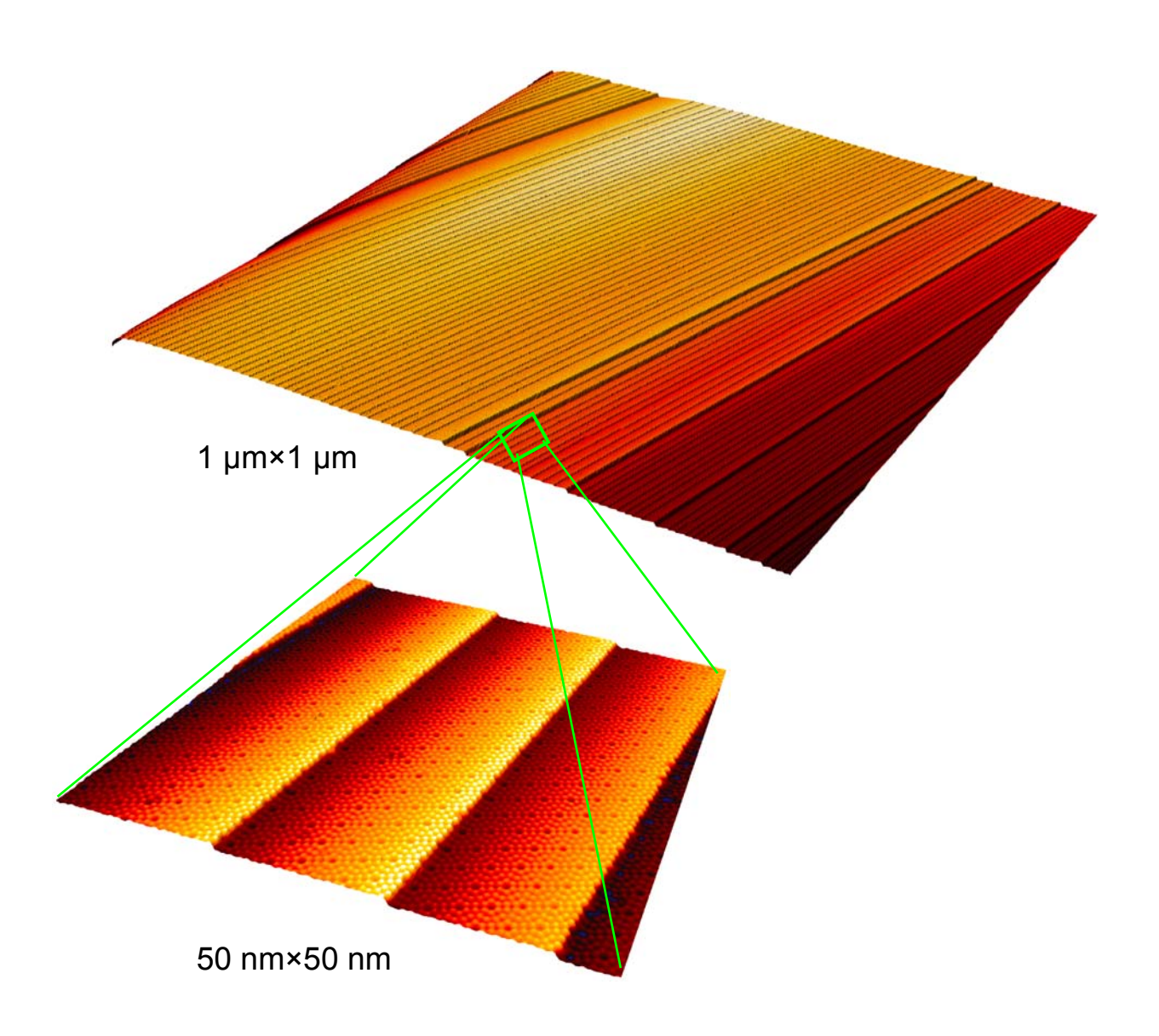


Figure 6. 4. Regular array of straight kink-free steps on a micrometer scale

The surface **Figure 6. 4** presents the system of atomically perfect 1 layer height steps. All steps have equal structure - **U(2,0)**. The method described in [63] can be improved to achieve equidistant steps ordering. Due to azimuthal deviation of the current to the step orientation we

have two components of the current: parallel and perpendicular to the $[\overline{1}\ \overline{1}\ 2]$ step direction **Figure 6. 5**. Parallel to the steps component induces kink bunching. The component perpendicular to the steps have an influence on the step ordering [65,77]. The orientation of the perpendicular component of the current in step up $[11\overline{2}]$ or step down $[\overline{1}\ \overline{1}\ 2]$ direction usually induces opposite effects: step bunching or step debunching, respectively. An intentional misorientation of the current in desired way (step up or step down) can be used to achieve an equidistant step ordering.

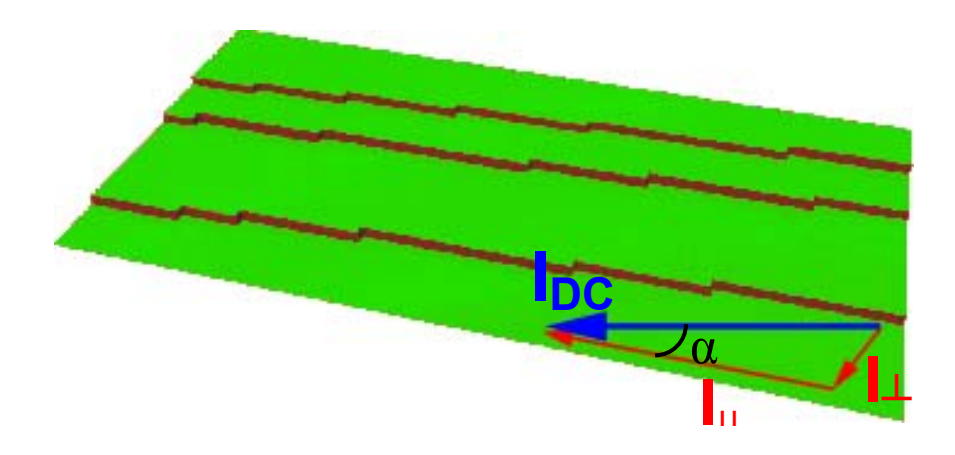


Figure 6. 5. Direct current is a vector sum of perpendicular to step and parallel to step direction projections I_{\perp} and I_{\parallel} , respectively. Step up or step down perpendicular projection of the current can be controlled by an intentional misorientation α .

6.3 Maintaining good step ordering during Bi termination

The Bi deposition on the clean Si(111)-7x7 surface at 300°C – 500°C changes the 7x7 surface structure to the Bi- $\sqrt{3} \times \sqrt{3}$. The Bi induced $\sqrt{3} \times \sqrt{3}$ reconstruction has two phases: the α – phase and the β – phase. The α – phase consists of 1/3 ML and β – phase 1 ML of Bi coverage, respectively [78]. The structure of α – phase has one Bi atom (monomer) bonded to T_4 site [78] **Figure 6. 6**, and the β – phase has three Bi atoms (trimer) bonded to T_4 site as shown on **Figure 6. 6** (b). The Bi monomer of the α – phase has 1.1 A of height over the underlying Si atoms and Bi trimer of the β – phase have 2.21 A of height over the underlying Si atoms [78]. The **Figure 6. 6** (a) presents the height of α – phase Bi atoms over unreconstructed Si(111) surface and the height difference between Bi atoms of α and β phases.

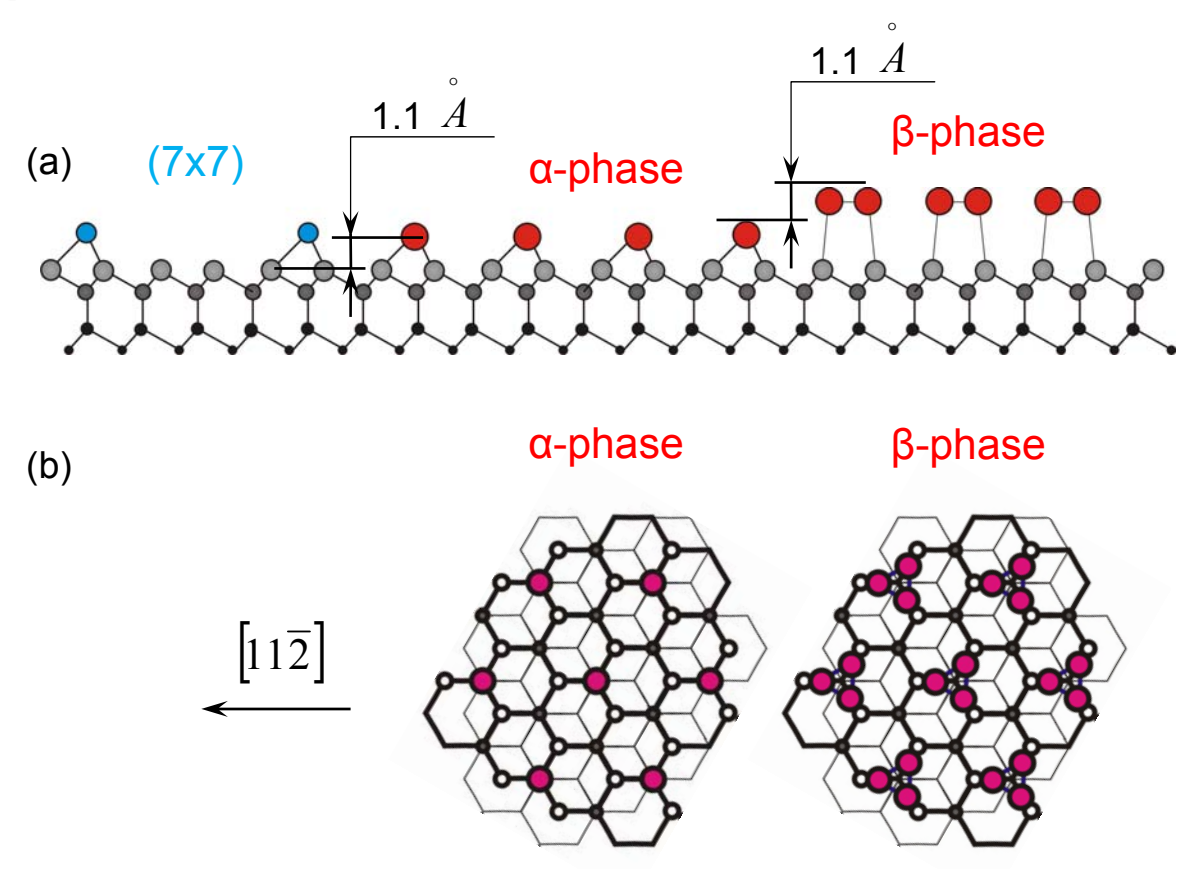
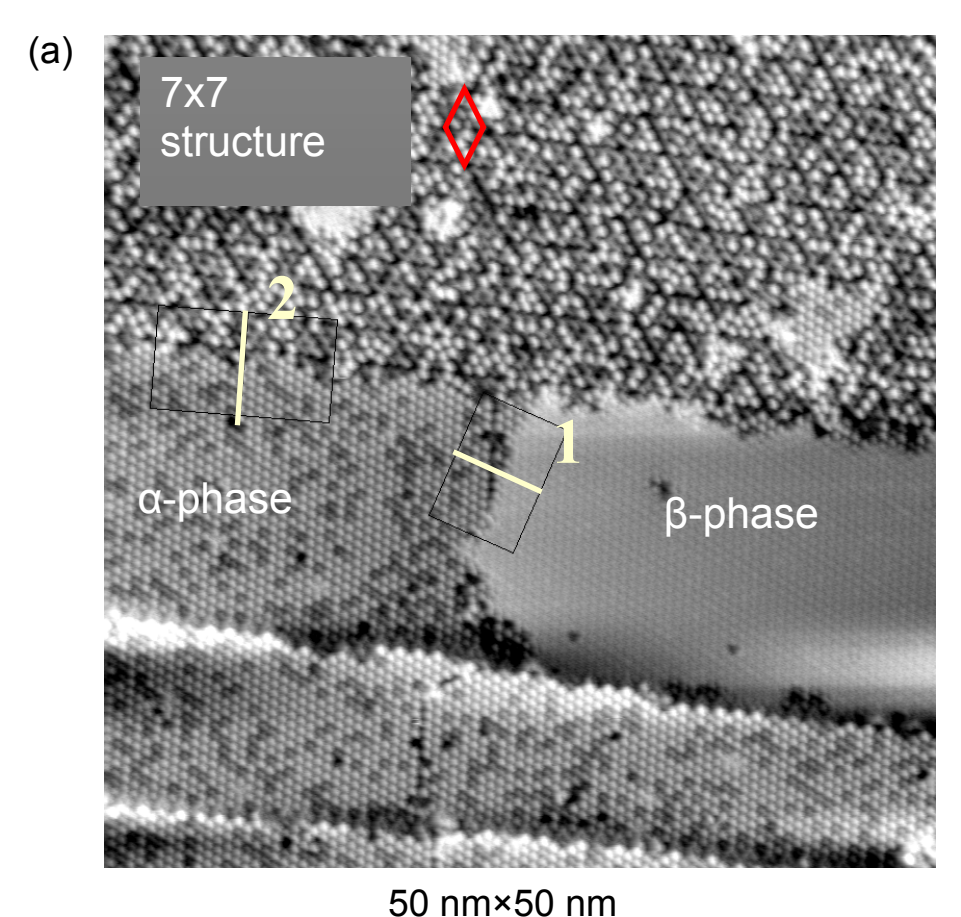


Figure 6. 6. Different phases of Bi on the Si(111) surface. (a) – side and (b) – top views of the α and β – phases. The height differences are defined according to ref. [78]. The Bi atoms are shown by red balls.

The additional deposition of Bi on the α – phase transforms the α – phase into β – phase. The adsorbed Bi atoms bond to the single Bi atoms on T_4 – site (monomers) of the α – phase until the number of atoms increases up to three. The **Figure 6. 7 (a)** presents an STM image of the Si(111) surface partly covered by α – phase, β – phase and 7x7. The line profiles show an

apparent height difference between different phases **Figure 6. 7 (b)**. The β – phase is higher than the α – phase on \approx 0.8 $\stackrel{\circ}{A}$ **Figure 6. 7 (b)**. The α – phase can be also identified as the phase containing more defects than the β – phase **Figure 6. 7 (a)**. The defects are present by dark spots on the STM image and correspond to Si adatoms.



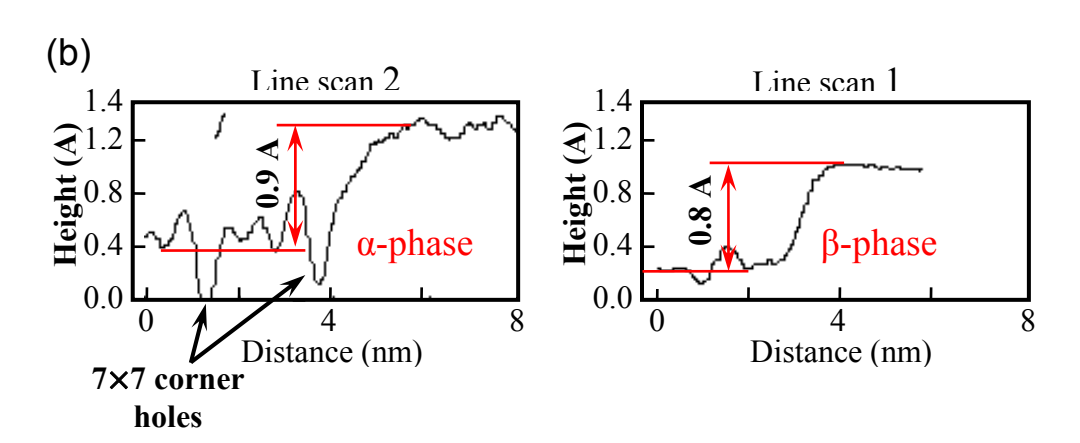


Figure 6. 7. Different phases of Bi on the Si(111) surface (a), filled state STM image, -2.07 V on the sample. (b) the apparent height difference between phases, the line scan 1 shows the apparent height difference between 7x7 and α -phase, the difference measured from the deep between adatoms is 0.9 A. The line scan 2 shows the height difference between the α -phase and the β -phase about 0.8 A. The line profiles were averaged on the area of rectangles.

The standard Bi surfactant mediated epitaxy [71,79,80] on the Si(111)-7x7 surface starts by terminating the surface with 1 ML of Bi which forms a $\sqrt{3} \times \sqrt{3}$ surface structure [78,81,82]. This is associated with a significant surface mass transport of Si, because 0.04 ML of Si atoms are released as a result of the lifting of the 7x7 surface reconstruction [83] **Figure 6.8**.

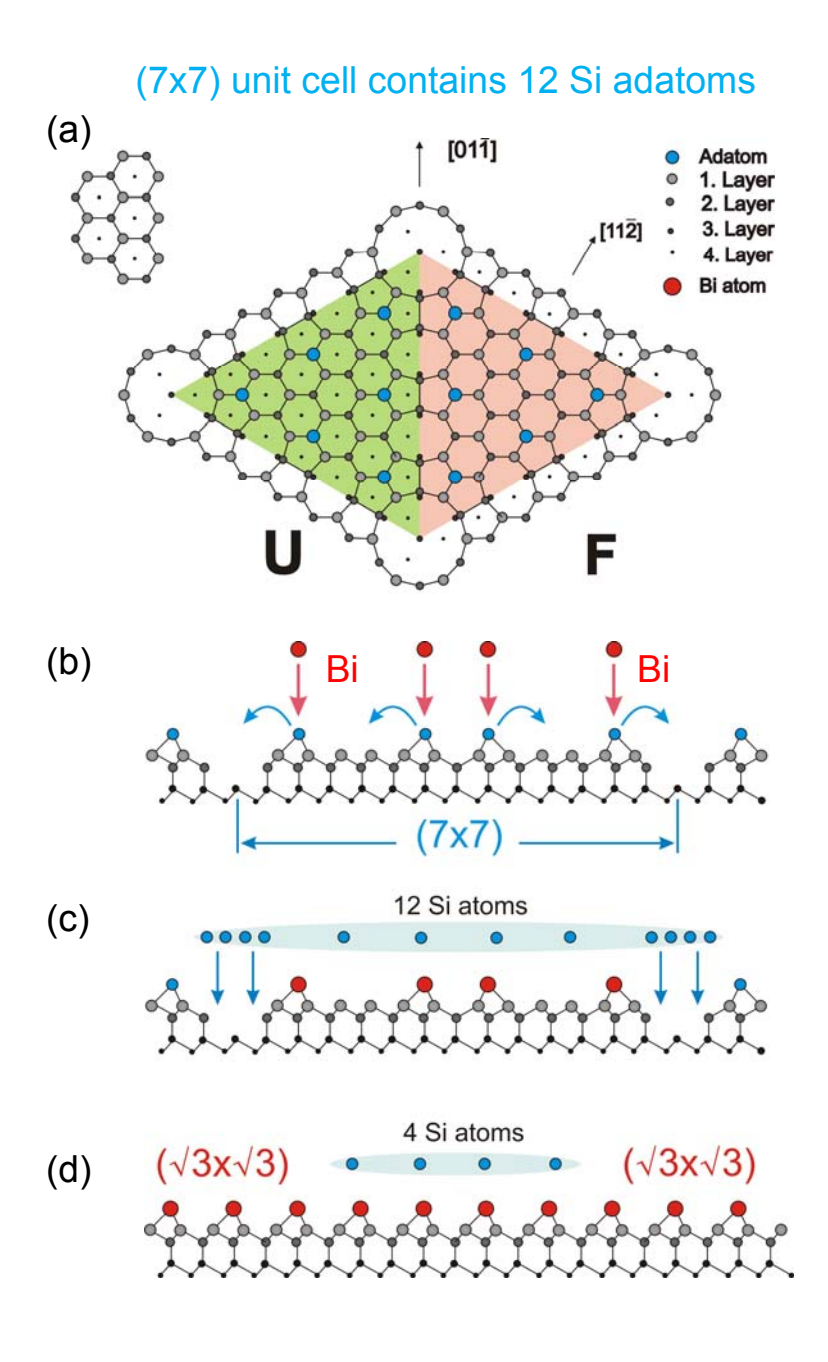


Figure 6. 8. The standard Bi termination of 7x7 reconstructed surface. The 7x7 reconstruction contains 12 adatoms (a). Bi replaces 12 Si adatoms of the 7x7 structure (b), 8 Si atoms fill the corner holes of the 7x7 (c). The remaining 4 Si extra atoms form 0.04 ML of Si coverage (d).

Bi replaces 12 Si adatoms of 7x7 structure **Figure 6. 8 (b)**, 8 adatoms fill the corner hole of the 7x7 and the remaining four Si atoms (0.04ML) incorporate at the surface step edges. Performing the termination in a standard way at substrate temperature $Ts = 500^{\circ}$ C and terminating with a Bi flux $F_{Bi} = 0.7$ ML/min for ≈ 10 min results in a need to incorporate 0.04 ML Si at the surface step edges in a relatively short time. In **Figure 6. 9 (b)** we show the result of such standard Bi termination performed on a highly ordered Si template **Figure 6. 9 (a)**. The steps become

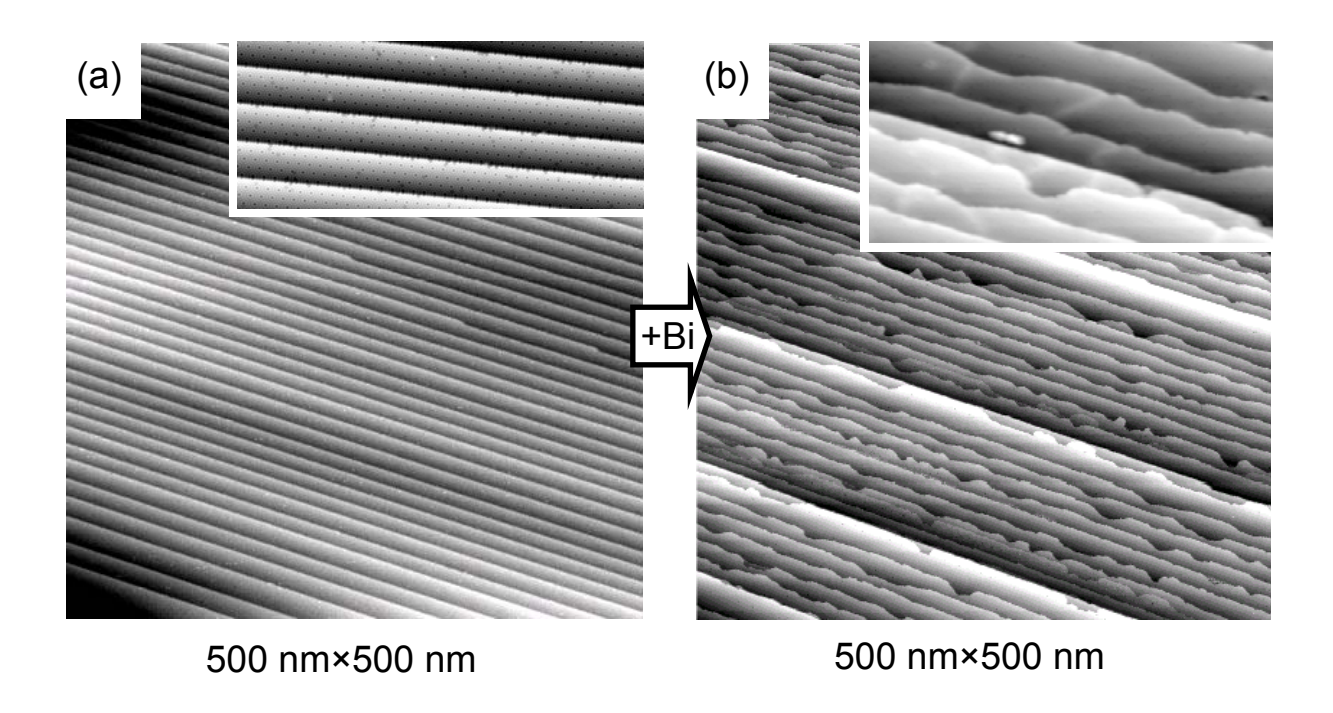


Figure 6. 9. Bi termination of the highly ordered Si(111)-7x7 template. Initially straight steps (a) become wavy (b) due to the related Si mass transport.

wavy on a short length scale and the step ordering is lost **Figure 6. 9 (b)**. To find a solution of the mass transport problem the Bi adsorption on the Si(111)-7x7 was studied at a different temperatures of the substrate. We studied adsorption of Bi on the Si(111)-7x7 surface at high temperatures in the range of $600^{\circ}\text{C} - 700^{\circ}\text{C}$. At the temperatures higher than 650°C the surface has a 7x7 structure as shown on **Figure 6. 10**, no α , β – phases were observed on the surface. But Bi coverage was found different from zero. We identified bright atoms in the 7x7 structure **Figure 6. 10** as Bi monomers bonded on T_4 site. To be sure we measured profiles through these atoms and compare with profiles at the phase boundary between 7x7 and $\sqrt{3} \times \sqrt{3}$ α and β – phases **Figure 6. 7**. We found that the height of bright atoms is lower than the height of the β – phase and close to the height of the α – phase.

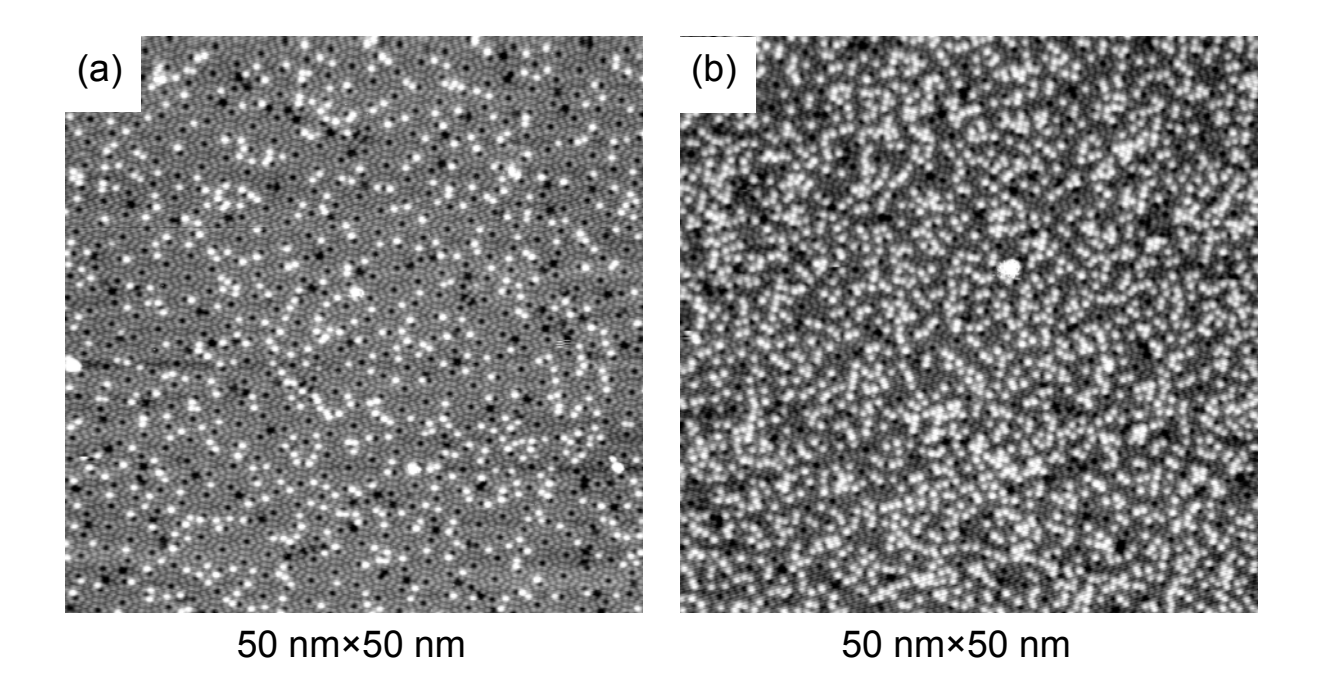


Figure 6. 10. Bright spots correspond to Bi monomers on the Si(111)-7x7 after Bi deposition at $T_s = 670^{\circ}$ C (a) and $T_s = 640^{\circ}$ C (b) with a deposition rate of 1.1 ML/min for 5 – 10 min.

During the long time deposition of 5-10 min at fluxes 1-3 ML/min a steady state concentration of Bi on the surface was achieved. The measurements of the steady state concentration of Bi at different Bi rates deposition (F) show a linear dependence **Figure 6. 11** (a). The density of bright spots was converted into a coverage of Bi. To calculate the Bi coverage a one bright spot was considered as one Bi atom. The model with two and three particles per bright spot gives the concentration behavior different from a linear one. The probability of the meeting of two or three particles is proportional to second or third power of the flux, F^2 and F^3 respectively. The last point at F = 3.1 ML/min on the plot **Figure 6. 11** (a) does not belong to the linear approximation. This deviation can be explained by a change of the Bi bonding energy due to interaction between Bi atoms on the Si(111)-7x7 surface at higher coverages. The Bi bonded to T_4 site modifies the 7x7 structure and decreases a desorption energy for neighbor Bi atoms. The measurements showed that deviation from linear dependence starts at ≈ 0.01 ML of Bi coverage **Figure 6. 11** (a).

The temperature dependence of the Bi coverage is shown on **Figure 6. 11 (b)**. The Arrhenius approximation of the plot gives the value energy desorption of 4.3 eV/atom. The theoretical energy calculations [84] predict for the α – phase the highest energy per Bi atom. Energy per atom for the β – phase is 6.01 eV and for the α – phase is 7.04 eV, respectively [84]. The desorption energy increases with bond energy per Bi atom, therefore the rate of Bi desorption for the α – phase must be lower than the rate of desorption for the β – phase. At Bi flux 3 ML/min and at temperatures lower than 650°C a Bi coverage achieves the critical value about 0.01 – 0.02 ML such that the α – phase starts nucleate at the step edges.

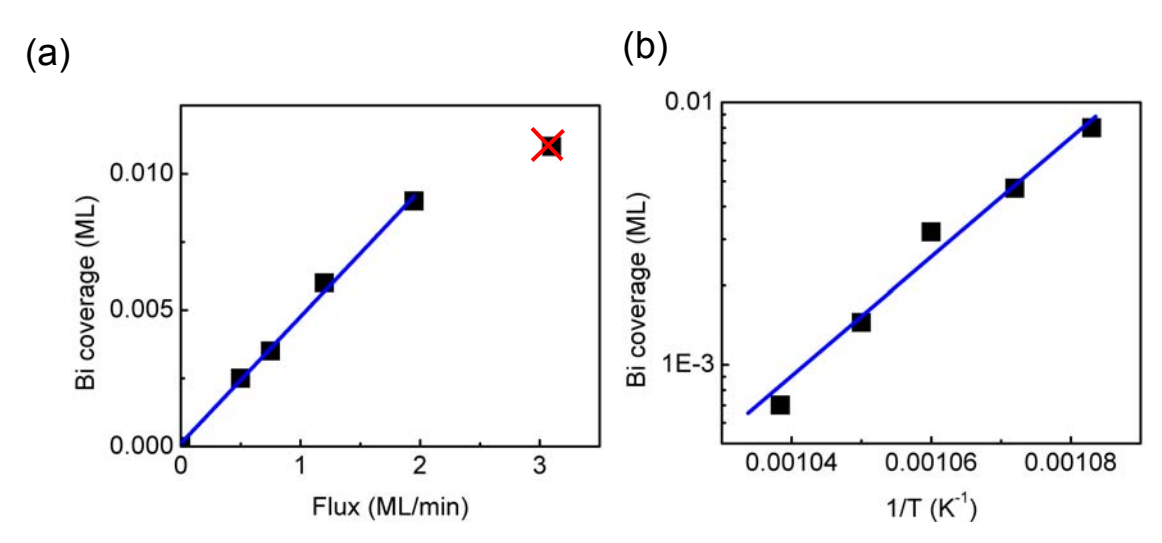


Figure 6. 11. Bi coverage in steady state regime as a function of Bi flux (a) was measured at $T_s = 650^{\circ}\text{C}$. (b). Bi coverage as a function of substrate temperature was measured at Bi flux 1.1 ML/min.

The **Figure 6. 12** shows a nucleation of α – phase on the lower terrace at the $\left[\overline{1}\ \overline{1}\ 2\right]$ - steps. The Bi- $\sqrt{3} \times \sqrt{3}$ reconstruction presents the unreconstructed Si(111)-1x1 layer with the Si bonds saturated by Bi. To form the unreconstructed Si layer we need to rebond a faulted HUC of 7x7. The nucleation of the $\sqrt{3} \times \sqrt{3}$ α – phase need for high activation energy to rotate bonds on 180° in the faulted halves of the 7x7 unit cell. The $\left[\overline{1}\ \overline{1}\ 2\right]$ - steps reduce the activation burier for adjacent faulted HUC on the lower terrace and make easier transformation of the 7x7 to the $\sqrt{3} \times \sqrt{3}$.

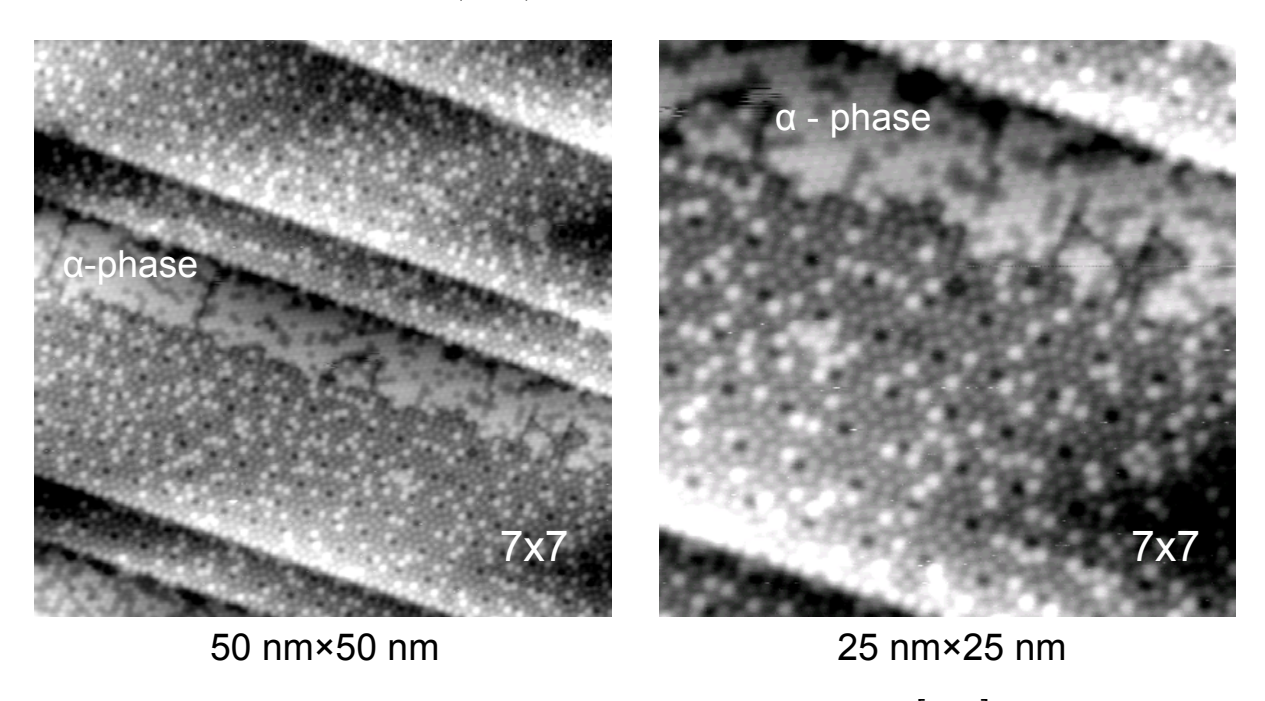


Figure 6. 12. The Bi- $\sqrt{3} \times \sqrt{3} \alpha$ – phase starts to grow on lower terraces at the $[\overline{1} \ \overline{1} \ 2]$ - steps. The steps are saved straight by a careful control of the Bi coverage at the terrace.

The mass transport problem was solved by a careful control of the Bi coverage at the terraces during Bi termination **Figure 6. 12**. The fact that Bi readily desorbs from the Si(111) surface at elevated temperatures was used. The rate of desorption is $F_{des} = 0.5$ ML/min at Ts=550°C [85,86]. Thus, for a constant Bi flux the Bi coverage can be controlled in a steady-state regime by adjusting the Ts.

In the optimized Bi termination procedure, the substrate was heated to Ts=700 °C and Bi was deposited at F_{Bi} = 3 ML/min. At this high temperature the Bi coverage is virtually zero. Afterward, Ts was reduced to 650 °C over 10 min. This leads to a slow increase of the Bi coverage, allowing a gradual Si mass transport during the lifting of the Si(111)-7x7 reconstruction. On **Figure 6. 13. (b)** the morphology of the surface after this preparation step is shown. The surface steps remained straight, indicating that the released Si atoms had enough time to evenly distribute along the step edges. The detailed view of the surface reveals an inhomogeneous $\sqrt{3} \times \sqrt{3}$ surface structure **Figure 6. 13. (c)**, indicative of a 1/3 ML Bi coverage [81]. The protrusions observed in the STM image of the 1/3 ML Bi structure correspond to Bi monomers on the Si(111) substrate.

Before Ge deposition, Bi coverage has to be increased to 1 ML because only 1 ML Bi termination prevents Ge-Si intermixing on the terraces during the growth of the Ge nanowires [71]. Thus, the Bi was deposited at $F_{\text{Bi}} = 3$ ML/min on the 1/3 ML Bi terminated surface at Ts=500 °C for 1 min. This causes a slight increase of the kink density. However, the step structure of the original highly ordered step train remains largely conserved, as we can see in **Figure 6. 13. (d)**. The surface reveals a homogeneous $\sqrt{3} \times \sqrt{3}$ surface structure indicative of 1 ML Bi coverage (**Figure 6. 13. (e))** [81]. The protrusions observed in the STM image of the 1 ML Bi structure correspond to Bi trimers on the Si(111) substrate. No Si mass transport is involved in this part of the process. The underlying 1×1 Si(111) structure is preserved, only the Bi monomers are converted to Bi trimers.

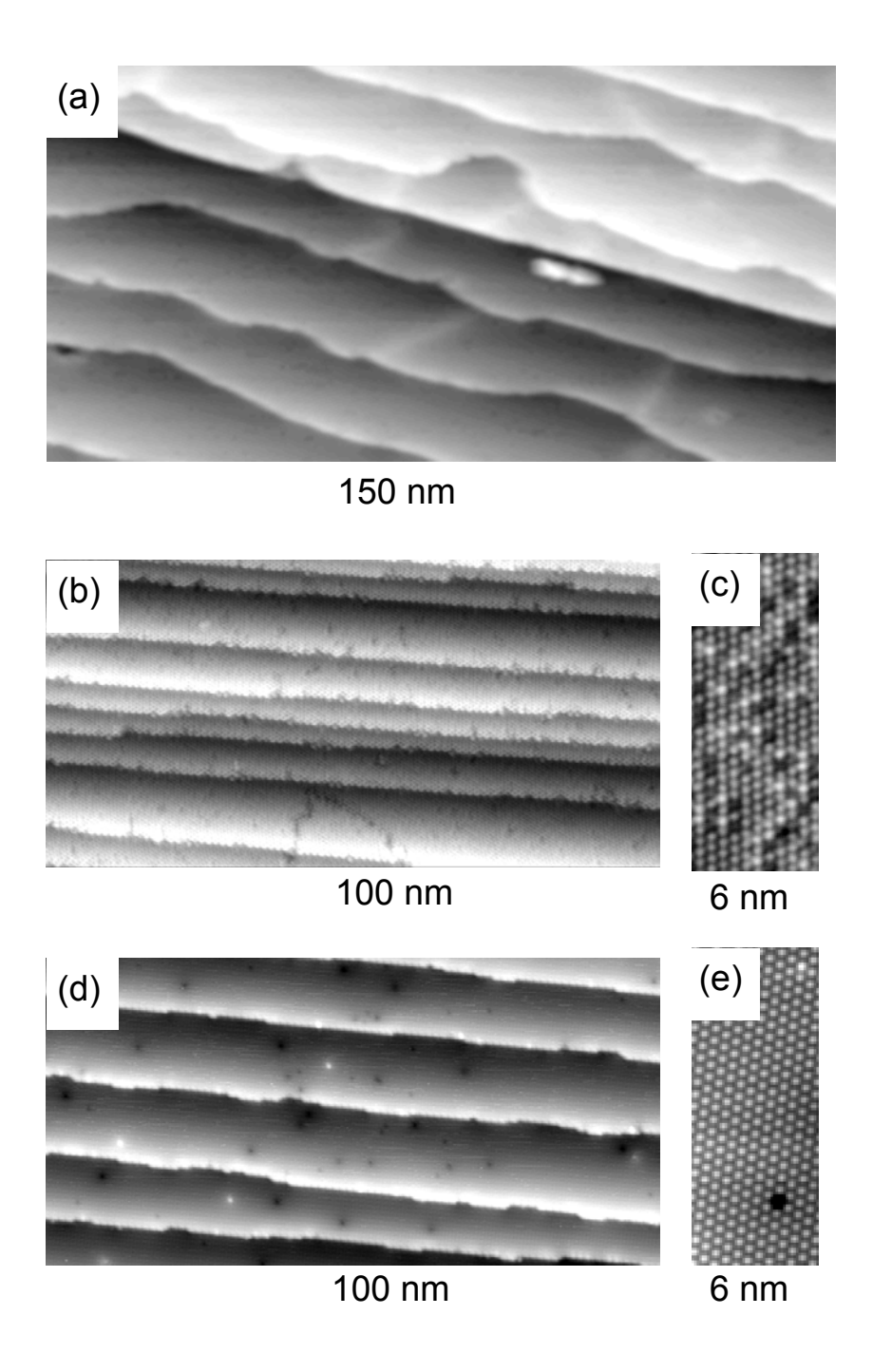


Figure 6. 13. The Bi termination of the highly ordered Si(111)-7x7 template Figure 6. 9 (a). (a) Standard surfactant mediated epitaxy. The step structure of the template has been destroyed. (b) – (e) Modified surfactant mediate epitaxy. (b) The surface after a slow increase of Bi coverage from 0 to 1/3 ML. The 1/3 ML Bi coverage is indicated by an inhomogeneous $\sqrt{3} \times \sqrt{3}$ structure (c). The surface termination at high temperatures preserves the original straight step arrangement. (d) The surface after completing the Bi coverage to 1 ML. The 1 ML Bi coverage is indicated by a homogeneous $\sqrt{3} \times \sqrt{3}$ structure (e).

6.4 Modified surfactant-mediated epitaxy

In the last preparation stage the Ge nanowires were grown along the step edges of the 1 ML Bi terminated template (**Figure 6. 13. (d)** and **(e)**) using surfactant mediated epitaxy [71,86,87,88,89,90]. Ge grows in a step flow growth mode and a thin stripe of Ge attaches to the step edge. In standard surfactant mediated epitaxy, materials are deposited under a constant supply of the surfactant to maintain the (saturated) 1 ML surfactant coverage [79,82]. However, performing the Ge deposition in the standard way at $F_{\text{Ge}} = 0.08$ ML/min, $T_S = 450$ °C, and Bi flux $F_{\text{Bi}} = 3$ ML/min does not yield straight Ge nanowires of homogenous width. In **Figure 6. 14 (a)** we can observe that Ge nanowires grown by standard surfactant mediated epitaxy develop step edges in the $\begin{bmatrix} 1 & 1 & 1 \end{bmatrix}$ directions which are 30° off the step direction of the template.

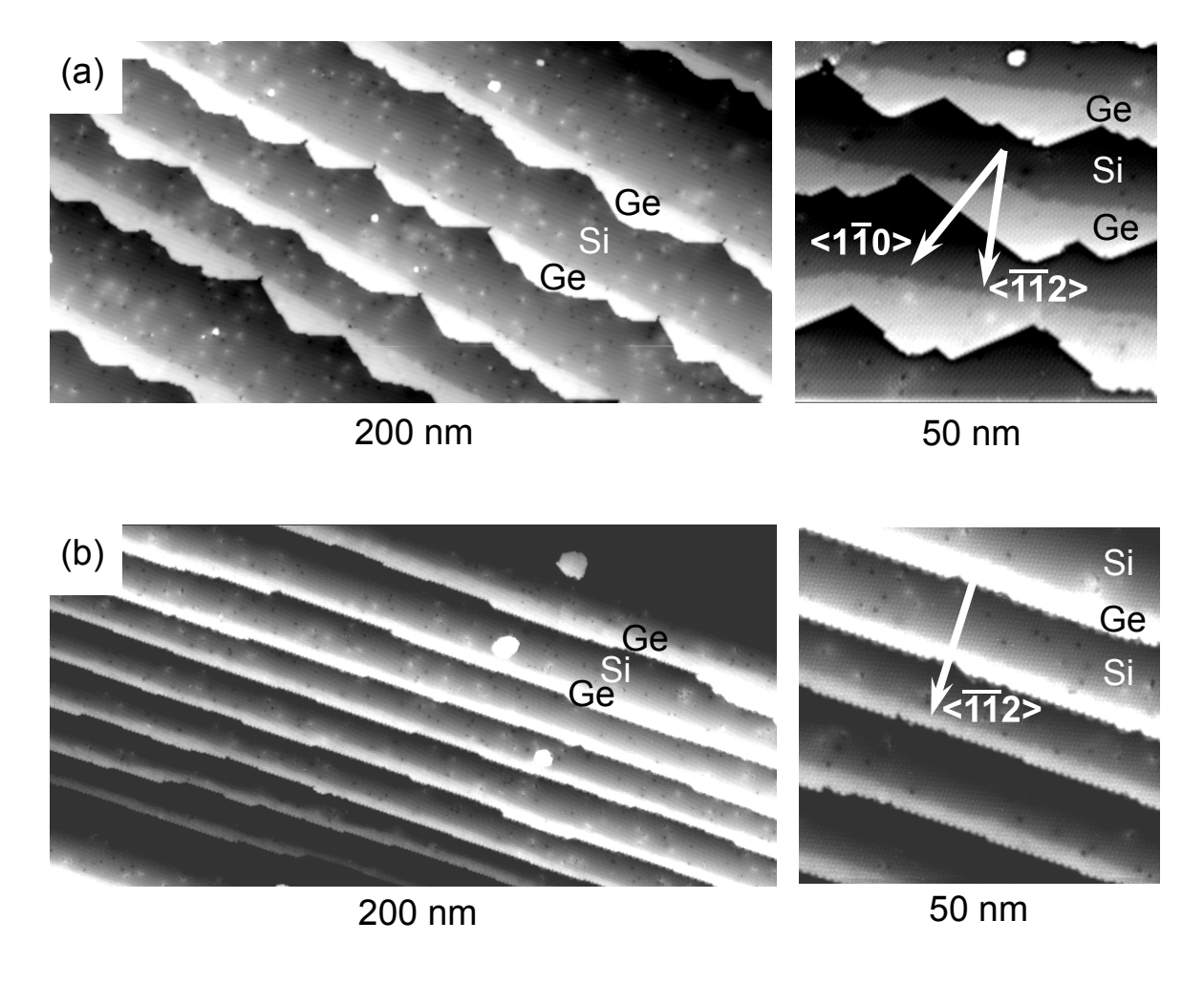


Figure 6. 14. Deposition of Ge on the ordered Bi – terminated surface (**Figure 6. 13. (d)**). (a) Standard surfactant mediate epitaxy. Ge and Bi are deposited simultaneously. The Ge step develops facets in $\langle 1\,\overline{1}\,0\rangle$ directions which are 30° off the original $\langle \overline{1}\,\overline{1}\,2\rangle$ step direction. (b) Modified surfactant mediated epitaxy. Ge is deposited without a Bi flux. The Ge step edges retain the original $\langle \overline{1}\,\overline{1}\,2\rangle$ step direction.

To obtain the desired regular growth of Ge nanowire arrays the reducing of Bi surfactant coverage is again considered. To minimize the Ge-Si intermixing the Bi flux was switched off only during Ge evaporation and Ge was deposited at Ts = 400 °C, $F_{Ge} = 0.02$ ML/min for 10 min. Afterward, the sample was cooled rapidly to room temperature. The result of this preparation step is shown in **Figure 6. 14 (b)**. The optimized growth of Ge at the template step edges, resulting in single-crystalline, high-aspect-ratio, low-kink density Ge nanowires with width of about 4 nm was obtained.

The success of the last preparation step shows that switching off the Bi flux at Ts=400 °C is sufficient to change the Ge growth scenario. Any significant reduction of Bi concentration on the terraces was not observed after this growth step. The $\sqrt{3} \times \sqrt{3}$ surface structure is homogeneous, indicating the saturation 1 ML Bi coverage **Figure 6. 15 (b)** [81]. Therefore, the change of growth scenario is attributed to a reduction of Bi coverage at the step edges.

The optimized growth of a Ge nanowire array on a highly ordered Si(111) template has been achieved by modified surfactant mediated epitaxy where the surfactant coverage on the terraces (stage (2)) or at step edges (stage (3)) is lowered below the saturation coverage. In the following we argue that the observed modifications of the growth scenario with changing Bi coverage are due to the modified equilibrium properties of step edges in combination with kinetic limitations during growth.

The $\langle \overline{1} \ \overline{1} \ 2 \rangle$ step direction of our highly ordered templates is the equilibrium step direction of the Si(111)-7x7 surface, [55,52] **Figure 6. 15 (a)**. An experiment was performed that shows that, upon a complete 1 ML Bi termination and after prolonged annealing of the surface under Bi flux, the preferred step direction on the Si(111)- $\sqrt{3} \times \sqrt{3}$ -Bi surface changes to $\langle 1 \ \overline{1} \ 0 \rangle$, i.e., it rotates by 30°. In **Figure 6. 15 (b)** it can be seen that at the $\langle 1 \ \overline{1} \ 0 \rangle$ -oriented equilibrium steps the trimers of the $\sqrt{3} \times \sqrt{3}$ surface reconstruction are most densely packed. The fact that the 1 ML Bi termination of the Si(111) surface changes the equilibrium step direction explains the general difficulty in growing Ge nanowires on Si(111)-7x7 stepped templates.

When the Si(111)-7x7 ordered template is terminated by 1/3 ML Bi (as in stage (2)), **Figure 6.** 13 (b) and **Figure** 6. 13 (c), the preferred low-energy step direction remains $\langle \overline{1} \overline{1} 2 \rangle$. The experiment shows that this step direction is stable in spite of the relatively open structure of the step edge that can be seen in **Figure 6.** 15 (c). This indicates that the equilibrium step direction is strongly influenced by the actual amount of Bi in the surface, and, in turn, at the step edges.

Given the above arguments, it could be expected that, after increasing the 1/3 ML Bi coverage of the highly ordered stepped template to 1 ML in stage (2), the step direction changes. However, this does not happen due to a kinetic limitation. The expected $\langle 1\,\overline{1}\,0\rangle$ facets do not form because the straight step edges of the template with 1/3 ML Bi do not emit enough Si adatoms at the temperature used in this preparation step ($Ts=500\,^{\circ}$ C) to allow a surface equilibration within the given time (1 min). The step orientation remains $\langle \overline{1}\,\overline{1}\,2\rangle$, **Figure 6. 13 (d)**. Finally, in stage (3), Ge is deposited on the 1 ML Bi terminated template. In this case the Ge adatoms do not have to detach from existing step edges but are supplied from outside. This, together with the lower effective activation energy for the Ge surface diffusion

on the Bi-terminated Si(111) surface [91], leads to the formation of $\langle 1\,\bar{1}\,0\rangle$ equilibrium facets that destroys the ordered step train **Figure 6. 14 (a)**. However, only a slight decrease of the Bi content on the surface during the Ge deposition is sufficient to preserve the original $\langle \bar{1}\,\bar{1}\,2\rangle$ orientation of the steps **Figure 6.** 14 (b). In **Figure 6.** 15 (d) we show that the microscopic structure of the $\langle \bar{1}\,\bar{1}\,2\rangle$ step edge of the Ge nanowire formed during growth without Bi codeposition considerably differs from the structure of the equilibrium steps on the 1 ML and 1/3 ML Bi-terminated surfaces **Figure 6. 15 (b)** and **Figure 6. 15 (c)**. This observation confirms that during Ge growth

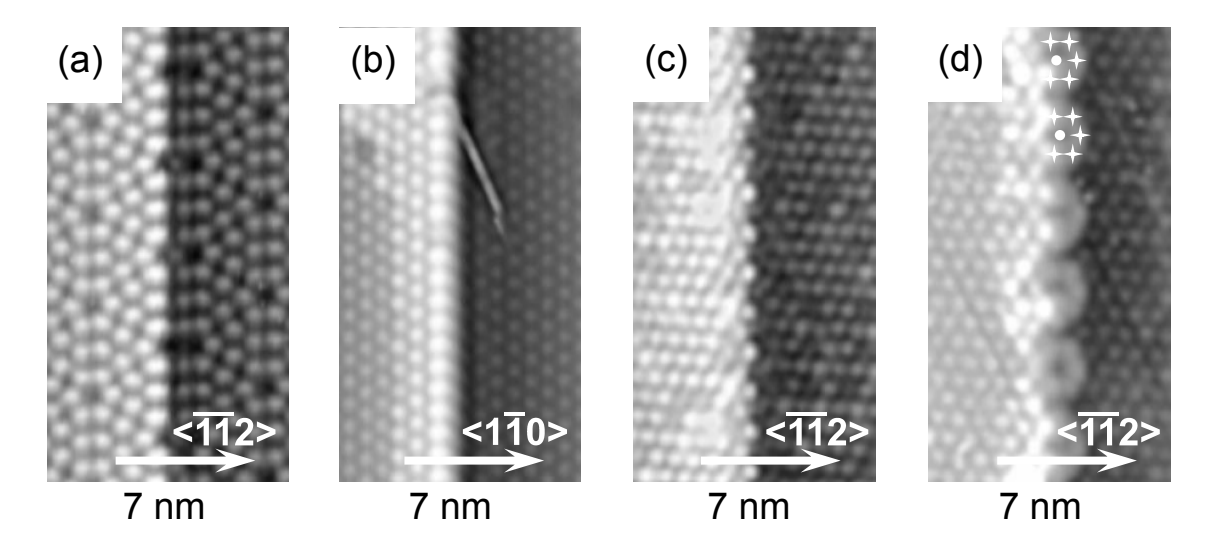


Figure 6. 15. Changing the Bi content in the surface changes the structure of the step edges and their growth and equilibrium properties. The equilibrium step directions are (a) $\langle \overline{1} \ \overline{1} \ 2 \rangle$ on the clean Si(111)-7x7 surface, (b) $\langle \overline{1} \ \overline{1} \ 0 \rangle$ on the Si(111)- $\sqrt{3} \times \sqrt{3}$ -Bi with 1 ML Bi, (c) $\langle \overline{1} \ \overline{1} \ 2 \rangle$ on the Si(111)- $\sqrt{3} \times \sqrt{3}$ -Bi surface with 1/3 ML Bi, and (d) $\langle \overline{1} \ \overline{1} \ 2 \rangle$ on the Ge nanowires grown by modified surfactant mediated epitaxy. In (d) the crosses and dots indicate the positions of the adatoms and corner holes of a 3×3 surface reconstruction.

the surfactant is removed from the step edges, which strongly influences the growth properties of the steps. We can directly observe the Bi depletion at the step edge in **Figure 6. 15 (d)**. The step edge has a periodic ringlike structure with a period corresponding to double the period of the Si(111)-3×3 surface reconstruction. The Si(111)-3×3 is commensurate with the $\sqrt{3} \times \sqrt{3}$. It is a metastable structure [92] which was observed on disordered Si(111) surfaces [93]. We can identify the corner holes (dots in **Figure 6. 15 (d)**) and the adatoms (crosses in **Figure 6. 15 (d)**) of the 3×3 structure located at the step edge. The adatoms have 2 Å lower apparent height than the Bi trimers on the upper terrace. This height difference corresponds to that one we measure on samples, where larger areas of 1 ML terminated

Si(111)- $\sqrt{3} \times \sqrt{3}$ -Bi and clean Si(111)-7x7 coexist **Figure 6.** 7 (a). This confirms the assignment of the ringlike arranged adatoms as Si or Ge without Bi termination.

Conclusions

A technique of modified surfactant mediated epitaxy was introduced, where the surfactant concentration is reduced on the surface to influence the growth and equilibrium properties of the surface steps in a desired way. This modified surfactant mediated epitaxy is shown relevant to nanotechnology since it allows fabricating arrays of long equidistant epitaxial Ge nanowires with a width in the one-digit nanometer range. In future these nanowire arrays could serve as templates for selective attachment of molecules, decoration with metals, or attachment of clusters and other nanoscale building blocks such as fullerenes. The study of charge transport through such very small nanowires will be another challenge. The present work focuses on one specific material combination. However, the use of surfactant coverage as a variable parameter opens up an additional dimension in the growth parameter space that can be explored in bottom-up nanofabrication studies in general.

7 Symmetry breaking in the growth of two-dimensional islands on Si(111)

The observation of faceted crystal shapes is a fascinating experience because it allows a direct look into the point group symmetry of the crystal. The equilibrium shape of a crystal has the same symmetry as the lattice of the atoms inside the crystal [94]. Also, for growth shapes of crystals, often a close relation between the crystal lattice symmetry and the morphology is found. The shape of the islands usually follows the symmetry of the underlying substrate. On the threefold symmetric Si(111) substrate epitaxially grown two-dimensional Si and Ge islands have triangular shape [7]. Also the tetrahedron-shaped three-dimensional Ge islands grown on Si(111) obey the threefold symmetry of the substrate [7]. At the $C_{2\nu}$ symmetric Si(001) surface two-dimensional Si or Ge islands and the three-dimensional hut clusters have an elongated shape consistent with the $C_{2\nu}$ symmetry [95]. It is well known that surface reconstructions can lower the symmetry of the crystal. For instance, for surface reconstructions induced by atomic layer thick adlayers of In and Au, the formation of linear stripes breaks the threefold symmetry of the underlying Si(111) surface [96,97]. However, this symmetry lowering due to the reconstruction does not imply a pronounced impact on the island shapes on these surfaces [98].

An analysis of the symmetry of the combined system of the reconstructed substrate and the reconstructed nanostructure is required to predict the symmetry of the shape of the nanostructures. Here we show that a surface reconstruction can lead to the growth of 2D epitaxial islands with a lower symmetry than the substrate. It is known that a relation between the internal symmetry and symmetry of macroscopic parameters of a system exists. For the case of 2D epitaxial island growth one example is the symmetry of the thermodynamic properties of the different step directions resulting into a shape symmetry.

Here we consider a model which describes a 2D island as combined system including the surface plane of the substrate and the surface plane of the 2D island Figure 7. 1. The combined system is based on the structure of the bulk lattice (basis vectors of the bulk lattice) and obeys the internal symmetry of the bulk lattice B without taking the reconstruction into account. In the model we consider the case when the surface planes of the island and substrate have the same reconstruction, i.e. the same symmetry (translation and point group symmetry). The surface reconstruction can reduce the 2D translation and/or point group symmetry of the surface. If the surface reconstruction has a lower point group symmetry R than the bulk the point group symmetry of the combined system is directly broken, since the point symmetry C of the combined system is the intersection of the individual symmetries for the surface and bulk $C = R \cap B$. If the surface reconstruction has a lower translation group symmetry R^t than the bulk the translation group symmetry of the combined system is directly broken, since the translation symmetry C^t of the combined system is the intersection of the of the surface and bulk symmetries $C^t = R^t \cap B^t$. In this case the surface reconstruction on the island can have different lateral phase positions to the reconstruction on the substrate. The phase positions differ by a shift vector which is equal to linear combinations of the basis lattice vectors for the unreconstructed 1×1 surface: $a \cdot n + b \cdot m$, where a and b are basis vectors and n, m are integer numbers 1, 2, 3,..., N. The cases when the surface reconstruction directly breaks the translational symmetry of the surface will be considered here.

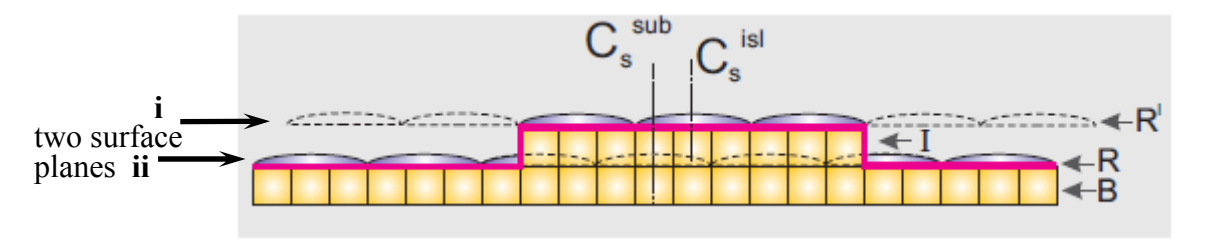


Figure 7. 1. The two level system, island surface plus substrate surface. Cross section through the combined a system of reconstructed substrate and reconstructed island (three times reconstruction on a simple cubic lattice). The subsystem of substrate and reconstruction has a Cs mirror symmetry as well as the subsystem of island and reconstruction. However, due to a shift between both reconstructions these mirror planes are not identical (shifted) and the complete system of substrate, island and the corresponding reconstructions obeys no mirror symmetry. We say that the mirror symmetry is broken by the combined system.

The 2D symmetry of the unreconstructed surface is a projection of the bulk symmetry to the surface plane. The symmetry of the unreconstructed surface obeys the symmetry group operations (point group operations and translation group operations) of the bulk lattice for this plane.

In the following we discuss several case studies of the symmetry analysis of the combined system of reconstructed substrate and island and deduce predictions for the island growth shapes. In particular we will introduce a method which we call "analysis of common fixed points" which is a simple way to analyze if the symmetry of the combined system is lower than symmetry of each of the two subsystems (reconstructed island or reconstructed substrate). This case we term "symmetry breaking".

Figure 7. 2 shows the symmetry elements of the five fundamental 2D Bravais lattices. Any symmetry element has several fixed points. A fixed point is a point that does not change upon application of a (map) symmetry group operations: mirror reflections C_s rotations C_n , inversions. The oblique lattice has four C_2 fixed points per unit cell, the rectangular lattice has four $C_{2\nu}$, the centered rectangular lattice has two C_2 and two $C_{2\nu}$ fixed points per unit cell, the hexagonal lattice has one $C_{6\nu}$ two $C_{3\nu}$ and three $C_{2\nu}$ and square lattice has two $C_{2\nu}$ and two $C_{4\nu}$ fixed points per unit cell.

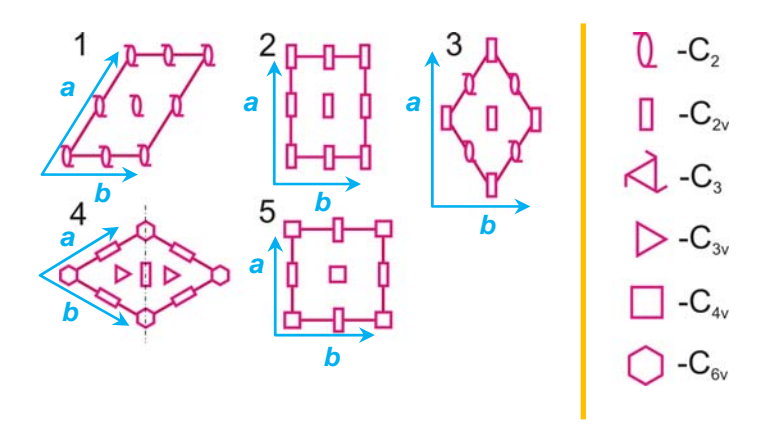


Figure 7. 2. Five basic symmetry elements for the five fundamental Bravais lattices: 1 oblique, 2 rectangular, 3 centered rectangular, 4 hexagonal, and 5 square. Basis vectors **a** and **b** are shown by blue arrows. Symbols for the fixed points are defined as shown in the right of the image.

Where C_2 , $C_{2\nu}$, $C_{2\nu}$, $C_{6\nu}$, and $C_{4\nu}$ are symmetries of these five fundamental Bravais lattices respectively.

Now we consider two Bravais lattices which can be identified with substrate reconstructed lattice and island reconstructed lattice. There exist only a limited number of combinations (shifts) between these lattices which fulfill the condition that the symmetry of the combined system is the same as the symmetry of the original lattices. Any lateral shift can be expressed in the lattice basis vectors \boldsymbol{a} and \boldsymbol{b} of the unreconstructed (1×1) surface unit cell:

$$(x,y) = \frac{\overline{a}}{\|a\|} x + \frac{\overline{b}}{\|b\|} y, \tag{7.1}$$

The oblique and the rectangular lattice symmetry element can be fixed in 4 different ways, the centered rectangular and square in two different ways and the hexagonal in one way. The combined system which is a combination of island plane plus substrate plane has a symmetry equal to the intersection of the symmetries of the common points with the same lateral position. The resulting symmetry is an intersection of the individual symmetries of these points $C_i \cap C_{ii}$. The symmetry of the combined system is the symmetry of the reconstructed surface if some symmetry elements of the reconstructed surface have the same lateral position as the symmetry elements of the substrate. Several special mutual shifts which leave the symmetry of combined system equal to the symmetry of the surface reconstruction are shown in **Figure 7. 3**. The symmetry of the combined system with oblique and rectangular lattices obeys the symmetry of the surface reconstruction for mutual lateral shifts which are half of the basis lattice vectors a, b and $(a \pm b)$ correspondingly **Figure 7. 3**.

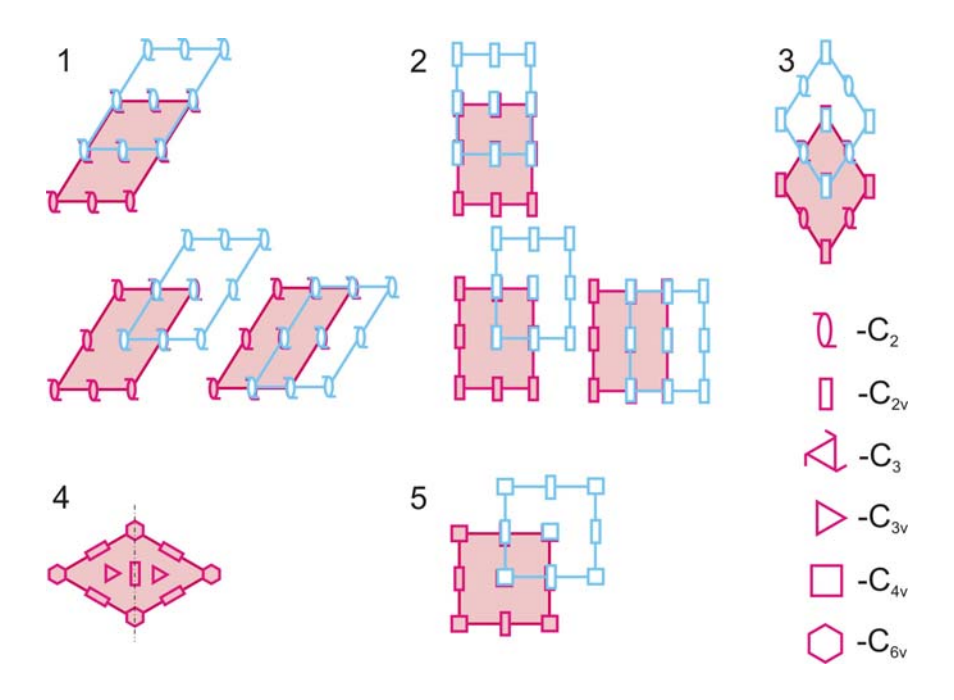


Figure 7. 3. The relative lateral positions for the five basic symmetry elements on the island surface and substrate surface which leave the original symmetry of the surface lattice structure for the combined system. According to (7. 1) the lateral position can be expressed as the following: 1-oblique: $\frac{1}{2}(a,0)$, $\frac{1}{2}(0,b)$, $\frac{1}{2}(a,b)$; 2-rectangular: $\frac{1}{2}(a,0)$, $\frac{1}{2}(a,b)$; 3-centered rectangular: $\frac{1}{2}(a,0)$; 4-hexagonal: (0,0); 5-square: $\frac{1}{2}(a,b)$.

For centered rectangular lattice the shifts are half of a and b; for hexagonal the shifts is on one third and two third of (a + b); for square lattice the shifts are half of $(a \pm b)$ basis lattice vectors leave the symmetry of the combined system equal to the original symmetry of the surface reconstruction **Figure 7.3**.

Other sets of shifts of the lattices results in a lowered symmetry are shown in **Figure 7. 4**. The symmetries C_2 , $C_{2\nu}$, $C_{2\nu}$, $C_{6\nu}$, and $C_{4\nu}$ of the five fundamental lattices can be lowered to the symmetries of subgroups. Subgroup of $C_{2\nu}$ point group are: C_2 , C_3 ; subgroup of $C_{6\nu}$ are: C_6 , $C_{2\nu}$, C_3 , C_2 , C_3 ; subgroup of $C_{4\nu}$ are: $C_{2\nu}$, C_4 , C_2 , C_5 . The corresponding symmetries and shifts are placed in **Table 7. 1**, the shifts are expressed according to (7. 1).

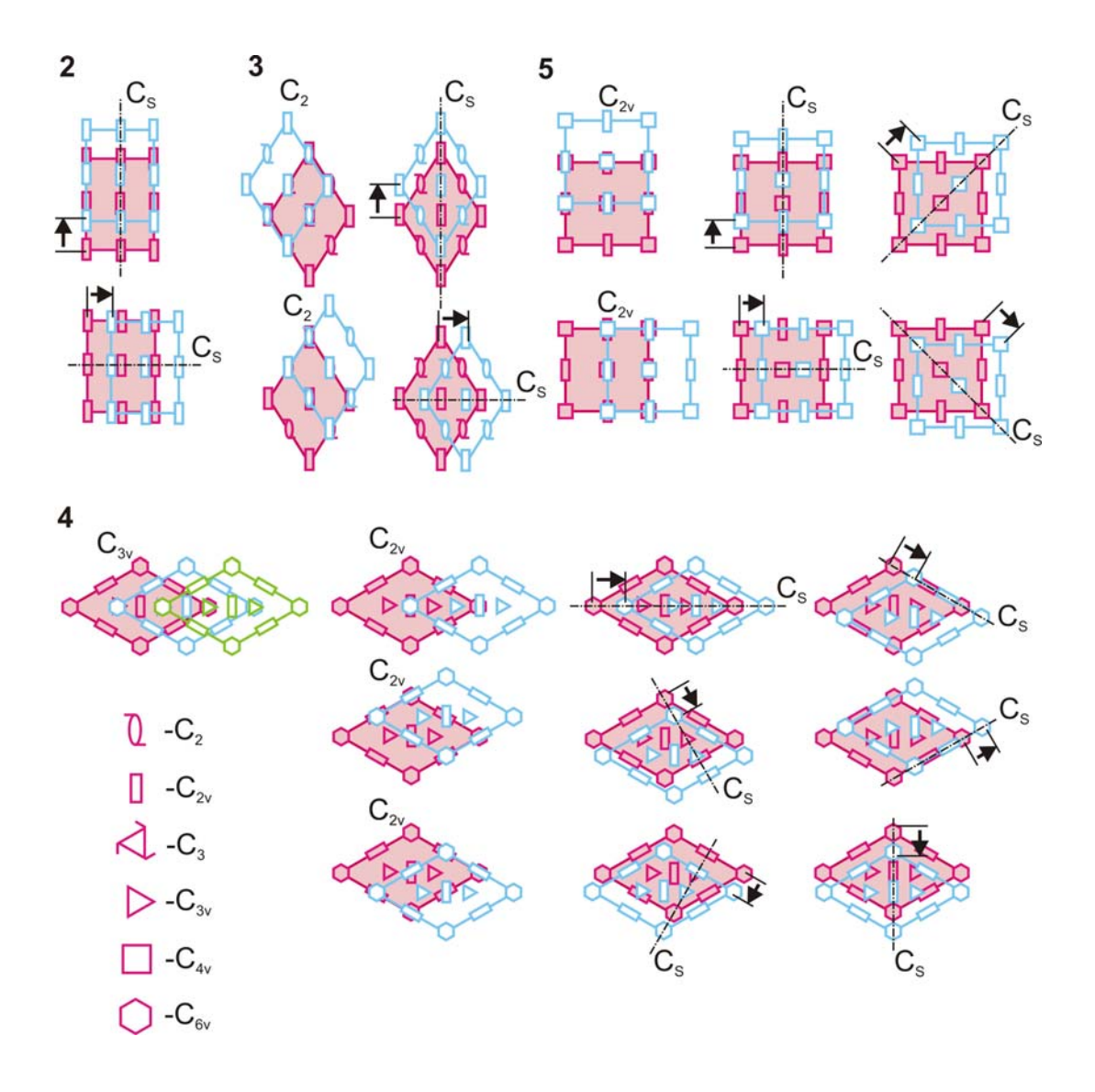


Figure 7. 4. The relative lateral positions and shifts which reduce the symmetry of combined system to a subgroup symmetry of the original surface lattice symmetry. Arbitrary shifts along mirror planes are shown by black arrows reduce the symmetry of combined system to the symmetry of mirror plane C_s .

Table 7. 1

Table 7. I		
Bravais lattices	Symmetries of	shifts
	combined system	
1 Oblique	C_2	$(0,0); \frac{1}{2}(a,0); \frac{1}{2}(0,b); \frac{1}{2}(a,b)$
	I	$(x,y) \notin \text{the shifts above}$
2 Rectangular	C_{2v}	$(0,0)$; $\frac{1}{2}(a,0)$; $\frac{1}{2}(0,b)$; $\frac{1}{2}(a,b)$
	C_s	$\alpha(a,0)$; $\alpha(0,b)$, where $\alpha \neq \frac{1}{2}$, <1
	I	(x,y)∉ the shifts above
3 Centered	C_{2v}	$(0,0)$; $\frac{1}{2}(a,0) = \frac{1}{2}(0,b)$
rectangular	C_2	$\frac{1}{4}(a,-b); \frac{1}{4}(a,b)$
	C_s	$\alpha(a,0)$; $\alpha(0,b)$, where $\alpha \neq \frac{1}{2}$, <1
	I	$(x,y) \notin \text{the shifts above}$
4 Hexagonal	C_{6v}	(0,0)
_	C_{3v}	1/3(a,b); $2/3(a,b)$
	C_{2v}	$\frac{1}{2}(a,0); \frac{1}{2}(0,b); \frac{1}{2}(a,b)$
	C_s	$\alpha(a,0)$; $\alpha(0,b)$; $\alpha(a,b)$; $\alpha(-a,b)$; $\alpha(-a,2b)$; $\alpha(-2a,b)$
	I	$(x,y) \notin \text{the shifts above}$
5 Square	C_{4v}	$(0,0)$; $\frac{1}{2}(a,b)$
	C_{2v}	$\frac{1}{2}(a,0); \frac{1}{2}(0,b)$
	C_s	$\alpha(a,0)$; $\alpha(0,b)$; $\alpha(a,b)$; $\alpha(-a,b)$, where $\alpha \neq \frac{1}{2}$, <1
	I	$(x,y) \notin \text{the shifts above}$

The shifts along mirror planes on arbitrary distances, which are not equal to the special positions in **Figure 7. 3** for rectangular, centered rectangular, hexagonal and square lattices reduces $C_{2\nu}$, $C_{6\nu}$, and $C_{4\nu}$ symmetries to C_s symmetry respectively. Combinations of common fixed points with different symmetries are resulting into symmetry of an intersection of these symmetries. Combination of $C_{2\nu}$ and $C_{2\nu}$ fixed points for centered rectangular lattice is $C_{2\nu}\cap C_2 = C_2$ symmetry **Figure 7. 4**. Combination of $C_{6\nu}$ and $C_{3\nu}$ fixed points for hexagonal lattice is $C_{6\nu}\cap C_{3\nu} = C_{3\nu}$, $C_{6\nu}$ and $C_{2\nu}$ is $C_{6\nu}\cap C_{2\nu} = C_{2\nu}$, respectively **Figure 7. 4**. Combination of $C_{4\nu}$ and $C_{2\nu}$ is $C_{4\nu}\cap C_{2\nu} = C_{2\nu}$ symmetry **Figure 7. 4**.

A surface reconstruction basis vectors $\left(\frac{\overline{a}'}{\overline{b}'}\right)$ can be expressed with the unreconstructed

surface basis vectors $\begin{pmatrix} \overline{a} \\ \overline{b} \end{pmatrix}$ as:

$$\begin{pmatrix} \overline{a}' \\ \overline{b}' \end{pmatrix} = \begin{pmatrix} n & m \\ k & l \end{pmatrix} \begin{pmatrix} \overline{a} \\ \overline{b} \end{pmatrix},$$

where integer n, m, k, l are indexes of the surface reconstruction. For example basis vectors for Si(111)7×7 are $\begin{pmatrix} \overline{a}' \\ \overline{b}' \end{pmatrix} = \begin{pmatrix} 7 & 0 \\ 0 & 7 \end{pmatrix} \begin{pmatrix} \overline{a} \\ \overline{b} \end{pmatrix} \Rightarrow \overline{a}' = 7\overline{a}, \ \overline{b}' = 7\overline{b}$.

The mutual shift between surface reconstructions of the combined system can take a limited number of different lateral positions, the number of positions is equal to the relation of the area of the reconstructed unit cell area to the area of unreconstructed surface unit cell

$$\frac{A_{rec}}{A_{l\times l}} = \frac{\left\|\overline{a}' \times \overline{b}'\right\|}{\left\|\overline{a} \times \overline{b}\right\|} = \frac{\left\|\left(n\overline{a} + m\overline{b}\right) \times \left(k\overline{a} + l\overline{b}\right)\right\|}{\left\|\overline{a} \times \overline{b}\right\|} = (n \cdot l - m \cdot k), \text{ where } n, m, k, l \text{ are integer numbers.}$$

3D crystal system sets the additional rules for the stacking of the island surface structure with substrate surface structure. The number of different lateral positions $(\frac{A_{rec}}{A_{bd}})$ and structure

of 3D crystal system define possible symmetries of the combined system. The described analysis can be used for prediction of 2D island shape. The 2D island presents combined system (**Figure 7. 1**) with two surface planes: substrate surface plane and island surface plane. The island steps connecting these two planes inherit the symmetry of the two level combined system resulting into symmetry of equal step directions and shape. To find the symmetry of the combined system we have to look into bulk lattice structure of the system. The following analysis will be made for the diamond lattice structure.

The nearest (111) surface planes of Si diamond structure are spaced with the distance equal to the one monolayer (ML) which is minimal height of 2D Si/Ge islands on the Si(111) surface. This distance is 3 times lower than translation shift in $\langle 111 \rangle$ direction (3 ML). For this reason the two nearest (111) surface planes have a natural mutual shift between two neighboring layers of the (111) stacking which is equal to $a_0 / \sqrt{3} [\overline{1} \ \overline{1} \ 2]$, where a_0 is length of 1×1 unit cell basis vector. Now we consider a surface reconstruction which obeys the $C_{3\nu}$ symmetry which is the intersection of the Bravais lattice symmetry $C_{6\nu}$ and symmetry of a diamond bulk basis: $C_{3\nu} = C_{6\nu} \cap C_{3\nu}$. Figure 7. 5 shows relative lateral positions for two symmetry elements: image (a) shows symmetry element of the surface structure of Si(111) surface which have the same orientation with the symmetry elements of the unreconstructed surface and image (b) shows the symmetry element 30° rotated to the substrate. The corner fixed points of the element Figure 7. 5 (b) have $C_{3\nu}$, symmetry while symmetry of inner fixed points is lowered to C_3 symmetry because of these fixed points have no common mirror planes with substrate.

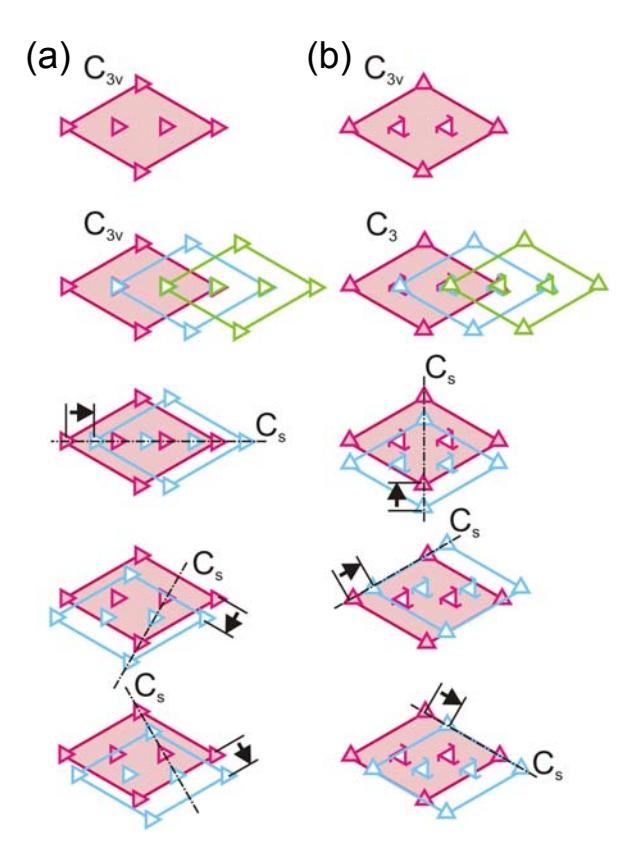


Figure 7. 5. The relative lateral positions and shifts for symmetry elements which reduce symmetry of combined system to a subgroup symmetry of the reconstructed surface. Arbitrary shifts along mirror planes are shown by black arrows reduce the symmetry of combined system to the symmetry of mirror plane C_s .

In general we consider a (N×N) reconstruction. First we consider unit cell Figure 7. 5 (a). The positions of the fixed points in the reconstruction unit cell are known from the symmetry to be at the corners of the unit cell and at the center of the triangular half unit cells, indicated by blue triangles in the unit cell shown in blue in Figure 7. 6 (a). There are only three possible independent shifts between the reconstruction unit cells which maintain the symmetry of the combined system, i.e. lead to a lattice of common fixed points. These three independent shifts of the reconstruction unit cell are shown in Figure 7. 6 (a) as full, dashed, and dotted lines. In a further the analysis the arrangement of the fixed points on the substrate and island with respect to the fixed points in the reconstructed layer will be considered. In the final analysis we study for which arrangement(s) of the reconstruction unit cells an "anchoring" of the unit cells on island and substrate is possible with the same local geometry. Before continuation of this analysis the arrangement of the fixed points with a certain local geometry on the substrate and island without reconstruction will be studied. In the (1×1) unit cell of the diamond structure (111) surface there are three types of fixed points, each with a different local environment. The local environment of these fixed points also can't be the same for all three points since it automatically reduces size of unit cell – this is contradicted with assumption that 1×1 is minimal unit cell. As shown in Figure 7. 6 (b) and (c) the fixed point indicated by 1 is located at the atom in the lower part (lower half layer) of the first bilayer, the fixed point of type 2 is located at the atom in the upper part (upper half layer) of the first (111) bi-layer, while the fixed point of type 3 is not located at any atom position of the first bilayer. All of these fixed points lie along the $[\overline{1}\ \overline{1}\ 2]$ direction each one shifted by $a/\sqrt{3}$ with respect to the others (a = surface lattice constant). The natural shift between two neighboring layers determines the simple rule for the relationship of the fixed points **Figure 7.6 (c)**. The stacking of the fixed points between two layers is the following: 3 lies below 1, 1 lies below 2 and 2 lies below 3 **Figure 7.6 (c)**.

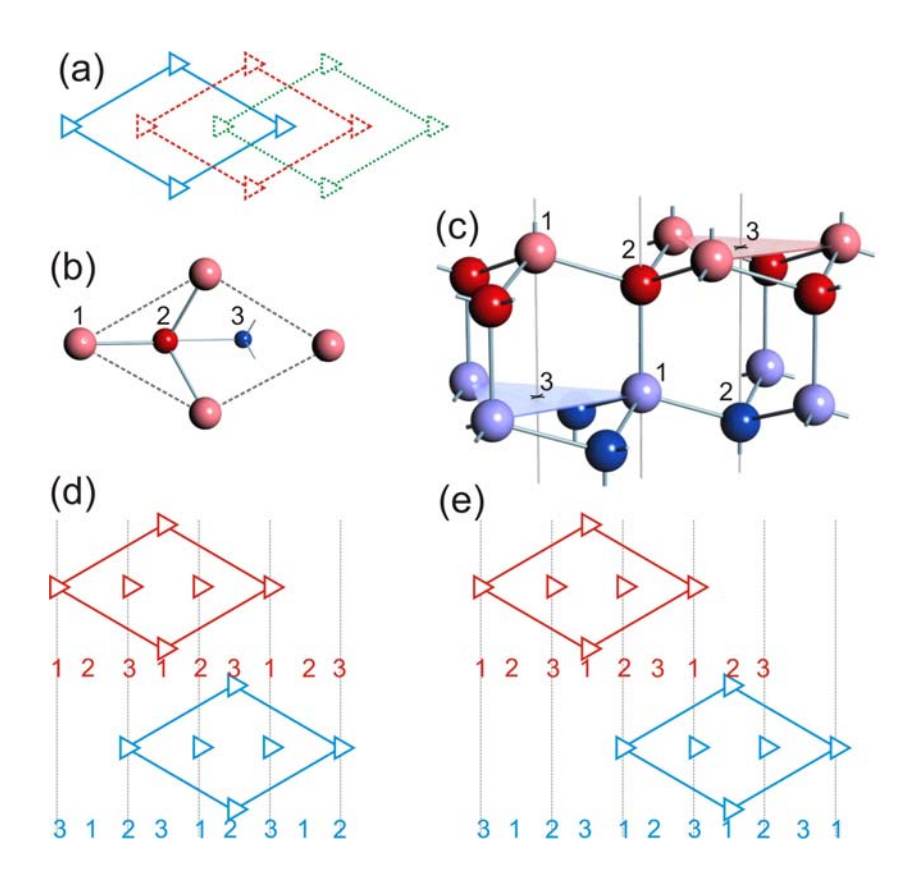


Figure 7. 6. (a) A reconstruction unit cell with C3v symmetry is shown by blue lines. The three fixed points are marked by triangles. There are only two shifts possible which maintain the original lattice of common points, shown in (a). (b) top view to the (111) diamond surface (upper two bi-layers) the unit cell is indicated by a dashed line. The unit cell contains three fixed points with different local structure, named 1, 2, and 3. (c) perspective view to the first and second bi-layer of the diamond lattice. There is a unique stacking of the type of fixed points in the first two bilayers: 3 below 1, 1 below 2 and 2 below 3. (d), (e) two different shifts leaving the original C_{3v} symmetry for 2×2 reconstructed combined system. Identical lateral position (zero shift) is not shown since this position is not possible due to stacking between neighboring layers (c). Due to this, the shift shown in (d) is not possible also, therefore only one shift (e) from 4 possible leaves the C_{3v} symmetry.

In total we have two constraints: one is given by the symmetry of the reconstruction unit cell this alone leads to a limited number of possible pairs of lattices which have common fixed points **Figure 7.6** (a). On the other hand the reconstructions on the island and on the substrate have to be "anchored" at the same local position to the substrate in both cases. In the course of the symmetry analysis it has to be found out if both conditions can be met simultaneously.

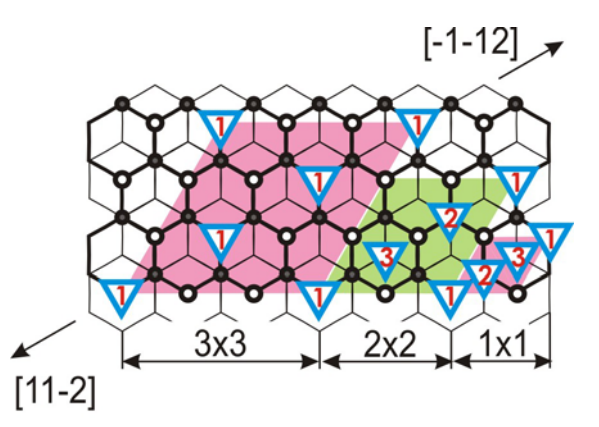
Now the case of a (N×N) reconstruction will be considered. For any $C_{3\nu}$ (N×N) reconstruction unit cell the number of fixed points is always still three. Therefore, the distance between the fixed points of the (N×N) reconstruction cell is always N times larger than on the spacing of the fixed points of the substrate $((1\times1))$. For a $(3N\times3N)$ unit cell one sees that always after 3N fixed points of the substrate the next fixed point of the reconstruction has the same type (for instance 1) as the first one. This is the case since the sequence of fixed points on the substrate along $[\overline{1} \ \overline{1} \ 2]$ mirror plane direction is always (1),2,3,(1),2,3,(1),..., as shown before. Therefore, in this case all fixed points of the reconstruction unit cell lie above the same type of fixed points of the substrate (for instance type 1), as shown for the example of the (3×3) reconstruction in **Figure 7.** 7. According to the stacking in the neighboring layers Figure 7. 6 (c) the same fixed points can't be combined in the 2D island of 1ML height. Therefore, the $C_{3\nu}$ symmetry of 1ML height islands is always broken for a (3N×3N) reconstruction. As was mentioned previously, the translational shift in (111) direction is equal to 3ML height, therefore 3ML heigh islands (usually observed during MBE growth Si/Ge on Si(111)(7×7) have no shift between the same type of fixed points of substrate plane and island plane: 1 below 1, 2 below 2, 3 below 3. In this case three of $(3N)^2$ (or one of $3N^2$) shifts Figure 7. 6 (a) leave the original $C_{3\nu}$ symmetry of the surface reconstruction in the combined 3ML heigh system.

For $C_{3\nu}$ (2×2) reconstruction we have the sequence of fixed points on the substrate along $[\overline{1}\ \overline{1}\ 2]$ direction (**Figure 7. 6 (d), (e) and Figure 7. 7**) (1),2,(3),1,(2),3,(1),2,..., here and further the number of common fixed points for the $C_{3\nu}$ (2×2) reconstruction will be shown in brackets. Natural shift of reconstruction on 1ML heigh 2D island plus shift on $a\sqrt{3}$ in $[\overline{1}\ \overline{1}\ 2]$ direction gives in result stacking of the fixed points between two neighboring layers: 3 lies below 1, 1 lies below 2 and 2 lies below 3; as shown below:

```
natural shift natural shift + a\sqrt{3} island= (1),2,(3),1,(2),3,(1),2,..., \rightarrow (1),2,(3),1,(2),3,(1),2,..., substrate= (1),2,(3),1,(2),3,(1),2,..., \rightarrow (1),2,(3),1,(2),3,(1),2,...,
```

Natural shift plus shift on $2a\sqrt{3}$ breaks $C_{3\nu}$ symmetry since no $C_{3\nu}$ fixed point of the substrate reconstruction (number in brackets) below fixed point on the island reconstructed surface:

```
island= natural shift + 2a\sqrt{3}
island= (1),2,(3),1,(2),3,(1),2,...,
substrate= (1),2,(3),1,(2),3,(1),2,...,
```



- O -1 plane Si atoms
- -2d plane Si atoms

Figure 7. 7. Three $C_{3\nu}$ common fixed points in $n \times n$ unit cell are shown with blue triangles. The reconstructions type of $3N \times 3N$ have only one type of common fixed points.

For the $(3N\pm1\times3N\pm1)$ reconstructions we have the sequences of fixed points on the substrate along $[\overline{1}\ \overline{1}\ 2]$ direction like (1),...,(3),...,(2),...,(1),..., or (1),...,(2),...,(3),...,(1),..., for these sequences the $C_{3\nu}$ symmetry can be saved for one of the shifts. A bit loosely explained the shift of the reconstruction unit cell between substrate and island in units of $3N\pm1$ can be compensated by a corresponding shift in the stacking of the fixed points of substrate and island due to the atomic step. In the general of the $(3N\pm1\times3N\pm1)$ reconstruction on the island can be shifted relative to reconstruction of the substrate in $(3N\pm1)^2$ different translational domains. Only for one of these shifts $C_{3\nu}$ symmetry is retained.

Another important type of structures on the $C_{3\nu}$ (111) surface are the structures with mirror planes 30° rotated to the mirror planes of (111) substrate. The common fixed points in the unit cell of the 30° rotated reconstruction are shifted by $a/\sqrt{3}$ along the $[1\,\overline{1}\,0]$ direction Figure 7. 8. The 30° rotated unit cell has three fixed points: one $C_{3\nu}$ in the corner and two C_3 inside. In Figure 7. 8 two examples of a $(\sqrt{3} \times \sqrt{3})R30^{\circ}$ reconstruction (pink shaded area at the top) and a $(2\sqrt{3}\times2\sqrt{3})R30^{\circ}$ reconstruction (pink shaded area at the bottom) are shown together with the underlying diamond lattice. It can be seen that in both cases (as also in all other cases of $\sqrt{3}$ reconstructions) the fixed points of the reconstruction unit cell lie (due to the symmetry of the unit cell) on identical positions (types of fixed points) of the substrate lattice; here we have chosen the type 2 (yellow dashed line – type 1). Therefore, also all of the possible shifts of the reconstruction layer will have their fixed points above a type 2 fixed point on the diamond lattice, since all shifts are multiples of the reconstruction fixed point distances. The fixed points of the reconstruction unit cell are shifted by $a/\sqrt{3}$ along the $\begin{bmatrix} 1 & 1 & 0 \end{bmatrix}$ direction. As discussed before the atomic step induces a shift in the stacking of the underlying substrate fixed points along the $[\overline{1}\ \overline{1}\ 2]$ direction. As can be seen from Fig. 9 such a shift can never shift a type 2 fixed point of the surface reconstruction to another type 2 point. This implies that an anchoring of the reconstruction unit cell to the same type of fixed points on the substrate and island diamond lattice is not possible. Therefore, for $\sqrt{3}$ type reconstructions the C3v symmetry is always broken to a Cs symmetry or I. As a result of this symmetry breaking the island shapes can be different from the C_{3v} symmetry of the substrate and islands

with one mirror plane (Cs symmetry) occur. This behavior was actually observed for the system of 2D Si or Ge islands on Si(111) where islands and substrate are terminated by a Bi $(\sqrt{3} \times \sqrt{3})$ R30° reconstruction. In this case islands with only one mirror plane were observed despite of the fact that a threefold $C_{3\nu}$ symmetry was present for the substrate and both, the island reconstruction and the substrate reconstruction.

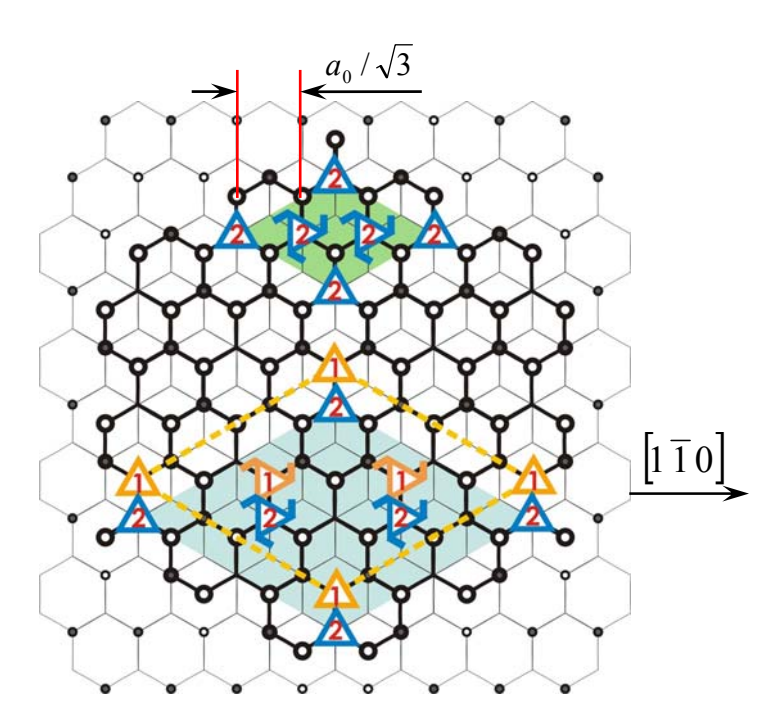


Figure 7. 8. The 30° rotated C_{3v} surface structures. The reconstructed surface has 3 common points which lie along $\begin{bmatrix} 1 & 1 & 0 \end{bmatrix}$ direction. The two common points inside of unit cell have C_3 symmetry and common point in the corner has C_{3v} symmetry. Blue triangles mark the common points with type of "2", yellow triangles mark the common points with type of "1".

Here an example of symmetry breaking in the Bi SME on Si(111) Bi $(\sqrt{3} \times \sqrt{3})$ R30° surface will be considered in details. In surfactant-mediated Si and Ge epitaxy on the threefold symmetric Si(111) substrate we observed the growth of arrow-shaped and rhomb-shaped two-dimensional islands respectively. These islands break the threefold symmetry of the substrate in spite of the fact that the $(\sqrt{3} \times \sqrt{3})$ R30° Bi reconstruction present at the surface has locally the same threefold symmetry $(C_{3\nu})$ as the Si(111) substrate. The reason for the symmetry breaking is a mutual shift between the reconstruction on the substrate and on the island, imposed by the diamond crystal structure of the Si substrate. The shape of the islands can be related to the growth velocities of the step edges via the kinematic Wulff construction resulting in a complete information on the growth kinetics of the islands shown in a kinematic Wulff plot. In the experiments we use surfactant-mediated growth [87,99], which means that an additional species floating at the growth front (Bi in our case) modifies

epitaxial growth. Prior to growth a saturation coverage of one atomic layer of Bi is deposited on the clean Si(111)-(7×7) at 740 K [100]. Subsequently, a submonolayer amount of Si or Ge was deposited at growth rates of about 0.02 atomic layers per min and at a temperature of 670 K. A Bi flux of one atomic layer per min was maintained during Ge growth to keep a complete Bi termination. After growth the surface was maged at room temperature by scanning tunneling microscopy (STM).

Figure 7. 9 (a) shows two-dimensional Si islands grown on the Si(111) surface in Bi mediated epitaxy. Clearly these arrow-shaped islands have a lower symmetry than the threefold symmetry ($C_{3\nu}$) of the underlying Si(111) surface. The symmetry of an island is reduced to C_s symmetry with only one mirror plane as symmetry operation. The arrow-shaped islands occur in three domains. The crystallographic directions of the steps terminating the islands were determined from comparison to atomically resolved STM images of the clean Si(111)-(7×7) surface taken before deposition of Bi.

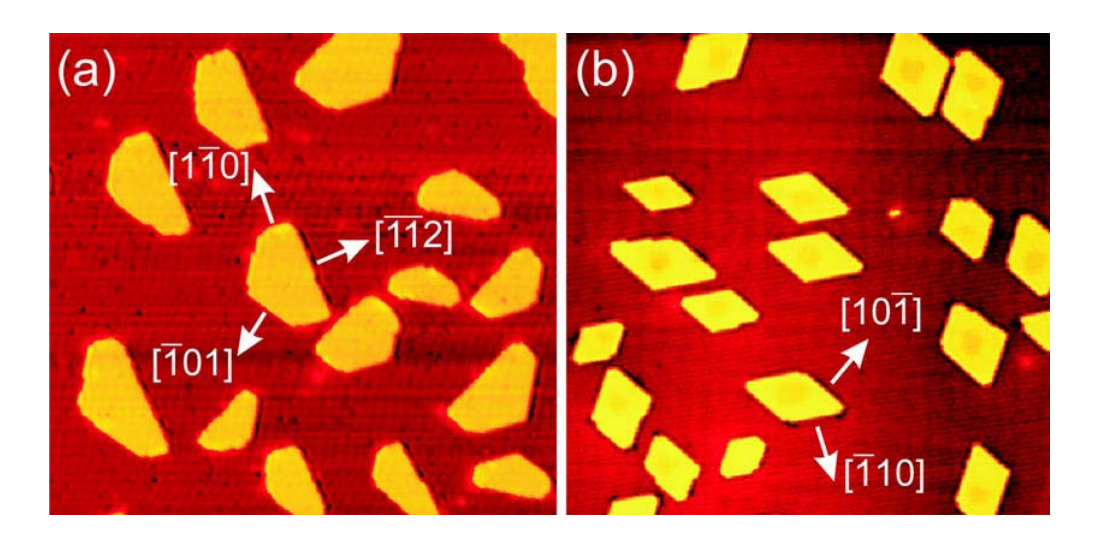


Figure 7. 9. (a) STM images of arrow-shaped Si islands on the Bi terminated Si(111) substrate. The shape of these islands breaks the threefold symmetry of the substrate surface. (b) Rhomb-shaped Ge islands on the Bi terminated Si(111) substrate breaking the threefold symmetry as well. Image sizes (a) 200 nm, (b) 110 nm.

The $(\sqrt{3} \times \sqrt{3})R30^\circ$ Bi reconstruction is present on the substrate as well as on the islands. For the growth of Ge on the Bi terminated Si(111) rhomb-shaped islands [terminated by the $(\sqrt{3} \times \sqrt{3})$ Bi reconstruction as well] were observed, also breaking the threefold symmetry of the Si(111) substrate surface [**Figure 7. 9 (b)**]. As will be shown later, the symmetry of the rhomb-shaped island is also C_s .

The observed symmetry breaking is a striking result because the Bi $(\sqrt{3} \times \sqrt{3})$ reconstructions on both, the island and the substrate, obey the same symmetry as the

substrate. The reason for the observed symmetry breaking is a mutual lateral shift between the reconstructions on the substrate and on the islands. **Figure 7. 10 (a)** shows two adjacent diamond structure (111) bilayers: the substrate bilayer and a hexagonal island residing on the substrate. The shape of the island was chosen such that all six experimentally observed step edges of the $\langle 1\,\overline{1}\,0 \rangle$ type (**Figure 7. 9**) are included. Without taking the Bi reconstruction into account, the combined system of island plus the substrate obeys the $C_{3\nu}$ symmetry with three mirror planes (the combined system without reconstruction is still part of the bulk crystal). This means also that the step edges marked as 1, 2, and 3 in **Figure 7. 10 (a)** have the same structure. Now we include

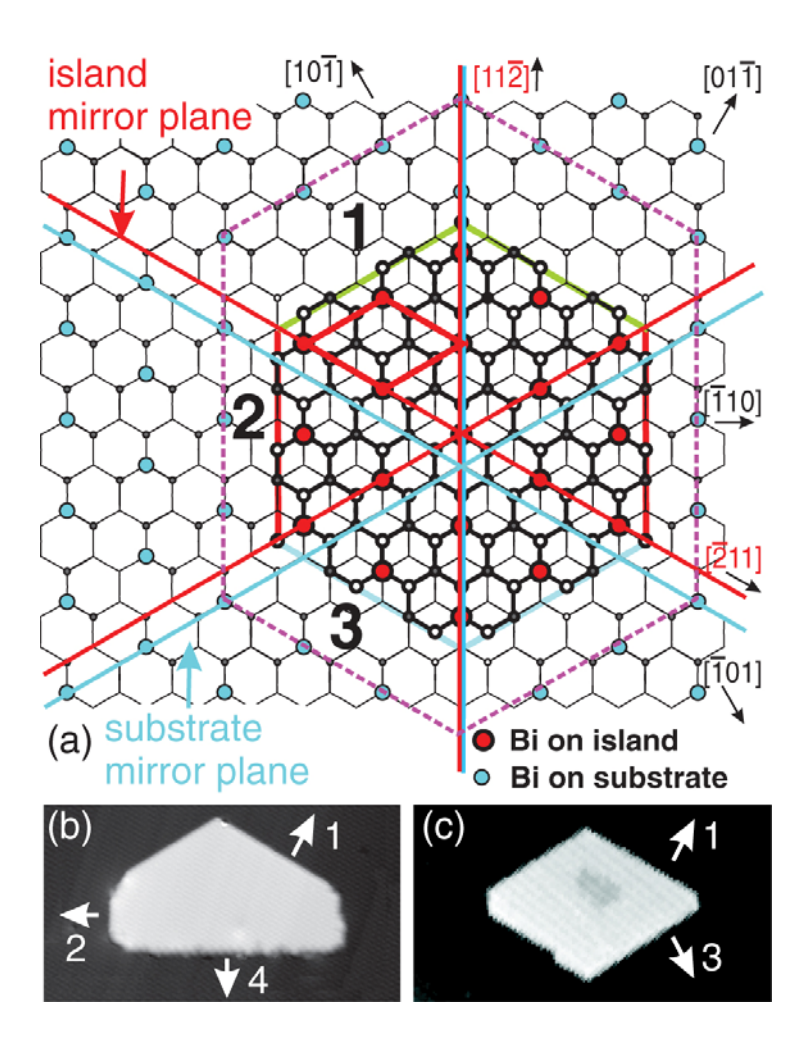


Figure 7. 10. (a) Schematic of the two level system of the substrate and a two-dimensional sland. While a threefold symmetric $(\sqrt{3} \times \sqrt{3})$ Bi reconstruction is present on each individual level, the $C_{3\nu}$ symmetry is broken for the combined system and is reduced to a C_s symmetry. (b) and (c) STM images of an arrow- and a rhomb-shaped shaped island, respectively.

the Bi reconstruction which is indicated by colored circles in **Figure 7. 10** (a) (one circle corresponds to a Bi trimer). Because of the reconstruction two of the mirror planes of the substrate reconstruction (blue lines) are not coincident with the mirror planes of the island reconstruction (red lines). While the two sets of substrate and island mirror planes run along the same directions the common point of the C_3 point symmetry operations is shifted between substrate and island by the vector $a_0 / \sqrt{3} \left[\overline{1} \ \overline{1} \ \overline{2} \right]$. Therefore, the symmetry of the combined system of island and substrate is lowered. Only the mirror plane running along $\left[11\overline{2}\right]$ is a symmetry element of the combined system. Because of the shift of the common point of the other two mirror planes between island and substrate reconstruction these symmetry operations are no longer point symmetry operations of the combined system.

The lateral shift between the reconstructions on the island and the substrate is induced by a lateral shift between two adjacent (111) bilayers of the diamond lattice of the same value $a_0 / \sqrt{3} [\overline{1} \ \overline{1} \ 2]$ [compare **Figure 7. 10 (a)**]. However, for the unreconstructed system this shift (which is a property of the bulk crystal structure) does not break the $C_{3\nu}$ symmetry. This mutual lateral shift between both bilayers also propagates to the Bi $(\sqrt{3} \times \sqrt{3})R30^{\circ}$ reconstruction layers in both levels. However, on the reconstructed surface the threefold symmetry of the underlying substrate is broken for the combined system because the common points of the point symmetry operations of both subsystems are shifted relative to each other due to the larger unit cell of the reconstructed surface. Generally, for two systems and the corresponding two sets of point group operations A and B the set of point group operations of the combined system D is the intersection $D = A \cap B$ [101]. This means that the only symmetry plane of the combined system is the $[11\overline{2}]$ mirror plane and the resulting symmetry group of the combined system is C_s [102]. The reduced symmetry of the combined system of reconstructed surface and island has important consequences for the shape of the islands. The neighboring steps 1, 2, and 3, respectively, are not connected by a symmetry operation as the $C_{3\nu}$ symmetry is broken for the combined system. Thus, these steps are all different. These differences in the structure of the step edges lead to different step speeds. The different step speeds in turn determine the island shapes, as we will show. While we do not know the detailed atomic step structure, the difference between the steps can also be inferred from the mutual shift of the reconstructions of the substrate and the island [Figure 7. 10 (a)]. For instance, at step 2 the Bi trimers on the substrate and the island (blue and red circles, respectively) have a much smaller mutual distance than for the step 1. These differences have important consequences on the Bi termination of the step edges. For instance, one might speculate that at step 2 a Bi termination of the step edge is not possible because the Bi on the lower terrace blocks the possible bonding sites, while for step 1 Bi passivation is easily possible. These different structures of the step edges (imposed by the symmetry) have important consequences on the growth properties of the islands. A Bi passivated step edge is expected to have a completely different incorporation kinetics than an unpassivated step edge [91]. For an initially arbitrary shape of an island, easy incorporation of material leads to a high step velocity (rate of advancement of the step edge perpendicular to the step edge). These step edges with a higher incorporation rate grow faster in the direction perpendicular to the step edge and can in some cases even finally disappear being overgrown by the nearest steps with lower growth rate. The formation of the observed rhomb-shaped islands is explained by a slow growth velocity of steps 1 and 3 which leads to a disappearance of the fast growing step 2. This is a consequence of the more general kinematic Wulff construction

[33]. The original Wulff construction (2D version) relates the *equilibrium* crystal shape to the step energy; the kinematic Wulff construction relates the crystal growth shape to the step velocities. The kinematic Wulff theorem (2D version) states that the shortest distances from the nucleation center to the step edge, h_i [inset in **Figure 7. 11 (a)**] are related to the step velocities v_i by

$$\frac{v_1}{h_1} = \frac{v_2}{h_2} = \frac{v_3}{h_3} = \dots = const \tag{7.2}$$

A prerequisite in the model underlying the kinematic Wulff construction is that the velocity of growth depends only on the surface orientation. This is true for a growth regime in which the incorporation into the steps is attachment limited and the adatom concentration on the surface is approximately constant due to a large incorporation barrier. Since strong step edge passivation was found in Bi surfactant-mediated epitaxy of

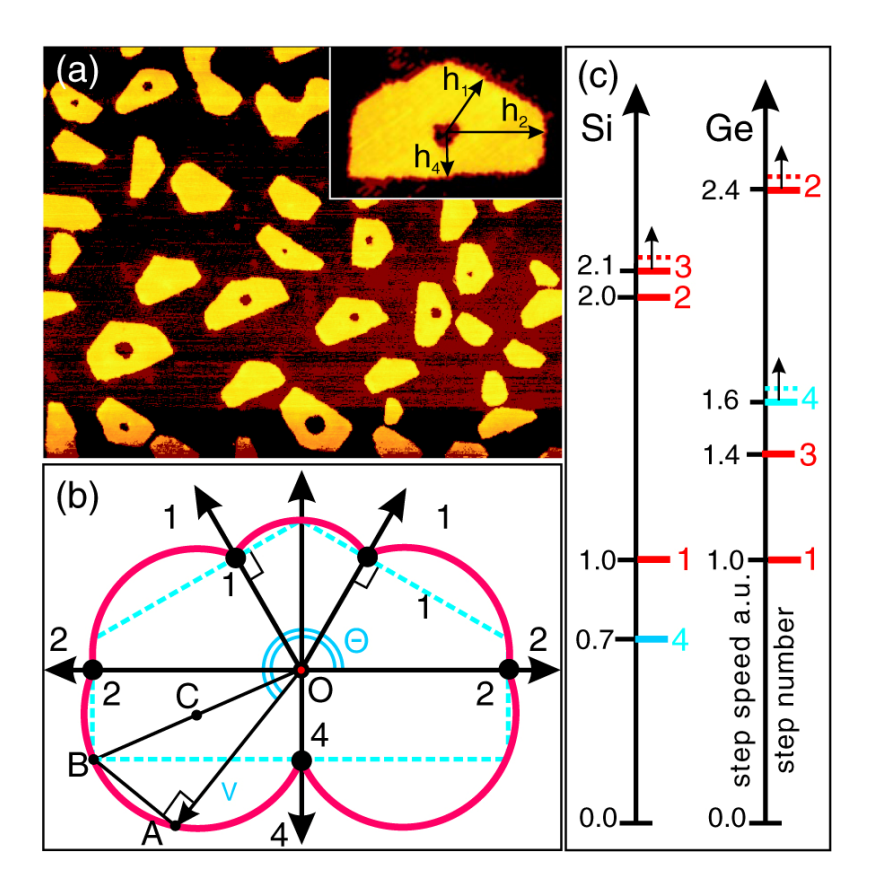


Figure 7. 11. (color online). (a) Using a marker technique the nucleation centers of the arrow-shaped islands are marked by holes. From the measured distances to the step edges the step velocities can be determined. Image size 400 nm. (b) Minimal kinematic Wulff Plot of arrow-shaped islands. (c) Step velocities for Si and Ge islands.

Ge [91], our experiments are performed under conditions in which this prerequisite for the kinematic Wulff theorem is fulfilled. Another requirement for the validity of the kinematic Wulff theorem is that the island shape is a growth shape and not influenced by the equilibrium shape due to the low growth rate used. STM experiments performed during epitaxial growth [2] of Si showed that the growth shape develops already for much lower growth rates than used here. In order to obtain the step velocities from Eq. (1) the nucleation point of the island has to be known, from which the distances hi are measured. Without this information often only a limited number of relations among the step velocities can be obtained. If the nucleation point of the island is known, the complete knowledge of the velocities of the observed steps results from the shape of the island. Therefore, we used a marker technique to determine the position of the nucleation center inside the arrow-shaped Si islands. Initially we deposited small Ge islands which served as markers of the nucleation centers. Subsequently, larger Si islands were grown around the marked nucleation centers. Actually, due to an effect induced by strain (which will not be discussed here in detail) the Ge diffuses away from its initial position (leading to a small < 5% Ge alloying of the Si islands) and the nucleation center of the island is marked by a small hole of one atomic layer height. With the nucleation point known, the distances hi to the island edges can be easily measured [inset in Figure 7. 11 (a)] and the relative step velocities can be determined from Eq. (1). Choosing $v_1 = 1$ results in: $v_2 = 2.0 \pm 0.1$ and $v_3 = 0.7 \pm 0.1$. These measured step velocities can be plotted in a kinematic Wulff plot [polar diagram of the step velocities $v(\theta)$] for the arrow-shaped islands. The measured values correspond to the five black dots in Figure 7. 11 (b). If the growth shape would be smooth without straight step segments, the inverse Wulff construction could be used to obtain the complete polar diagram of the step velocities from the measured island shape [33]. Because of the presence of the straight step edges (facets) in the island shape the inverse Wulff construction is not possible. However, one can learn more than just the determination of the five measured points on the kinematicWulff plot. In the following it will be shown that the step velocities have to lie outside the red contour in Figure 7. 11 (b) which we call the "minimal" kinematic Wulff plot. According to the kinematic Wulff construction a line perpendicular to the radius vector is constructed at each point where the radius vector crosses the polar plot of the step velocity. The crystal shape is formed from the inner envelope of these perpendicular lines for all radius vectors. The inverse Wulff construction which constructs the step velocities from the crystal shape is impossible for step velocities inside the minimal kinematic Wulff plot. Therefore, the step velocities have to lie outside the minimal kinematic Wulff plot. The geometric construction rule for the border of the minimal kinematic Wulff plot is given in the following. For a certain polar angle θ the closest point for which the perpendicular line does not cut the crystal is point A in Figure 7. 11 (b). This perpendicular line just reaches the island corner in B. If we now consider the rectangular triangle OAB, the converse Thales' theorem states that a right triangle's hypotenuse is a diameter of its circumcircle. This means that all points B lie on a circle around point C. With C lying in the middle between the nucleation center and the respective island corner.

The measured step velocities for Si islands can also be displayed as a "spectrum" shown in **Figure 7. 11 (c)**. The (relative) velocities for steps 1, 2, and 4 have a defined value, while for step 3 the step velocity has to be larger than the value given from the minimal kinematic Wulff plot. An interesting result from the determination of the step velocities is that the

velocities of the different kinds of $\langle 1\,\overline{1}\,0\rangle$ type steps [marked in red in **Figure 7. 11 (c)**] differ by more than a factor of 2. This is the case in spite of the fact that the local step structure, without taking the reconstruction into account, is the same for all $\langle 1\,\overline{1}\,0\rangle$ type steps (i.e. steps 1, 2, and 3). The difference between these steps is their shift with respect to the substrate reconstruction and the related differences of the Bi termination. These results show that these effects have a stronger influence on the step velocities than the difference between $\langle 1\,\overline{1}\,0\rangle$ and the $\langle \overline{1}\,\overline{1}\,2\rangle$ - type steps (step 4 is a $\langle \overline{1}\,\overline{1}\,2\rangle$ - type step marked in blue) which have a genuine different structure even without taking the substrate reconstruction into account. Coming back to the rhomb-shaped islands, also here a marker technique can be used to learn more about the kinematic properties of growth expressed by the step velocities. The STM images in **Figure 7. 10 (c)** and **Figure 7. 12** show an islands for which an initial small Si island marks the nucleation position. Si and Ge can be distinguished in Bi mediated epitaxy by an apparent height in

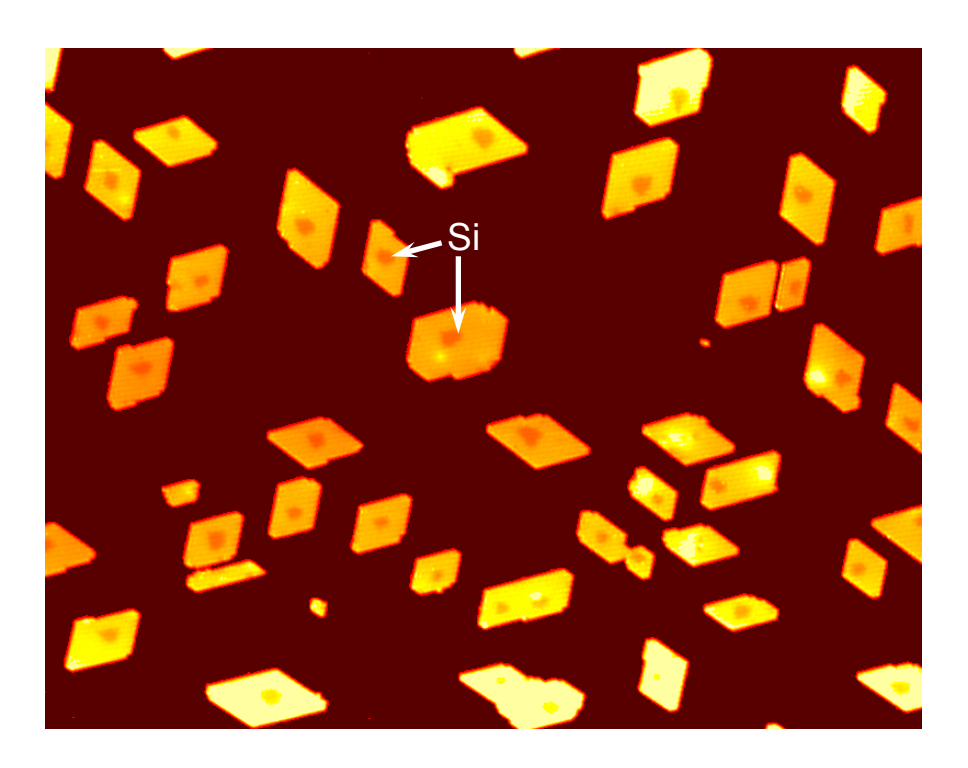


Figure 7. 12. (a) STM images of rhomb-shaped Ge islands on the Bi terminated Si(111) substrate. Image sizes 200 nm. The nucleation centers of the rhomb - shaped islands are marked by Si core.

the STM images. Ge areas are imaged $\sim 1~A$ higher than Si areas [71]. It is clearly visible that the nucleation center is not located in the center of the rhomb [Figure 7. 10 (c)]. This proves

experimentally that the growth velocities of steps 1 and 3 are different which was already concluded from symmetry considerations. A detailed analysis shows that the average step velocity of step 3 is 1.4±0:1 times larger than that of step 1. While the apparent growth shape of the island is rhomb-shaped, the true shape has *Cs* symmetry. Symmetry considerations and the marker technique prove that steps 1 and 3 are different on the atomic scale leading to different growth velocities. Because of geometric constraints the length of both steps is the same leading to a rhomb shape of the islands.

It is an intriguing fact that in spite of the similarity of Si and Ge the epitaxial islands have so different shapes. These different shapes are related, via the step velocities, to different step structures. Since Si and Ge have the same crystal structure one would not expect much different step structures. However, the Bi termination at the step edges can be very different for Si and Ge. For instance in an earlier experiment we found that Si step edges are less Bi passivated than Ge step edges [91]. Because of the different bonding of Bi and strain effects at Si and Ge steps a different Bi passivation, or (partial) depassivation may occur at some step edges. We speculate that a largely different step structure due to different Bi passivation of the steps can lead to substantially modified step velocities for Si and Ge and can explain the observed different Si and Ge island shapes.

Conclusions

These findings are not limited to a specific system. Generally one can conclude that on reconstructed surfaces the symmetry of the combined system of epitaxially grown islands and substrate can break the symmetry of the original surface. This broken symmetry has consequences on the step structure which in turn influences the growth rates and in turn also the island shapes. This effect could be used to fabricate 2D nanostructures directed along one specific direction on a substrate of higher symmetry. If one of the step velocities would be much larger than the others the island shape would develop a pronounced oblong shape. In order to grow elongated nanostructures (surfactant induced) reconstructions which generate a large anisotropy in step velocities have to be found.

8. Step edge passivation during SiGe epitaxy

The preferred step orientation and shape of the 2D nanostructures are result of the step kinetics and/or energy minimization of the step configuration [12.33,35,36]. The preferred step directions observed during growth of two dimensional nanostructures have a minimal step energy and/or minimal step propagation speed. Different contributions, for example surface reconstructions, have an influence on the preferred step directions [35, 36]. The 30° rotated Bi induced $\sqrt{3} \times \sqrt{3}$ reconstruction on the Si(111) surface changes the preferred $\langle \overline{1} \ \overline{1} \ 2 \rangle$ step directions for the clean Si(111)-7x7 surface to $\langle 1 \ \overline{1} \ 0 \rangle$ step directions [35]. The influence of the Bi vapor pressure on the preferred step direction during growth of Ge nanostructures on the Si(111)- $\sqrt{3} \times \sqrt{3}$ -Bi surface was found in [35]. At zero rate of Bi deposition $\langle \overline{1} \overline{1} 2 \rangle$ step directions were present on the Si(111) surface, at high Bi rate deposition $\langle 1\overline{1}0 \rangle$ step directions were present on the surface [35]. Bi saturates the dangling bonds at step edges, reduces the step energy and increases barriers for attachment [91]. The change of kinetic and energy properties of $\langle \overline{1} \overline{1} 2 \rangle$ and $\langle 1 \overline{1} 0 \rangle$ steps can be also attributed to the change of the Bi amount at the step edges [35]. The change of the amount of Bi at step edges can be associated with a change of the Bi passivation effect at the step edges. No Bi at step edges means no passivation of the steps. A method based on the investigation of island size distributions [91] will be used here to study the influence of the Bi deposition rate on the step edge passivation effect.

Experimental investigations of the density and size distribution of submonolayer island populations yield qualitative and in certain cases even quantitative information regarding microscopic mechanisms that determine the growth mechanism of this system. In the standard growth model [33], atoms arrive at a substrate with a flux F and diffuse on the substrate with a temperature dependent diffusion rate D. No desorption of atoms from the surface is allowed. When two or more diffusing atoms meet, a two-dimensional (2D) one monolayer (ML) thick island nucleates and grows further by adatom capture limited diffusion. In this way a population of 2D islands covering a fraction θ of the surface develops. In the precoalescence regime of growth the island population is characterized by the island size distribution N_s . For various amounts of deposited material expressed in terms of the surface coverage θ , N_s scales onto a single function f(x):

$$N_{s} = \theta / \langle s \rangle^{2} f(s / \langle s \rangle), \tag{8.1}$$

where $\langle s \rangle$ denotes the mean island size [103]. In the standard growth model f(x) is a peak function with a peak at x = 1 [103,104,105,106]. In addition, the total island density N is a power law of F and D [33]:

$$N \propto \left(\frac{F}{D}\right)^{\chi}, \frac{1}{3} \leq \chi < 1.$$
 (8.2)

When the above conditions are met, predictions of the standard growth model can be used to measure D and other model parameters [107,108]. On the other hand, the experimentally observed deviations from the behavior predicted by Eqs. (8. 1) and (8. 2) can be used to identify important growth mechanisms beyond the standard model. Examples include observations of growth with $\chi = 0$ in systems with post-deposition [109] or displacive [110,111] nucleation, occurrence of a decreasing scaling function f(x) caused by these mechanisms [109,110,111] or by a strong anisotropy of the surface structure [112], growth with $\chi > 1$ in systems with hindered incorporation of atoms into the islands [113,114], and the observation of a multipeak island size distribution when stable islands of "magic" sizes exist [115]. Additionally, transition from a peaked scaling function to a decreasing one with the increasing growth temperature was predicted theoretically for systems with prominent desorption of deposited particles [116,117]. In surfactant mediated epitaxy (SME) [87,118,90,119,19] particles of the deposited material arrive at a surface, where a monolayer of another species, so called surfactant, is adsorbed. This modifies the growth scenario compared to the growth without surfactant, allowing, e.g., layer-by-layer growth of relaxed layers in highly strained Ge/Si heteroepitaxy [118,90]. SME systems are good candidates to have a behavior different from that predicted by the standard growth model. Indeed, $\chi > 1$ was measured in submonolayer growth of Ge on the Pb-covered Si(111) surface [120].

The size distribution of 2D Ge and Si islands at SME on the Si(111) surface was studied in [91]. For Ge, a scaling function with a peak strongly shifted towards small island sizes was found. The peak of scaling function $f(s/\langle s \rangle)$ was shifted from the position of standard model $s/\langle s \rangle = 1$ toward smaller island sizes $s/\langle s \rangle < 1$. This nonstandard scaling is temperature dependent: for higher temperatures the scaling function approaches the standard one. The observed scaling phenomena was explained considering exchange and deexchange processes of deposited atoms with surfactant and the passivation of step edges in the presence of surfactant [22]. The kinetic Monte Carlo (KMC) simulations of a generalized diffusion—deexchange—passivation (DDP) model of surfactant mediated epitaxy were performed [23]. The DDP model assumes three basic processes that happen during the SME growth (Figure 8. 1): diffusion of deposited atoms on top of the surfactant, exchange of material atoms with surfactant to incorporate below the surfactant layer, and de-exchange of material atoms with surfactant atoms to get back on top of the surfactant. The processes are considered to be

thermally activated with rates v_i having an Arrhenius form $v_i = v_0 \exp\left(\frac{-E_i}{k_B T}\right)$ where v_0 is

the common prefactor of the order 10^{13} s⁻¹, k_B is the Boltzmann's constant, T is a temperature, and E_i is the activation energy of the ith process with E_D , $E_{\rm ex}$, $E_{\rm dex}$ standing for diffusion, exchange and de-exchange processes, respectively. Generally, $E_{\rm dex} > E_{\rm ex}$, to account for the increase of the binding energy of single material atoms upon incorporation. Important is a definition of the behavior of material atoms at step edges. In the DDP model, not only terraces but also step edges are passivated, i.e., incorporation of atoms into step edges does not happen automatically. Upon incorporation of an atom at the step edge, its binding energy increases more than that of an atom on the terrace. In terms of the DDP model, stronger passivation of the step edges for Ge atoms than for Si atoms was required to obtain the experimentally observed difference of the submonolayer scaling in Ge and Si Bi-MBE on the Si(111) surface [91].

Deviation of the peak from the standard position of $s/\langle s \rangle = 1$ can be used as a qualitative estimate of the Bi step edge passivation effect. A larger shift toward smaller island sizes means stronger passivation of the step edges or/and larger energy activation for exchange at the step edges $E_{\rm ex}$ [91].

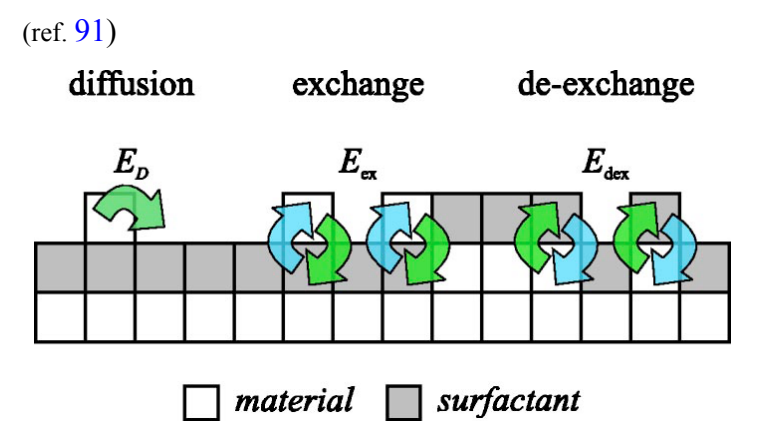


Figure 8. 1. Growth processes considered in the DDP model of SME (Refs. 22 and 23). Related activation energies of these processes E_D , $E_{\rm ex}$, $E_{\rm dex}$ generally differ for material atoms in plane and material atoms at step edges.

The influence of the Bi deposition rate on the step edge passivation effect was studied for two cases: i – a standard SME with high Bi deposition rate of ≈ 3 ML/min during growth, and ii – a modified SME (chapter 6 and ref. [35]) with zero Bi deposition rate during growth. In both cases the surface was completely passivated with the Bi before Ge/Si growth. The 2D Ge islands grown by standard SME Figure 8. 2 (a) and by modified SME Figure 8. 2 (b) have different shapes and different size distributions. The corresponding scaling functions are shown on Figure 8. 2 (c), (d). 0.2 ML of Ge was deposited at temperature of substrate $T_s = 440$ °C and at rate of 0.2 ML/min. In a standard SME the Bi and the Ge were deposited simultaneously. The Bi deposition rate was 3 ML/min. The rhombic shape of the Ge islands was observed Figure 8. 2 (a). The peak of the scaling function was found strongly shifted toward smaller island sizes $s/\langle s \rangle < 0.2$ Figure 8. 2 (c). Upon modified SME [35] the Bi flux was switched off during Ge deposition. Round or triangular shapes of the islands were observed Figure 8. 2 (b), Figure 8. 6. The peak of the scaling function was found at $s/\langle s \rangle = 0.75$ Figure 8. 2 (d). A smaller shift of the peak of the scaling function Figure 8. 2 (d) means weaker passivation or/and lower activation energy for exchange $E_{\rm ex}$ [91] at the step edges. The lower passivation of the step edges in modified SME can be attributed to the reduction of the Bi coverage at the step edges [35]. Therefore, the different deviations of the scaling functions Figure 8. 2 (c), (d) from the standard and the different island shape Figure **8. 2 (a), (b)** are a result of a change of the step edge passivation. Stronger passivated steps in standard SME have preferred steps with $\langle 1\overline{1}0 \rangle$ orientation which is different from the preffered $\langle \overline{1} \ \overline{1} \ 2 \rangle$ direction initially present on the clean Si(111) surface.

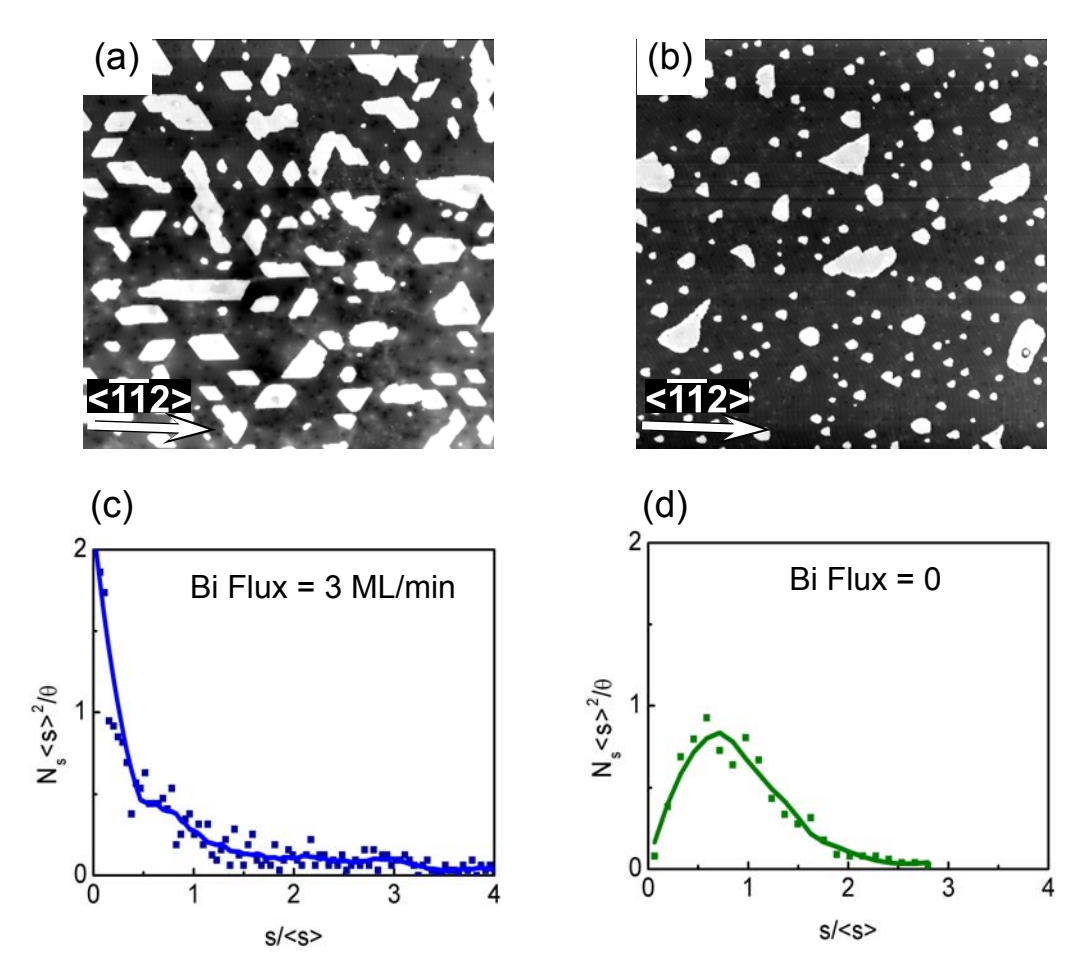


Figure 8. 2. Morphology of Ge islands (a) grown by standard SME with high Bi deposition rate of 3ML/min during growth, and (b) Ge islands grown by modified SME with zero Bi deposition rate during growth. Island size distribution for standard SME (c), and island size distribution for modified SME (d). 0.2ML of Ge was deposited at $T_s = 440$ °C at rate of 0.2 ML/min. Image sizes 500 nm.

Another contribution to the change of step kinetics may come from the different chemical compositions (Ge and Si) at the step edges. The depassivated step edges on modified SME have a lower energy activation for the growth front induced intermixing process since Ge atoms at depassivated step edges are not bound by Bi atoms. Indeed, the apparent height difference between Si and Ge grown by modified SME is $\sim 0.5 \,^{\circ}A$ Figure 8. 3 (d). Therefore, the Ge islands grown by modified SME consist of > 50% of Si, while the apparent height difference between Si and Ge grown by standard SME is $\sim 1 \,^{\circ}A$ Figure 8. 3 (c). The growth conditions (except Bi flux): temperature of substrate, Ge coverage and Ge rate of deposition were the same for standard and modified SME. 0.2 ML of Ge was deposited at $T_s = 440 \,^{\circ}C$ at rate of 0.2 ML/min. Therefore, a different composition of SiGe islands Figure 8. 3 (Figure 8. 2) is a result of a different activation energy for growth front induced intermixing in modified and standard SME.

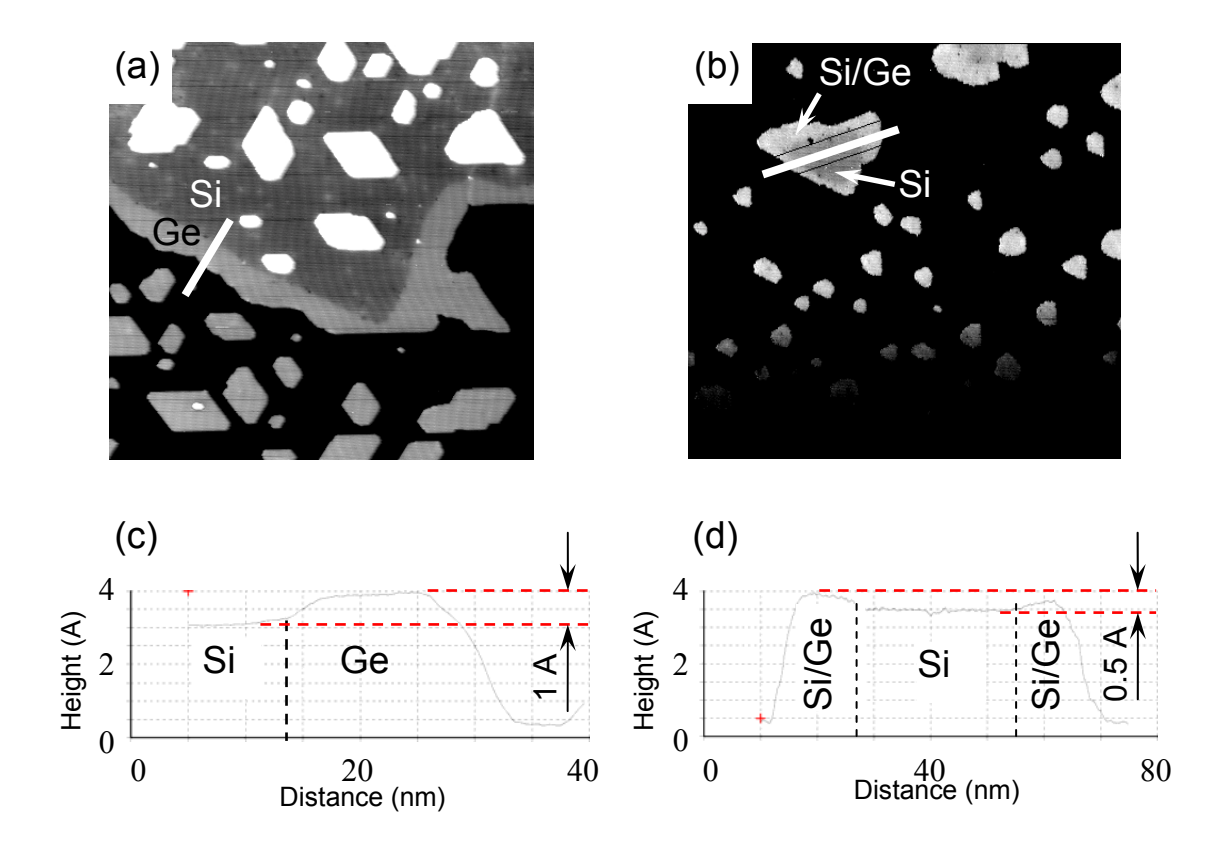


Figure 8. 3. The height differences between Si and Ge. (a) STM image of Ge grown by standard SME at a Si step edge, (c) apparent height difference between Ge and Si is $1 \stackrel{\circ}{A}$. (b) STM image of SiGe grown by modified SME at step edges of a Si island. (d) apparent height difference of $0.5 \stackrel{\circ}{A}$ corresponds to $\sim 50\%$ of Si in the SiGe composition. 0.2ML of Ge was deposited at $T_s = 440$ °C at rate of 0.02 ML/min. Image sizes 200 nm.

A different preferred step direction and different passivation of the steps **Figure 8. 2** can be explained by a different SiGe composition at the steps:

- The change of SiGe composition at the steps can change the preferred step direction since the step directions of the Si and Ge islands are different (chapter 7) [36].
- The passivation of the steps in modified SME can be also decreased due to an increase of the Si content at the step edges since the Ge steps are stronger passivated than Si steps [91].

To separate the influence of the Bi content at step edges on the step edge passivation from the composition effect the size distributions of Si islands were measured **Figure 8. 4**. The Si islands were grown by deposition of 0.2 ML of Si by standard and modified SME **Figure 8. 4 (a), (b)**, the temperature of substrate and the rate of Si deposition were 440°C and 0.02 ML/min, respectively. The shapes of Si islands grown by modified SME and by standard SME are different.

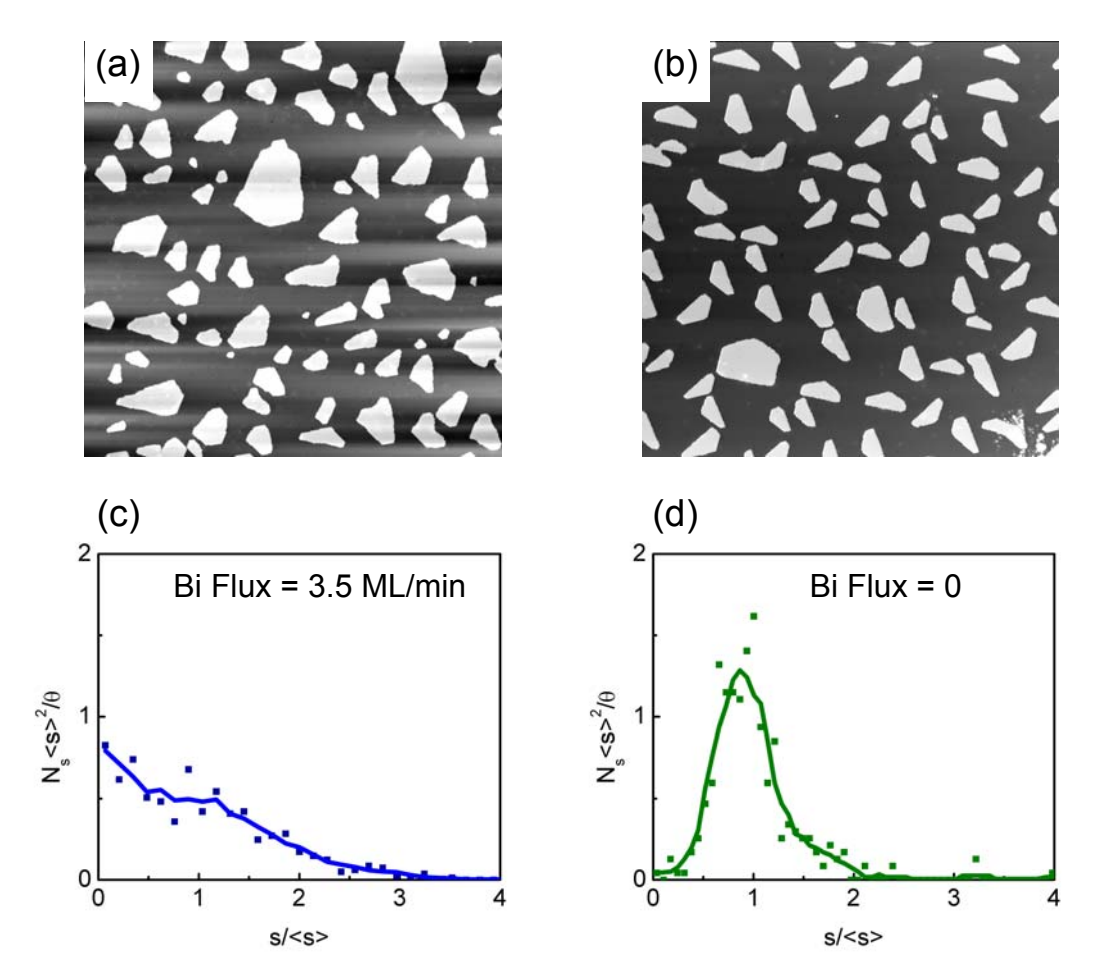


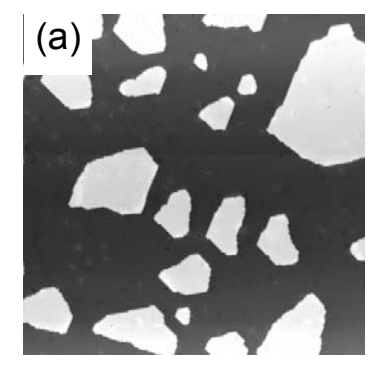
Figure 8. 4. Si islands (a) grown by standard SME with high Bi deposition rate of 3ML/min, and (b) Si islands grown by modified SME with zero Bi deposition rate during Si growth. Island size distribution for standard SME (c), and islands size distribution for modified SME (d). 0.2ML of Si was deposited at $T_s = 440^{\circ}C$ at rate of 0.02 ML/min. Image sizes 400 mm.

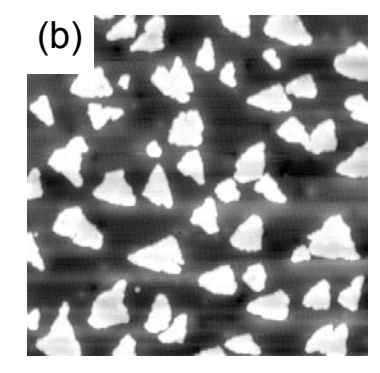
The shapes of islands grown by modified SME are more uniform **Figure 8. 4 (b)**, the arrow shaped islands are bounded by straight steps with definite orientation [36]. The islands grown by standard SME have various shapes and the straight step segments are too short, which makes the identification of the preferred step directions difficult. The island size distribution for the standard and modified SME is clearly different **Figure 8. 4 (c)**, **(d)**. The scaling function of islands grown by modified SME **Figure 8. 4 (d)** is close to the standard peaked function [91] with a peak position of $s/\langle s \rangle = 0.9$. In contrast to the case of modified SME the scaling function for the standard SME **Figure 8. 4 (c)** is asymmetric with the peak strongly shifted toward smaller island sizes. (Our previous measurements in [91] showed a symmetric island size distribution with the peak position of $s/\langle s \rangle \approx 1$ (at $T_s = 440^{\circ}$ C), it can be explained by using of 1 ML/min, lower than 3.5 ML/min, Bi rate deposition). A case with Si islands is more clear since only Si is present at the step edges. Different shapes and different scaling functions of the Si islands at a different Bi rate deposition can be directly attributed to the different content of Bi at the step edges resulting into different passivation of the steps.

The transition from the standard model of growth to the model with a strong step edge passivation is the transition from a growth limited by the surface diffusion to a growth limited by the attachment kinetics [121]. In the growth limited by the attachment kinetics the 2D islands nucleate continuously during deposition. The fractal growth of 2D islands **Figure 8. 5** (b), (c) is a result of the continuous nucleation of the kinks (1D islands) at step edges in *hit-and stick* regime described by *diffusion limited aggregation* (DLA) model [12,122]. Upon the Bi-SME of Si/Ge on the Si(111) we have two subsystems of adatoms:

- The high mobile adatoms (*mobile diffusion* mechanism) in precursor state (on top of Bi layer), can also attach to the steps and diffuse along the step edges in precursor state until reach the kink and exchange with Bi atom.
- And the chemisorbed adatoms (the adatoms bonded to the substrate) which are immobilized (hopping diffusion mechanism) since for diffusion into neighbour position the adatoms need to broke chemical bonds.

In 2D (on terrace) and 1D (at step edge) cases the chemisorbed atoms are immobilized, i.e. we have *hit-and stick* regime with the chemisorbed atoms. If the mobile adatoms are not isolated form the chemisorbed adatoms by high activation energy for exchange E_{ex} and can be easy transferred into chemisorbed adatoms, then the growth described by standard model is observed **Figure 8. 4 (b), (d)**. We assume that activation energy for exchange E_{ex} is different for exchange at terrace, step and kink, $E_{ex}^{terrace} > E_{ex}^{step} > E_{ex}^{kink}$. The exchange energy E_{ex} of Ge/Si atoms with Bi is related to the bond energy of Bi E_{Bi} to the substrate, therefore we can assume that the bond energies for Bi at terrace, step and kink have the same relations: $E_{Bi}^{terrace} > E_{Bi}^{step} > E_{Bi}^{kink}$. These relations are in agreement with experimental data. The fractal growth of Si islands **Figure 8. 5 (b), (c)** observed at low temperatures is a result of 1D growth at step edges limited by the attachment kinetics to the kinks (1D growth with strong passivation of the kinks).





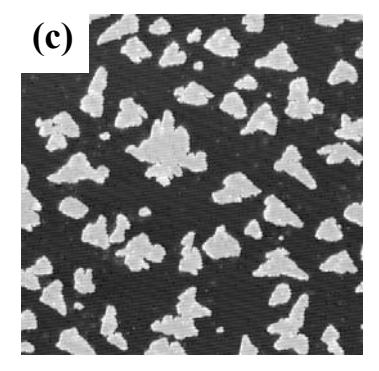


Figure 8. 5. Evolution of the shape of Si islands grown by standard (Bi deposition rate 3.5 ML/min) SME at different temperatures of the substrate. (a) $T_s = 440^{\circ}\text{C}$, (b) $T_s = 400^{\circ}\text{C}$, (c) $T_s = 380^{\circ}\text{C}$. The fractal shape of the islands grown at lower temperatures (b), (c) is a result of the strong passivation of steps and step kinks. 0.2ML of Si was deposited at rate of 0.02 ML/min. Image sizes 200 nm.

At a high temperature of the substrate $T_s \ge 440^{\circ}\text{C}$ the step kinks are depassivated and no fractal growth was observed **Figure 8. 5 (a)**, **Figure 8. 4 (a)**. But the scaling of **Figure 8. 4 (c)** shows that the step edges are still strongly passivated. It can be concluded that depassivation of the step kinks is easier than depassivation of the straight step edges. At temperatures higher than 480°C [91] or at zero Bi rate deposition during growth the step edges are depassivated and the island size distribution described by the standard model of growth was observed **Figure 8. 4 (d)**, **Figure 8. 2 (d)**.

The shape of Ge islands can be varied from triangular Figure 8. 6 to rhombic shape Figure 8. 7 [Figure 8. 2 (a), Figure 8. 3 (a)] by a change of the step edge passivation. The step edge passivation can be tuned by the Bi deposition rate and by the temperature of the substrate independently. The islands shown on Figure 8. 7 (a), (b) were grown at zero Bi rate deposition, but islands **Figure 8.** 7 (a) were grown at higher temperature, therefore the islands on Figure 8. 7 (a) have a lowest Bi step edge passivation. The islands (Figure 8. 7 (b), (c)) were grown at the same temperature of substrate, but the islands Figure 8. 7 (c) were grown with a high Bi rate deposition, therefore the islands (Figure 8. 7 (c)) have the highest Bi step edge passivation. From the island shapes we can identify the preferred step directions which are present by step directions with minimal step speed propagation (kinematic Wulff construction). Rhombic islands (**Figure 8.** 7 (c)) are bounded by $\langle 1\overline{1}0 \rangle$ steps and triangular islands (**Figure 8.** 7 (a)) by $\langle \overline{1} \ \overline{1} \ 2 \rangle$ steps. The triangular shape islands ($\langle \overline{1} \ \overline{1} \ 2 \rangle$ steps) are observed in the regime of the lowest step edge passivation (zero Bi flux, high temperatures), the rhombic shape islands ($\langle 1\,\overline{1}\,0\rangle$ steps) are observed at a strong step edge passivation (high Bi flux, low temperatures). In the intermediate regime, the round shaped islands were observed **Figure 8.** 7 (b).

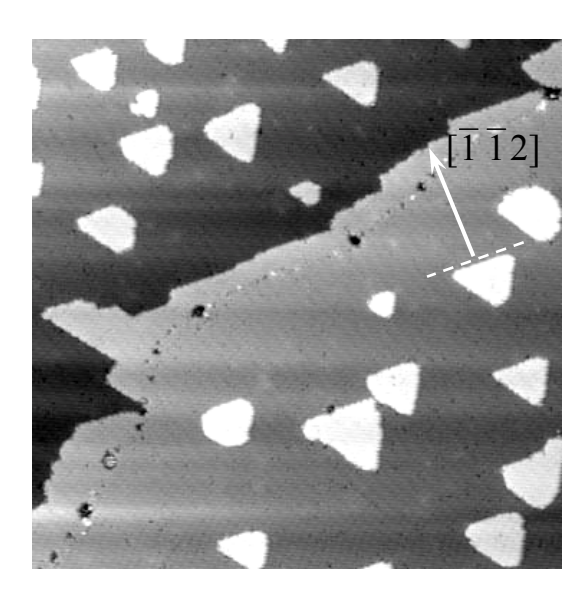


Figure 8. 6. Triangular islands grown on Si(111)- $\sqrt{3} \times \sqrt{3}$ -Bi surface in modified SME. The islands are bounded by $\langle \overline{1} \ \overline{1} \ 2 \rangle$ steps. 0.2ML of Ge deposited at $T_s = 450^{\circ} C$ at a rate of 0.02 ML/min. Image size 200 nm.

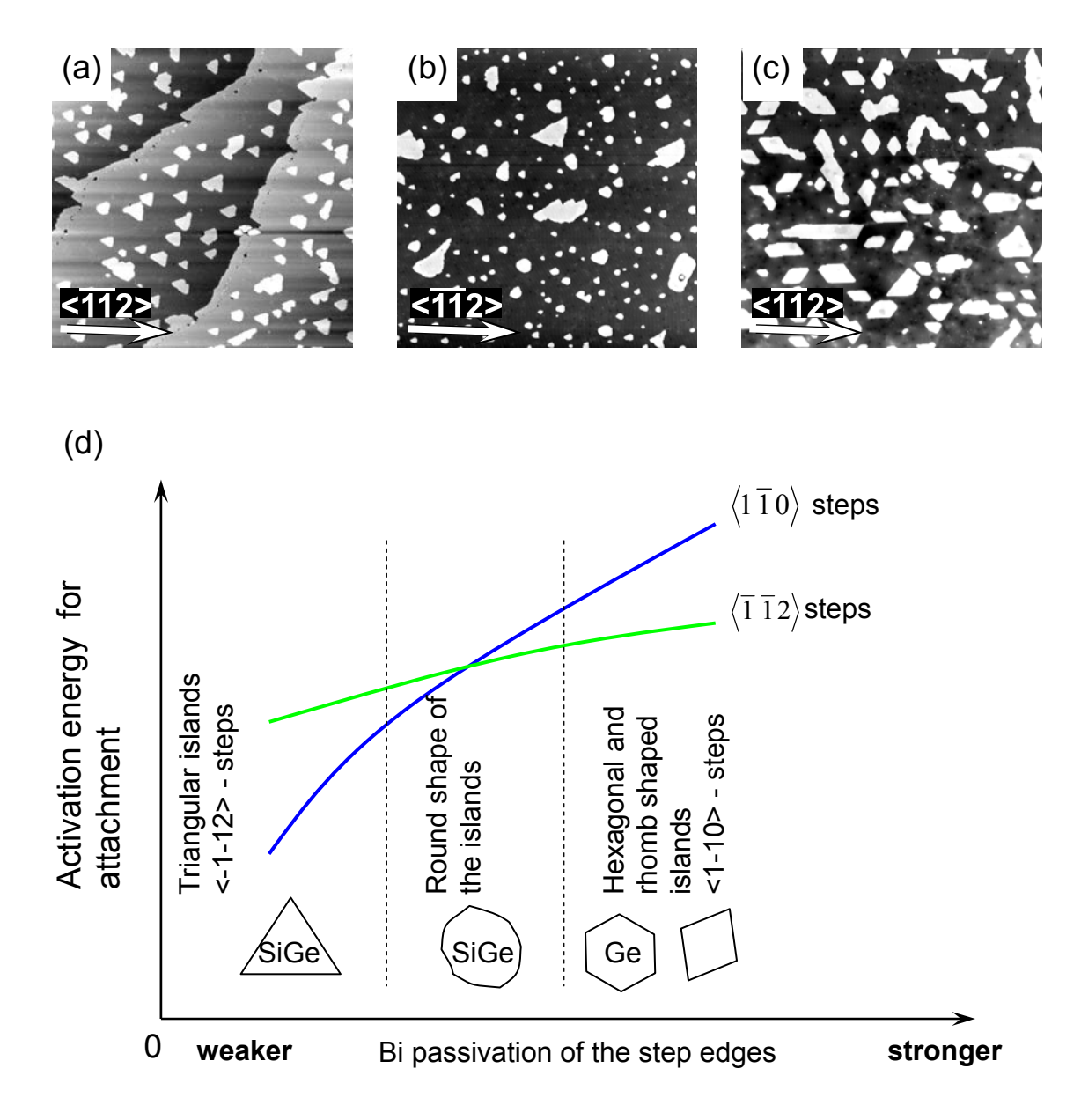


Figure 8. 7. Different shapes of SiGe islands (a) – (c) at different passivation of step edges. The (a) and (b) islands were grown by modified SME and (c) in standard SME with a Bi deposition rate of 3.5 ML/min. (a) 0.2ML of Ge was deposited at T_s = 450°C at a rate of 0.02 ML/min. (b) and (c) 0.2ML of Ge was deposited at T_s = 440°C at a rate of 0.2 ML/min. Image sizes 500 nm. (d) Schematic diagram which shows the shape variation of SiGe islands and activation energy for attachment into steps at different Bi step edge passivations. The activation energy for attachment and passivation of step edges are shown qualitatively. The activation energy for attachment into $\langle 1\,\overline{1}\,0 \rangle$ steps – blue curve and into $\langle \overline{1}\,\overline{1}\,2 \rangle$ steps – green curve, respectively. The triangular islands are bounded by $\langle \overline{1}\,\overline{1}\,2 \rangle$ steps, hexagonal and rhombic islands are bounded by $\langle 1\,\overline{1}\,0 \rangle$ steps.

The preferred step direction depends on the Bi step edge passivation. The schematic diagram **Figure 8.** 7 shows a shape evolution and change of the activation energy for attachment for the $\langle 1\,\overline{1}\,0 \rangle$ and $\langle \overline{1}\,\overline{1}\,2 \rangle$ steps with the step edge passivation. The activation energy for attachment and passivation of the step edges **Figure 8.** 7 (**d**) are shown qualitatively. The step direction with the highest activation energy for attachment is the preferred step direction which determines the observed shape of the islands (**Figure 8.** 7). The growth shape of islands is bounded by the steps with a minimal step speed propagation (kinematic Wulff construction [33]). The step speed propagation is proportional to the rate of attachment k_s^+ of adatoms into step edge. The rate of attachment is decreased with activation energy for attachment E_s^+ as $k_s^+ = v \exp\left(\frac{-E_s^+}{k_BT}\right)$. The steps with the highest activation energy have a minimal step speed propagation, therefore, the steps of the islands have the highest activation

minimal step speed propagation, therefore, the steps of the islands have the highest activation energy for attachment.

Conclusions

The step edge passivation can be tuned independently by substrate temperature and by Bi rate deposition.

The change of the Bi content at the step edges changes simultaneously the step edge passivation (E_{ex}) with the activation energy for growth front induced intermixing.

According to the data of the Si island size distributions at different growth temperatures and different Bi deposition rates (the SiGe composition effect can be excluded) the change of SiGe island shape and preferred step directions [35,36] can be attributed to the change of the step edge passivation.

The observed evolution of the Si island shapes and island size distributions let establish the sequence of depassivation as a function of temperature: Firstly, the easiest depassivation of the step kinks occurs at low temperatures ($T \ge 400^{\circ}\text{C}$, standard SME); Secondly, the depassivation of the straight step edges occurs at $T \ge 440^{\circ}\text{C}$ in standard SME; And at last the depassivation of terraces occurs at high temperatures ($T \ge 500^{\circ}\text{C}$), $E_{ex}^{terrace} > E_{ex}^{step} > E_{ex}^{kink}$. This is associated with different Bi bonding energies: the lowest bonding energy for Bi atoms at the kinks, higher bonding energy at the straight step edges and the highest bonding energy at the terrace.

The observed change of the step edge passivation is followed by a change of the preferred steps direction resulting into different islands shapes.

9 Influence of entropy and energy on pit formation in 2D Ge layer

The structural instability of nanostructures during annealing is an important issue which, along with the compositional instability, can be a serious thread for the functionality of nanodevices. Since the diffusion energies and intermixing barriers are particularly low at surfaces, the stability of surface nanostructures is most delicate. In the GeSi heteroepitaxial system there is a strong thermodynamic driving force for intermixing, since intermixing reduces strain and increases entropy [123,124,125]. The evolution of hetero-epitaxial nanostructures is complicated, since both morphology and composition determine the system energy [126]. Moreover, the system is often far from equilibrium due to kinetic barriers. From the experimental point of view the challenge is to supply a most complete data basis in order to be able to understand the evolution of the hetero-epitaxial nanostructures, specifically simultaneous measurements of morphology and composition are desirable [127,24]. In the present letter it will be shown that the driving force for intermixing occurs to be so strong that it provokes drastic morphological changes during equilibration. These structural changes are a way to bypasses the kinetic barriers for direct intermixing. In particular, we show that one monolayer (ML) high Ge stripes grown at Si(111) step edges are unstable towards pit formation during annealing. The Ge leaving the stripe during pit formation attaches at the (Si covered) Ge stripe and intermixes with the subjacent Si (Figure 9. 1).

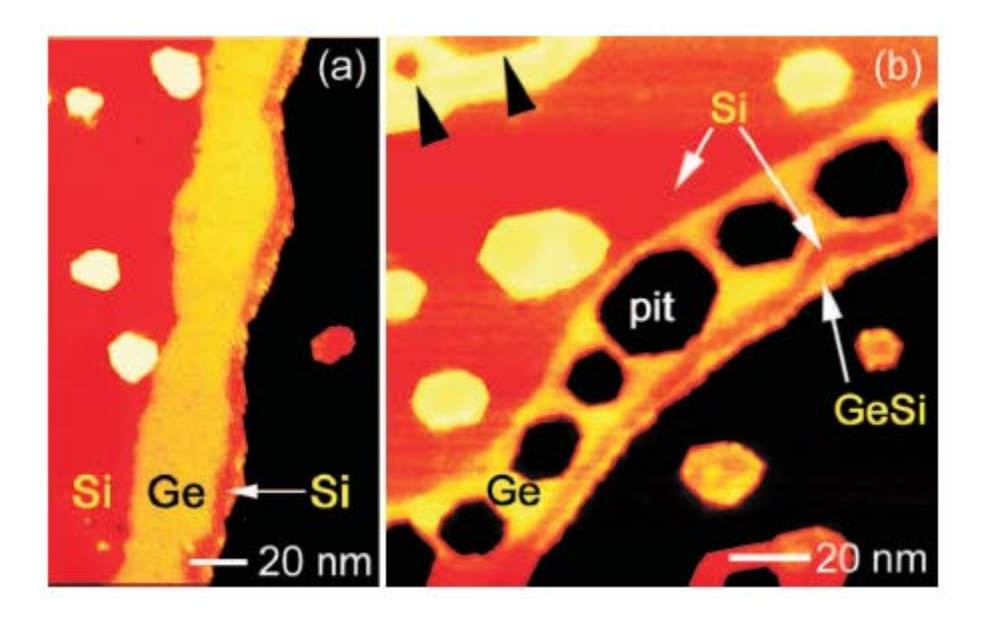


Figure 9. 1. (a) STM image of a one atomic layer high Ge stripe grown at a Si step edge. After Ge deposition a thin outer Si rim was grown. The apparent height contrast between Si and Ge is induced by the Bi termination of the whole surface. (b) After annealing at 733K unanticipated formation of pits and motion of the Ge originating from the pits to the outer Si rim is observed.

The pit formation arises by a concerted action of processes driven by an energy gain of the system and processes driven by an increase of the entropy of the system due to intermixing. The question arises why this rather complicated mechanism of pit formation is followed instead of the much simpler direct vertical intermixing of Ge with the subjacent Si. We will show that while the direct intermixing process results in a final state of even lower energy as the final state after pit formation, the kinetic barrier involved is much smaller than the barrier for direct vertical intermixing which favors the pit formation.

In our experiments first a Bi terminated Si(111) surface was prepared by deposition of one atomic layer of Bi on the clean Si(111)-(7×7) at 875 K. Then a submonolayer amount of Ge was deposited at 655–675K at a rate of 0.015 ML/min (1ML corresponds to 1.56×10¹⁵ atoms/cm²). During Ge growth the Bi floats up at the surface as usual in surfactant mediated growth [87,99]. In the following we will not mention that the complete surface is always terminated by one atomic layer of Bi. After submonolayer deposition of Ge atoms attach to

the step edges and form Ge stripes (**Figure 9. 1 (a)**). Atomic layer high ($\sim 3.2\,\text{Å}$) stripes with a width of more than 10 nm can be formed without any pit formation. More distant from the step edges also Ge islands grow. It was found that the apparent height measured in STM is \sim

1 A higher on Bi terminated Ge areas compared to Bi terminated Si areas, allowing a distinction between Si and Ge on the nano scale [71]. For a GeSi mixture the apparent height is a measure of the Ge concentration in the surface layer [24]. While attempting to grow alternating two-dimensional GeSi superlattices [35], we observed the formation of pits inside of Ge stripes for certain growth conditions. The formation of one atomic layer deep pits is pronounced if the growth of a sufficiently wide (≥ 5 nm) Ge stripe deposition is followed by the deposition of a Si stripe and subsequent annealing. Pit formation was observed for example after the following growth sequence: 0.23 ML Ge was grown at T= 675 K, followed by 0.045 ML Si at 675 K before annealing for 10 min at 735 K. The STM image in Figure 9. 1 (b) shows the resulting structure including 10–20 nm wide pits formed in the Ge stripe. The pit formation occurs by the same mechanism also at isolated Ge/Si islands (Ge core surrounded by a Si rim) on terraces far from the step edge, as indicated by the arrow heads in (Figure 9. 1 (b)). The material in the outer GeSi step edge is less than the missing material in the pits since some Ge attaches at Si islands also present at the surface. In the following a model is described which explains the observed pit formation. In the first part of the pit formation process an initial amount of Ge is moving from the Ge stripe (pits) to the outer Si rim (**Figure 9. 2 (b)**). For simplicity we leave out the actual nucleation event. The driving force for the first part of the pit formation process is bond energy gain. Ge-Ge bonds present in the Ge area are replaced by stronger Si-Ge bonds [128,129] when Ge atoms attach to the Si terminated step edges. This process decreases the system energy and supplies a driving force for Ge to form pits and to diffuse to the Si terminated step edge.

While the above reasoning can explain the initial pit formation, the pit formation should stop quickly if all Si step edges are terminated by Ge atoms (**Figure 9. 2 (b)**). Subsequent Ge attachment at the step edges would not result in any bond energy gain. A further growth of pits, as observed in the experiment, would not be expected because it would only increase the step energy. In a second step of pit formation the entropy driven GeSi intermixing acts at then outer step edge. The amount of GeSi intermixing can be close to 50% under usual conditions as obtained from the measured apparent height differences [24]. Due to the entropy driven intermixing at the step edge fresh Si is present at the outer step edge again. This Si starts the

energy gain driven Ge diffusion from the pits towards the Si containing step edge again (**Figure 9. 2 (b)**). The atomic processes shown in **Figure 9. 2 (b)** and **(c)** can be considered as the subsequent energy driven and entropy driven parts of an energy—entropy cycle.

While we have shown that the above outlined pathway of pit formation describes the experimental data we will now turn to an analysis of the free energy and kinetic barriers during pit formation. This will elucidate why an unanticipated, complicated process of pit formation is favored over the much simpler process of direct intermixing with the underlying Si (Figure 9. 2 (d)) which has an even lower free energy than the final state of pit formation.

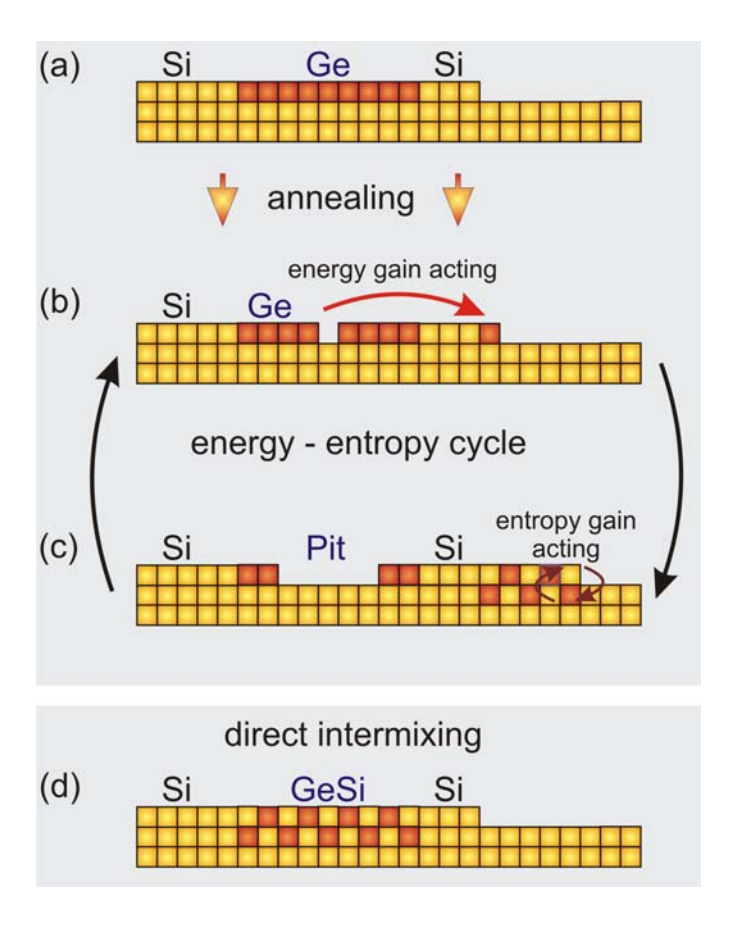


Figure 9. 2. In (a) and (c) the initial and final states before and after pit formation are shown. In the first part of the energy—entropy cycle (b) the energy is reduced by replacing Ge-Ge bonds (at the Ge stripe) through stronger Ge-Si bonds at the Si terminated step edge. The subsequent GeSi intermixing is driven by a gain in mixing entropy (c). Due to the intermixing the Si at the step edge is (partly) restored activating the energy driven part of the cycle again. An alternative simpler intermixing process without pit formation is direct intermixing with the Si form the lower layer (d).

Since the pit formation occurs after annealing, we assume that the final state (**Figure 9. 2** (c)) with pits formed is a state close to local equilibrium. Since the system is a quite complicated heteroepitaxial strained partially intermixed system there are several contributions to the free energy. As the initial state we consider a Ge one monolayer thick stripe at a Si step edge and a thin Si rim at the Ge stripe (**Figure 9. 2** (a)). The final state is the Ge stripe with one monolayer deep pits, the thin Si stripe, and an outer GeSi stripe consisting of the Ge originally filling the pits intermixed with the underlying Si layer (**Figure 9. 2** (c)). For the amount of GeSi intermixing (x) in the outer GeSi stripe we assume x = 0.5 which corresponds roughly to the experimentally observed range of intermixing. We consider here only intermixing at the surface since bulk diffusion does not operate at the temperatures and timescales used here due to the high activation barrier of 4 - 5 eV [130]. The free energy contributions for going from the initial to the final state were estimated (see the Appendix A) and are shown in **Table 9. 1**. As calculated from elasticity theory the elastic energy decreases by 14 meV/Ge-atom in the final state due to **Table 9. 1**: Free energy contributions for pit formation.

Table 9.1

$E_{elastic}$	-17 meV/Ge atom
E_{mix}	+13 meV/Ge atom
Mixing entropy	-88 meV/Ge atom
$E_{step,rel} + E_{step,form}$	-2 – 2 meV/Ge atom
$E_{int,bound}$ (E_{wet})	-3 meV/Ge atom

the reduced strain in the outer intermixed GeSi-stripe [131]. Energy per Ge-atom means per Ge-atom moved away from the pits to the outside stripe. The mixing enthalpy of GeSi is known to be positive [132,133], resulting in a mixing energy of 10 meV/Ge-atom, favoring the initial state without pits. The mixing entropy term gives a large negative contribution of -63 meV/Ge-atom favoring the final intermixed state. A further contribution to the elastic relaxation energy is the step edge relaxation energy evaluated according to [134]. When this contribution is combined with the step edge formation energy which increases during pit formation a net step related energy gain is estimated and converted to of -5 – 1 meV/Geatom (assuming an average pit diameter of 15 nm). This range is estimated from the extreme cases: zero step edge formation energy and the step energy of clean Si(111) [13]. The actual step formation energy on Bi terminated surface is expected to lie between this extreme cases. The last contribution to the free energy $(E_{int,bound})$ arises as follows: when the first Ge-atoms move from the pits to the Si rim weaker Ge-Ge bonds are replaced (partly due to intermixing) by stronger Si-Ge bonds. We estimated this line energy and convert it again to an equivalent energy per (moved) Ge atom of about -3 meV/Ge atom. Taking all the contributions to the free energy together the final state with pits formed has clearly lower free energy than the initial state. This seems to be a convincing energetic argument for the pit formation. However, let us now consider a much simpler final state namely the direct vertical intermixing of the Ge stripe with the underlying Si (Figure 9. 2 (d)). Most of the energy terms considered before apply to the vertical intermixed state as well. Only the step energies are not present because no steps are formed during direct vertical intermixing. Since this is a small contribution, the free energy of the direct vertically intermixed state is also lower than

the initial state. Even more, the free energy of the directly intermixed state is lower than the final energy of pit formation since the intermixing would act at the whole Ge stripe, while the pits only form on a fraction of the stripe (usually less than one half). The question arises why the system takes the complicated pathway like the pit formation instead of the much simpler and lower free energy process of direct vertical intermixing with the underlying Si? During vertical intermixing high energy barriers have to be overcome in order to reach the low free energy configuration. The relevant barrier for direct vertical intermixing is the barrier for intermixing between the first and second layer which was recently measured for the Bi/Ge/Si(111) system as $U^{terrace}_{ex} = 2.2 \text{ eV}$ [24]. The corresponding barrier at the step edge is lower ($U^{step}_{ex} = 1.9 \text{ eV}$) because the atoms are less confined by neighboring atoms at the step edges [24]. The pits are formed because pit formation allows a path towards the minimum free energy configuration which involves a lower barrier than the direct exchange path. Due to the decreased energy barrier for GeSi exchange at the step edge, entropy can act more easily at the step edge while on the terrace the lower entropy intermixed state is not realized due to the large energy barrier involved with the GeSi exchange at the terrace. Now we turn to the question why in the above described pit formation process the intermixing occurs only at the outer Ge stripe while it does not occur at the pit step edge? There is a kinetic reason for this. At the beginning of the pit formation the step length at the pits is much smaller than the length of the outer step. Therefore, the step speed at the pits is much larger than the step speed at the outer step. It is known that the GeSi exchange at the step edges depends critically on the step speed, being lowest at the largest step speeds [24] due to the shorter time a specific atom is located at the step edge. Therefore, the GeSi intermixing effect at the pits is initially much smaller than the intermixing at the outer GeSi step edges. When the pits grow larger their step speed reduces and GeSi intermixing starts to occur at the pit step edges as well. This is also the reason why the pits stop to grow at some point. The energetic driving force for pit formation disappears when the Si content at the pit step edge becomes close to the Si content at the GeSi stripe.

A measurement of the average pit area as function of annealing time shows that the pit formation stops after about 90 sec (inset in **Figure 9. 3**). For simplicity, we fit the experimental points (inset in **Figure 9. 3**) with exponential decay. From a fit to this time dependence the average step speeds of the pits are calculated by differentiation. Furthermore, using the data on the Ge concentration at step edges as function of step speed [24] we obtain the average Ge concentration at step edges plotted in **Figure 9. 3** as function of annealing time. Initially the difference in Ge concentration at both kinds of step edges, which is the driving force for pit formation, is large. For longer annealing times this driving force reduces and leads finally to a stop in further pit growth. An additional effect, not considered here, is that Si accumulates at the pit step edges due to the out diffusion of Ge which is another mechanism for the decrease of the Ge concentration with time.

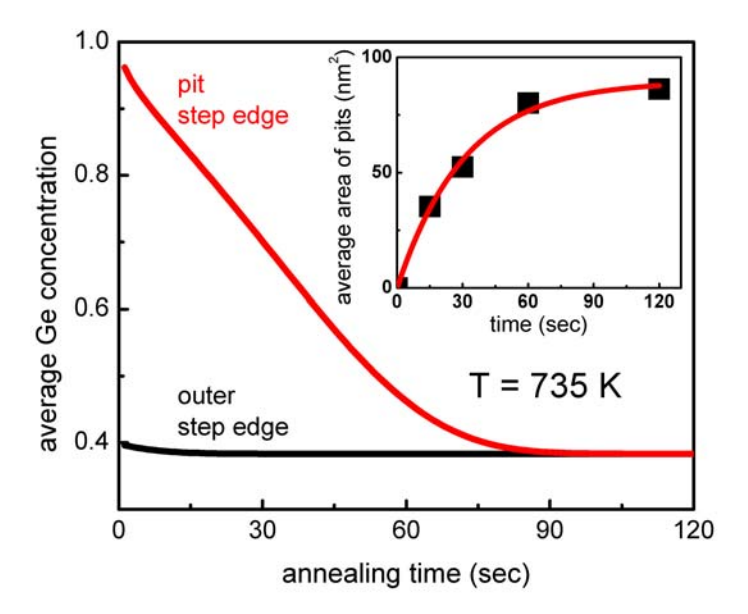
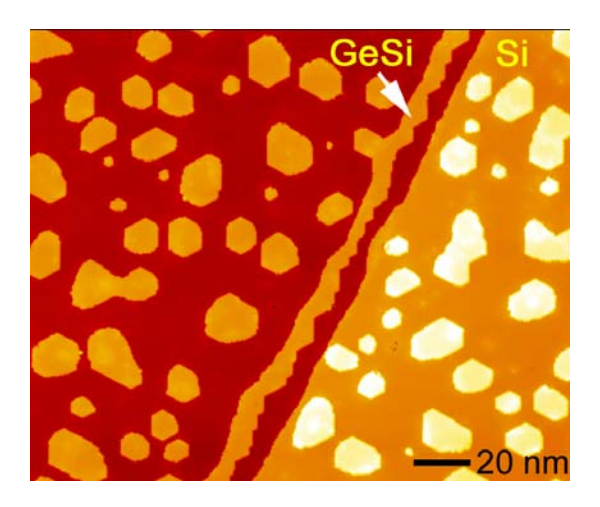


Figure 9. 3. Average Ge concentration at the pit step edge and at the outer GeSi step edge as function of annealing time. The pit size measurements are shown in the inset.

Effective pit formation occurs only in a certain temperature range. For too low temperatures the GeSi exchange is not activated and the pit formation stops quickly after all Si steps have been terminated by Ge. For too high temperatures the difference in Ge concentration be tween both types of step edges, vanishes due to strong intermixing and the corresponding chemical potentials become the same. The pit formation can be also used for nanostructuring. Using conditions at which pit formation is enhanced the fabrication of freestanding GeSi stipes with single digit nanometer width is possible. The sinks for the Ge during pit formation are Si step edges. In order to enhance pit formation we guided epitaxial growth in a way that a lot of Si islands were nucleated on the surface (0.08ML Ge was grown at T= 693K for 6 min, followed by 0.22 ML Si grown at 653 K for 14 min before annealing for 10 min at 753–773 K.). These Si islands provide a high density of sinks in order to drag the Ge out of the pits and finally leading to pit coalescence. Figure 9. 4 shows an example of nanostructuring by pit coalescence. A continuous ~ 8 nm wide freestanding GeSi wire has been fabricated by pit coalescence. This wire is separated about ~ 8 - 10 nm from the step edge. Here the complete initial Ge stripe was removed. The Ge moved to the step edges of the Si islands and the GeSi stripe. Such nanostructured templates can be used for next stage nanostructuring as for instance anchoring molecular nanostructures selectively at the wire or in the groove between the step and the freestanding nanowire.



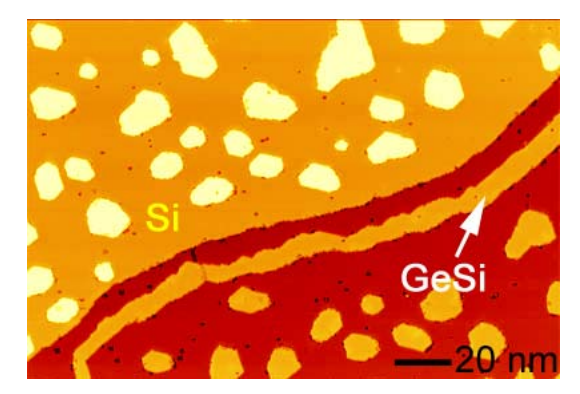


Figure 9. 4. Fabrication of a freestanding 8nm GeSi wire on the Si(111) substrate obtained by pit coalescence.

Conclusions

Nanoscale pit formation in 2D Ge stripes was observed due to a concerted action of energy and entropy. The energy driven motion of the Ge atoms out of the Ge stripe towards stronger binding sites at the Si terminated step edge is followed by an entropy driven GeSi intermixing which restores a Si content at the outer step edge and fuels the energy driven process again. This unanticipated complicated pathway of pit formation as a way to reach the final state of GeSi intermixing is followed instead of the much simpler direct vertical intermixing due to the high kinetic barriers present for the latter process. Finally we have shown that the pit formation effect can also been used for nanostructuring ~ 8nm wide freestanding GeSi nanowires on the Si substrate.

10 Summary

A technique of modified surfactant mediated epitaxy was introduced, where the surfactant concentration on the surface was reduced to influence the growth and equilibrium properties of the surface steps in a desired way. It was shown that this modified surfactant mediated epitaxy is relevant to nanotechnology since it allows fabricating arrays of long equidistant epitaxial Ge nanowires with a width in the one-digit nanometer range. In future these nanowire arrays could serve as templates for selective attachment of molecules, decoration with metals, or attachment of clusters and other nanoscale building blocks such as fullerenes. The use of surfactant coverage as a variable parameter opens up an additional dimension in the growth parameter space that can be explored in bottom-up nanofabrication studies in general.

The analysis of island size distributions showed that the step edge passivation in modified SME can be tuned independently by substrate temperature and by Bi rate deposition. The measurement of the island size distributions for Si and Ge in surfactant mediated growth reveal different scaling functions for different Bi deposition rates and different substrate temperatures on the Bi terminated Si(111) surface. According to the data of the Si island size distributions at different growth temperatures and different Bi deposition rates the change of SiGe island shape and preferred step directions were attributed to the change of the step edge passivation. It was shown that the change of the step edge passivation is followed by a change of the preferred step direction resulting into different islands shapes.

A method to analyze the symmetry of the combined system of reconstructed island plus reconstructed substrate from the symmetries of the bulk substrate lattice, and reconstruction on the substrate, and reconstruction on the island was developed. The symmetry analysis is based on the analysis of common fixed points. The method was used to analyze the symmetry of the shape of reconstructed 2D islands on diamond lattice of Si (111) surfaces. The symmetry breaking in the Bi SME growth of 2D Si/Ge islands on Si(111) was explained with the symmetry analysis method. The broken symmetry has consequences on the step structure which in turn influences the growth rates and finally also the island shapes. This effect could be used to fabricate 2D nanostructures directed along one specific direction on a substrate of higher symmetry.

Nanoscale pit formation in 2D Ge stripes was observed due to a concerted action of energy and entropy. The energy driven motion of the Ge atoms out of the Ge stripe towards stronger binding sites at the Si terminated step edge is followed by an entropy driven GeSi intermixing which restores a Si content at the outer step edge and fuels the energy driven process again. This unanticipated complicated pathway of pit formation as a way to reach the final state of GeSi intermixing is followed instead of the much simpler direct vertical intermixing due to the high kinetic barriers present for the latter process. It has shown that the pit formation effect can also been used for nanostructuring ~ 8nm wide freestanding GeSi nanowires on the Si substrate.

11 Appendix

Appendix A: Evaluation of energies relevant for pit formation

Formation of the pits was observed at different growth conditions:

- 1 during Si deposition
- 2 during annealing after Si deposition

An analysis of the mechanisms of the pit formation for every condition will be given in the following.

1 Pit formation during Si deposition

After submonolayer deposition of Ge in the step flow growth mode Ge atoms attach to the step edges and Ge stripes of a certain width form. The width of the stripes is determined by the coverage and the step distance. Atomic layer $(\sim 3,2^\circ A)$ high stripes with a width of more than 10nm can be formed without any pit formation as shown in the STM image of **Figure 9.5 (a)**.

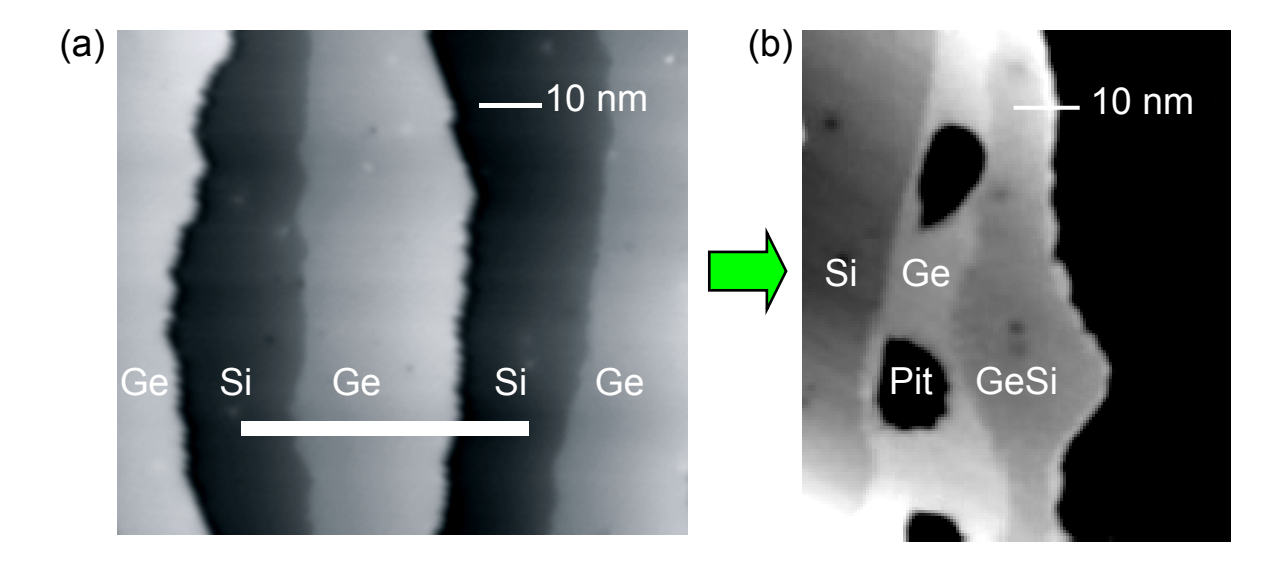


Figure 9. 5. Ge stripes with width more than 10 nm. was formed at Si steps without pits (a); During the following deposition of 0.22 ML of Si for 2.5 min at 450°C the pits were formed in Ge stripes (b), [This experimental result was obtained by Dr. Jacek Brona].

The following deposition of Si can induce the pit formation in the Ge layer **Figure 9. 5 (b)**. Pit formation was observed for example after the following growth conditions: temperature of substrate $T_{\text{subst}} = 450^{\circ}\text{C}$, Ge deposition of 0.15 ML for 2 min, after Ge deposition 0.22 ML of Si was deposited for 2.5 min.; during Ge/Si deposition Bi rate was maintained at 3.4 ML/min. The observed pit formation associates with mass transport of Ge from the pits into outer step edges since no significant sublimation is expected at temperatures below 850°C [135] (rate of Si(Ge) sublimation lower than 10^{-5} ML/sec at 850°C). The high resolution image **Figure 9. 6**. (a) shows that the outer step edges adsorb Ge together with Si resulting into SiGe stripe **Figure 9. 6.** It assumes that Si deposition induces mass transport of Ge from the pits to the outer step edges and the GeSi alloy is formed as result of simultaneous incorporation of Ge and Si atoms into outer step edges. The observed mass transport of Ge assumes the force or difference of the chemical potentials $\Delta \mu = \mu_{outer-step} - \mu_{pit-step} < 0$ which moves Ge atoms from the pits to the outer step edges.

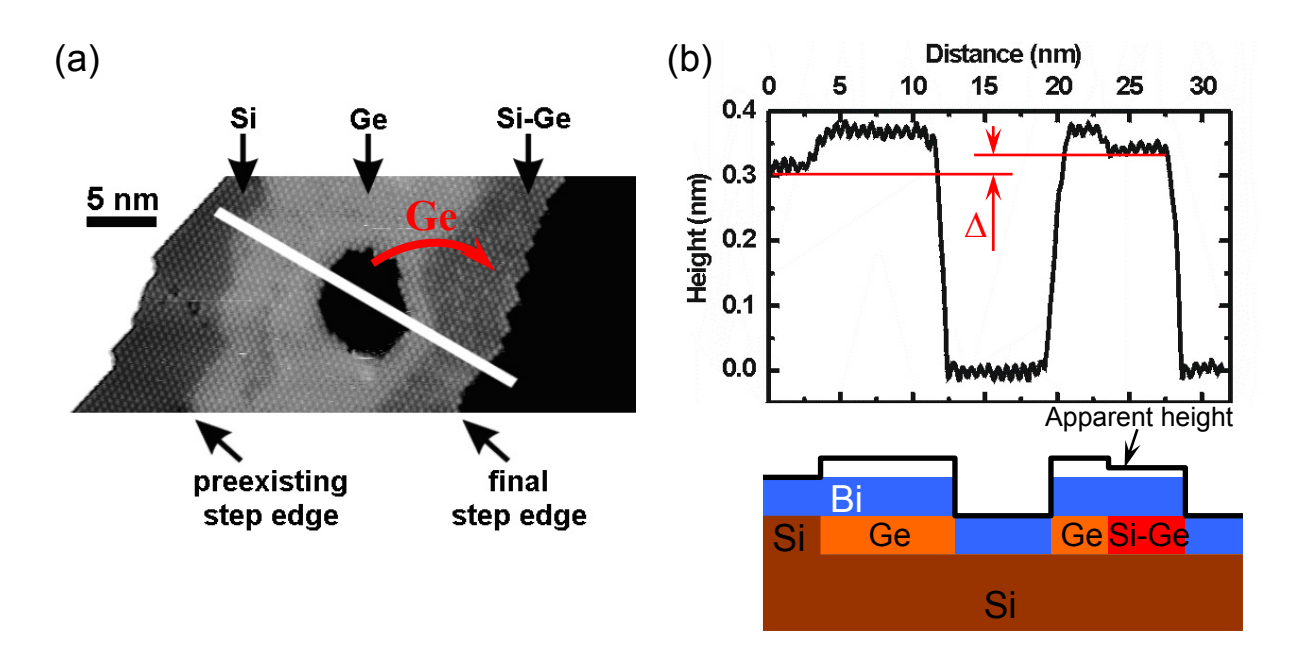


Figure 9. 6. The pit was formed in Ge layer during Si deposition for 20 min with rate of adsorption 0.01 BL/min at temperature of substrate $460^{\circ}\text{C} - 490^{\circ}\text{C}$ (a), high resolution image (a) and line profile (b) show that Si-Ge alloy was formed at outer of pit step edges. The apparent height difference between Si layer and the Si-Ge layer (b) at outer of pit step edge marked by $\Delta = 0.3 \text{A}$ (b). [This experimental result was obtained by Dr. Jacek Brona].

The behavior of the system can be described by kinetic or/and energy model. The energy model assumes that equilibrium or quasi-equilibrium state is achieved in the system. The kinetic model is more complete since it takes into account evolution of the system toward equilibrium. Equilibrium state of the thermodynamic system is described by a minimum of thermodynamic potential which consists of internal energy and entropy parts ($G = E - TS \rightarrow \min$). The driven force (energy) for kinetic model can be determined from energy of the system, therefore, the energy analysis in frame of the energy model will be given first.

Energies relevant for pit formation

To calculate the energy of the system a simple model which takes into consideration only initial and final state will be used. **Figure 9. 7** presents the schematic model of the pit formation during Si deposition.

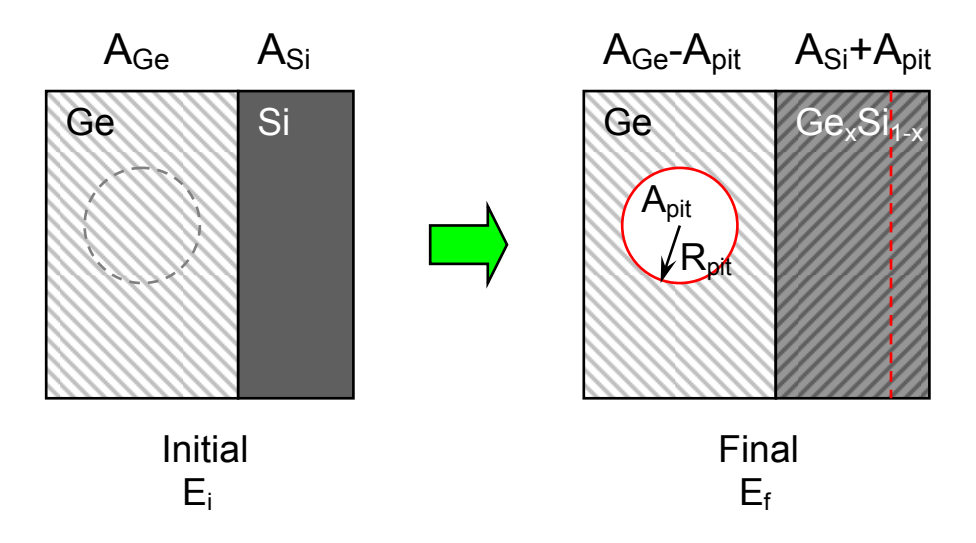


Figure 9. 7. The model considers initial and final states with full energies E_i and E_f correspondingly. The initial state presents Si and Ge layers of volume A_{si} and A_{Ge} without pits. The final state presents Ge layer of volume $(A_{Ge} - A_{pit})$ with pit of area A_{pit} and GeSi layer with homogenous composition of Ge of volume A_{pit} and Si of volume A_{si} .

The initial state (**Figure 9.** 7 – left image) presents the case without pits and consists of strained Ge layer of volume A_{Ge} and Si layer of volume A_{Si} . The final state (**Figure 9. 5 (b)**, **Figure 9.** 7 – right image) consists of Ge layer of volume ($A_{Ge} - A_{Si}$) with pit of area A_{pit} and GeSi composition layer of volume ($A_{pit} + A_{Si}$). The approximation of the pits with round shape and GeSi layers with homogenous composition are used in the model to simplify the calculations of the energies of the system.

According to the model, the internal energy of the system can include four different energy contributions:

 $E_{elastic}$ – elastic energy of strained Ge and GeSi layers on Si(111) substrate;

 E_{mix} – energy of mixing of disordered GeSi alloy;

 E_{step} – energy of step formation;

Full internal energy of the system can be written as: $E = E_{elastic} + E_{mix} + E_{step}$.

To define mechanisms of the pit formation all energies will be studied and numerical estimations will be given. The numbers and estimations of these energies will be used as a basis data for the following analysis of the different experiments and possible mechanisms of the pit formation.

• Elastic energy

The elastic energy of thin layers of 1 ML height at the surface can differ from those in the bulk. But in some cases it is possible to neglect by the surface and use approaching with the bulk model, for the described here system it will be supported in the following with experimental data. For calculation of elastic energy of Ge layer of 1ML height the theory for a bulk crystalline solid will be used.

The state of strain in a solid is described by the dependence of a displacement vector \mathbf{u} on the position denoted by \mathbf{r} . The second rank tensor of infinitesimal strain ε_{ij} is defined by

$$\varepsilon_{ij} = \frac{1}{2} \left\{ \frac{\partial u_i}{\partial x_j} + \frac{\partial u_j}{\partial x_i} \right\}.$$

Stresses and strains are related by Hooke's law. In its most general form Hooke's law reads [131,25]

$$au_{kl} = \sum_{ij} c_{klij} arepsilon_{ij}$$
 ,

in which c_{klij} are the components of the forth rank tensor of the elastic modules. Because of the symmetry of the stress and strain tensors τ_{kl} and ε_{ij} one has the relation $c_{klij} = c_{lkij} = c_{klji}$. The number of independent components of the elastic tensor is further reduced by the requirement that the elastic energy be a unique function of the state of strain. The energy density U_{elast} is

$$U_{elast} = \sum_{kl} \int \tau_{kl} d\varepsilon_{kl} = \frac{1}{2} \sum_{ijkl} c_{klij} \varepsilon_{ij} \varepsilon_{kl} ,$$

 ε_{ij} and ε_{kl} are the functions $\varepsilon_{ij}(r)$ and $\varepsilon_{kl}(r)$ of position $r = (r_x, r_y, r_z)$. In general case, full elastic energy of a crystalline solid E_{elast} is an integral of energy density U_{elast} over volume of the solid

$$E_{elast} = \iiint_{V} U_{elast}(r) dx dy dz = \iiint_{V} \frac{1}{2} \sum_{ijkl} c_{klij} \varepsilon_{ij}(r) \varepsilon_{kl}(r) dx dy dz.$$

Here the integration region V corresponds to the volume of solid. Geometry of the system is shown on **Figure 9. 8**. The volume of the solid V consists of volume of Si substrate V_2 and volume of Ge layer V_1 . The following relations assume some approaches for elastic energy of the system:

- 1. The Si crystalline solid have a close elasticity with Ge crystalline solid, and Si is more hard material than Ge;
- 2. Lateral size of Ge layer is much larger than thickness (height) of Ge layer, $L/h_{Ge} > 10$;
- 3. The thickness of substrate is much larger than thickness of 1 BL of Ge, $h_{Si}/h_{Ge} > 10^6$. Strain $\varepsilon_{ij}(r)$ has a maximal value at the place of localization (Si/Ge interface) of the force applied to the solid. The equivalence of the forces at the interface $F_{Si} = -F_{Ge}$ can be written:

$$k_{Ge}h_{Ge}\varepsilon_{Ge} = k_{Si}h_{Si}\varepsilon_{Si}, \ k_{Ge} \approx k_{Si} \rightarrow \varepsilon_{Ge} = \frac{h_{Si}}{h_{Ge}}\varepsilon_{Si}, \text{ where } k_{Ge} \text{ and } k_{Si} \text{ are the force constants}$$
 for Ge and Si respectively.

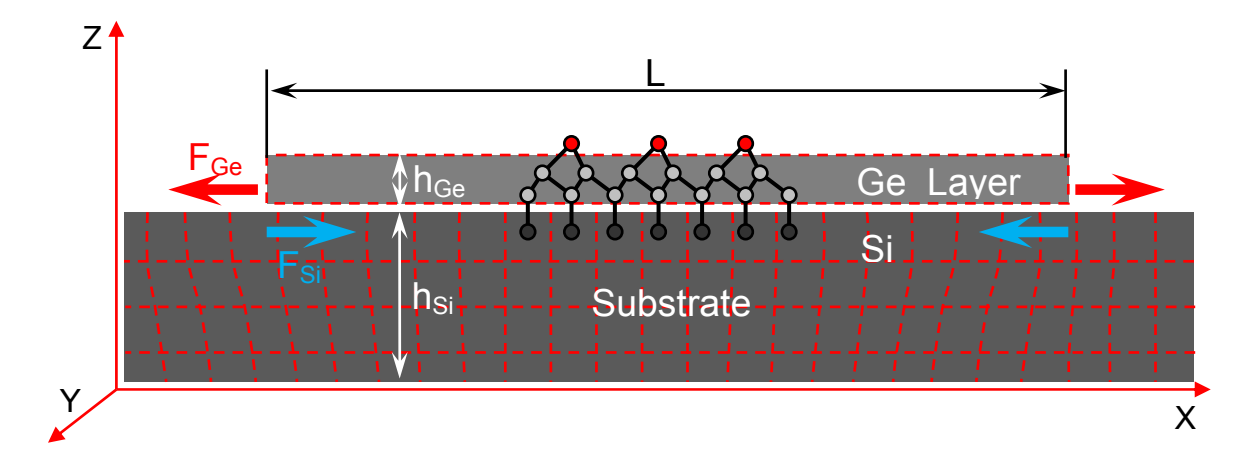


Figure 9. 8. The strained Ge layer on Si substrate. Ge have a 4% lager lattice constant. The maximal strain of 4% is applied at Si/Ge interface. Ge layer takes larger part of 4% strain due to geometry of the system: $L/h_{Ge} > 10$, $h_{Si}/h_{Ge} > 10^6$.

Because of geometry of the system $h_{Si'}/h_{Ge} > 10^6$ (**Figure 9. 8**) Ge layer takes more strain than Si substrate takes strain near Si/Ge interface: $\varepsilon_{Ge} >> \varepsilon_{Si}$, here ε_{Ge} – strain in the Ge layer, ε_{Si} – strain in the Si substrate at Si/Ge interface. The elastic energies of Ge layer and Si substrate associated with the force at Si/Ge interface $F_{Si} = -F_{Ge} = F$ are proportional to the strain $U_{elast} = F\varepsilon$. $\varepsilon_{Ge} >> \varepsilon_{Si} \rightarrow F\varepsilon_{Ge} >> F\varepsilon_{Si}$, therefore, the energy of Ge layer is the largest part of elastic energy of the system. Then, in the first approach we can neglect by elastic energy in volume V_2 of the Si substrate:

$$\begin{split} E_{elast} &= \iiint_{V=V1+V2} U_{elast}(r) dx dy dz = \iiint_{V1} U_{elast}(r) dx dy dz + \iiint_{V2} U_{elast}(r) dx dy dz \approx \\ &\approx \iiint_{V1} U_{elast}(r) dx dy dz \end{split}$$

The energy of the displacement field u induced in the Si substrate by the force applied at the step edges of Ge (GeSi) layer will be considered in the next paragraph as the energy of relaxation at the step edges of the Ge or/and GeSi layer.

The energy density of thin isotropic strained layer can be found from inverse form of Hooke's law:

$$\varepsilon_{kl} = \sum_{ii} s_{klij} \tau_{ij}$$
,

Isotropic strain has no distortion forces ($\tau_{44} = \tau_{55} = \tau_{66} = 0$), then the lateral strain ε of Si/Ge layer can be expressed as (x \rightarrow 1, y \rightarrow 2, z \rightarrow 3):

$$\varepsilon_{11} = s_{11}\tau_{11} + s_{12}\tau_{22} + s_{13}\tau_{33}$$

$$\varepsilon_{22} = s_{21}\tau_{11} + s_{22}\tau_{22} + s_{23}\tau_{33}$$

here and further a short notation by the Voigt indices is used: $11 \rightarrow 1$; $22 \rightarrow 2$; $33 \rightarrow 3$; $23 \rightarrow 4$; $13 \rightarrow 5$; $12 \rightarrow 6$. $s_{11} = s_{22}$ and $s_{12} = s_{21}$ by the symmetry of the Ge (Si) crystal. A hexagonal crystal is elastically isotropic in its basal plane (111), therefore, $\varepsilon_{11} = \varepsilon_{22} = \varepsilon$, $\tau_{11} = \tau_{22} = \tau$, the Si/Ge layer is free in z (3) direction **Figure 9. 8**, therefore, $\tau_{33} = 0$, then the strain takes the form:

$$\varepsilon = (s_{11} + s_{12})\tau, \rightarrow \tau = \frac{\varepsilon}{(s_{11} + s_{12})},$$

the differential of energy density $dU_{\mbox{\tiny elast}}$ can be written as:

$$dU_{elast} = 2\tau \cdot d\varepsilon = \frac{2\varepsilon \cdot d\varepsilon}{s_{11} + s_{12}},$$

for isotropic solid
$$Y = \frac{1}{s_{11}}$$
 and $\nu = -\frac{s_{12}}{s_{11}}$ [131], then $\rightarrow \frac{1}{s_{11} + s_{12}} = \frac{Y}{1 - \nu}$.

The energy density per area γ_{elast} :

$$\gamma_{elast} = t\varepsilon^2 \frac{Y}{1 - \nu} = k\varepsilon^2, \tag{1.1}$$

Where the force constant $k = t \frac{Y}{1 - v}$, t is the film thickness, ε – is a strain, v is Poisson-

number and **Y** is Young's modulus. Elastic energy of the layer of area A ca be written as:

$$E_{elast} = Ak\varepsilon^2, (1.2)$$

Young's modulus $Y_{(III)} = 13.8 \times 10^{10} \text{N/m}^2$, Poisson-number $v_{(III)} = 0.252$ for (111) plane of Ge crystal [131] and $Y_{(III)} = 16.9 \times 10^{10} \text{N/m}^2$, $v_{(III)} = 0.262$ for Si can be found in reff. [131]. The force constant k_{Si} for one layer (3.14 A) of Si is 71.9 N/m, and k_{Ge} of Ge one layer is 57.9 N/m. k_{Si} is 25% larger than k_{Ge} . The force constant for Ge_xSi_{1-x} composition layer k can be estimated as proportions of k_{Si} and k_{Ge} :

$$k = k_{Ge}x + k_{Si}(1-x) = k_{Ge}(1.24 - 0.24x),$$
(1.3)

According to Vegard's law the lattice parameter of the bulk of Ge_xSi_{1-x} can be varied linear with composition from the natural lattice constant of Si to the natural constant of Ge. Therefore, the strain of compound Ge_xSi_{1-x} layer on the Si surface is proportional to the ratio of Ge in alloy:

$$\varepsilon = \varepsilon_0 x, \tag{1.4}$$

where $\varepsilon_{\theta} = 4\%$ – is the strain of Ge layer on Si substrate. According to the model **Figure 9. 7**, the ratio x of Ge in compound layer is:

$$x = A_{pit}/(A_{pit} + A_{si}). \tag{1.5}$$

Let's take $k = k_{Ge}$ and let's take into account only strained epitaxial Ge and Ge_xSi_{1-x} layers, then elastic energy can be found by combining (1.2), (1.4) and (1.5). The elastic energy of initial state can be written as:

 $E_{elastic}^{i} = A_{Ge} k_{Ge} \varepsilon_{\theta}^{2} + A_{Si} k_{Si} \varepsilon_{Si}^{2}$, the expression $A_{Si} k_{Si} \varepsilon_{Si}^{2}$ - is the strain energy of Si on Si which is identical 0, then:

$$E_{elastic}^{i} = A_{Ge} k_{Ge} \varepsilon_{\theta}^{2}. \tag{1.6}$$

The elastic energy of final state (**Figure 9. 7**):

$$E_{elastic}^{f} = (A_{Ge} - A_{pit}) k_{Ge} \varepsilon_{\theta}^{2} + (A_{pit} + A_{si}) k_{Ge} \varepsilon_{\theta}^{2} (A_{pit} / (A_{pit} + A_{si}))^{2}, \tag{1.7}$$

Energy gain $E_{elastic}^{f-i} = E_{elastic}^{i} - E_{elastic}^{f}$ after simplifications takes the form:

$$E_{elastic}^{f-i} = -k_{Ge} \, \varepsilon_0^2 \, A_{si} \, x \,, \tag{1.8}$$

The increase of x decreases the elastic energy. From (1.8) and (1.5) it follows that system will decrease elastic energy with increase size of pits A_{pit} at fixed A_{si} . The Bi layer on the top of Ge/GeSi layer (**Figure 9.9**) reduces the energy gain (1.8).

To calculate elastic energy of Ge_xSi_{1-x} layer covered with Bi the following denotes will be used:

the strain of Ge_xSi_{1-x} layer on Si(111) substrate

the strain of Bi layer on Si(111) substrate

the strain of Bi layer on Ge_xSi_{1-x} layer

the strain of Bi + Ge_xSi_{1-x} layer on Si(111) substrate \mathcal{E}_{Bi} , $\mathcal{E}_{Bi} - \mathcal{E}_{O}x$, $\mathcal{E}_{O}x + \mathcal{E}_{O}x$,

The Ge_xSi_{1-x} layer terminated with Bi is under additional stress of Bi layer. The strain of Bi terminated Ge_xSi_{1-x} layer is differ on δ from original one. δ can be found from equivalence of the forces $F_{Bi} = F_{GeSi}$ for free layer Figure 9. 9 (right image). As well as in the previous cases the approaching $k = k_{Ge}$ is used, then the expressions for the forces F_{SiGe} and F_{Bi} (Figure 9. 9) yield:

$$F_{SiGe} = k_{Ge}((\varepsilon_{\theta}x + \delta) - \varepsilon_{\theta}x),$$

$$F_{Bi} = k_{Bi}((\varepsilon_{\theta}x + \delta) - \varepsilon_{Bi}),$$

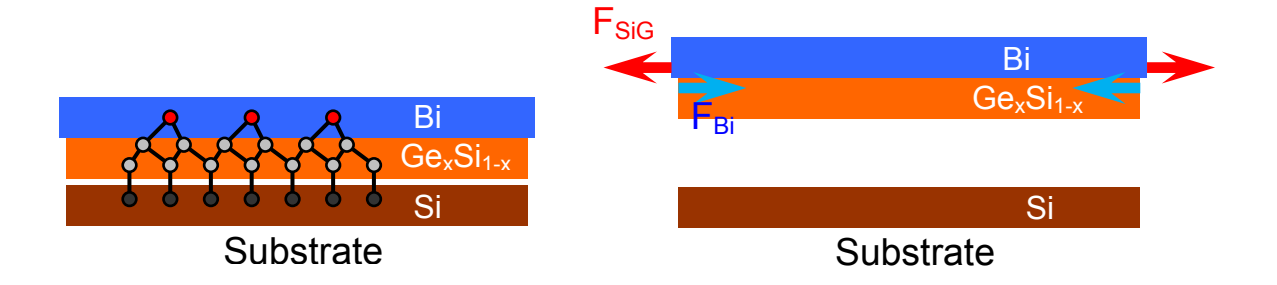


Figure 9. 9. The underlying Ge_xSi_{1-x} layer is squeezed by Bi.

from equivalence of the forces $F_{SiGe} = -F_{Bi} \rightarrow k_{Bi} ((\varepsilon_{Bi} - \varepsilon_{\theta} x) - \delta) = k_{Ge} \delta$, we obtain:

$$\delta = (\varepsilon_{Bi} - \varepsilon_{\theta} x) k_{Bi} / k^{\parallel}$$
, (1.9) where $k^{\parallel} = k_{Ge} + k_{Bi}$, in the case of pure Ge layer, $x = 1$ we have $\delta_{\theta} = (\varepsilon_{Bi} - \varepsilon_{\theta}) k_{Bi} / k^{\parallel}$, then the elastic energy of initial and final states can be written:

 $E_{elastic}^{i} = A_{Ge} k^{\perp} (\varepsilon_{\theta} + \delta_{\theta})^{2} + A_{si} k^{\perp} (\theta + \delta)$, with (1.9) it gives:

$$E_{elastic}^{i} = A_{Ge} k^{\dagger} (\varepsilon_{\theta} + \delta_{\theta})^{2} + A_{si} k_{Bi}^{2} \varepsilon_{Bi}^{2} / \chi^{\dagger}$$

$$\begin{split} E_{elastic}{}^{i} &= A_{Ge} \ k^{\parallel} \left(\varepsilon_{\theta} + \delta_{\theta} \right)^{2} + A_{si} \ k_{Bi}{}^{2} \ \varepsilon_{Bi}{}^{2} / \chi^{\parallel} \ , \\ E_{elastic}{}^{f} &= \left(A_{Ge} - A_{pit} \right) \ k^{\parallel} \left(\varepsilon_{\theta} + \delta_{\theta} \right)^{2} + \left(A_{Si} + A_{pit} \right) \ k^{\parallel} \left(\varepsilon_{\theta} \chi + \delta \right)^{2} \ , \ \text{combining} \ E_{elastic}{}^{i} \ \text{and} \ E_{elastic}{}^{f} \end{split}$$
we obtain expression for energy gain:

 $E_{elastic}^{f-i} = -A_{pit} k^{\dagger} (\varepsilon_{\theta} + \delta_{\theta})^{2} + (A_{Si} + A_{pit}) k^{\dagger} (\varepsilon_{\theta} x + \delta)^{2} - A_{Si} k_{Bi}^{2} \varepsilon_{Bi}^{2} / k^{\dagger}, \rightarrow$ $E_{elastic}^{f-i} = -A_{Si} x k^{\dagger} \varepsilon_{\theta}^{2} + A_{pit} k^{\dagger} 2\varepsilon_{\theta} (\delta - \delta_{\theta}^{2}) + ((A_{Si} + A_{pit}) k^{\dagger} \delta^{2} - A_{pit} k^{\dagger} \delta_{\theta}^{2}) - A_{Si} k_{Bi}^{2}$ $\varepsilon_{Bi}^{2} / k^{\dagger}, \text{ combining with } (\delta - \delta_{\theta}^{2}) = \varepsilon_{\theta} (1-x) k_{Bi}^{2} / k^{\dagger} \text{ and after combinations (see appendix B)}$ the energy gain can be simplified:

$$E_{elastic}^{f-i} = -(k_{Ge} \, \varepsilon_{\theta}^{2} \, A_{si} \, x) \, k_{Ge} \, / \, k^{\parallel} = -k_{Ge}^{2} / (k_{Ge} + k_{Bi}) \, \varepsilon_{\theta}^{2} \, A_{si} \, x,$$
it can be also represent as:

$$E_{elastic}^{f-i} = -\left(k_{Ge} - k_{Ge} k_{Bi} / (k_{Ge} + k_{Bi})\right) \varepsilon_0^2 A_{si} x, \tag{1.11}$$

The elastic energy of Bi terminated GeSi layer depends on additional parameter which is the force constant k_{Bi} . The energy gain $E_{elastic}^{f-i}$ decreases with increase of k_{Bi} . At $k_{Bi} = 0$ elastic energy takes the maxima value which is equivalent to the energy of one GeSi bulk layer (1.8). Generally, surface reconstruction changes the surface stress and modulus of the surface layer. In the case of Bi-SME Bi saturates dandling bonds, decreases surface stress and changes modulus of the surface layer. In the following estimations the data of Sb and Ge deposition on Si(111) surface [136] will be used. The authors found that the stress caused by 1ML of Sb is equivalent to the stress caused by 2ML of Ge. Actually, the Sb decreases the surface stress of the (7x7) from original value 2.98 N/m [137] down to 1 N/m. The surface stress of Ge on Sb terminated Si(111) surface is linear proportional to the Ge coverage Figure 9. 10 and corresponds to 2.0 (N/m)/ML in the range of coverages of Ge from 0 to 4 ML. I. e. first deposited layer produces the same stress as second, third, ..., until S-K growth mode or dislocations start generate. The surface stress (Figure 9. 10) is dropped linear with Ge coverage in range of from 0 to 4 ML. The same slope of the dependence on Ge coverage in the ranges of $0 < \theta < 1$ and $1 < \theta < 2$ is result of the same stress induced by Si(111) $\sqrt{3}$ x $\sqrt{3}$ -Sb surface phase and by $Ge(111)\sqrt{3}x\sqrt{3}$ -Sb surface phase. Therefore the stress caused by Sb surface phase can be taken into account separately from the underling Si and Ge layers. This linear dependence also shows that we can neglect by the surface and use bulk crystalline solid elasticity theory.

Unreconstructed Si(111)1x1 surface have a negative surface tension (-0.7 N/m) [138] which become positive and corresponds to 1 N/m after Sb termination. Let's consider the stress caused by $\sqrt{3}$ x $\sqrt{3}$ -Sb-1ML surface phase separately from the underlying unreconstructed Si(111)1x1 surface, then, the stress caused by Sb can be found as a difference of the surface tensions for Si(111)1x1 and Si(111) $\sqrt{3}x\sqrt{3}$ -Sb-1ML surfaces. The difference is 1.7 N/m **Table 1**. The surface tensions used here are placed in **Table 1**. The last surface tension 1.7 N/m in the table is used in the following as a stress caused by Sb trimers.



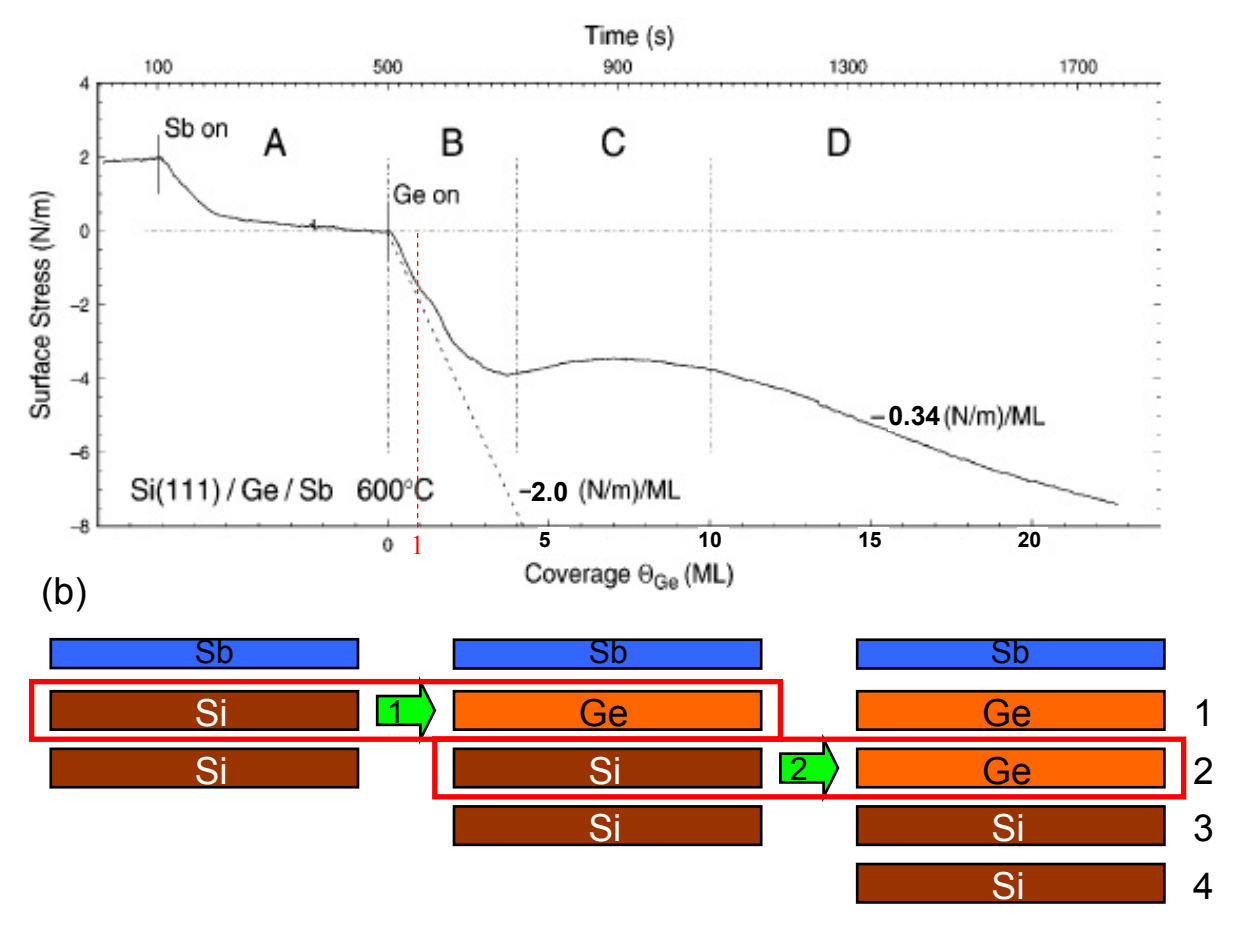


Figure 9. 10. The calculated surface stress during Sb deposition and Ge growth on Si(111) at 600° C is shown (a) by data of P. Zahl, P. Kury, M. Horn von Hoegen [136]. Sb adsorption (regime A) causes strong change in stress of ≈ 2 N/m. During the coherent stage of growth (regime B) Ge deposition results in an initially linear increase of compressive film stress. The slope of 2.0 (N/m)/ML Ge compares well with the behavior expected from bulk elasticity constants. (b) The first(upper) deposited Ge layer produces double change: 1. it produces own 4% strain relative to Si substrate and 2. it changes the surface stress because of Si and Ge surfaces have a different surface energies and surface tensions. Actually, the pure Ge surface have lower values of the energies and surface tensions than Si surface. Apart from the first layer the second and the next layers produce equivalent changes in the bulk structure of the system by additional strained Ge layer.

Table 1

Tuble 1			
Substrate	Surface	Change of	reference
	tension	surface tension	
(i) Si(111)1x1	-0.7 N/m		[138]
(ii) Si(111)7x7	2.98 N/m		[137]
(iii)		- 2 N/m	[136]
$Si(111)7x7 \rightarrow Si(111) \sqrt{3}x\sqrt{3}-Sb-1ML$			
(iv)		+ 1.7 N/m	Calculated from (i),
$Si(111)1x1 \rightarrow Si(111)\sqrt{3}x\sqrt{3}-Sb-1ML$			(ii) and (iii):
			1.7≈2.98 - 2+0.7

Bi have a less bond energies and is more soft material than Sb [139,140,141]. Bi has a less elastic constants than Sb and can cause less surface tension:

$$c_{11}^{Bi} = 63.7, c_{12}^{Bi} = 24.6, c_{14}^{Bi} = 7.2, c_{33}^{Bi} = 38.1, c_{44}^{Bi} = 11.26, c_{66}^{Bi} = 19.4;$$

$$c_{11}^{Sb} = 101.4, c_{12}^{Sb} = 29.4, c_{14}^{Sb} = 20.9, c_{33}^{Sb} = 45.0, c_{44}^{Sb} = 39.2, c_{66}^{Sb} = 33.4, \times 10^{10} \text{ dyn/cm}.$$

The "stress" data with Sb (**Figure 9. 10**) can be used to estimate upper limit of Bi effect on the elastic energy (1.10), (1.11). For estimation of the force constant k_{Bi} the stress data of Sb and geometry of Bi trimers will be used. The character of the chemical bonding of Bi trimers on Si(111) surface is close to p³ [142], that induces the right angles [143]. The length of Bi-Bi bonds in trimer (β -phase) is 3.1 A [144,145,146], the distance between underlying Si atoms is 3.84 A, and \angle Bi-Bi-Si is near the right angle (98°) **Figure 9. 11**.

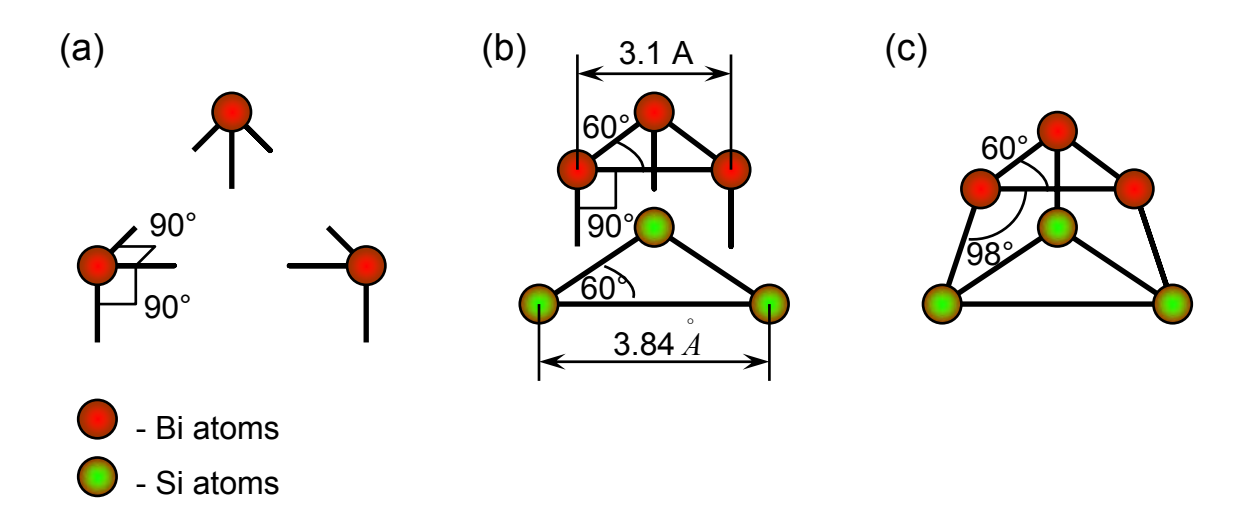


Figure 9. 11. Bi trimer on Si(111) surface. p³ character of the chemical bonding of Bi trimers on Si(111) surface induces the right angles (a), these angels are transformed by geometry of structure of underlying substrate into values which is different from 90° and that difference induces the strain; Bi atoms of trimer form equilateral triangle with base of 3.1 A, that is 24% less than base of underlying Si(111)1x1 unit sell 3.84A (b); the 24% of the lateral difference is compensated by lager (than 90°) angle 98° (c). That 24% strain of trimer structure induces surface tension about 1.7 N/m.

The strain of Bi trimers can be estimated from geometry. Deformation of the bond angle from 90° to 98° corresponds to 24% of deformation of base of Bi trimer. Approximation by Hooke's law also gives upper estimation of Bi effect on the strain energy (1.10), (1.11). The strain of Bi trimers is 24% - that is six times larger than the strain of single Ge layer (4%), and stress of Bi trimer no more than 0.85 times larger than stress of single Ge layer, then:

$$k_{Bi} = k_{Ge} 0.85 \frac{4\%}{24\%} = k_{Ge} \frac{0.85}{6} = 0.14 k_{Ge},$$
 (1.12)

Combining (1.12) with (1.11) gives:

$$-1.0 k_{Ge} \varepsilon_{\theta}^{2} A_{si} x \leq E_{elastic}^{f-i} \leq -0.88 k_{Ge} \varepsilon_{\theta}^{2} A_{si} x$$

we will use upper limit – 0.88 $k_{Ge} \varepsilon_{\theta}^2 A_{si} x$. To represent the energy per atom we multiply this expression by constant – $0.157 \times 10^{20} \frac{atom}{m^2}$:

$$E_{elastic}^{f-i} = -0.157 \times 10^{20} \frac{atom}{m^2} \cdot 0.88 k_{Ge} \, \varepsilon_0^2 \, A_{si} \, x,$$

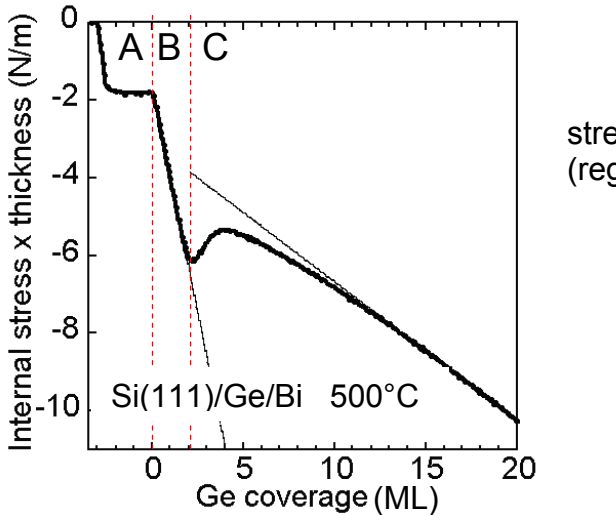
$$E_{elastic}^{f-i} = -33 \frac{meV}{atom} N(1-x)x ,$$

$$(1.13)$$

where N is number of particles, $N = N_{Ge} + N_{Si}$.

Recently, evolution of the surface stress during Bi deposition and Ge growth on Bi terminated Si(111) surface was studied by H. Asaoka (**Figure 9. 12**). The results are surprisingly similar and have qualitative and numerical data which are mostly the same with data obtained for Sb by P. Zahl, P. Kury, M. Horn von Hoegen [136] (**Figure 9. 10**). As it was assumed above, the stress caused by 1ML of Bi 1.8 N/m is slightly lower than stress caused by 1ML of Sb 2 N/m (**Figure 9. 10**, **Figure 9. 12**). Therefore, calculations above can be well attributed to the surface terminated with Bi.

H. Asaoka



stress gradient -2.30 (N/m)/ML (regime B)

Figure 9. 12. The calculated surface stress during Bi deposition (regime A) and Ge growth on Bi terminated Si(111) at 500° C obtained by Hidehito Asaoka. Bi adsorption (regime A) causes change in stress of ≈ 1.8 N/m. During the coherent stage of growth (regime B) Ge deposition results in an initially linear increase of compressive film stress. The slope of 2.3 (N/m)/BL Ge compares well with the behavior expected from bulk elasticity constants.

• Energy of mixing

The cohesive energy is energy required to form separated neutral atoms in their ground electronic state from the solid at 0 K and at 1 atm. The cohesive energy of Si is 15% higher than Ge [129,128, 147,148,149], (**Figure 9. 13**).

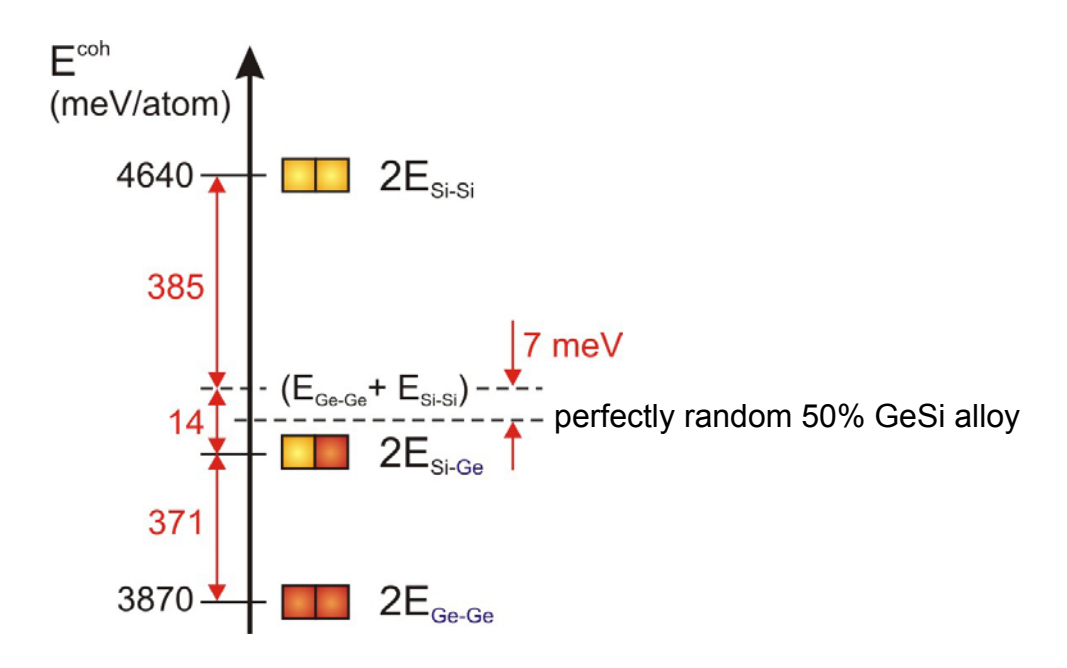


Figure 9. 13. The energy diagram shows cohesive energies per atom for Ge, Si [147] and perfectly random 50% GeSi alloy. The mixing energy of perfectly random 50% GeSi alloy is = 7 meV/atom [132,133,150,151]. Cohesive energy per atom is equal double energy per bond since two bonds per atom are present. Then the bond energies have the next relations: $E_{Si-Si} - E_{Si-Ge} = 200 \text{ meV/bond}$ and $E_{Si-Ge} - E_{Ge-Ge} = 185 \text{ meV/bond}$, $(E_{Ge-Ge} + E_{Si-Si})/2 - E_{Si-Ge} = 7 \text{ meV}$.

The cohesive energy of 50% GeSi alloy is approximately in the middle between Si-Si and Ge-Ge cohesive energies. Investigations [132,133,150,151] showed that cohesive energy of GeSi alloy is lower than average of Si and Ge cohesive energies per atom, i.e.:

$$E_{Si-Ge}^{coh} < (E_{Si-Si}^{coh} + E_{Ge-Ge}^{coh})/2,$$

The difference $((E_{Si-Si}^{coh} + E_{Ge-Ge}^{coh})/2 - E_{Si-Ge}^{coh})$ in the case of perfectly random 50% Si-Ge alloy is about 7 meV/atom [132,133,150,151]. The energy gain is so small that segregation of Ge and Si can occur only at temperatures lower than 170K [132].

The energy of mixing can be found from probability relations as a function of Ge concentration x. The probability to have a Ge neighbor atom at one bond is equal to P(Ge) = x, the probability to have a Si neighbor atom at one bond is equal to P(Si) = (1-x).

Let's take Ge crystal with $N \cdot x$ Ge atoms and Si crystal with $N \cdot (1-x)$ Si atoms. The sum cohesive energy of the Ge and Si crystals (non intermixing state) is

$$E_{Si+Ge}^{i} = E_{Si} + E_{Ge} = -N \left(x E_{Ge-Ge}^{coh} + (1-x) E_{Si-Si}^{coh} \right), \tag{1.14}$$

where N is the full number of particles, $N = N_{Ge} + N_{Si}$. The mixture of Ge $N \cdot x$ atoms with Si $N \cdot (1-x)$ atoms gives Ge_xSi_{1-x} alloy. Every atom has 4 neighbors = 4 bonds. To exclude double accounting of the bonds we have to take only half, i.e. 2 bonds per atom. Therefore, Ge_xSi_{1-x} random alloy includes $2N_{Si} \cdot P(Ge) + 2N_{Ge} \cdot P(Si) = 4x(1-x)$ of Si-Ge bonds, $N_{Ge} \cdot P(Ge) = 2x^2$ of Ge-Ge bonds and $N_{Si} \cdot P(Si) = 2(1-x)^2$ of Si-Si bonds per atom. The cohesive energy of Ge_xSi_{1-x} alloy (intermixed state) can be written in term of bond energies

$$E_{GeSi}^{f} = -2N(2x(1-x)E_{Si-Ge} + (1-x)^{2}E_{Si-Si} + x^{2}E_{Ge-Ge}),$$
(1. 15)

where $E_{Ge-Ge} = \frac{E_{Ge-Ge}^{coh}}{2}$, E_{Si-Ge} , $E_{Si-Si} = \frac{E_{Si-Si}^{coh}}{2}$ are bond energies between Ge-Ge, Si-Ge and Si-Si atoms respectively. Then, the sum cohesive energy of Ge and Si crystals (1. 14) in term of bond energies is

$$E_{Si+Ge}^{i} = -2N(xE_{Ge-Ge} + (1-x)E_{Si-Si}), (1.16)$$

The energy difference between final (1. 15) and initial (1. 16) states is

$$E_{Si+Ge}^{f-i} = -2N(2x(1-x)E_{Si-Ge} + (1-x)^2E_{Si-Si} + x^2E_{Ge-Ge} - xE_{Ge-Ge} - (1-x)E_{Si-Si}) =$$

$$= -2Nx(1-x)(2E_{Si-Ge} - (E_{Si-Si} + E_{Ge-Ge}))$$

Mixture energy of random alloy can be expressed in energy per atom $\frac{E_{Si+Ge}^{f-i}}{N} = E_{mix}$:

$$E_{mix} = -4 \left(E_{Si-Ge} - \frac{(E_{Si-Si} + E_{Ge-Ge})}{2} \right) x(1-x) , \qquad (1.17)$$

$$E_{mix} = \Omega x (1-x)$$

where $\Omega = -4 \left(E_{Si-Ge} - \frac{(E_{Si-Si} + E_{Ge-Ge})}{2} \right)$ is called the interaction parameter. The mixing energy of 50% SiGe random alloy is $E_{mix} = - \left(E_{Si-Ge} - \frac{(E_{Si-Si} + E_{Ge-Ge})}{2} \right) = 7 \, meV / atom$, then $\mathbf{\Omega} = 28 \, \text{meV/atom}$.

Bond energy between two atoms depends on their neighbors (Ge or Si) **Figure 9. 14**. The significant dependence can be expected for elements with ionic type of bonds. Si and Ge are similar elements with covalent type of bonds. In the following, to estimate Si-Ge, Ge-Ge, Si-Si bond energies in the bulk only two interacting atoms (without neighbors) will be taken into account (this simplification was also used in previous computations): $E_{Ge-Ge} = \frac{E_{Ge-Ge}^{coh}}{2}$,

$$E_{Si-Si} = \frac{E_{Si-Si}^{coh}}{2} \, , \; E_{Si-Ge} = \frac{(E_{Si-Si} + E_{Ge-Ge})}{2} - 7meV \, .$$

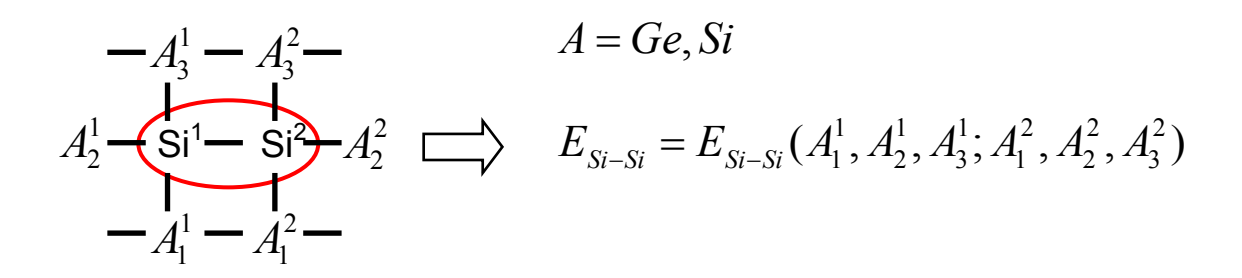


Figure 9. 14. The bonding energy is a function of the nearest neighbors. The variable parameter *A* can be either Si or Ge atoms.

The interaction parameter of thin monolayer film will be different from the interaction parameter of the bulk crystal due to influence of the surface interfaces. For estimation of effective interaction parameter the initial not intermixed state and final intermixed state will be considered **Figure 9. 15** with random distribution of Si and Ge atoms in the height of GeSi layer **Figure 9. 15** (a). The monolayer films have two interface surfaces: vacuum/Ge_x, Si_{1-x} layers, Ge_x, Si_{1-x} layers/Si substrate for initial state, and vacuum/Ge_xSi_{1-x} layer, Ge_xSi_{1-x} layer/Si substrate for final state **Figure 9. 15**. Ge_xSi_{1-x} layer spend 1/8 number of bonds to connect with Si substrate and 1/8 number of bonds are saturated with Bi. The 1/8 part of the bonds which are saturated with Bi has no energy difference in the initial and final state with random alloy **Figure 9. 15**. Number of Si-Si and Si-Ge bonds between Ge/Si layers and Si substrate are the same for initial and final state with Ge_xSi_{1-x} random alloy because of the number of Si and Ge atoms are conserved at the interface. Both considered above 1/8 parts of the bonds can be neglected. The resulting intermixing energy Ω_{eff} of one Ge_xSi_{1-x} monolayer

on the Si substrate is 3/4 times less than intermixing energy in the bulk of the crystal, i.e. Ω_{eff} = 21 meV/atom or 5.2 meV/atom for 50% GeSi random alloy. The mixing energy for the layers with areas A_{pit} and A_{si} in the model shown in **Figure 9.7** is:

$$E_{mix}^{f-i} = N\Omega_{eff}(1-x)x$$
, where $N = (N_{Si} + N_{Ge}) = (A_{pit} + A_{si}) \times 0.312 \times 10^{20}$ atom/m²,

using (1.5) we can write $(1-x) = A_{si}(A_{pit} + A_{si})$ and put it into equation for E_{mix}^{f-i} , then

$$E_{mix}^{f-i} = 0.157 \times 10^{20} \frac{atom}{m^2} \Omega_{eff} A_{Si} x,$$

$$E_{mix}^{f-i} = 21 \frac{meV}{atom} N(1-x) x.$$
(1.18)

The mixing energy increases with x. From (1.18) and (1.5) it follows that mixing energy of the system increases with increase of pit size A_{pit} . This result is based on the model with random distribution of Si and Ge atoms in the height of GeSi layer Figure 9. 15 (a). The segregation of Ge atoms on top of the layer Figure 9. 15 (b) will decrease the mixing energy. The Bi termination reduces the surface energy and can reduce segregation energy. Experimental measurements in [24] show that Ge does not segregate at Bi terminated Si(111) surface. Therefore, in the following we use the model with random distribution of Si and Ge atoms in the height of GeSi layer Figure 9. 15 (a).

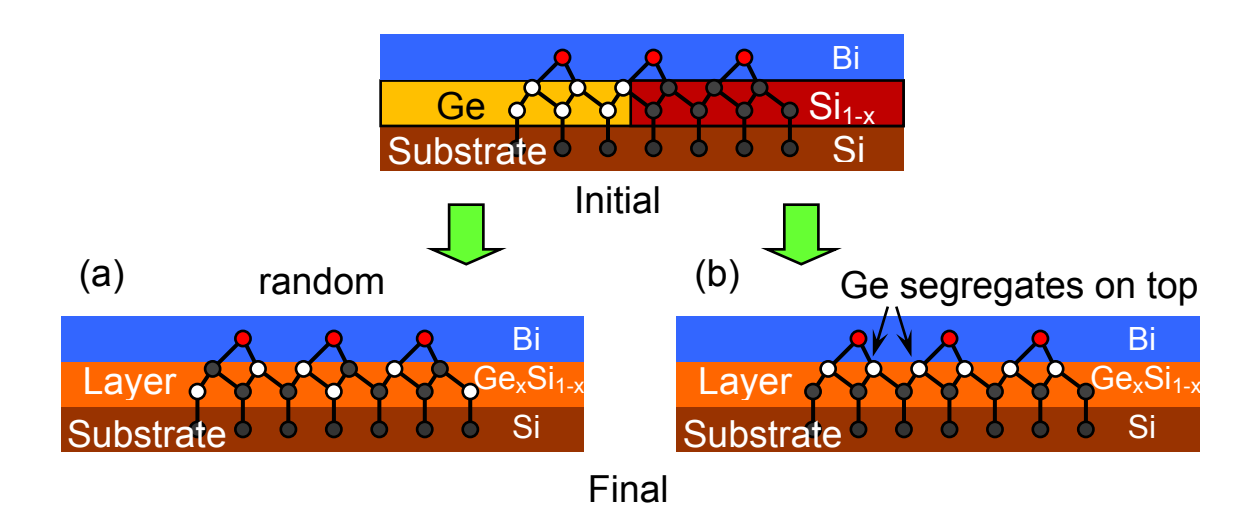


Figure 9. 15. The energy of compound Ge_xSi_{1-x} layer depend on interior combination of bonds, due to that we lose some part of the intermixing energy in the interface regions. There are presented two cases: a) randomly distributed Ge atoms in vertical direction and b) complete segregation of the Ge atoms on top of the layer.

• Energy of step formation

The step free energy of the pits can be calculated from the step free energy per unit length γ which is generally a function $\gamma(\theta)$ of the in plane step orientation angle θ . In the following under step energy the step free energy will be assumed. The energy U of an arbitrary step configuration y(x) can be obtained by integrating along the step,

$$U = \int ds \cdot \gamma(\theta(s)),$$

where s denotes the length along the step. In the case of round pits **Figure 9. 16** the step energy can be expressed as:

$$U = 2\pi R \bar{\gamma}, \qquad (1.19)$$

$$- \oint \gamma(s) ds \quad \oint \gamma(s) ds$$

where $\bar{\gamma} = \frac{\oint \gamma(s)ds}{\oint ds} = \frac{\oint \gamma(s)ds}{2\pi R}$ is average step energy per unit length.

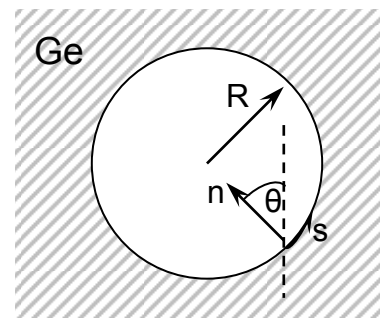


Figure 9. 16. The pit of round shape.

The step energy is associated with increase of the surface area induced by shift a part of a crystal on an atomic distance perpendicular to the surface. That shift produces additional surface area proportional to the height of step. The step energy is related to the surface energy as $d\sigma/d\theta$, where σ is the surface energy as a function of angle of the surface orientation θ . Reconstructed surface has a lower surface energy and usually lower step energy formation. The energy values for different step orientations on the Si(111) surface are given in table **Table 2**.

Table 2

Table 2		
Structure	Step free energy	reference
$(1x1)$ terrace $[\overline{1}\overline{1}2]$ Step	$0.240 \ eV/\mathring{A}, (T = 0K)$	[152,153]
$(1x1)$ terrace $[11\overline{2}]$ Step	$0.202 \ eV/\mathring{A}, (T = 0K)$	[152,153]
$(1x1)$ terrace $[\overline{1}01]$ Step	$0.324 \ eV/\mathring{A}, (T = 0K)$	[152, 153]
$(7x7)$ terrace $[\overline{1}\overline{1}2]$ and $[11\overline{2}]$ Steps	$0.0356 \pm 0.0052 \; eV/A$	[13,154,153]
	0.14 <i>eV/atom</i> (T=700°C)	
$[1x1)$ -As terrace $[11\overline{2}]$ Step, Si replaced by As	$0.0935 \ eV/\mathring{A} \ (T = ??)$	[155]
(1x1)-As terrace $[\overline{1} \overline{1} 2]$ Step, Si replaced by As	$0.1104 \ eV/\mathring{A} \ (T = ??)$	[155]

The highest step energies was observed for unreconstructed - 1x1 Si(111) surfaces. The lowest energy of step formation in **Table 2** corresponds to the reconstructed surface (0.0356 eV/\mathring{A}). For Bi passivated Si(111) surface the step energy formation can be even lower than for Si(111)-7x7 - 0.0356 eV/\mathring{A} due to lower Si(111) $\sqrt{3}x\sqrt{3}$ -Bi surface energy. The step energy for As passivated surface is 0.0935 eV/\mathring{A} . Let's take the value of 0.0356 eV/\mathring{A} for the Si(111)-7x7 reconstructed surface to estimate upper limit of average energy of step formation in Ge layer on Si(111) $\sqrt{3}x\sqrt{3}$ -Bi surface.

The average step energy $\bar{\gamma}$ depends on curvature of the step and also includes energy of relaxation near step edges of strained Ge layer. Elastic relaxation energy at step edges will be considered in the following.

• Elastic relaxation energy at step edges

The strained Ge layer can relax at step edges as shown on Figure 9. 17.

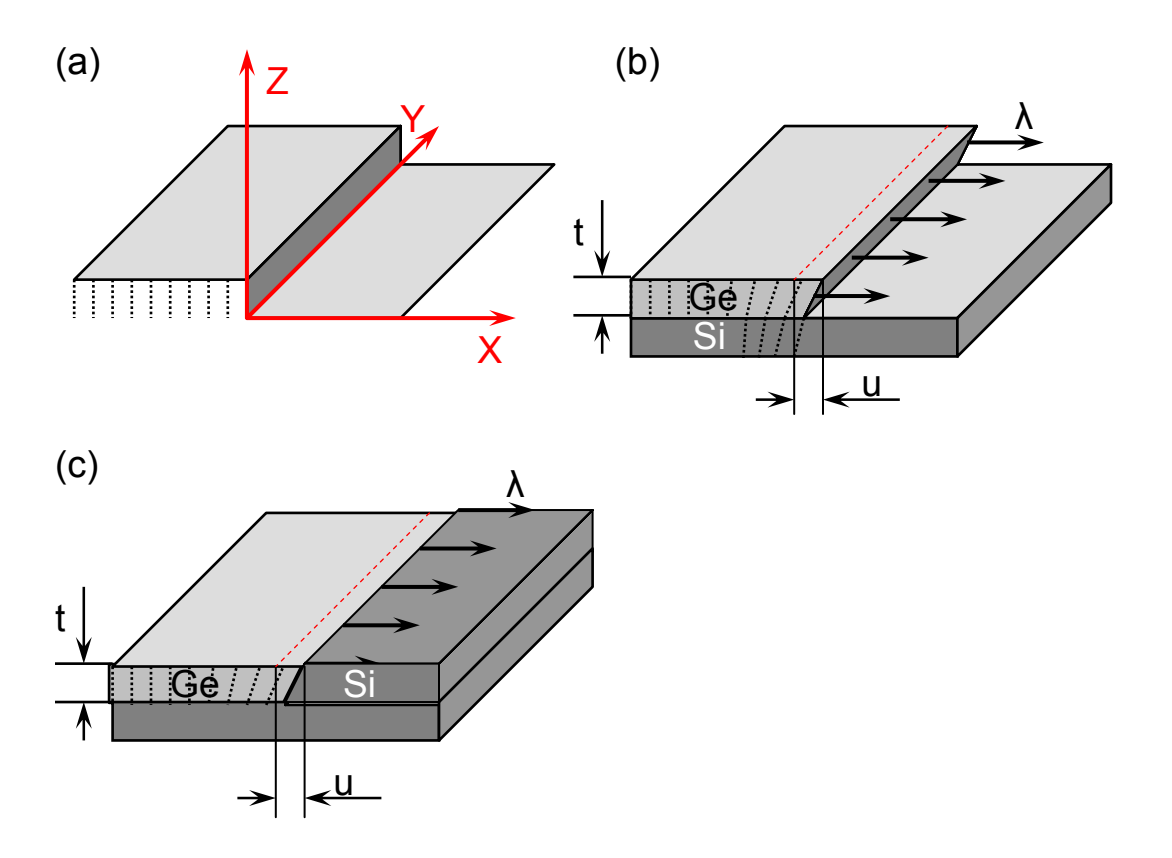


Figure 9. 17. Geometry for computing the elastic relaxation step energy (a); Displacement field of the force λ achieve maximum value u at the step edge (b). The two cases are shown, (b) - relaxation at open step edge and (c) - relaxation at interface boundary between Ge and Si layers.

This elastic relaxation energy at step edge can be found with expression:

$$E_{el}(F) = -\frac{1}{2} \int \lambda(x, y, z) \cdot u(x, y, z) d^{3}r, \qquad (1.20)$$

where u is the displacement field associated with force λ . The force λ is produced by one Si/Ge monolayer with composition of $x = A_{Ge}/(A_{Si} + A_{Ge})$ and can be written as:

$$\lambda = k_{G_{\rho}} \varepsilon_0 x \,, \tag{1.21}$$

Displacement field of localized force $F = F_0 \delta(x) \delta(y) \delta(z)$ has been given by Landau and Lifshitz [156], at z = 0 in plane (x,y) of the surface that is:

$$u_{x}(x,y) = \frac{1+\nu}{\pi Y} \frac{1}{r} \left[(1-\nu)F_{x} + \frac{\nu x}{r^{2}} (xF_{x} + yF_{y}) \right],$$

$$u_{y}(x,y) = \frac{1+\nu}{\pi Y} \frac{1}{r} \left[(1-\nu)F_{y} + \frac{\nu y}{r^{2}} (xF_{x} + yF_{y}) \right],$$

$$u_{z}(x,y) = \frac{1+\nu}{\pi Y} \frac{1}{r} \left[\frac{1-2\nu}{2r} (xF_{x} + yF_{y}) \right],$$
(1.22)

where v is Poisson's ratio, Y is Young's modulus and r is the distance from the force location. The arbitrary force of magnitude f(x,y,z), can be presented as the linear combination of the forces $F = F_0 \delta(x_1) \delta(y_1) \delta(z_1)$ with amplitudes $F_0 = f(x_1, y_1, z_1)$, i.e.

$$f(x, y, z) = \int_{-\infty}^{\infty} f(x, y, z) \delta(x - x_1) \delta(y - y_1) \delta(z - z_1) dx_1 dy_1 dz_1,$$
(1.23)

The $u_i(x,y)$ is solution of a linear differential equation for the force $F = F_0 \delta(x) \delta(y) \delta(z)$, then solution for arbitrary force f(x,y,z) can be found as linear combinations of solutions of the force $F = F_0 \delta(x_1) \delta(y_1) \delta(z_1)$, i.e.:

$$u_i(x, y, z) = \iint G_{ik}(x - x_1, y - y_1, z - z_1) f_k(x_1, y_1, z_1) dx_1 dy_1 dz_1,$$
(1.24)

Equations (1.22) present sums: $u_i(x,y,z) = G_{ix} + G_{iy} + G_{iz}$. $\lambda(x)$ force of magnitude λ in Figure 9. 17 (b) is directed normal to the boundary (or step edge) which is parallel to y direction, the force has only x component and can be expressed as $\lambda(x,y,z) = \lambda \delta(x)\delta(z)$. According to (1.24) displacement field $u_x(x,y)$ can be found as:

$$u_{x}(x,y,z) = \iint u_{x}(x-x_{1},y-y_{1},z-z_{1})\lambda\delta(x_{1})\delta(z_{1})dx_{1}dy_{1}dz_{1} = \int u_{x}(x,y-y_{1},z)\lambda dy_{1}.$$
(1.25)

Solution of (1.25) at x = 0, z = 0 for a straight step edge segment of length L, which coincides with y axis, can be done as the following:

$$u_{x}(0,y,0) = \frac{1-v^{2}}{\pi Y} \lambda \int_{0}^{L} \frac{1}{|y-y_{1}|} dy_{1},$$
 (1.26)

According to (1.20) the energy of relaxation per unit length is:

$$E_{el} = -\frac{1}{2} \int u_x(x, y, z) \lambda \delta(x) \delta(z) dx dy dz = -\frac{1}{2} \lambda \int u_x(0, y, 0) dy,$$
(1.27)

Solution of (1.27) with force $\lambda(x,y,z) = \lambda \delta(x)\delta(z)$ was found in [134] (see Appendix E). The singularity problem at r = (0,y,0) was resolved in [134] by taking lower limit of the integration equal to the interatomic distance a. Another way to solve the singularity problem is the following. The singularity problem at r = (0,y,0) does not exist for dispersed forces. The force homogeneously distributed in cylinder around r = (0,y,0) Figure 9. 18 (a) is one of the possible approximation of a dispersed force. While the integration of the dispersed force Figure 9. 18 (a) is complicated, the displacement field at r = (x,y,0), for x = 0 and x >> a will be calculated with the force located along y axis on cylinder radius of $a = \sqrt{z_1^2 + x_1^2}$ Figure 9. 18 (b), $F_x(x,y,z) = \frac{\lambda}{2\pi a} \delta(\sqrt{z^2 + x^2} - a)$, $\iint F_x(x,z) dx dz = \lambda$. The

subsequent integration of the displacement field in (1.20) will be taken, for simplicity, with the force (1.27) localized at r = (0, y, 0), $\lambda(x, y, z) = \lambda \delta(x) \delta(z)$.

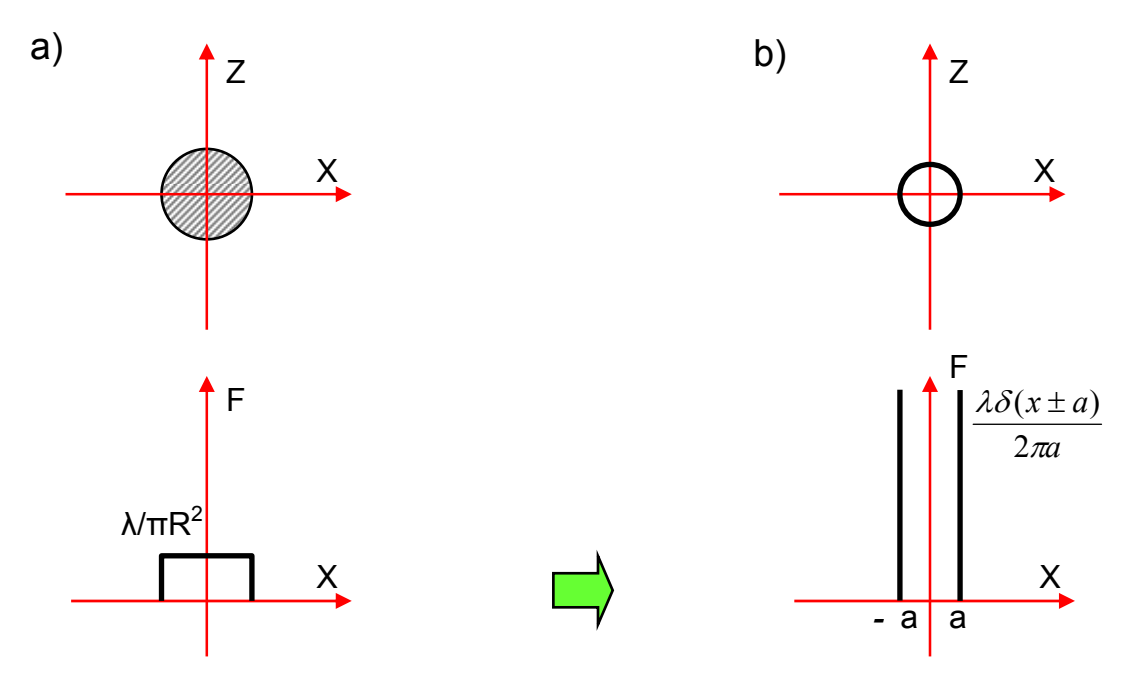


Figure 9. 18. The force distributions. Distribution of the force can be approximated with homogeneous distribution in the cylinder a). Next approximation is a delta function on cylinder radius of a b).

The original solution for $u_i(x,y,z)$ in [134] still can be simplified with relations (1.22) because the force $F_x(x,y,z)$ is distributed on cylinder with small size: 0 < z < a, 0 < x < a, where size a is too small in comparison with length of the steps L, $a/L \rightarrow 0$. With x component of the force $F_x(x,y,z)$ equations (1.22) takes the form:

$$\begin{split} u_{x}(x,y,z) &= \frac{1+\nu}{\pi Y} \frac{1}{r} \bigg[(1-\nu)F_{x} + \frac{\nu x}{r^{2}} (xF_{x} + yF_{y}) \bigg], \\ u_{y}(x,y,z) &= \frac{1+\nu}{\pi Y} \frac{1}{r} \bigg[(1-\nu)F_{y} + \frac{\nu y}{r^{2}} (xF_{x} + yF_{y}) \bigg], \\ u_{z}(x,y,z) &= \frac{1+\nu}{\pi Y} \frac{1}{r} \bigg[\frac{1-2\nu}{2r} (xF_{x} + yF_{y}) \bigg] \end{split}$$



$$\begin{split} u_x(x,y,z) &= \frac{1+\nu}{\pi Y} \frac{1}{r} \left[(1-\nu)F_x + \frac{\nu x}{r^2} x F_x \right], \\ u_y(x,y,z) &= \frac{1+\nu}{\pi Y} \frac{1}{r} \left[\frac{\nu y}{r^2} x F_x \right], \\ u_z(x,y,z) &= \frac{1+\nu}{\pi Y} \frac{1}{r} \left[\frac{1-2\nu}{2r} x F_x \right] \end{split}$$

The force with only x component is present, then for calculation of the energy (1.20) only x component of the displacement field is needed. After integration of $u_x(x, y, z)$ (1.22) with the

force
$$F_x(x, y) = \frac{\lambda}{2\pi a} \delta(\sqrt{z^2 + x^2} - a)$$
 we obtain:



$$u_{x}(x,y,z) = \frac{1-v^{2}}{\pi Y} \int_{0}^{L} \iint \frac{\lambda}{2\pi a} \delta(\sqrt{z_{1}^{2} + x_{1}^{2}} - a) \frac{1}{\sqrt{(x-x_{1})^{2} + (z-z_{1})^{2} + (y-y_{1})^{2}}} dx_{1} dz_{1} dy_{1} + \frac{1+v}{\pi Y} \int_{0}^{L} \iint \frac{\lambda}{2\pi a} \delta(\sqrt{z_{1}^{2} + x_{1}^{2}} - a) \frac{v(x-x_{1})^{2}}{\left((x-x_{1})^{2} + (z-z_{1})^{2} + (y-y_{1})^{2}\right)^{\frac{3}{2}}} dx_{1} dz_{1} dy_{1}$$

To calculate the energy (1.27) the displacement field at the surface, i.e. at z = 0 is required. After transition to the integration in polar coordinates $x_I = acos\alpha$, $z_I = asin\alpha$ the displacement field takes the form:



$$u_{x}(x,y,0) = \frac{1-v^{2}}{\pi Y} \int_{0}^{L} \int_{0}^{2\pi} \frac{\lambda}{2\pi a} \frac{1}{\sqrt{(x-a\cos\alpha)^{2} + a\sin^{2}\alpha + (y-y_{1})^{2}}} \cdot a \cdot d\alpha \cdot dy_{1} + \frac{1+v}{\pi Y} \int_{0}^{L} \int_{0}^{2\pi} \frac{\lambda}{2\pi a} \frac{v(x-a\cos\alpha)^{2}}{((x-a\cos\alpha)^{2} + a\sin^{2}\alpha + (y-y_{1})^{2})^{\frac{3}{2}}} \cdot a \cdot d\alpha \cdot dy_{1} = \frac{1-v^{2}}{\pi Y} \int_{0}^{L^{2}\pi} \frac{\lambda}{2\pi} \frac{1}{\sqrt{x^{2} + a^{2} - 2xa\cos\alpha + (y-y_{1})^{2}}} \cdot d\alpha \cdot dy_{1} + \frac{1+v}{\pi Y} \int_{0}^{L^{2}\pi} \frac{\lambda}{2\pi} \frac{v(x-a\cos\alpha)^{2}}{(x^{2} + a^{2} - 2xa\cos\alpha + (y-y_{1})^{2})^{\frac{3}{2}}} \cdot d\alpha \cdot dy_{1} + \frac{1+v}{\pi Y} \int_{0}^{L^{2}\pi} \frac{\lambda}{2\pi} \frac{1}{\sqrt{x^{2} + a^{2} - 2xa\cos\alpha + (y-y_{1})^{2}}} \cdot d\alpha \cdot dy_{1} + \frac{1+v}{\pi Y} \int_{0}^{L^{2}\pi} \frac{\lambda}{2\pi} \frac{v(x-a\cos\alpha)^{2}}{(x^{2} + a^{2} - 2xa\cos\alpha + (y-y_{1})^{2})^{\frac{3}{2}}} \cdot d\alpha \cdot dy_{1}$$

$$(1.28)$$

For the force applied at x = 0 the integral (1. 28) will be simplified to:

$$\begin{split} u_{x}(0,y) &= \frac{1-v^{2}}{\pi Y} \int_{0}^{L^{2}\pi} \frac{\lambda}{2\pi} \frac{1}{\sqrt{a^{2}+(y-y_{1})^{2}}} \cdot d\alpha \cdot dy_{1} + \\ &+ \frac{1+v}{\pi Y} \int_{0}^{L^{2}\pi} \frac{\lambda}{2\pi} \frac{v \cdot a^{2} \cos^{2}\alpha}{\left(a^{2}+(y-y_{1})^{2}\right)^{\frac{3}{2}}} \cdot d\alpha \cdot dy_{1} = \\ &= \frac{1-v^{2}}{\pi Y} \lambda \int_{0}^{L} \frac{1}{\sqrt{a^{2}+(y-y_{1})^{2}}} \cdot dy_{1} + \frac{1+v}{\pi Y} \frac{\lambda}{2} \int_{0}^{L} \frac{v \cdot a^{2}}{\left(a^{2}+(y-y_{1})^{2}\right)^{\frac{3}{2}}} \cdot dy_{1} \end{split}$$

Finally at x = 0 we have:

$$u_{x}(0,y) = \underbrace{\frac{1-v^{2}}{\pi Y} \lambda \int_{0}^{L} \frac{1}{\sqrt{a^{2} + (y-y_{1})^{2}}} \cdot dy_{1} + \underbrace{\frac{1+v}{\pi Y} \frac{\lambda}{2} \int_{0}^{L} \frac{v \cdot a^{2}}{\left(a^{2} + (y-y_{1})^{2}\right)^{\frac{3}{2}}} \cdot dy_{1}}_{I_{2}}.$$

$$(1.29)$$

The second part I_2 of the relation is less than the first I_1 . The maximal value of I_2/I_1 relation can be estimated:

$$\frac{I_{2}}{I_{1}} = \frac{\frac{1+\nu}{\pi Y} \frac{\lambda}{2} \int_{0}^{L} \frac{\nu \cdot a^{2}}{\left(a^{2}+(y-y_{1})^{2}\right)^{\frac{3}{2}}} \cdot dy_{1}}{\frac{1-\nu^{2}}{\pi Y} \lambda \int_{0}^{L} \frac{1}{\sqrt{a^{2}+(y-y_{1})^{2}}} \cdot dy_{1}} = \frac{\lambda \nu}{2(1-\nu)} \frac{a^{2}}{L^{2}} \cdot \frac{\int_{0}^{1} \frac{1}{\left(\frac{a^{2}}{L^{2}}+(t-t_{1})^{2}\right)^{\frac{3}{2}}} \cdot dt_{1}}{\int_{0}^{1} \frac{1}{\sqrt{\frac{a^{2}}{L^{2}}+(t-t_{1})^{2}}} \cdot dt_{1}} = [L \to \infty] = \frac{\lambda \nu}{\sqrt{\frac{a^{2}}{L^{2}}+(t-t_{1})^{2}}} \cdot dt_{1}$$

$$= \frac{\lambda \nu}{2(1-\nu)} \frac{a^2}{L^2} \cdot \frac{\int_0^1 \frac{1}{(t-t_1)^3} \cdot dt_1}{\int_0^1 \frac{1}{(t-t_1)} \cdot dt_1} = \frac{\lambda \nu}{2(1-\nu)} \frac{a^2}{L^2} \cdot \frac{\frac{1-2t}{t^2(1-t)^2}}{\ln \left| \frac{1-t}{t} \right|}$$

$$\frac{I_2}{I_1} = \frac{v}{2(1-v)} \frac{a^2}{L^2} \cdot \frac{\frac{1-2t}{t^2(1-t)^2}}{\ln \left| \frac{1-t}{t} \right|}, \text{ where } t = y/L$$

The upper relation $\frac{1-2t}{t^2(1-t)^2} \to \infty$ at $t \to 0$, at $t \to 1$ and equal to 0 at t = 0.5, for the lower relation $\ln \left| \frac{1-t}{t} \right|$ the same limit points are present $t \to 0$, $t \to 1$ and t = 0.5.

$$Lim_{t\to 0} \left(\frac{\frac{1-2t}{t^2(1-t)^2}}{\ln\left|\frac{1-t}{t}\right|} \right) \to \frac{1}{t^2}, \frac{1}{(1-t)^2},$$

$$Lim_{t\to 0.5} \left(\frac{\frac{1-2t}{t^2(1-t)^2}}{\ln \left| \frac{1-t}{t} \right|} \right) = 8.$$

Then we can estimate the relation I_2/I_1 at limit points $t = y/L \rightarrow 0$ and t = 0.5:

$$Lim_{t\to 0} \frac{I_2}{I_1} = \frac{v}{2(1-v)} \frac{a^2}{L^2} \cdot \frac{L^2}{y^2} = 0.18 \cdot \frac{a^2}{y^2},$$

$$Lim_{t\to 1} \frac{I_2}{I_1} = \frac{v}{2(1-v)} \frac{a^2}{L^2} \cdot \frac{L^2}{(L-v)^2} = 0.18 \cdot \frac{a^2}{(L-v)^2},$$

$$Lim_{t\to 0.5} \frac{I_2}{I_1} = \frac{v}{2(1-v)} \frac{a^2}{L^2} \cdot 8 = 1.4 \frac{a^2}{L^2} \to 0$$
, because of $\frac{a^2}{L^2} \to 0$.

At (L-2a) > y > 2a we can neglect by I_2 which has the value less than 5% of the value I_1 , then $u_x(a, y)$ can be simplified to:

$$u_{x}(0,y) = \frac{1-v^{2}}{\pi Y} \lambda \int_{0}^{L} \frac{1}{\sqrt{a^{2} + (y-y_{1})^{2}}} dy_{1},$$
(1.30)

The displacement field (1. 38) at big distances x >> a can be approached with:

$$u_{x}(x,y) = \underbrace{\frac{1-v^{2}}{\pi Y} \lambda \int_{0}^{L} \frac{1}{\sqrt{x^{2} + (y-y_{1})^{2}}} \cdot dy_{1} + \underbrace{\frac{1+v}{\pi Y} \lambda \int_{0}^{L} \frac{vx^{2}}{\left(x^{2} + (y-y_{1})^{2}\right)^{\frac{3}{2}}} \cdot dy_{1}}_{I_{2}},$$

$$(1.31)$$

Relation (1. 41) for $u_x(x, y)$ at x = a is equal to relation (1. 29). At $x/L \to 0$, and at (L-2x) > y > 2x integral I_2 has the value less than 5% of the value I_1 and can be neglected. The relations for $u_y(x, y)$ and $u_z(x, y)$ can be simplified at $x/L \to 0$:

$$u_{y}(x,y) = \frac{1+\nu}{\pi Y} \lambda \int_{0}^{L} \frac{\nu(y-y_{1})x}{\left(x^{2}+(y-y_{1})^{2}\right)^{\frac{3}{2}}} dy_{1} = \left[t_{1} = \frac{y_{1}}{L}, t = \frac{y}{L}\right] = \frac{1+\nu}{\pi Y} \lambda \frac{x}{L} \int_{0}^{1} \frac{\nu(t-t_{1})}{\left(\frac{x}{L^{2}}^{2}+(t-t_{1})^{2}\right)^{\frac{3}{2}}} dt_{1} \to 0$$

$$u_{z}(x,y) = \frac{1+\nu}{2\pi Y} \lambda \int_{0}^{L} \frac{(1-2\nu)x}{x^{2} + (y-y_{1})^{2}} \cdot dy_{1} = \left[t_{1} = \frac{y_{1}}{L}, t = \frac{y}{L}\right] =$$

$$= \frac{1+\nu}{2\pi Y} \lambda \frac{x}{L} \int_{0}^{L} \frac{(1-2\nu)}{\frac{x^{2}}{L^{2}} + (t-t_{1})^{2}} \cdot dt_{1} \to 0$$

Finally relation (1. 31) for $u_x(a, y)$ can be written as:

$$u_{x}(x,y) = \frac{1-v^{2}}{\pi Y} \lambda \int_{0}^{L} \frac{1}{\sqrt{x^{2} + (y-y_{1})^{2}}} dy_{1},$$
 (1.32)

where $x \ge a$. Solution of (1.30) is (see Appendix C):

$$u_{x}(x,y) = -2\frac{1-v^{2}}{\pi Y}\lambda \ln \left| \frac{\sqrt{x^{2} + (y-L)^{2}} + (y-L)}{\sqrt{x^{2} + y^{2}} + y} \right|.$$
(1.33)

This relation works at $x \ge a$. At x < a equation (1.30) can be used. Solution of (1.30) is relation (1.33) at x = a:

$$u_{x}(0,y) = -2\frac{1-v^{2}}{\pi Y}\lambda \ln \left| \frac{\sqrt{a^{2} + (y-L)^{2}} + (y-L)}{\sqrt{a^{2} + y^{2}} + y} \right|,$$
(1. 34)

Figure 9. 19 shows an example of distribution of displacement field for x component induced by the force with radius localization of a along the step segment length of L at x = 0. The dependence was calculated for relation L/a = 100.

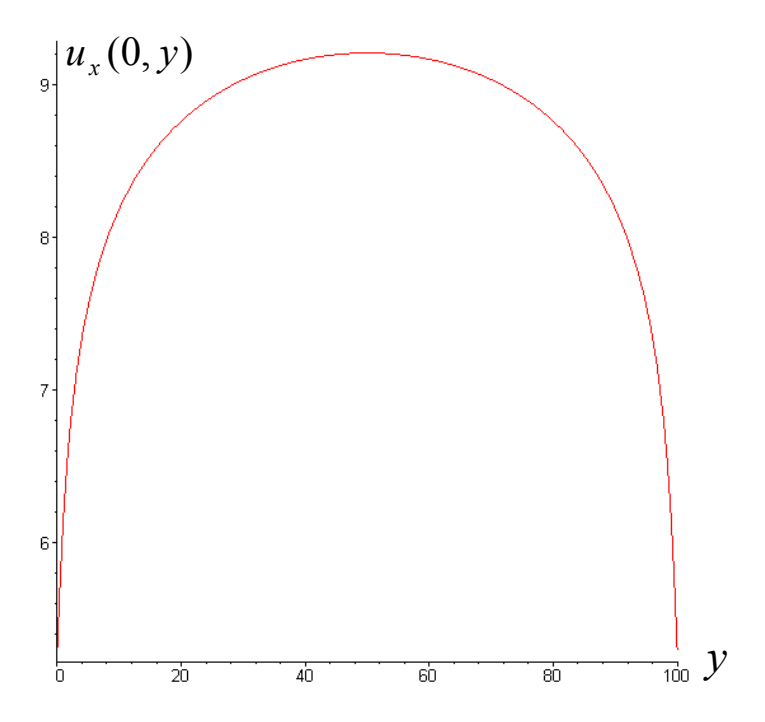


Figure 9. 19. The displacement field $u_x(0, y)$ as a function of distance y along the step segment has a maximum at the middle of the straight step segment y = L/2. The size of localization of the force was taken a = 1 and length of step segment L = 100.

To calculate relaxation energy we take displacement field (induced by the force $F_x(x,y) = \frac{\lambda}{2\pi a} \delta(\sqrt{z^2 + x^2} - a)$) (1. 34) and integrate this displacement field with the force of the same power λ , $\lambda(x,y,z) = \lambda \delta(x)\delta(z)$, then (1.27) takes the form:

$$E_{el} = \frac{1}{2} \frac{1 - v^2}{\pi Y} \lambda^2 \int_0^L \ln \left| \frac{\sqrt{a^2 + (y - L)^2} + (y - L)}{\sqrt{a^2 + y^2} + y} \right| dy.$$
 (1.35)

Integration of (1.35) by parts gives the next relation:

$$\int \ln(f(y))dy = y\ln(f(y)) - \int \frac{yf'(y)}{f(y)}dy.$$
(1.36)

Integral type of $\int \frac{yf'(y)}{f(y)} dy$, where function f(y) is $f(y) = \sqrt{1 + y^2} + y$, can be computed as the following:

$$\int \frac{xf'(y)}{f(y)} dy = \int \frac{y\left(1 + \frac{y}{\sqrt{1 + y^2}}\right)}{y + \sqrt{1 + y^2}} dy = \int \frac{y}{\sqrt{1 + y^2}} dy = \left[y = \tan \alpha\right] =$$

$$= \int \frac{\sin \alpha}{\cos^2 \alpha} d\alpha = \frac{1}{\cos \alpha} = \sqrt{1 + y^2}$$
(1.37)

After transformation of integral (1.35) into appropriate form and after calculations (see Appendix D) we obtain:

$$E_{el} = \frac{1}{2} \frac{1 - v^2}{\pi Y} \lambda^2 \int_0^L \ln \left| \frac{\sqrt{a^2 + (y - L)^2} + (y - L)}{\sqrt{a^2 + y^2} + y} \right| dy =$$

$$= -\lambda^2 \frac{1 - v^2}{\pi Y} L \left(\ln \left| \frac{1 + \sqrt{1 + \left(\frac{a}{L}\right)^2}}{\frac{a}{L}} \right| - \left(\sqrt{1 + \left(\frac{a}{L}\right)^2} - \frac{a}{L}\right) \right).$$
(1.38)

This expression can be simplified at $\frac{a}{L} \rightarrow 0$, then the relaxation energy per unit length is:

$$\frac{E_{el}}{L} = \left[\frac{a}{L} \to 0\right] = -\lambda^2 \frac{1 - v^2}{\pi Y} (\ln \frac{2L}{a} - 1). \tag{1.39}$$

This equation is valid for the situation of a single step, as shown in **Figure 9. 17 (b)**. The same solution for relaxation energy E_{el} was found in [134], also see Appendix E.

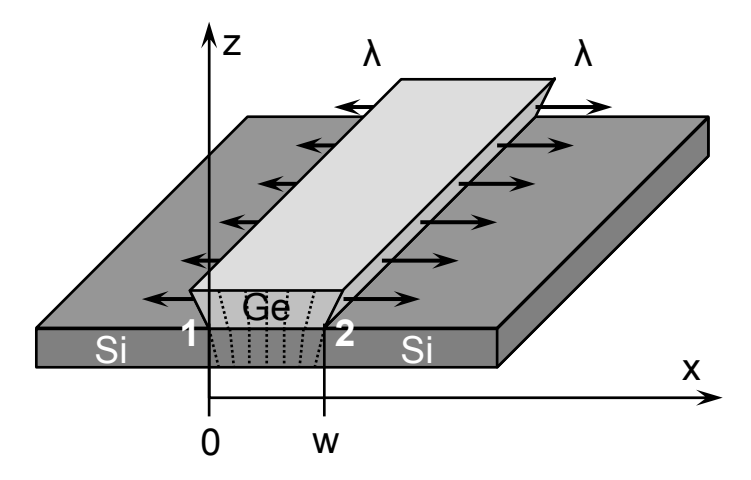


Figure 9. 20. Ge stripe width of w and length of L, L >> w.

In the case of a Ge stripe **Figure 9. 20** the interaction of displacement fields between parallel steps (**Figure 9. 20**) will be taken into account. Superposition method allows to sum the displacement fields from both sides of the Ge stripe. To calculate energy of the stripe the displacement fields at steps 1 and 2 will be calculated. The displacement field $u_x(x)$ at step 1 (x = 0) is sum of the displacement fields of (1.33), displacement field induced with step 1 u_x^1 plus field induced with step 2 u_x^2 :

$$u_x(0) = u_x^1(0, y) + u_x^2(0, y). (1.40)$$

The same algorithm for the displacement field $u_x(w)$ at step 2:

$$u_{x}(w) = u_{x}^{1}(w, y) + u_{x}^{2}(w, y), \qquad (1.41)$$

where $u_x^{1,2}(-x,y) = u_x^{1,2}(x,y)$ and $u_x^1(x,y) = -u_x^2(x+w,y) = u_x(x,y)$. We assume that amplitude of the λ force does not depend on width of the stripe. Then substitution of (1. 40) and (1. 41) into (1.27) gives the energies for steps 1 and 2 which depend on stripe width w:

$$E_{el}^{1}(w) = -\frac{1}{2}(-\lambda)\int (u_{x}^{1}(a, y) + u_{x}^{2}(a, y))dy,$$

$$E_{el}^{2}(w) = -\frac{1}{2}\lambda \int (u_{x}^{1}(w, y) + u_{x}^{2}(w, y))dy,$$

The energy of stripe is sum $E_{el}^1 + E_{el}^2$:

$$E_{el}^{stripe}(w) = \frac{1}{2} \lambda \int (u_x^1(a, y) + u_x^2(a, y)) dy - \frac{1}{2} \lambda \int (u_x^1(w, y) + u_x^2(w, y)) dy,$$

after transposition we obtain:

$$\begin{split} E_{el}^{stripe}(x) &= -\frac{1}{2}\lambda \int \left(-u_x^1(w, y) + u_x^2(a, y) \right) dy - \frac{1}{2}\lambda \int \left(u_x^1(a, y) - u_x^2(w, y) \right) dy = \\ &= \lambda \int u_x(w, y) dy - \lambda \int u_x(a, y) dy \end{split}$$

here the first integral $\lambda \int u_x(x,y)dy$ - is an interaction energy $\frac{E_i(x)}{L}$. Width of the stripe is

much less than length $\frac{w}{L}$ << 1 (**Figure 9. 20**), therefore the relation (1.39) can be used. Then interaction energy takes the form:

$$\frac{E_i(w)}{L} = 2\lambda^2 \frac{1 - v^2}{\pi Y} (\ln \frac{2L}{w} - 1), \tag{1.42}$$

To write relation for $\frac{E_i(w)}{L}$ we put a = w in (1.39). Then the energy of relaxation $\frac{E_{el}^{stripe}(w)}{L}$ at edges of free standing Ge stripe width of w is:

$$\frac{E_{el}^{stripe}(w)}{L} = 2\lambda^{2} \frac{1-v^{2}}{\pi Y} (\ln \frac{2L}{w} - 1) - 2\lambda^{2} \frac{1-v^{2}}{\pi Y} (\ln \frac{2L}{a} - 1) =
= -2\lambda^{2} \frac{1-v^{2}}{\pi Y} \ln \frac{w}{a}$$
(1.43)

The relaxation energy per unit length does not depend on length of stripe at $L \gg w$. Similar logarithmic dependence on width for the striped structure was found in [157].

To calculate elastic energy of round pits of radius R the approximation with rectangular shape (61) in [134] will be used. After replacement of s and t in the (61) by 2R the elastic energy takes the form:

$$E_{el}^{sq} = 8R \frac{1+\nu}{\pi Y} \lambda^{2} - 8R \frac{1-\nu^{2}}{\pi Y} \lambda^{2} \left(\sqrt{2} + \ln \frac{2R}{a} - \frac{1}{2} \ln \frac{\sqrt{2}+1}{\sqrt{2}-1} \right) \approx$$

$$\approx 8R \frac{1+\nu}{\pi Y} \lambda^{2} \left(1 - (1-\nu) \left(0.533 + \ln \frac{2R}{a} \right) \right)$$
(1.44)

Non symmetric case with Ge stripe attached to the Si step is shown in **Figure 9. 21 (a)**. The relaxation energy of the stripe with open Ge step edge at one side and with Si/Ge interface at another side **Figure 9. 21 (a)** will be different from (**1.43**). An additional force induced by one Si layer (from left) reduces displacement field at Si/Ge interface **Figure 9. 21 (a)**. The same value of the force is induced by $\frac{1}{2}a$ of the Si layer **Figure 9. 21 (b)**. To take into account the additional force radius of the force **Figure 9. 18 (b)** equal to $1 + \frac{1}{2} = \frac{3}{2}a$ will be used.

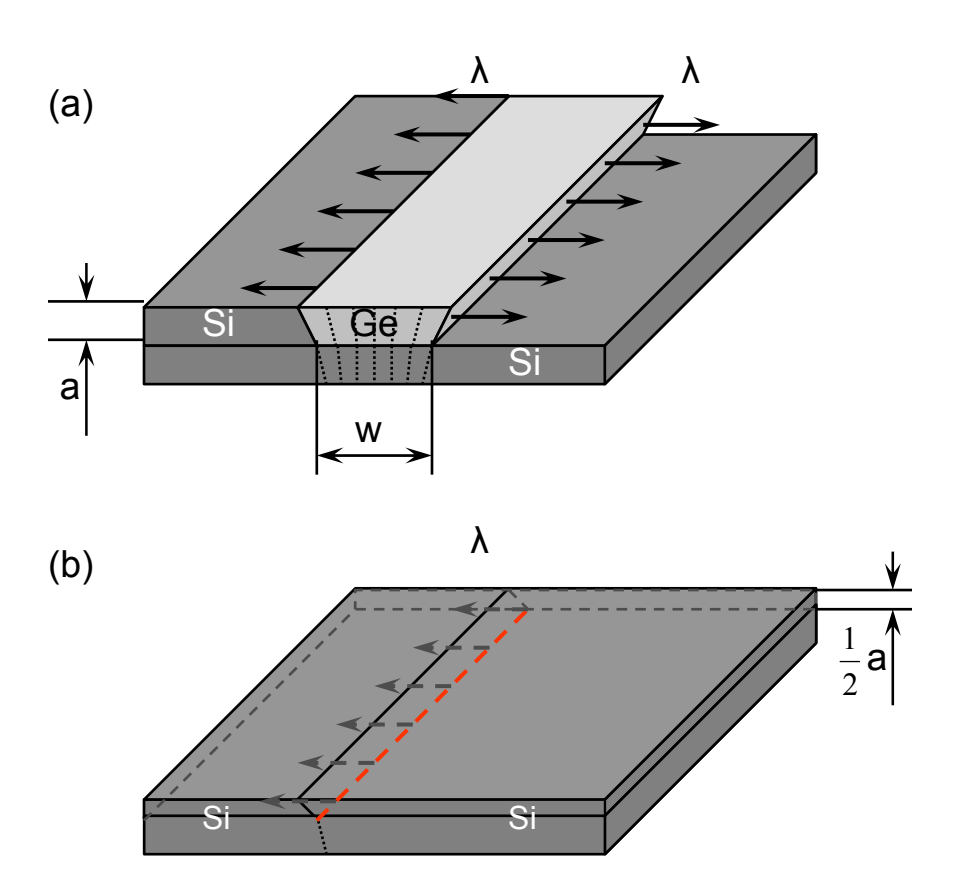


Figure 9. 21. Ge stripe width of w and length of L >> w (a). Ge stripe borders with Si from left and has open step edge at right side (a), the additional force induced by Si layer from left side can be approximated with the force induced by $\frac{1}{2}$ of the surface layer (b).

Interaction energy for Ge stripe with Si/Ge interface at both sides can be written as:

$$\frac{E_i}{L} = 2\lambda^2 \frac{1 - v^2}{\pi Y} \left(\ln \frac{2L}{w + \frac{1}{2}a} - 1 \right),$$

resulting relaxation energy at the edges for the Ge stripe with Si/Ge interfaces is:

$$\frac{E_{el}^{stripe}}{L} = 2\lambda^{2} \frac{1 - v^{2}}{\pi Y} \left(\ln \frac{2L}{w + \frac{1}{2}a} - 1 \right) - 2\lambda^{2} \frac{1 - v^{2}}{\pi Y} \left(\ln \frac{2L}{\frac{3}{2}a} - 1 \right) =$$

$$= -2\lambda^{2} \frac{1 - v^{2}}{\pi Y} \ln \frac{w + \frac{1}{2}a}{\frac{3}{2}a}$$
(1. 45)

These calculations were made with the same algorithm as for relation (1.43). Relaxation energy for non symmetry case (Figure 9. 21 (a)) is average of the energies for free standing Ge stripe (1.43) and for Ge stripe with Si/Ge interfaces (1.45):

$$\frac{E_{el}^{stripe}}{L} = -\lambda^2 \frac{1 - v^2}{\pi Y} \ln \left(\frac{w \left(w + \frac{1}{2} a \right)}{\frac{3}{2} a^2} \right) \approx -2\lambda^2 \frac{1 - v^2}{\pi Y} \ln \left(\sqrt{\frac{2}{3}} \frac{w}{a} \right). \tag{1.46}$$

Relation (1.46) will be used for Ge stripes and relation (1.44) will be used for round pits in Ge layer. Equations and numbers for the step energy $\bar{\gamma}$ are placed in **Table 3**:

Table 3

Step energy formation on Si(111) surface from Table 2	$\gamma_0 = 0.0356, \ eV / \stackrel{\circ}{A}$	
Young's modulus for Si ((111) – plane) from [25]	$Y = 16.9 \times 10^{10}$, N/m ²	
Poisson's ratio for Si ((111) – plane) from [25]	v = 0.262	
The force per unit length along the boundary of magnitude λ from (1.21)	$\lambda = x \times 2.32$, N/m	
Energy of relaxation per unit length of pits radius R from (1.44)	$\frac{E_{el}^{2R}}{8R} = 0.0048 - 0.0061 \ln \frac{2R}{a}, \ eV/A$	
Energy of relaxation per unit length of Si/Ge stripe width of <i>w</i> from (1.46)	$\frac{E_{el}^{stripe}}{L} = \left(-0.012 \ln 0.8 \frac{w}{a}\right) x^2, \ eV/A$	

The expression for the step energy of round pit (1.19) can be written as sum of the step energy formation and relaxation energy at the step edges (**Table 3**):

$$U = 2\pi R \left(\gamma_0 + \frac{E_{el}^{2R}}{8R} \right) = 2\pi R \left(0.0356 + 0.0048 - 0.0061 \ln \frac{2R}{a} \right) = 0.0061 \left(6.62 - \ln \frac{2R}{a} \right) 2\pi R$$

$$(1.47)$$

Pit formation is followed with formation of Ge (GeSi) stripe at outer Si steps. The sum energy of the pit's steps (1.44) plus relaxation energy in Ge stripe (1.46) at outer step edges can be written as:

$$U = 0.0061 \left(6.62 - \ln \frac{2R}{a} \right) 2\pi R - \left(0.012 \ln 0.8 \frac{w}{a} \right) x^2 L, \text{ eV}$$
[pit's step energy] | relax. energy at outer steps]

The sum energy gain (1.48) can achieve a negative value by means of relaxation energy at pit's steps and outer step edges. Formation of the pit's steps can be energetically favorable because the relaxation energy at the step edges can be larger than step formation energy (γ_{θ} =

0.0356, eV/A). Figure 9. 22 shows energies for the pit's step and for the relaxation energy at outer steps. Relaxation energy per Ge atom at outer step edge (1.46) was divided by number of Ge atoms per unit length of Ge stripe width of w, the energy dependence is shown as a function of width w in Figure 9. 22 (a). The relaxation energy achieves a maximal value about -7 meV/atom at width of Ge outer stripe about 1 nm Figure 9. 22 (a). The maximal

value of pit's step energy gain ($\gamma_{\theta} = 0.0356$, eV/A) is about -0.025 meV/atom at pit radius of 300 nm **Figure 9. 22 (b)**. Negative value of the pit's step energy is achieved at pits radius of 100 nm. Experimentally observed pits have a radius about $1 \div 15$ nm. The sum energy gain with relaxation at outer steps can provide pit radius much lower than 100 nm. The Si/GeSi outer stripe **Figure 9. 23** is very important since it gives the space for reduction of displacement field from original Ge stripe. The space between original Ge stripe and outer Ge stripe reduces interaction energy and increases negative energy gain.

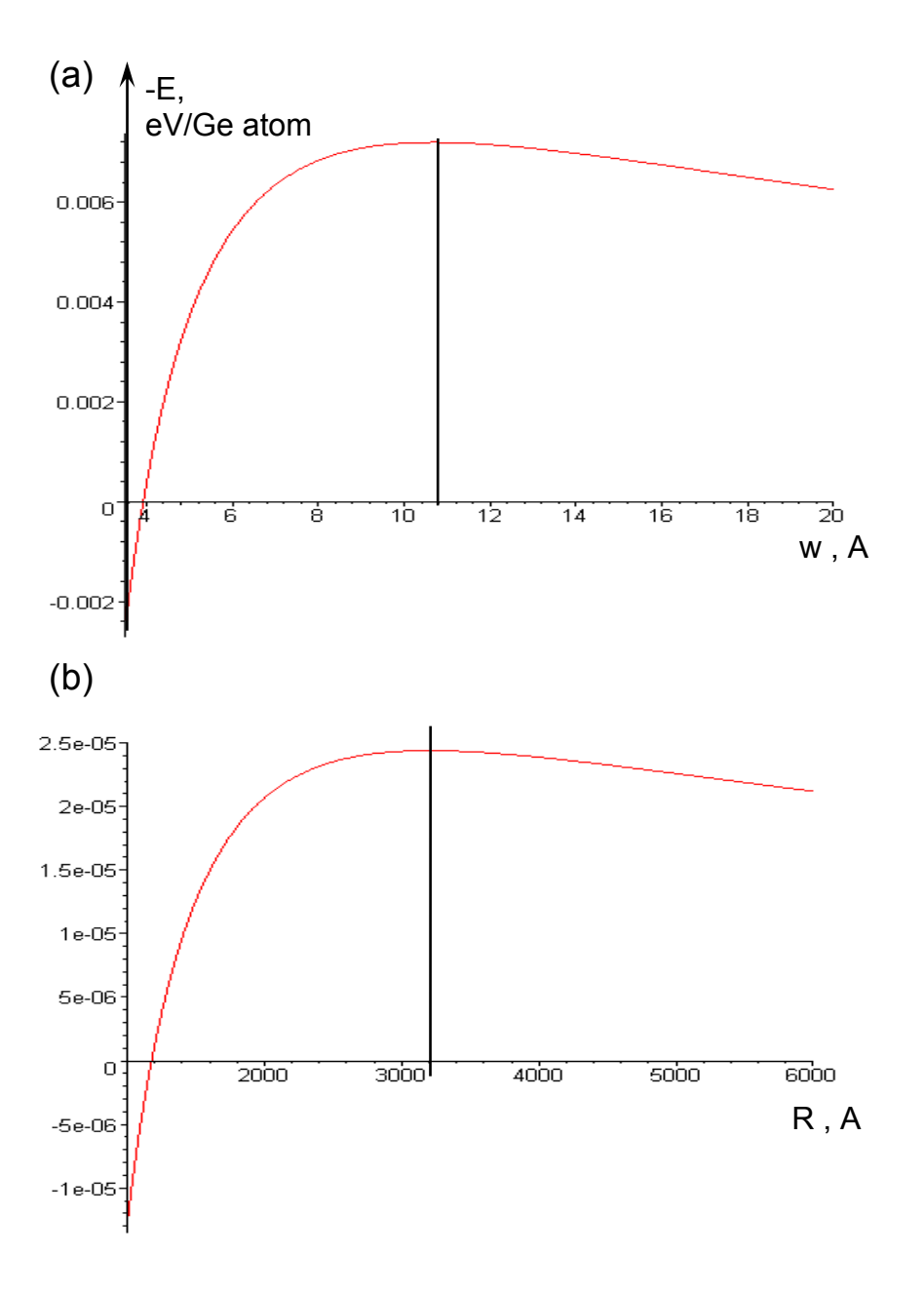


Figure 9. 22. (a) relaxation energy in Ge stripe per Ge atom moved away from the pits to the outside Ge stripe width of w, (b) pit step energy per Ge atom moved away from the pits radius of R.

Relaxation energy at outer sink steps (right part of the expression (1.48)) is proportional to the length L of the outer steps. Length L can be increased with Si/Ge coverage, density of Si/Ge islands and adatom diffusion length on the surface. Si/Ge deposition at low temperature gives high density of Si/Ge islands. The following pit formation can be enhanced with increase of temperature. High density of Ge islands and larger diffusion length at higher temperature should enhance the pit formation and decrease the minimal radius of the pits. The pits should also form more effectively in broad Ge layers since broad layer is less relaxed (1.46).

To calculate the relaxation energy for the system shown in **Figure 9. 23** the displacement fields from every border must be taken into account. The important alternative case is shown on **Figure 9. 24**. Final state **Figure 9. 24** (b) is created by removing Ge stripe width of w from the centre of the preexisting Ge layer width of w_{Ge} **Figure 9. 24** (a). Minimal radius of the pits can be taken equal to the minimal size w for geometry in **Figure 9. 24** (b). Energy gain between final **Figure 9. 24** (b) and initial **Figure 9. 24** (a) states can be written as:

$$\frac{E_{elastic}^{f-i}}{L} = -2\lambda^2 \frac{1-\nu^2}{\pi Y} \left(\ln \frac{w_{Ge1}}{a} + \ln \frac{w_{Ge2}}{a} + x^2 \ln \frac{w_{Ge3}}{a \cdot x} - \ln \frac{w_{Ge1} + w_{Ge2} + w_{Ge3}}{a} + \ln \left(f(w, w_{Si}, w_{Ge1}, w_{Ge2}, w_{Ge3}) \right) \right), \tag{1.49}$$

where function $f(w, w_{Si}, w_{Ge1}, w_{Ge2}, w_{Ge3})$ contains result of combinations of the displacement fields from every border (**Figure 9. 24 (b)**)

$$f(w, w_{Si}, w_{Ge1}, w_{Ge2}, w_{Ge3}) = (1.50)$$

$$\frac{w \cdot w_{Si} \cdot w_{Ge}^{i}(w_{Ge1} + w_{Ge2} + w_{Ge3} + w + w_{Si})(w + w_{Si} + w_{Ge2})(w_{Si} + w_{Ge2} + w_{Ge3})}{(w + w_{Ge1})(w + w_{Ge2})(w_{Si} + w_{Ge2})(w_{Si} + w_{Ge3})(w_{Ge1} + w_{Ge2} + w + w_{Si})(w_{Ge2} + w_{Ge3} + w + w_{Si})},$$

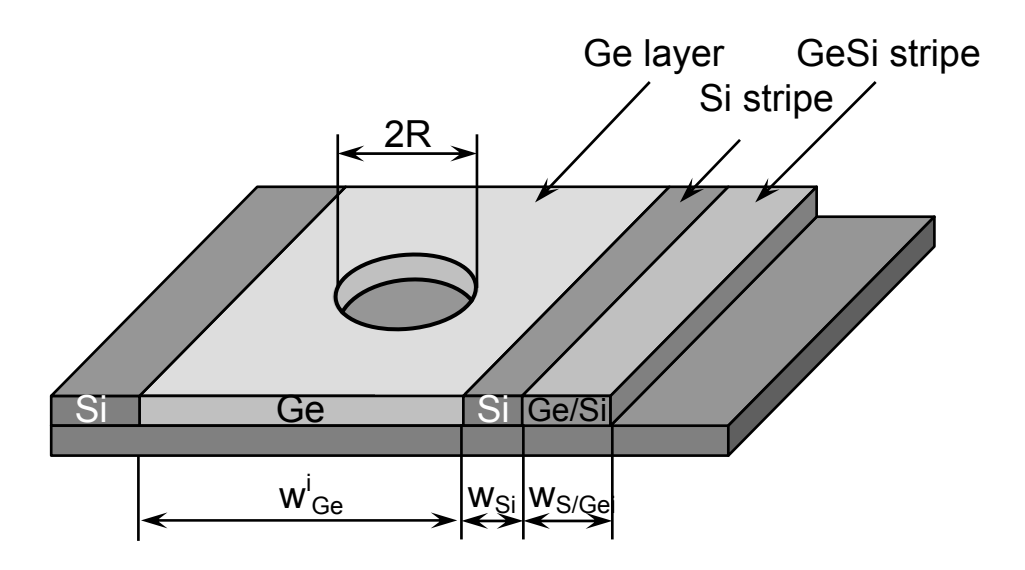


Figure 9. 23. Geometry of the system with pits.

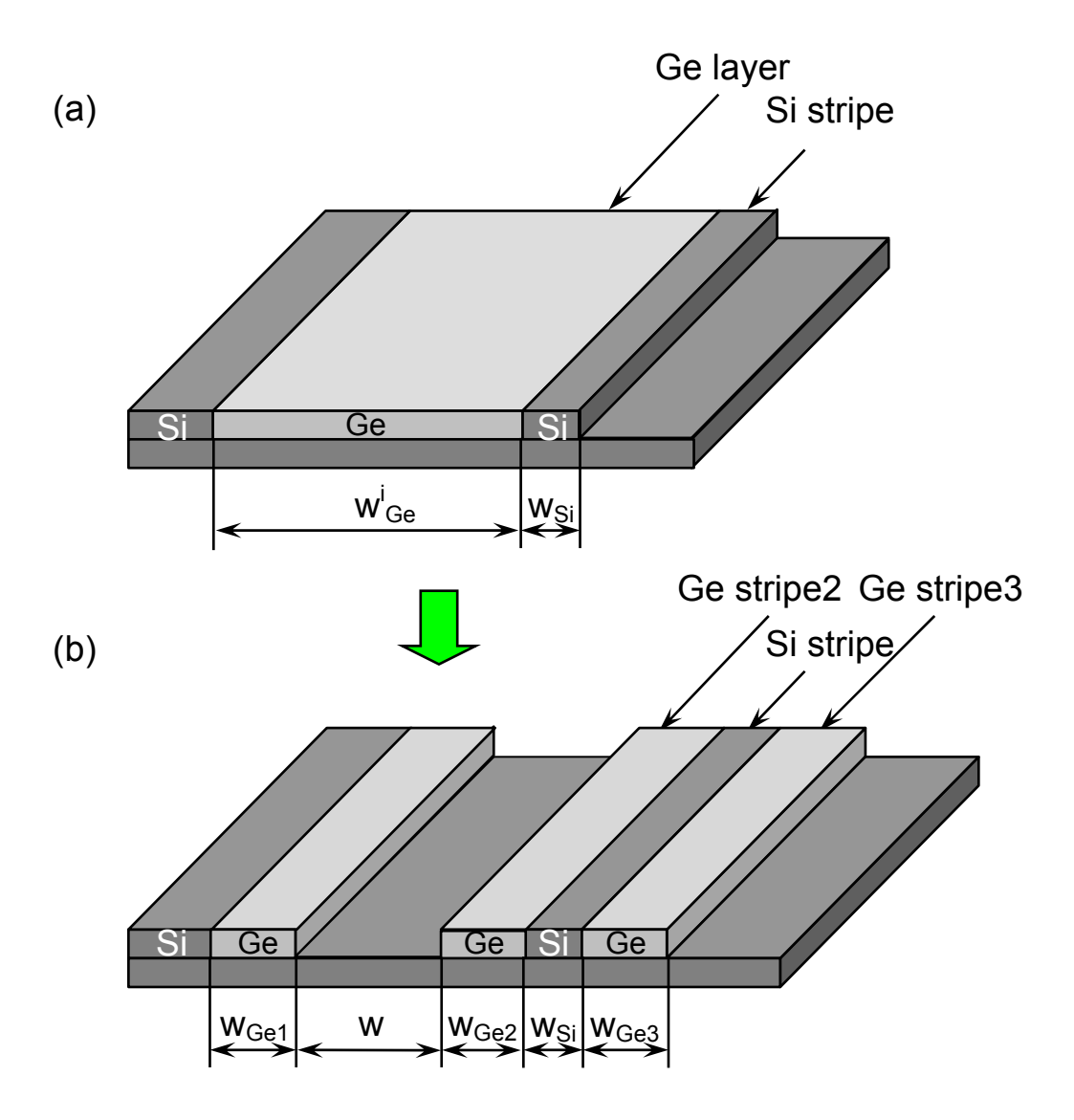


Figure 9. 24. The initial (a) and final (b) state for geometry with free standing Si/Ge stripe.

Maximal energy gain per unit length is achieved at $w \to \infty$, $w_{Si} \to \infty$. If $w_{Gel}/a \approx w_{Ge2}/a \approx$

$$w_{Ge3}/a$$
 are big numbers (>>10), then $\frac{E_{elastic}^{f-i}}{L} \approx -2\lambda^2 \frac{1-v^2}{\pi M} \left(2 \ln \frac{w_{Ge}^i}{a}\right)$. This approximation

shows that relaxation energy gain per unit length increases with width of preexisting Ge stripes and increase of Si stripe (spacer) between outer Ge stripe and preexisting Ge stripe.

3D dependence for the energy gain per atom of (1.49) is built in **Figure 9. 25** with the following approximations: $w_{Gel} = w_{Ge2} = w_{Ge3} = w = y$; $w_{Si} = t$. The relaxation energy achieves a maximum -8.4 meV/Ge atom at width of $y \sim 2$ nm.

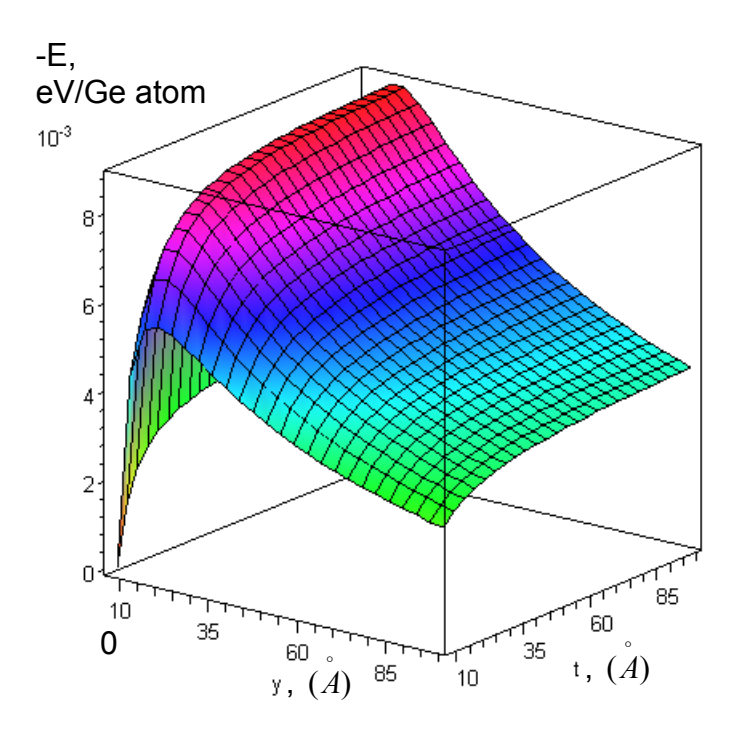


Figure 9. 25. The relaxation energy gain dependence (x = 1) per Ge atom for geometry shown in **Figure 9.** 24 with the following parameters: $w_{Ge1} = w_{Ge2} = w_{Ge3} = w = y$ and $w_{Si} = t$.

The total step energy gain of the model **Figure 9. 24** is shown in **Figure 9. 26**, the step energy formation was taken 0.036 eV/A (**Table 2**). The maximal value of total energy gain is about -0.5 meV/Ge atom (**Figure 9. 26**) at Ge concentration x = 1. This energy gain is achieved at width y larger than 20 nm. The energy gain becomes positive at $y_{min} > 15$ nm. It is smaller than 100 nm but still much higher than 1 nm. According to the data in **Figure 9. 26** the minimal width of the Ge stripe will be about $3 \times y_{min} = 45$ nm. The model with relaxation at outer step edges gives better agreement with experimental data, but the minimal size for the pit formation is still larger than minimal pit size observed in the experiments ~ 1 nm. Better agreement can be provided with the step energy formation lower than $0.036 \ eV/A$. At step free energy of $0.005 \ eV/A$ (T = 450°C) the maximal energy gain is equal -5.6 meV/Ge atom (**Figure 9. 25**) and minimal size of Ge stripe is ~ 3 nm. The step free energy of $0.005 \ eV/A$ ($\sim 0.02 \ eV/A \ total minimal size of Ge stripe is <math>\sim 3$ nm. The step free energy of $0.005 \ eV/A$ ($\sim 0.02 \ eV/A \ total minimal size of Ge stripe is <math>\sim 3$ nm. The step free energy of $0.005 \ eV/A \ total minimal size of Ge stripe is <math>\sim 3$ nm. The step free energy of $0.005 \ eV/A \ total minimal size of Ge stripe is <math>\sim 3$ nm. The step free energy of $0.005 \ eV/A \ total minimal size of Ge stripe is <math>\sim 3$ nm. The step free energy of $0.005 \ eV/A \ total minimal size of Ge stripe is <math>\sim 3$ nm. The step free energy of $0.005 \ eV/A \ total minimal size of Ge stripe is <math>\sim 3$ nm. The step free energy of $0.005 \ eV/A \ total minimal size of Ge stripe is <math>\sim 3$ nm. The step free energy of $0.005 \ eV/A \ total minimal size of Ge stripe is <math>\sim 3$ nm. The step free energy of $0.005 \ eV/A \ total minimal size of Ge stripe is <math>\sim 3$ nm. The step free energy of $0.005 \ eV/A \ total minimal size of Ge stripe is <math>\sim 3$ nm. The step free energy of $0.005 \ eV/A \ total minimal size of Ge str$

 $E_{elastic}^{f-i} = -(1-x)x \cdot 29 \text{ meV/Ge atom, where } x_{Si} = A_{Si}/(A_{Si} + A_{pit}).$

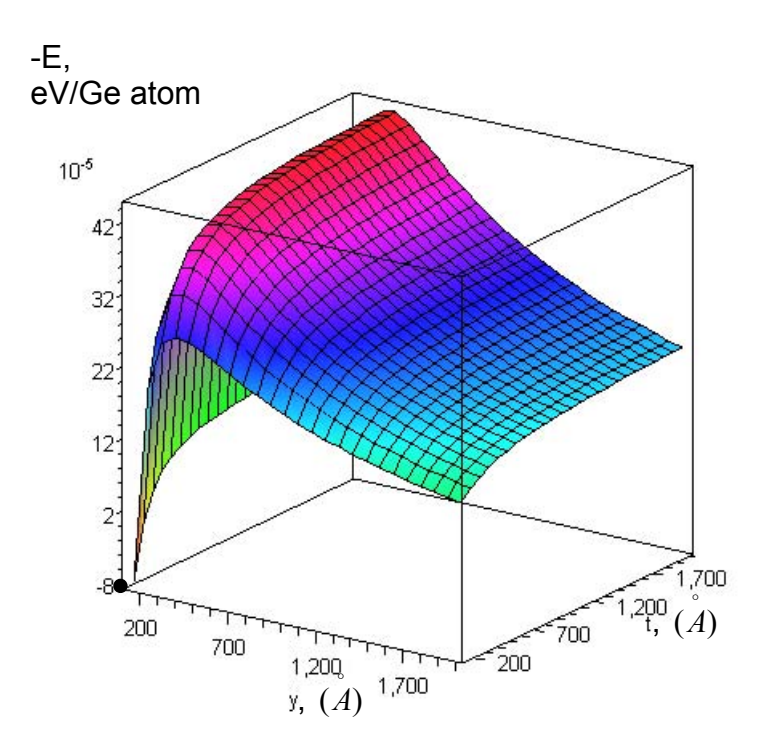


Figure 9. 26. Total step energy gain dependence (x = 1) per atom for geometry shown in **Figure 9. 24** with fixed parameters $w_{Ge1} = w_{Ge2} = w_{Ge3} = w = y$ and with $w_{Si} = t$. Energy of the step formation was taken 36 meV/A.

Maximal value of $E_{elastic}^{f-i}$ (at x=0.5) is 14.5 meV/Ge atom, this is much higher than the maximal total step energy gain (at x=0.5, $\gamma_{\theta}=0.005$ eV/ $\overset{\circ}{A}$) which is < 2 meV/Ge atom.

The mixing energies give the largest contribution for energy gain at x = 0.5. At x = 1 the mixing energy is zero while the step edge relaxation energy (1.48) gives the largest contribution which can achieve the value of 5 meV/atom.

• Gibbs free energy – collecting all energy terms

Irreversible processes are followed by a change of quantity of heat ΔQ which is lower than that change in equivalent of the entropy T ΔS . That can be written as:

$$\frac{dQ}{dt} \le T \frac{dS}{dt},$$

$$\frac{dE}{dt} + P \frac{dV}{dt} < T \frac{dS}{dt},$$
(1.51)

where E – internal energy, P – pressure, V – volume, T – temperature, and t - time. From (1.51) at T = const and P = const \rightarrow

$$\frac{d(E+PV-TS)}{dt} = \frac{dG}{dt} < 0, \tag{1.52}$$

I.e. during irreversible process at fixed T and P the Gibbs free energy is decreased, $G \rightarrow \min$. This general thermodynamics law for irreversible processes can be found in [158]. The Gibbs free energy can be found as

$$G = E - TS_{mix}, (1.53)$$

where E is complete internal energy and S_{mix} is entropy of mixing. Entropy of mixing of two components corresponds to the number of possibilities for an exchange of atoms A with atoms B is [25]:

$$S_{mix} = k_B \ln \left(\frac{N!}{(N_A! N_B!)} \right)$$

With Stirling's approximation for large numbers N>>1 one obtains

$$S_{mix} = -Nk_B T [x \ln(x) + (1-x) \ln(1-x)], \tag{1.54}$$

where $N = (A_{Si} + A_{pit}) \cdot 0.312 \cdot 10^{20} \frac{atom}{m^2}$, and $x = \frac{A_{pit}}{A_{pit} + A_{Si}}$. With the following approximation $\ln(1-x) \approx -x$, $\ln x \approx -(1-x)$, we obtain:

$$TS_{mix} = 2Nk_BT \cdot x(1-x), \qquad (1.55)$$

or

$$TS_{mix} = 2k_B T \cdot A_{Si} x \cdot 0.312 \cdot 10^{20} \frac{atom}{m^2}.$$

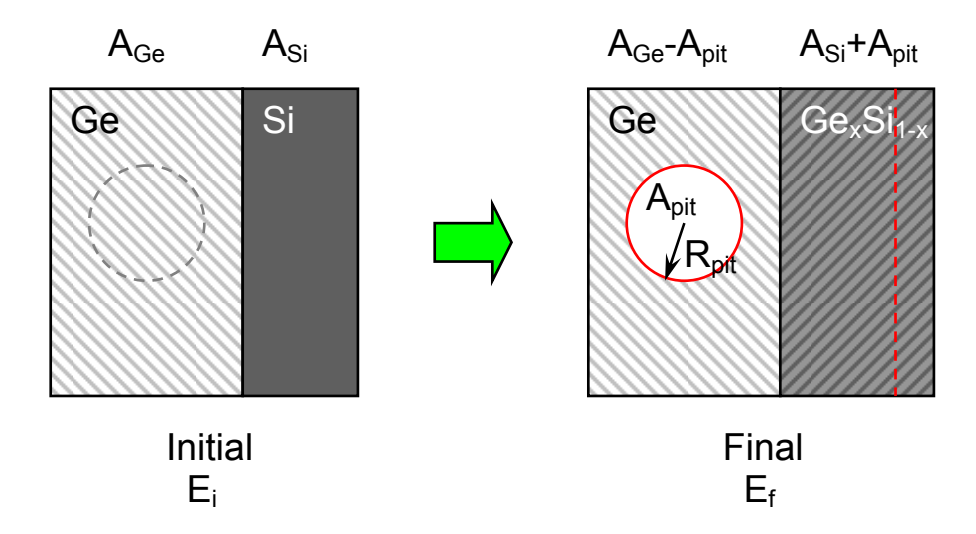


Figure 9. 27. The model considers initial and final states with energies E_i and E_f correspondingly. The initial state presents Si and Ge layers of volume A_{si} and A_{Ge} without pits. The final state presents Ge layer of volume $(A_{Ge} - A_{pit})$ with pit of area A_{pit} and Si-Ge layer which is homogenous composition of Ge of volume A_{pit} and Si of volume A_{si} .

The number of atoms of A_{Si} and A_{pit} involved into intermixing process defines entropy of the system **Figure 9. 27**. Final and initial state of the system is considered as shown on **Figure 9. 27**.

Complete internal energy of the system consist of three parts, $E_{step+steprelax}$, $E_{elastic}$ and E_{mixing} , then the Gibbs free energy of the system can be present as:

$$G^{f-i} = E_{step+steprelax} + E_{elastic} + E_{mixing} - TS_{mix}, \qquad (1.56)$$

Complete internal energy is sum of three parts of the internal energies (1.13), (1.18) and (1.48) with entropy (1.55) this gives the Gibbs free energy of the system:

Step energy:
energy formation + relaxation at the edges

pit steps

outer steps

$$G^{f-i} = 0.0061 \frac{eV}{A} \left(6.62 - \ln \frac{2R}{a} \right) 2\pi R - \left(0.012 \frac{eV}{A} \ln 0.8 \frac{w}{a} \right) x^2 L$$

$$+ N \left(-0.78 \kappa_{Ge} \varepsilon_0^2 + \Omega_{eff} - k_B T \right) (1-x) x$$

[Elastic energy + Mixing energy + Entropy]

[Step energy:
energy:
outer steps

(1. 57)

where L – length of sink outer steps per one pit $L = (6.4 \frac{A^2}{atom} \cdot N)/w$ (A), where w – width

of Si/Ge stripe (w > 3.14A), and
$$\frac{\pi R^2}{6.4 \frac{A^2}{atom}} = Nx \to 2\pi R = \frac{2Nx}{R} 6.4 \frac{A^2}{atom}$$
. $N = N_{Ge} + N_{Si}$ - is

sum number of Si (A_{Si}) and Ge (A_{pit}) atoms. After calculations, the Gibbs free energy (1.57) can be written as:

$$E_{step} \leq -0.5 \div 5.6 \text{ } meV/atom \text{ (Figure 9. 26)}, \text{ at } x = 1$$

$$G^{f-i} = -\left[\left(38.4 \frac{A \cdot meV}{atom} \ln 0.8 \frac{w}{a}\right) \frac{1}{w} x - \overline{\gamma}(R) \frac{2}{R}\right] xN + \left[-33 \frac{meV}{atom} + 21 \frac{meV}{atom} - 123 \frac{meV}{atom}\right] (1-x)xN$$

$$G_{mix}$$

$$(1. 58)$$

The numbers are given at temperature of the system 450°C, step energy formation $5 \div 36$ meV/A, pits radius ≤ 5 nm, Ge concentration $x_{Ge} = 0.5$. The entropy part in (1. 58) gives the largest contribution at $x_{Ge} = 0.5$. Together with elastic and segregation energy it can be a driving force for the pits formation.

The expression (1. 58) contains two different parts: the step edge relaxation part E_{step} and mixing energy part G_{mix} . At x=1 the mixing energy part is equal zero and only the step edge relaxation energy can be a driving force. At $x \approx 0.5$ the mixing energy part is essential part of the Gibbs free energy. Experiments show that Ge concentration x is usually about 0.5 **Figure 9. 6 (b)**. Without the smallest energy part which is the step relaxation energy ($E_{step\ relax} \leq 8.4$ $meV/atom\ Figure\ 9.\ 25$) we obtain:

$$\frac{G^{f-i}}{N} = \overline{\gamma}(R) \frac{2}{R} x 6.4 \frac{A^2}{atom} + (-33 \frac{meV}{atom} + 21 \frac{meV}{atom} - 123 \frac{meV}{atom})(1-x)x =$$

$$= \left(\overline{\gamma}(R) \frac{2}{R} 6.4 \frac{A^2}{atom} + (-12 \frac{meV}{atom} - 123 \frac{meV}{atom})(1-x)\right)x$$

$$E_{step} \qquad E_{elast + mix} \quad TS_{mix}$$
(1.59)

The step energy part in (1. 59) is significant with the step energy formation 0.036 eV/A at small radiuses R when relaxation at pits step edges is negligible. Then, with the step energy formation 0.036 eV/A (**Table 2**) one takes the form:

$$\frac{G_{\max}^{f-i}}{N_{Ge}} = \frac{460}{R} \frac{A \cdot meV}{atom} + \left(-12 \frac{meV}{atom} - 123 \frac{meV}{atom}\right) \frac{A_{Si}}{\pi R^2 + A_{Si}}.$$
 (1.60)

For the following analysis a short notation of (1. 60) will be used:

$$\frac{G^{f-i}}{N_{Ge}} = \bar{\gamma} \frac{2}{R} + (E_{mix} - TS_{mix}) \frac{A_{Si}}{\pi R^2 + A_{Si}}.$$
(1.61)

 $\frac{G^{f^{-i}}(A_{Si},R)}{N_{Ge}}$ - function of two system parameters (A_{Si},R) is qualitatively shown on **Figure**

9. 28. According to (1.52) the pits can form if the Gibbs free energy (1.61) is negative, then:

$$2\pi \bar{\gamma} R^2 + (E_{mix} - TS_{mix}) A_{Si} R + 2\bar{\gamma} A_{Si} < 0, \qquad (1.62)$$

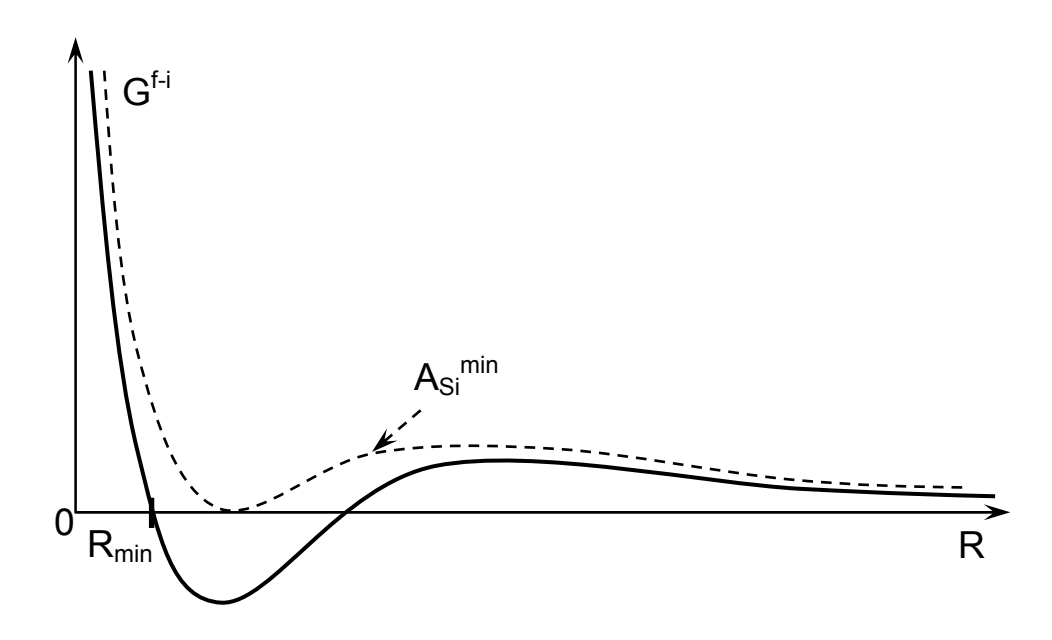


Figure 9. 28. Gibbs free energy of the system at different A_{Si} as a function of the pit's radius R (1. 61), qualitative behavior.

The equation can be solved if $(E_{\rm mix}-TS_{\rm mix})^2A_{\rm Si}^2-16\pi\bar{\gamma}^2A_{\rm Si}>0$, then

$$A_{Si} > \frac{16\pi\bar{\gamma}^2}{(E_{mix} - TS_{mix})^2} = A_{Si}^{min}.$$
 (1.63)

It means that the pits can form when amount of deposited Si per "diffusion area" is larger than A_{Si}^{\min} , $A_{Si} > A_{Si}^{\min}$. The minimal radius of the pits can be found from (1.62):

$$R_{\min} = \frac{-(E_{mix} - TS_{mix})A_{Si}}{4\pi\bar{\gamma}} \left(1 - \sqrt{1 - \frac{16\pi\bar{\gamma}^2}{(E_{mix} - TS_{mix})^2 A_{Si}}}\right),\,$$

at $A_{Si} = A_{Si}^{min}$ the minimal radius of the pits is:

$$R_{\min} = \frac{-4\bar{\gamma}}{(E_{mix} - TS_{mix})}.$$
(1.64)

This is a minimal size of the pits which can be estimated with the step energy formation of 0.036 eV/A (**Table 2**) as:

$$R_{\min} = \frac{-4\bar{\gamma}}{(E_{mix} - TS_{mix})} = \frac{4 \cdot 240}{135} = 7 \stackrel{\circ}{A}. \tag{1.65}$$

The minimal size of the pits can be 50% decreased with increase of A_{Si} (**Figure 9. 29**).

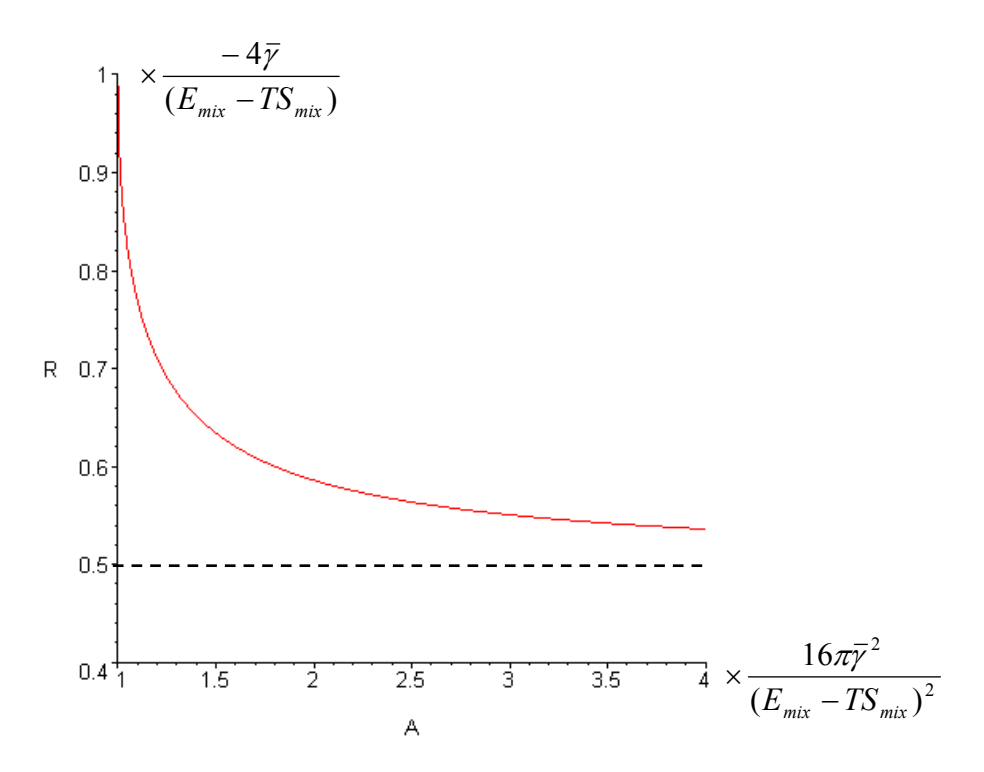


Figure 9. 29. Critical pit size R_{min} as a function of Si coverage A_{Si} per area per one pit.

The Si deposition is required to induce the pit formation since the Gibbs free energy (1.61) can achieve a negative value when amount of deposited Si per pit is larger than A_{Si}^{min} (1.63). Another important condition for the pit formation is minimal size of the pits which is ranged from 0.35 to 0.7 nm. (1.65), (Figure 9.29).

More detailed description can be done in term of chemical potential with continuum model in **Figure 9. 30** which considers behavior of the system during Si deposition.

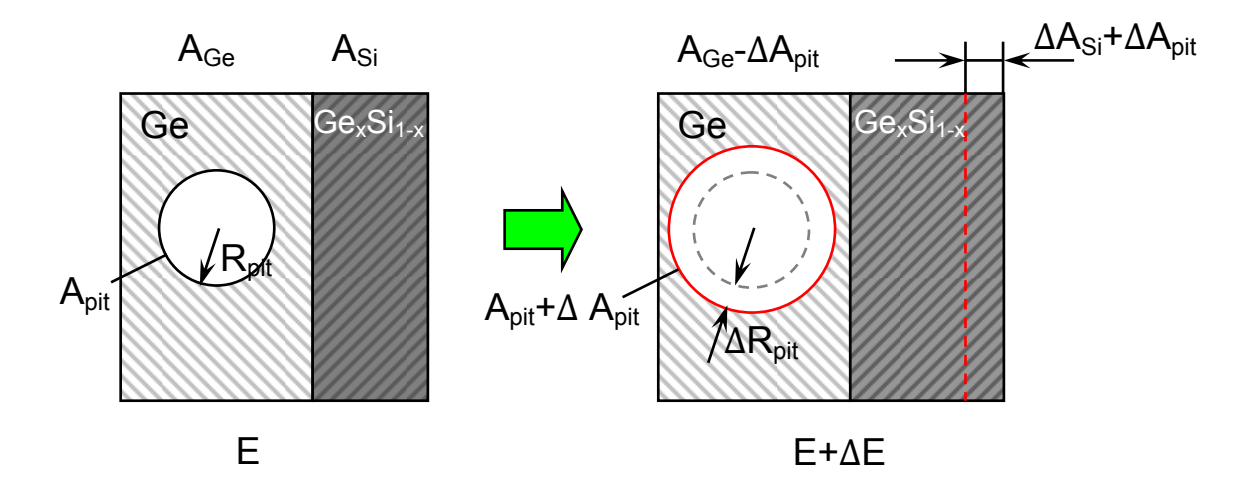


Figure 9. 30. The continuum model considers change of the system energy ΔE corresponding to the change of pit area ΔA_{pit} (ΔN_{Ge}) with Si area ΔA_{Si} (ΔN_{Si}).

Now composition x at step edge is a function of time, then change of the Gibbs free energy for the model shown in **Figure 9. 30** can be written as:

$$\begin{split} &\Delta G = \overline{\gamma} \, 4\pi \Delta R + (E_{mix} - TS_{mix}) \frac{\Delta A_{Si}}{2\pi R \Delta R + \Delta A_{Si}} \, 2\pi R \Delta R = \\ &= 2\overline{\gamma} \, \frac{\Delta N_{Ge}}{R} + (E_{mix} - TS_{mix}) \frac{\Delta N_{Si}}{\Delta N_{Ge} + \Delta N_{Si}} \, \Delta N_{Ge} = \left(2\, \frac{\overline{\gamma}}{R} + (E_{mix} - TS_{mix}) \frac{1}{\eta + 1}\right) \Delta N_{Ge} \end{split},$$

here $\eta = \frac{\Delta A_{pit}}{\Delta A_{Si}} = \frac{2\pi R\Delta R}{\Delta A_{Si}} = \frac{x}{1-x}$, $(x = \frac{\eta}{1+\eta})$. Change of the Gibbs free energy per Ge atom

 ΔN_{Ge} is change of chemical $\Delta \mu_{Ge}$ potential when Ge atom moves from the pit to the outer step edge:

$$\Delta\mu_{Ge} = 2\frac{\bar{\gamma}}{R} + (E_{mix} - TS_{mix})\frac{1}{\eta + 1},$$
(1.66)

The pits can grow if the difference of chemical potential is lower zero, $\Delta \mu < 0$:

$$2\frac{\overline{\gamma}}{R} + (E_{mix} - TS_{mix})\frac{1}{\eta + 1} < 0 \rightarrow R > -\frac{2\overline{\gamma}(\eta + 1)}{(E_{mix} - TS_{mix})}$$

The minimal or critical size of the pits R_c can be determined at $\Delta \mu = 0$:

$$R_c = -\frac{2\bar{\gamma}(\eta + 1)}{(E_{mix} - TS_{mix})}.$$

Critical size of the pits R_c depends on the ratio $\eta = \frac{2\pi R \Delta R}{\Delta A_{Si}}$, at $\eta \cong 0$ the critical pit size is minimal:

$$R_c = -\frac{2\bar{\gamma}}{(E_{mix} - TS_{mix})} = 3.5 \mathring{A}. \tag{1.67}$$

At $\eta \cong 0$ the chemical potential (1. 66) takes the simple form which is qualitatively the same for the 2D islands:

$$\Delta\mu_{Ge} = \frac{1}{R} 2\bar{\gamma} + (E_{mix} - TS_{mix}). \tag{1.68}$$

This is interesting result since thermodynamics of the pits growth (nucleation) at $\eta \cong 0$ can be the same like for growth and nucleation of 2D islands. Probably the pits could coalescence and form big trenches along Si step edges. The meaning of the critical pit size (1. 67) can be also the same like for critical 2D island size. The pits were not observed in Ge stripes with width lower than $\cong 2 \div 4$ nm, this can be explained by critical pit size. The pits can grow further if those have a size larger than critical pit size, at lower size the pits are not stable and will disappear.

Behavior of the system can be described as reaction of the system on addition particle which is Si atom in our case, therefore, to study behavior of our system we rewrite the chemical potential for Ge atoms (1.66) into chemical potential for Si atoms:

$$\mu_{Si}(\rho) = \frac{2\bar{\gamma}\eta}{R} + (E_{mix} - TS_{mix})\frac{\eta}{\eta + 1},$$
(1.69)

We assume that chemical potential of the system **Figure 9. 30** is capable to reach the minimum, i.e., in frame of our model, every small portion of Si atoms can intermix with Ge atoms with optimal ratio η giving local energy minimum (1. 69) of the system. Absolute energy minimum of the system is not achieved due to kinetic limitations, Si and Ge atoms are able to intermix in desired proportion until those don't blocked at the step edges with the next atoms incorporating into the step edges. The chemical potential $\mu_{Si}(\eta)$ as a function of ratio

$$\eta = \frac{2\pi R\Delta R}{\Delta A_{Si}}$$
 reaches the minimum, when $\frac{\partial \mu_{Si}}{\partial \rho} = 0$, then:

$$\frac{\partial \mu_{Si}}{\partial t} = \frac{2\bar{\gamma}}{R} + \frac{(E_{mix} - TS_{mix})}{\eta + 1} - \frac{(E_{mix} - TS_{mix})\eta}{(\eta + 1)^2} = 0, \to
\frac{2\bar{\gamma}}{R}\eta^2 + \frac{4\gamma \cdot \eta}{R} + \left(\frac{2\gamma}{R} + (E_{mix} - TS_{mix})\right) = 0$$
(1. 70)

Solution of equation (1. 70) is: $\eta = -1 \pm \sqrt{-\frac{(E_{mix} - TS_{mix})R}{2\gamma}}$. Since η is positive during pit

growth ($\Delta R > 0$, $\Delta A_{Si} > 0$), then:

$$\eta = \sqrt{\frac{R}{R_c}} - 1, \tag{1.71}$$

where
$$R_c = -\frac{2\overline{\gamma}}{(E_{mix} - TS_{mix})}$$
. The ratio $\eta = \frac{2\pi R\Delta R}{\Delta A_{Si}}$ can be expressed as $\eta = \frac{2\pi R\frac{\partial R}{\partial t}}{\frac{\partial A_{Si}}{\partial t}}$, where

 $\frac{\partial A_{Si}}{\partial t}$ is proportional to the Si flux: $\frac{\partial A_{Si}}{\partial t} = A_0 F$, here A_0 - is area per one pit. Then equation (1.71) takes the form:

$$\frac{2\pi R}{A_0 F} \frac{\partial R}{\partial t} = \sqrt{\frac{R}{R_c}} - 1. \tag{1.72}$$

Solution of differential equation (1. 72) (see Appendix F) is:

$$\ln|z-1| + \frac{z^3}{3} + \frac{z^2}{2} + z = \frac{t-t_0}{C}$$
, where $z = \sqrt{\frac{R}{R_c}}$, $C = \frac{4\pi R_c^2}{A_0 F}$. (1.73)

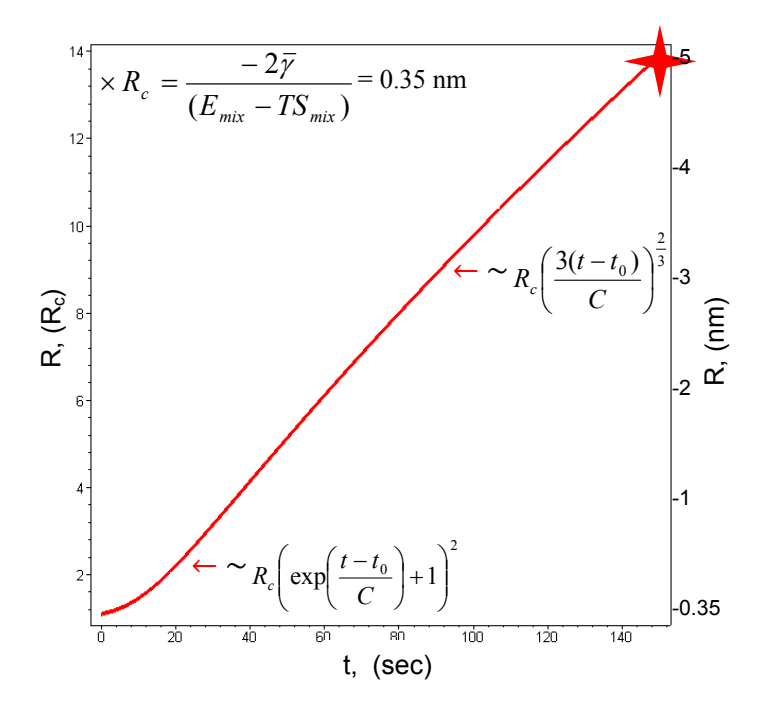


Figure 9. 31. Pit radius as a function of time during Si deposition was calculated for critical pit size of $R_c = 0.35$ nm and $C = \frac{4\pi R_c^2}{A_0 F} = 2.5$.

The radius dependence on time is shown in **Figure 9. 31**. The dependence was built up at the following conditions: $R(t=0)=1.01 \cdot R_c$, C=2.5, $R_c(\bar{\gamma}=0.036eV/A)=0.35\,\mathrm{nm}$, $T=450^{\circ}\mathrm{C}$. The pits grown at substrate temperature of $T=450^{\circ}\mathrm{C}$, Si deposition rate of $F_{Si}=0.0015\,ML/sec$, and deposition time of 150 sec (2.5 min) are shown in **Figure 9. 32**. Average pit radius is about 5 nm (maximal $\sim 10\,nm$), pit density is about $n_{pit}=2.6\times 10^{-5}\,nm^{-2}$. Average area per pit is equal $A_0^{\exp}=\frac{1}{n_{pit}}=3800\,nm^2$ (from the experimental data of **Figure 9. 32**). From condition $C=\frac{4\pi R_c^2}{A_0F}=2.5$ (**Figure 9. 31**) average area per pit is equal $A_0=\frac{4\pi R_c}{2F}=\frac{12.6\cdot0.35\cdot0.35}{2.5\cdot0.0015}=412\,nm^2$, this is 9 times lower than $A_0^{\exp}=3800\,\mathrm{nm}^2$. From relation $C=\frac{4\pi R_c^2}{A_0F}=2.5$ and $A_0^{\exp}=3800\,nm^2$ the critical pit size and step energy formation can be estimated as $R_c(\bar{\gamma}=0.108eV/A)=1.05\,nm$ and $\bar{\gamma}=0.108eV/A$ correspondingly. The step energy formation of $\bar{\gamma}=0.108eV/A$ was calculated Ab-initio for As-covered Si(111)-1x1 surface in [155] (also see **Table 2**). Step energy formation can be also high for the pits radius of $\sim 1\,nm$ due to increase of the step energy with decrease of radius of step curvature.

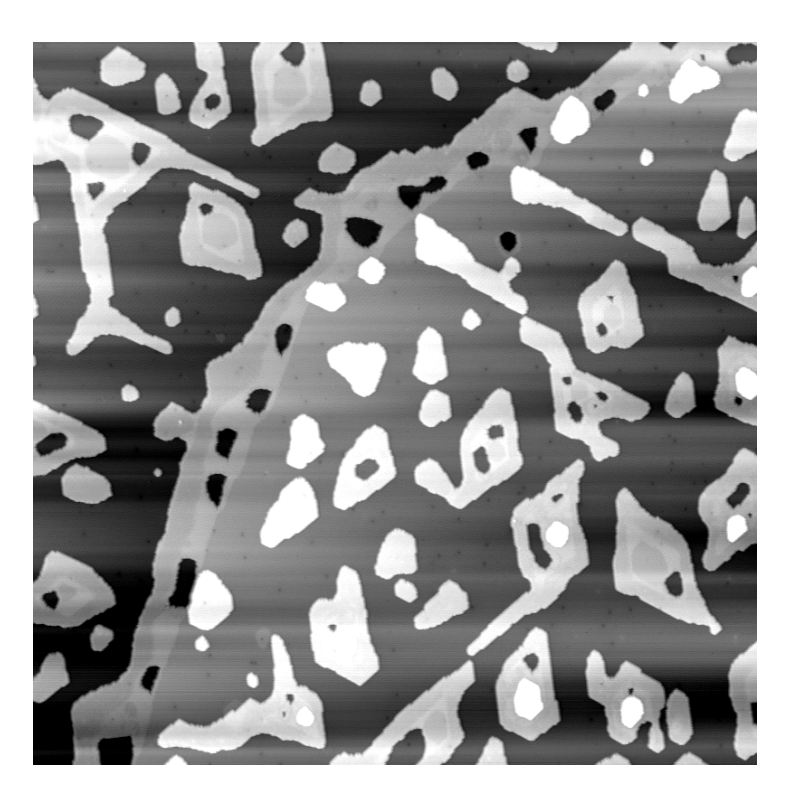


Figure 9. 32. The pits were formed during deposition of 0.22 ML of Si for 2.5 min at 450°C. Image size 400 nm [This experimental result was obtained by Dr. Jacek Brona].

Temperature and flux dependence of the pit radius can be complicated since $A_0 = \frac{1}{n_{pit}}$ $(n_{pit} = n_{pit}(T, F_{Si}))$ in (1. 73) is also function of the temperature and Si flux.

The energy model gives qualitative description of the behavior of the system and gives quantitative estimations for the step energy formation $\bar{\gamma} = 0.108eV/\mathring{A}$ and for critical pit size $R_c(\bar{\gamma} = 0.108eV/\mathring{A}) = 1.05\,nm$, $(R_c(\bar{\gamma} = 0.036eV/\mathring{A}) = 0.35\,nm)$. Predicted critical pit size $R_c = 1\,nm$ is comparable with experimental data in **Figure 9. 32**, the minimal pit size was experimentally observed (**Figure 9. 32**) about $1 \div 2\,nm$.

The entropy has the largest contribution in Gibbs free energy (1. 59), 10 times larger than sum of internal energies.

The mechanism of the pit formation in term of attachment – detachment events can be explained as the following: Ge atoms detach from Ge step (pit step) and attach to the GeSi outer steps due to stronger of Si type bonds than Ge type [128,129], Si also prefers to incorporate into GeSi outer steps due to stronger Si type bonds than Ge type bonds. The pit growth continues if the pit steps and outer step edges have a different GeSi composition and as consequence different chemical potentials. To study kinetics of the pit formation several experiments were made with the pits formed during annealing without Si deposition.

Pits formation during annealing after Si deposition

In the previous analysis it was shown that internal energy of the system is small in comparison with entropy (1. 59). It is still not clear how the entropy can drive the pits growth. To understand the kinetics and mechanisms of the pit formation a series of the experiments without Si deposition were performed.

The pits shown in **Figure 9. 33** were grown during annealing without Si deposition. The first part of the experiment is preparation of the system of Ge and Si stripes which is shown in left image of **Figure 9. 33**. The system was prepared by standard SME procedure, Ge was deposited at 400°C during 15 *min*, then Si was deposited during 3 min., rate of Ge and Si deposition was about 0.015 *BL/min*. At low temperature (400°C) kinetic processes are slow while no pits were formed during Si deposition. Broad Ge stripe and thin outer Si rim was formed as shown in left image **Figure 9. 33**. During annealing at 460°C, the pits (right image of **Figure 9. 33**) were formed even more effectively than during Si deposition at 460°C.

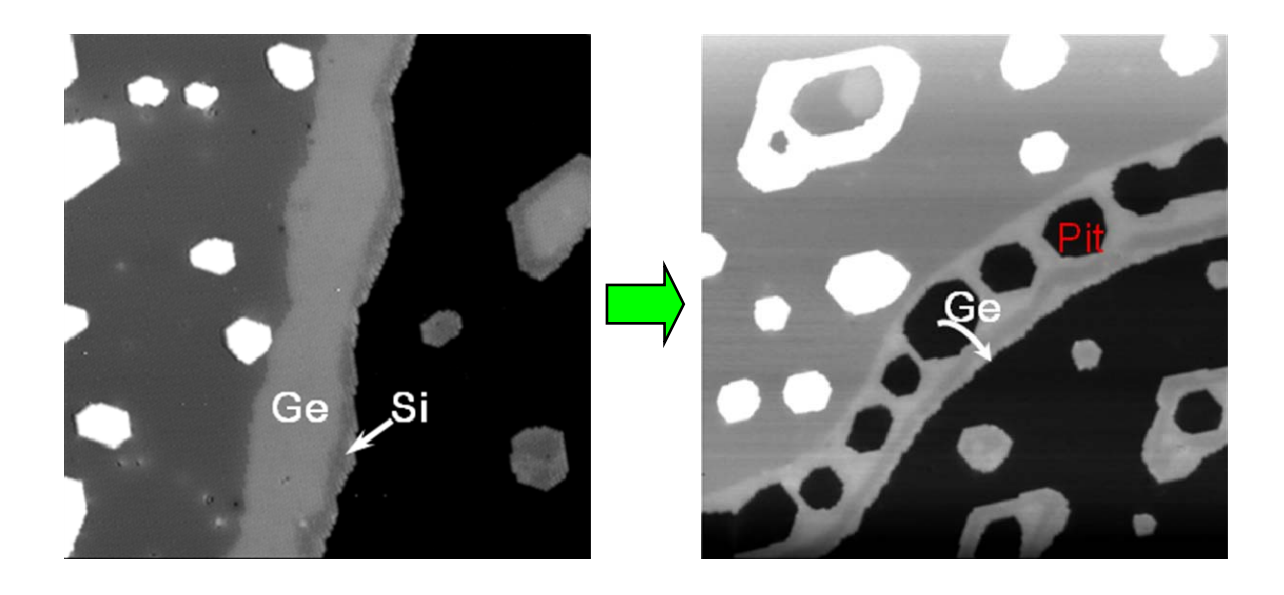


Figure 9. 33. Left image - the system of broad Ge and thin Si stripe grown at 400°C without any pits. The right image – the pits formed during annealing for 10 min at 460°C.

The observed pit formation is unexpected since the negative energy gain (1. 62) in the system can be provided by Si deposition as it was shown in previous paragraph. During annealing at high temperatures (460°C) Ge also goes from the pits to the outer Si step edges. Line profile measurements in **Figure 9. 34** showed that Si can be taken from the Si substrate: Ge incorporation into outer step edges is followed with growth front intermixing! Line profile in **Figure 9. 34** shows that apparent height of Si/Ge stripe is 0.5 A lower than height of pure Ge stripe **Figure 9. 34**. Si/Ge outer stripe has more than 50% of Si. After incorporation of Ge into Si steps the Si step edges become Si/Ge step edges.

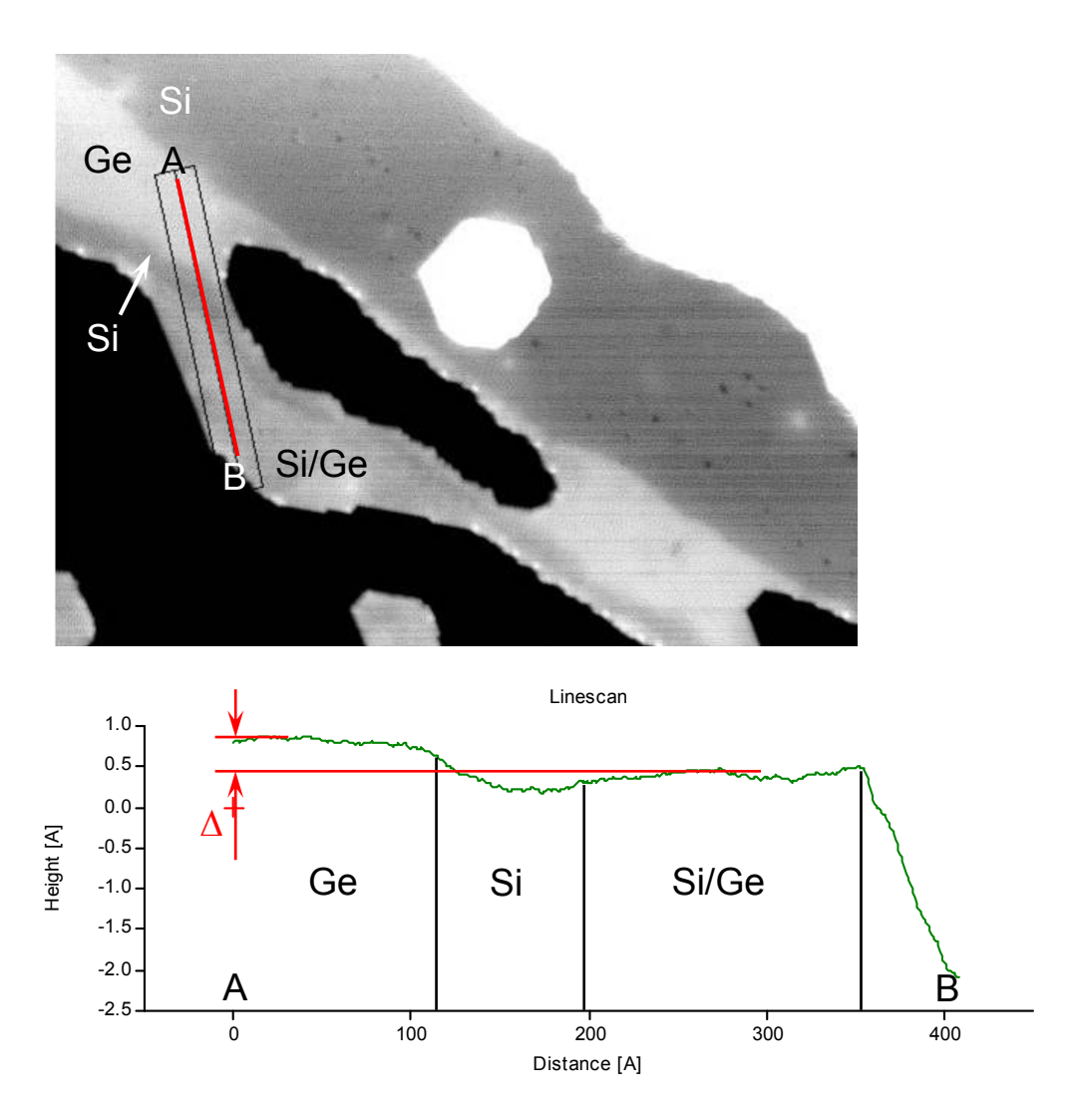


Figure 9. 34. Cross sectional profile A-B at step edge. △ - height difference between Ge and Si/Ge layer is about 0.5 A, that correspond more than 50% of Si. The pits were formed during annealing at 450°C for 10 min plus 500°C for 5 min.

The atoms at open step edges have a less neighbors than the atoms at the terrace, therefore the atoms at open step edges have a lower activation energy for intermixing with underlying Si atoms **Figure 9. 35**. Line profile of **Figure 9. 34** shows that concentration of Si provided by vertical intermixing in Ge layer is too small in comparison with concentration of Si provided by growth front induced intermixing at the outer step edges.

The mass transport of Ge from the pits to the outer steps induces the step propagation for the pit steps and for the outer steps. The step propagation speed v is different due to different length of the pit's steps l_{pit} and outer sink steps l, Figure 9. 36. Relation for the steps propagation speed can be found from balance equation:

$$v_{pit}l_{pit} = vl, (1.74)$$

where v_{pit} is the pit's step propagation speed.

N. Paul, S. Filimonov, V. Cherepanov, et al. Phys. Rev. Lett. 98,

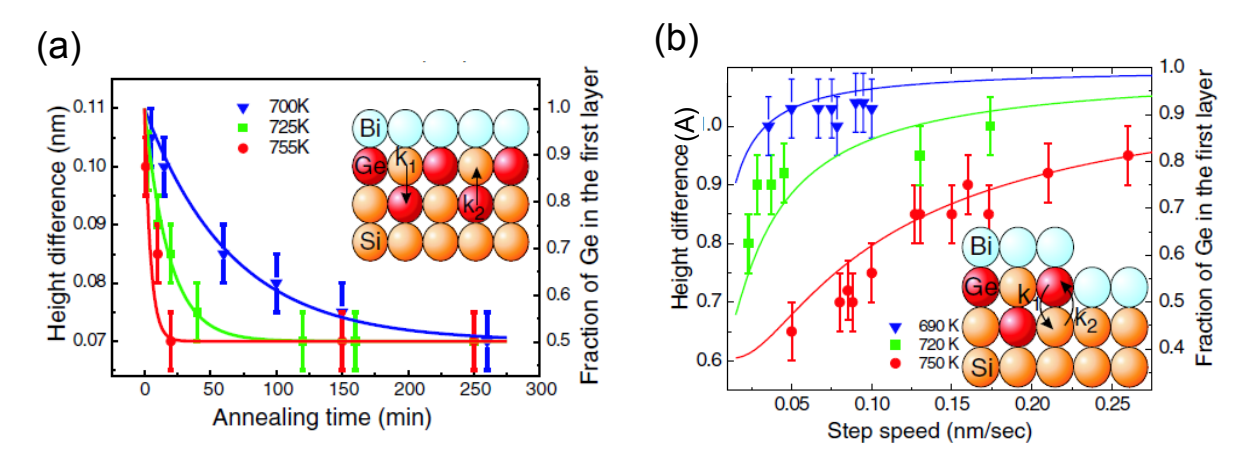


Figure 9. 35. Experimental observed height difference of two type of intermixing process for three different temperatures; (a) – vertical Ge intermixing with Si, height difference as function of annealing time; (b) – growth front induced intermixing acting at step edges, height difference as function of step speed. According to reff. [24].

At the nucleation stage the pits have much lower step length: $l > l_{pit} \rightarrow v_{pit} > v$. Due to difference of the steps propagation speeds $(v_{pit} > v)$ the growth front induced intermixing induces different rates of the intermixing at the steps resulting into different compositions of Si/Ge at the step edges of the pit's steps and outer steps. Nucleation and growth of the pits is driven by net effect, weak Ge-Ge bond is replaced by a stronger Si-Ge bond. During pit formation the growth front induced intermixing generates more Si at sink steps and less Si at pit's steps due to different step speed propagation, $v_{pit} > v$.

Since the pit formation occurs after annealing, we assume that the final state with pits formed is a state close to local equilibrium.

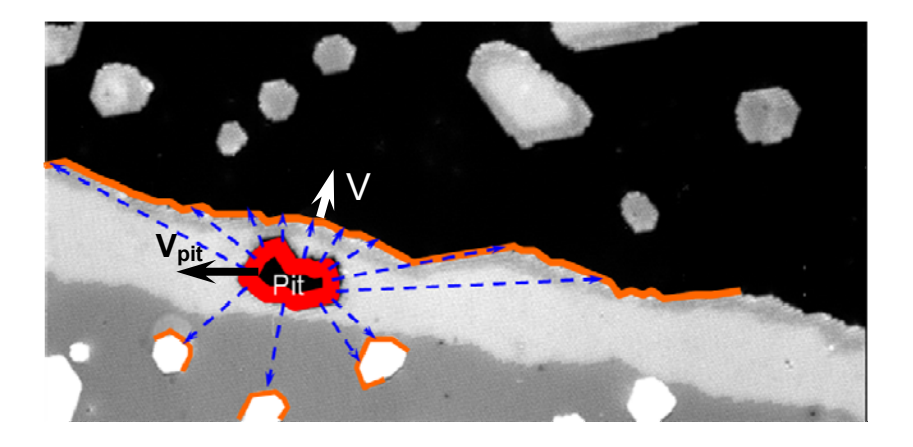


Figure 9. 36. The length of the pit's step shown by red colour and length of the sink steps are shown by light red colour. The mass transport of Ge is schematically shown by blue arrows. The volume of Ge detached from the pit is equal to the volume of Ge attached to the sink steps. The step speed propagation of pit v_{pit} is larger than step speed propagation of sink steps due to sink step length lager than pit's step length.

The energy gain of the system $G^{f-i} = E_{step+steprelax} + E_{elastic} + E_{mixing} - TS_{mix}$ can be written according with (1. 57) and with the model shown in **Figure 9. 37**. The step relaxation energy for the pits is the same like in (1. 57), i.e. equal to $0.0061 \frac{eV}{A} \left(6.62 - \ln \frac{2R}{a} \right) 2\pi R$; the step relaxation at outer step edges is the same like in (1. 57), i.e. equal to $-\left(0.012 \frac{eV}{A} \ln 0.8 \frac{w}{a} \right) x^2 L$ at x = 1 since the sum ratio of Ge per unit area in two upper layers of outer GeSi stripe is: x + (1 - x) = 1 (**Figure 9. 37**). Width of outer GeSi stripe w can be written as $w = \frac{\pi R^2}{L}$, where L is length of outer steps per one pit, then relaxation energy at outer step edge takes the form: $-\left(0.012 \frac{eV}{A} \ln 0.8 \frac{\pi R^2}{aL}\right) L$. Then step energy is:

$$E_{step+steprelax} = 0.0061 \frac{eV}{A} \left(6.62 - \ln \frac{2R}{a} \right) 2\pi R - \left(0.012 \frac{eV}{A} \ln 0.8 \frac{\pi R^2}{aL} \right) L.$$
 (1.75)

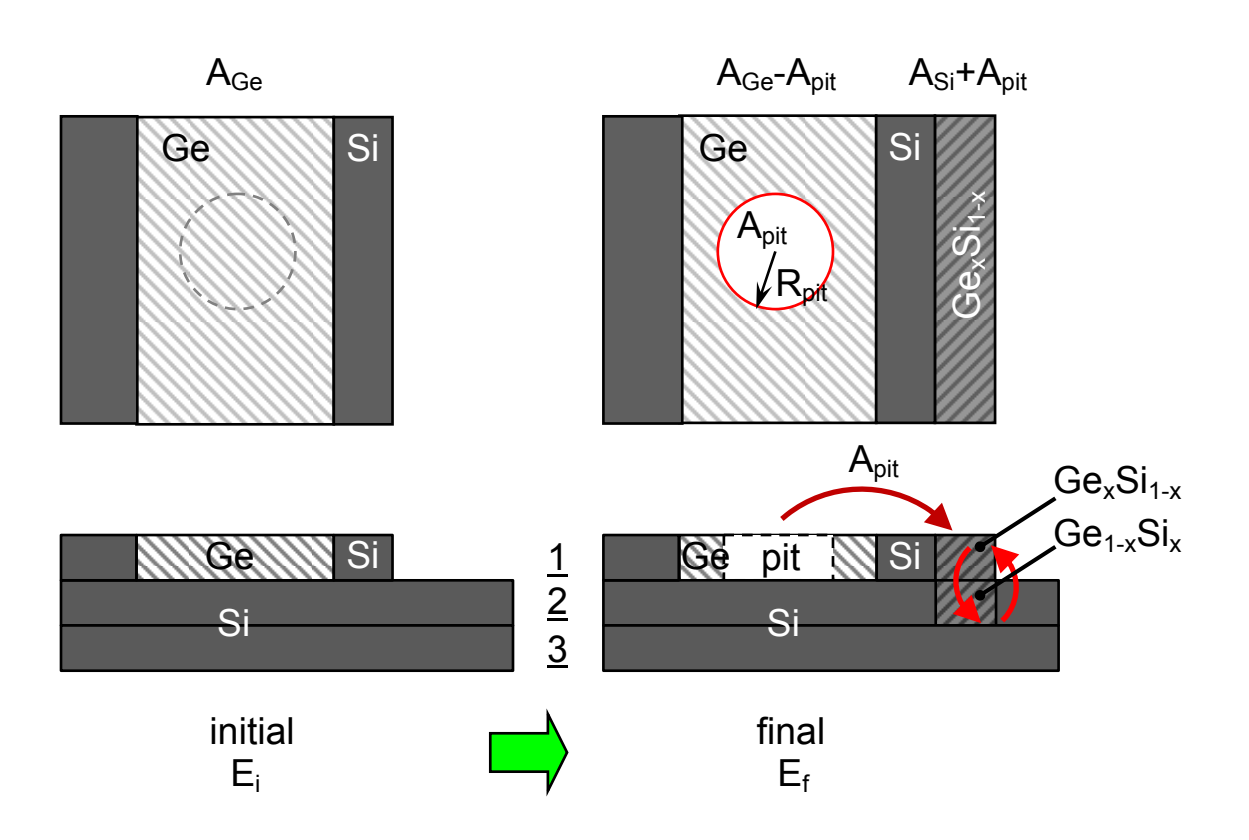


Figure 9. 37. The model considers initial and final states with energies E_i and E_f correspondingly. The initial state presents Ge layers of volume A_{Ge} without pits. The final state presents Ge layer of volume $(A_{Ge} - A_{pit})$ with pit of area A_{pit} and GeSi layer which is homogenous composition of Ge of volume xA_{pit} with Si of volume $A_{si} = (1 - x)A_{pit}$ in the first layer and Ge of volume $(1 - x)A_{pit}$ with Si of volume $A_{si} = xA_{pit}$ in the second layer.

Elastic energy gain can be written as sum of elastic energy gains for the first and second layers of outer GeSi stripe:

$$E_{elastic} = (0.88k_{Ge}\varepsilon_0^2(1-x)x + k_{Ge}\varepsilon_0^2x(1-x))\frac{N}{2} = 1.88k_{Ge}\varepsilon_0^2(1-x)x\frac{N}{2},$$

where $N = N_{Ge} + N_{Si} = 2N_{Ge}$, because $N_{Ge} = N_{Si}$ Figure 9. 37. Then elastic energy can be written as:

$$E_{elastic} = 1.88k_{Ge} \varepsilon_0^2 (1 - x) x N_{Ge}. \tag{1.76}$$

the interaction parameter in the layers can be lower than interaction parameter in the bulk because of interfaces, $\Omega_{\it eff} \approx \frac{7}{8} \Omega \approx 25 \ \it meV/atom$.

Complete internal energy is sum of three parts of the internal energies (1.75), (1.76) and (1.18) at $\Omega_{eff} = 25$ meV/atom with entropy (1.55) this gives the Gibbs free energy of the

system. At temperature of the system 450°C, step energy formation $5 \div 36 \ meV/A$, pits radius ≤ 5 nm, Ge concentration $x_{Ge} = 0.5$ the Gibbs free energy of the system can be written as:

$$E_{step} \leq -2 \div +2 \text{ meV/atom}$$
outer steps
$$G^{f-i} = -\left[\left(9.6 \frac{A \cdot meV}{atom} \ln 0.8 \frac{w}{a}\right) \frac{x}{w} - \bar{\gamma}(R) \frac{2}{R} 6.4 \frac{A^2}{atom}\right] N_{Ge} + \left(-17 \frac{meV}{atom} + 13 \frac{meV}{atom} - 63 \frac{meV}{atom}\right) N_{Ge}$$

$$E_{elastic} E_{mixing} TS_{mix}$$

$$(1.77)$$

Without the smallest energy part which is the step relaxation energy ($E_{step\ relax} \leq 8.4$ meV/atom Figure 9. 25) (1. 77) takes the form:

$$G^{f-i} = (\overline{\gamma}(R) \frac{2}{R} 6.4 \frac{A^{2}}{atom}) N_{Ge} - 4 \frac{meV}{atom} - 63 \frac{meV}{atom}) N_{Ge},$$

$$E_{step} \qquad E_{sum} \qquad TS_{mix}$$

$$(1.78)$$

here the step energy formation $\bar{\gamma}(R) \approx 0.036 eV/A$, E_{sum} – is sum of elastic and mixing energy. E_{sum} is mainly positive and can't be a driving force for the pit formation, now only entropy part can drive the pit formation by means of "Energy – Entropy cycle" process.

The free energy contributions for going from the initial to the final state were estimated and are shown in **Table 4**.

Table 4: Free energy contributions for pit formation

$E_{elastic}$	-17 meV/Ge atom
E_{mix}	+13 meV/Ge atom
Mixing entropy	-88 meV/Ge atom
$E_{step,rel} + E_{step,form}$	-2 – 2 meV/Ge atom
E _{int,bound} (E _{wet})	-3 meV/Ge atom

$$\begin{split} S_{mix} &= \left[x_{Ge} = 0.5 \right] = -2N_{Ge}k_BT \left[x \ln(x) + (1-x) \ln(1-x) \right] = \\ &= -2N_{Ge} \cdot 63 \cdot \frac{meV}{atom} \left[x \ln(x) + (1-x) \ln(1-x) \right] = -88 \frac{meV}{Geatom} N_{Ge} \, . \end{split}$$

Appendix B:

```
Definitions:
 the strain of Ge layer on Si(111) substrate
                                                                                                                                                                   \varepsilon_0 = 0.04
 the strain of Bi layer on Si(111) substrate
                                                                                                                                                                   \varepsilon_{Bi},
 the strain of Bi layer on Ge<sub>x</sub>Si<sub>1-x</sub> layer
                                                                                                                                                                   (\varepsilon_{Bi} - \varepsilon_0 x),
 the strain of Bi + Ge_xSi_{1-x} layer on Si(111) substrate
                                                                                                                                                                   (\varepsilon_{\theta}x + \delta),
 the strain of Ge_xSi_{1-x} layer is modified by Bi layer by the value of \delta, where
 \delta = (\varepsilon_{Bi} - \varepsilon_{\theta} x) k_{Bi} / k^{\perp}
 \delta_{\theta} = (\varepsilon_{Bi} - \varepsilon_{\theta}) k_{Bi} / k^{\perp}, \delta_{\theta} correspond to \delta in the case of pure Ge layer when x = 1,
 where k^{\perp} = k_{Ge} + k_{Bi} and x = A_{pit}/(A_{pit} + A_{si});
 The combining parts in the next expressions are colored.
 E_{elastic}^{f-i} = -A_{pit} k^{\perp} (\varepsilon_{\theta} + \delta_{\theta})^{2} + (A_{Si} + A_{pit}) k^{\perp} (\varepsilon_{\theta} x + \delta)^{2} - A_{Si} k_{Bi}^{2} \varepsilon_{Bi}^{2} / k^{\perp}, \rightarrow
E_{elastic}^{f-i} = -A_{nit} k^{\perp} (\varepsilon_0^2 + 2\varepsilon_0 \delta_0 + \delta_0^2) + (A_{Si} + A_{nit}) k^{\perp} (\varepsilon_0^2 x^2 + 2\varepsilon_0 \delta x + \delta^2) - A_{Si} k_{Bi}^2 \varepsilon_{Bi}^2 / k^{\perp}
-A_{nit} k^{\parallel} (\varepsilon_{\theta}^{2} - \varepsilon_{\theta}^{2} x) = k^{\parallel} \varepsilon_{\theta}^{2} (x - 1) A_{pit} = k^{\parallel} \varepsilon_{\theta}^{2} (-A_{Si}/(A_{Si} + A_{pit})) A_{pit} = -A_{Si} x k^{\parallel} \varepsilon_{\theta}^{2}, \rightarrow
E_{elastic}^{f-i} = -A_{Si} x k^{\parallel} \varepsilon_{\theta}^{2} + A_{pit} k^{\parallel} 2\varepsilon_{\theta} (\delta - \delta_{\theta}) + \underbrace{((A_{Si} + A_{pit}) \times \delta^{2} - A_{pit} k^{\parallel} \delta_{\theta}^{2})}_{[(\delta - \delta_{\theta}) = \varepsilon_{\theta} (1 - x) k_{Bi}^{2} / k^{\parallel}]} + \underbrace{((A_{Si} + A_{pit}) \times \delta^{2} - A_{pit} k^{\parallel} \delta_{\theta}^{2})}_{[A_{pit} k^{\parallel} (\delta^{2} / x - \delta_{\theta}^{2})]}
 then:
E_{elastic}^{f-i} = -A_{Si} x k^{\parallel} \varepsilon_{\theta}^{2} + A_{pit} k^{\parallel} 2\varepsilon_{\theta}^{2} (1-x) \chi_{Bi}^{2} / k^{\parallel} + A_{pit} k^{\parallel} (\delta^{2}/x - \delta_{\theta}^{2}) - A_{si} k_{Bi}^{2} \varepsilon_{Bi}^{2} / k^{\parallel},
 E_{elastic}^{f-i} = -A_{Si} x k^{\dagger} \varepsilon_{\theta}^{2} + 2\varepsilon_{\theta}^{2} k_{Bi}^{2} A_{Si} x + A_{pit} k^{\dagger} (\delta^{2}/x - \delta_{\theta}^{2}) - A_{si} k_{Bi}^{2} \varepsilon_{Bi}^{2}/k^{\dagger},
          \begin{aligned} &A_{pit} \ k^{\parallel} \left(\delta^{2} / x - \ \delta_{\theta}^{\ 2}\right) = A_{pit} \ k^{\parallel} (k_{Bi} / \ k^{\parallel})^{2} \left(\left(\varepsilon_{Bi}^{\ 2} - 2\ \varepsilon_{Bi}\ \varepsilon_{\theta} x + \varepsilon_{\theta}^{\ 2} x^{2}\right) / x - \left(\varepsilon_{Bi}^{\ 2} - 2\ \varepsilon_{Bi}\ \varepsilon_{\theta} + \varepsilon_{\theta}^{\ 2}\right)\right) \ , \\ &A_{pit} \ k^{\parallel} \left(\delta^{2} / x - \ \delta_{\theta}^{\ 2}\right) = \left(\varepsilon_{Bi}^{\ 2} (1 / x - 1) + \varepsilon_{\theta}^{\ 2} (x - 1)\right) \ A_{pit} \ k_{Bi}^{\ 2} / \ k^{\parallel} \ , \end{aligned}
put it into expression for energy gain (1*), then:

E_{elastic}^{f-i} = (-A_{Si} x k^{l} \varepsilon_{\theta}^{2} + 2\varepsilon_{\theta}^{2} k_{Bi}^{2} A_{Si} x) + (\varepsilon_{Bi}^{2} (1/x - 1) + \varepsilon_{\theta}^{2} (x - 1)) A_{pit} k_{Bi}^{2} / k^{l} - A_{si} k_{Bi}^{2} \varepsilon_{Bi}^{2} / k^{l},
 E_{elastic}^{f-i} = -(k_{Ge} - k_{Bi})\varepsilon_0^2 A_{Si}x + A_{nit} k_{Bi}^2 \varepsilon_{Bi}^2 / k^1 - \varepsilon_0^2 A_{Si}x k_{Bi}^2 / k^1 - A_{Si} k_{Bi}^2 \varepsilon_{Bi}^2 / k^1 \rightarrow
 E_{elastic}^{f-i} = -(k_{Bi}^2/k^1 + (k_{Ge} - k_{Bi}))\epsilon_0^2 A_{Si}x = [\text{using } k^1 = k_{Ge} + k_{Bi}] = (k_{Ge}^2/k^1) \epsilon_0^2 A_{Si}x, and
 finally elastic energy modified by Bi is:
```

$$E_{elastic}^{f-i} = - (k_{Ge} \varepsilon_{\theta}^2 A_{si} x) k_{Ge} / k^1$$

Appendix C:

$$\int_{0}^{L} \frac{1}{\sqrt{x^{2} + (y - y_{1})^{2}}} dy_{1} = \left[\left(\frac{y - y_{1}}{x} \right) = t \right] = -\int \frac{dt}{\sqrt{1 + t^{2}}} = \left[t = \tan \alpha \right] = -\int \frac{1}{\cos^{2} \alpha} \sqrt{\frac{1}{\cos^{2} \alpha}} d\alpha =$$

$$= -\int \frac{d\alpha}{\cos \alpha} = -\int \frac{1}{1 - \sin^{2} \alpha} d(\sin \alpha) = \left[\sin \alpha = z \right] = -\int \frac{dz}{1 - z^{2}} = -\int \left(\frac{1}{1 - z} + \frac{1}{1 + z} \right) dz =$$

$$= -\ln \left| \frac{z + 1}{z - 1} \right| = \left[z = \frac{y - y_{1}}{\sqrt{x^{2} + (y - y_{1})^{2}}} \right] = -\ln \left| \frac{(y - L) + \sqrt{x^{2} + (y - L)^{2}}}{(y - L) - \sqrt{x^{2} + (y - L)^{2}}} \right| + \ln \left| \frac{y + \sqrt{x^{2} + y^{2}}}{y - \sqrt{x^{2} + y^{2}}} \right| =$$

$$= -\ln \left| \frac{((y - L) + \sqrt{x^{2} + (y - L)^{2}})^{2}}{(y - L)^{2} - (\sqrt{x^{2} + (y - L)^{2}})^{2}} \right| + \ln \left| \frac{(y + \sqrt{x^{2} + y^{2}})^{2}}{y^{2} - (\sqrt{x^{2} + y^{2}})^{2}} \right| =$$

$$= -2\ln \left| \frac{\sqrt{x^{2} + (L - y)^{2}} - (L - y)}{\sqrt{x^{2} + y^{2}} + y} \right| = -2\ln \left| \frac{\sqrt{x^{2} + (y - L)^{2}} + (y - L)}{\sqrt{x^{2} + y^{2}} + y} \right| =$$

Appendix D:

$$\begin{split} &\int_{0}^{L} \ln \left| \frac{\sqrt{a^{2} + (y - L)^{2}} + (y - L)}{\sqrt{a^{2} + y^{2}} + y} \right| dy = \int_{0}^{L} \ln \left| \sqrt{a^{2} + (y - L)^{2}} + (y - L) \right| dy - \int_{0}^{L} \ln \left| \sqrt{a^{2} + y^{2}} + y \right| dy = \\ &= a \int \ln \left| a \left(\sqrt{1 + \left(\frac{y - L}{a} \right)^{2}} + \frac{y - L}{a} \right) \right| d \left(\frac{y - L}{a} \right) - a \int \ln \left| a \left(\sqrt{1 + \left(\frac{y}{a} \right)^{2}} + \frac{y}{a} \right) \right| d \left(\frac{y}{a} \right) = \\ &= \left[t_{1} = \frac{y - L}{a} ; t_{2} = \frac{y}{a} \right] = a \int \left(\ln a + \ln \left| \sqrt{1 + t_{1}^{2}} + t_{1} \right| \right) dt_{1} - a \int \left(\ln a + \ln \left| \sqrt{1 + t_{2}^{2}} + t_{2} \right| \right) dt_{2} = \\ &= \left[from_{-}(1.46) - and_{-}(1.47) \right] \rightarrow \\ &\rightarrow \left[\int \ln (f(y)) dy = y \ln (f(y)) - \int \frac{yf'(y)}{f(y)} dy = y \ln \left| \sqrt{1 + y^{2}} + y \right| - \sqrt{1 + y^{2}} \right] = \\ &= t_{1} a \ln a + t_{1} a \ln \left(\sqrt{1 + t_{1}^{2}} + t_{1} \right) - a \sqrt{1 + t_{1}^{2}} - \left(t_{2} a \ln a + t_{2} a \ln \left(\sqrt{1 + t_{2}^{2}} + t_{2} \right) - a \sqrt{1 + t_{2}^{2}} \right) = \\ &= (y - L) \ln \left| a \sqrt{1 + \left(\frac{y - L}{a} \right)^{2}} + a \frac{y - L}{a} \right| - a \sqrt{1 + \left(\frac{y - L}{a} \right)^{2}} - y \ln \left| a \sqrt{1 + \left(\frac{y}{a} \right)^{2}} + a \frac{y}{a} \right| + \\ &+ a \sqrt{1 + \left(\frac{y}{a} \right)^{2}} = \\ &\left[(y - L) \ln \left(\sqrt{a^{2} + (y - L)^{2}} + (y - L) \right) - \sqrt{a^{2} + (y - L)^{2}} - y \ln \left(\sqrt{a^{2} + y^{2}} + y \right) + \sqrt{a^{2} + y^{2}} \right|_{0}^{L} = \\ &= L \ln \left| \frac{\sqrt{a^{2} + L^{2}} - L}{\sqrt{a^{2} + L^{2}} + L} \right| + 2 \left(\sqrt{a^{2} + L^{2}} - a \right) = 2 L \left(\ln \left| \frac{a}{\sqrt{a^{2} + L^{2}} + L} \right| + \left(\sqrt{1 + \left(\frac{a}{L} \right)^{2}} - \frac{a}{L} \right) \right) = \\ &= 2 L \left(\ln \left| \frac{a}{1 + \sqrt{1 + \left(\frac{a}{L} \right)^{2}}} \right| + \left(\sqrt{1 + \left(\frac{a}{L} \right)^{2}} - \frac{a}{L} \right) \right) = \left(\ln \left| \frac{a}{1 + \sqrt{1 + \left(\frac{a}{L} \right)^{2}}} \right| + \left(\ln \left| \frac{a}{L} \right|$$

Appendix E:

The solution for the energy with localized force $F = \lambda \delta(x)\delta(y)\delta(z)$ was presented in [134]:

$$E_{el} = -\frac{1}{2}\int u_x(x,y,z)\lambda\delta(x)\delta(z)dxdydz = -\frac{1}{2}\lambda\int u_x(0,y)dy\,,$$

The change of elastic energy as function of L is:

$$\frac{dE_{el}}{dL} = \frac{d}{dL} \left(-\frac{1}{2} \lambda \int_{a}^{L} u_{x}(0, y) dy \right) = \frac{d}{dL} \left(-\frac{1}{2} \lambda \int_{a}^{L} \left(\frac{1 - v^{2}}{\pi Y} \lambda \int_{a}^{L} \frac{1}{|y - y_{1}|} dy_{1} \right) dy \right) =
= -\frac{1}{2} \lambda \frac{1 - v^{2}}{\pi Y} \left(\lambda \int_{a}^{L} \frac{1}{|L - y_{1}|} dy_{1} \right) - \frac{1}{2} \lambda \int_{a}^{L} \left(\frac{1 - v^{2}}{\pi Y} \frac{d}{dL} \left(\lambda \int_{a}^{L} \frac{1}{|y - y_{1}|} dy_{1} \right) \right) dy =
= -\frac{1}{2} \lambda^{2} \frac{1 - v^{2}}{\pi Y} \left(\int_{a}^{L} \frac{1}{|y - L|} dy + \int_{a}^{L} \frac{1}{|L - y_{1}|} dy_{1} \right) = -\lambda^{2} \frac{1 - v^{2}}{\pi Y} \int_{a}^{L} \frac{1}{y} dy =
= -\lambda^{2} \frac{1 - v^{2}}{\pi Y} \ln \frac{L}{a}$$
(e2)

Equation (e2) can be integrated directly by (d1) to give $E_{\it el}$:

$$E_{el} = -\lambda^2 \frac{1 - v^2}{\pi Y} L \left(\ln \frac{L}{a} - 1 \right) + \varepsilon_{el}(a),$$

Then the elastic energy per unit length is:

$$\frac{E_{el}}{L} = -\lambda^2 \frac{1 - \nu^2}{\pi Y} \left(\ln \frac{L}{a} - 1 \right) + \frac{\varepsilon_{el}(a)}{L}, \tag{e3}$$

The constant of integration, $\varepsilon_{el}(a)$, depends on the value of a and on how cutoff is implemented [134].

The lower limit a of the integral in (e2) defined by interatomic distance. The energy of relaxation per unit length for infinite step length at $L \rightarrow \infty$ have unlimited results, this is correct for the layer with unlimited width.

Appendix F:

Equation $\frac{2\pi R}{A_0 F} \frac{\partial R}{\partial t} = \sqrt{\frac{R}{R_c}} - 1$ can be written as:

$$C \cdot z^3 \frac{\partial z}{\partial t} = z - 1,\tag{f1}$$

where $z = \sqrt{\frac{R}{R_c}}$, $C = \frac{4\pi R_c^2}{A_0 F}$. Solution of equation (f1) can be found by integration:

$$C\int \frac{z^3 dz}{z - 1} = \int dt \ . \tag{f2}$$

Integral type of $\int \frac{z^n dz}{z-1}$ can be found as the following:

$$\int \frac{z^{n}dz}{z-1} = \int \frac{z^{n-2}(z-1)(z+1)dz}{z-1} + \int \frac{z^{n-2}dz}{z-1} = \frac{z^{n}}{n} + \frac{z^{n-1}}{n-1} + \int \frac{z^{n-4}(z-1)(z+1)dz}{z-1} + \int \frac{z^{n-4}dz}{z-1} = \dots = \frac{z^{n}}{n} + \frac{z^{n-1}}{n-1} + \dots + \frac{z^{n-1}}{n-1} + \dots + \frac{z^{n-k}}{n-k} + \dots + \frac{z^{2}}{2} + z + \begin{cases} 0, & \text{if } n-\text{even number} \\ \ln|z-1|, & \text{if } n-\text{odd number} \end{cases}$$

After integration (f2) takes the form:

$$C\left(\ln|z-1| + \frac{z^3}{3} + \frac{z^2}{2} + z\right) = t - t_0.$$
 (f3)

12 Acknowledgments

I would like to thank all people who work in the institute of Bio- and Nanosystems in Research Center Jülich who supported me during the time I have spent in Jülich.

I would like to acknowledge Prof. Stefan Tautz, who is the institute leader, for the opportunity to perform my work in the Institute of Bio- and Nanosystems in Research Center Jülich and for kindly agreeing to act as co-referee of my thesis.

I would like to thank my supervisor Prof. Bert Voigtländer, for his guidance and support throughout my thesis project, for his fruitful and interesting discussions and for his authentic scientific interest. I thank him kindly for sharing his scientific experience starting from the planning of experiments to the proper presentation of the results.

I would like to thanks Dr. Boris Olshanetsky, leader of our research group in Novosibirsk, and Dr. Sergey Teys, scientific adviser of my master diploma work, who introduced me into MBE and STM methods and supplied me with the skills and knowledge for the following scientific work.

This thesis also would not be possible without contribution of a number of people. I wish to thank Dr. Vasily Cherepanov for his help in many technical questions and for the helpful discussions. I want to thank Dr. Josef Myslivicek and Dr. Sergey Filimonov who took an active part in the discussion of the results.

I also would like to thank my colleagues of the group: Dr. Jacek Brona, Dr. Anna Strozecka, Dr. Michel Kazempoor, Dr. Philip Jaschinsky, Bastian Schnitzler, Leonid Kliuienko and Evgeny Zubkov for the discussions and the nice time working together.

Also I would like to thank the technician and the engeneer of our group Helmut Stollwerk and Peter Coenen. Their help always make the work in the laboratory effective and pleasant.

Bibliography

¹ Irving Langmuir. J. Am. Chem. Soc., 38 (11), 2221, (1916).

³ P. J. Rous, T. L. Einstein, E. D. Williams, Surf. Sci. Lett. 315, L995 (1994).

⁴ D. N. Bly and P. J. Rous, Phys. Rev. B. 53, 13909 (1995).

⁶ H. J. Scheel, J. Cryst. Growth, 211, 1-12, (2000).

⁷ B. Voigtländer, Surf. Sci. Rep. 43, 127 (2001).

⁸ J. A. Venables, Philos. Mag. 27, 697 (1973).

⁹ J. A. Venables, G. D. T. Spiller, M. Hanbüken, Rep. Prog. Phys. 47, 399 (1984).

¹⁰ J. A. Venables, Surf. Sci. 299/300, 798 (1994).

J. G. Amar, F. Family, P. M. Lam, Phys. Rev. B., 50, 8781 (1994).

T. Michely, J. Krug, Islands, Mounds and Atoms. Patterns and Processes in Crystal Growth Far from Equilibrium. (Springer, Heidelberg 2004).

¹³ D. J. Eaglesham, A. E. White, L. C. Feldman, N. Moriya, and D. C. Jacobson, Phys. Rev. Lett. 70, 1643 (1993).

14 S. Surmev, K. Arenhold, P. Coenen, B. Voigtlander, and H. P. Bonzel, P. Wynblatt, J. Vac. Sci. Technol. A. 16, 1059 (1998).

¹⁵ Ch. Steimer, M. Giesen, L. Verheij, and H. Ibach, Phys. Rev. B. 64, 085416 (2001).

¹⁶ H. P. Bonzel, Physics Reports 385, 1-67 (2003).

¹⁷ M. Ozdemir, and A. Zangwill, Phys. Rev. B 45, 3718 (1992).

¹⁸ T. A. Witten, and L. M. Sander, Phys. Rev. Lett., 47, 1400 (1981).

¹⁹ B. Voigtlander, A. Zinner, T. Weber, H. P. Bonzel, Phys. Rev. B 51, 7583 (1995).

²⁰ Y.-J. Ko, K. J. Chang, J.-Y. Yi, Phys. Rev. B 60, 1777 (1999).

²¹ K. Schroeder, A. Antons, R. Berger, and S. Blügel, Phys. Rev. Lett. 88, 046101 (2002).

²² D. Kandel, E. Kaxiras, Phys. Rev. Lett. 75, 2742 (1995).

²³ D. Kandel, E. Kaxiras, Sol. St. Phys. 54, 219 (2000).

²⁴ N. Paul, S. Filimonov, V. Cherepanov, M. Cakmak, and B. Voigtlander, Phys. Rev. Lett. 98, 166104 (2007).

25 H. Ibach, H. Lüth, "Solid-State Physics", Springer-Verlag Berlin Heidelberg 2003.

²⁶ K. Takayanagi, Y. Tanishiro, M. Takahashi, and S. Takahashi, J. Vac. Sci. Technol. A 3, 1502 (1985), Surf. Sci. 164, 367 (1985).

²⁷ H. Tochihara, W. Shimada, M. Itoh, H. Tanaka, M. Udagawa, and I. Sumita, Phys. Rev. B 45, 11332 (1992).

²⁸ W. Shimada, H. Tochihara, Surf. Sci. 311, 107 (1994).

²⁹ J. Krug, Introduction to Step Dynamics and Step Instabilities, Mathematics Subject Classification (2000).

³⁰ M. Giesen, Prog. Surf. Sci. 68, 1–153 (2001).

³¹ T. Michely, J. Krug, *Islands, Mounds and Atoms*. Patterns and Processes in Crystal Growth Far from Equilibrium. Springer, Heidelberg 2004.

P. Nozi'eres, Shape and Growth of Crystals. In C. Godr'eche (Ed.), Solids Far from Equilibrium (Cambridge University Press, 1991), pp.1–154.

² K. Oura, V. G. Lifshits, A. A. Saranin, A. V. Zotov, M. Katayama, Surface Science An Introduction, (Springer-Verlag Berlin Heidelberg, 2003).

⁵ W. Seifert, N. Carlson, M. Miller, M.-E. Pistol, L. Samuelson, L. R. Wallenberg, Prog. Cryst. Growth & Charact. 33, 423 (1996).

- ³³ A. Pimpinelli and J. Villain, *Physics of Crystal Growth* (Cambridge University Press, Cambridge, England, 1998).
- ³⁴ R. J. Hammers, U. M. Köhler, and J. E. Demuth, Ultramicroscopy 31, 10 (1989).
- ³⁵ K. Romanyuk, J. Mysliveček, V. Cherepanov, T. Sekiguchi, S. Yoshida, K. M. Itoh, and B. Voigtländer, Phys. Rev. B. 75, 241309(R) (2007).
- ³⁶ K. Romanyuk, V. Cherepanov, and B. Voigtländer, Phys. Rev. Lett. 99, 126103 (2007).
- ³⁷ V.V. Voronkov, The movement of an elementary step by means of the formation of onedimensional nuclei. Sov. Phys. Crystallogr. 15, 8 (1970).
- ³⁸ M.C. Bartelt, J.W. Evans, Phys. Rev. B 46, 12675 (1992).
- ³⁹ J. Villain, A. Pimpinelli, L. Tang, D. Wolf, Terrace sizes in molecular beam epitaxy. J. Phys. I France 2, 2107 (1992).
- ⁴⁰ C. Roland, G.H. Gilmer, Phys. Rev. B 46, 13437 (1992).
- J. Kallunki, J. Krug, Phys. Rev. B 65, 205411 (2002).
 W. Burton, N. Cabrera, F.C. Frank, Philos. Trans. R. Soc. London Ser. A 243, 299 (1951).
- ⁴³ O. Pierre-Louis, M.R. D'Orsogna, T.L. Einstein, Phys. Rev. Lett. 82, 3661 (1999).
- ⁴⁴ M.V. Ramana Murty, B.H. Cooper, Phys. Rev. Lett. 83, 352 (1999).
- ⁴⁵ J. Kallunki, J. Krug, Surf. Sci. 523, L53 (2003).
- ⁴⁶ R.L. Schwoebel, J. Appl. Phys. 40, 614 (1969).
- ⁴⁷ R.L. Schwoebel, E.J. Shipsey, J. Appl. Phys. 37, 3682 (1966),.
- ⁴⁸ S. Tanaka, N.C. Bartelt, C.C. Umbach, R.M. Tromp, and J.M. Blakely, Phys. Rev. Lett. 78, 3342 (1997).
- ⁴⁹ S. Stoyanov, V. Tonchev, Phys. Rev. B 58, 1590 (1998).
- ⁵⁰ S.N. Filimonov, Yu.Yu. Hervieu, Surf. Sci. 507-510, 270 (2002).
- ⁵¹ M. Gavelle, El M. Bazizi, E. Scheid, C. Armand, P. F. Fazzini, O. Marcelot, Y. Campidelli, A. Halimaoui, F. Cristiano, Materials Science and Engineering B. (2008).
- ⁵² J. Viernow, J. L. Lin, D. Y. Petrovykh, F. M. Leibsle, F. K. Men, and F. J. Himpsel, Appl. Phys. Lett. 72, 948 (1998).
- ⁵³ F. J. Himpsel, J. L. McChesney, J. N. Crain, A. Kirakosian, V. Perez-Dieste, N. L. Abbott, Yan-Yeung Luk, P. F. Nealey, and D. Y. Petrovykh, J. Phys. Chem. B. 108, 14484 (2004).
- ⁵⁴ A. Baski, S. C. Erwin, L. J. Whitman, Science, 169, 1556 (1995).
- ⁵⁵ J. L. Lin, D. Y. Petrovykh, J. Viernow, F. K. Men, D. J. Seo, and F. J. Himpsel, J. of Appl. Phys. 84, 255 (1998).
- ⁵⁶ R. J. Phaneuf and E. D. Williams, Phys. Rev. B. 41, 2991 (1990).
- ⁵⁷ So. Tanaka, C. C. Umbach, and J. M. Blakely, Appl. Phys. Lett. 69, 1235 (1996).
- ⁵⁸ H. Omi and T. Ogino, J. Vac. Sci. Technol. A. 17, 1610 (1999).
- ⁵⁹ U. Köhler, J. E. Demuth, and R. J. Hammers, J. Vac. Sci. Technol. A. 7, 2860 (1989).
- ⁶⁰ W. Shimada and H. Tochihara, Surf. Sci. 311, 107 (1994); 296, 186 (1993).
- 61 T. Ogino, Y. Homma, Y. Kobayashi, H. Hibino, K. Prabhakaran, K. Sumitomo, H. Omi, S. Suzuki, T. Yamashita, D. J. Bottomley, F. Ling, A. Kaneko, Surf. Sci. 514, 1 (2002).
- ⁶² K. N. Romanyuk, S. A. Teys, and B. Z. Olshanetsky, Phys. Solid State, 48, 1820 (2006).
- 63 S. Yoshida, T. Sekiguchi, and K. M. Itoh, Appl. Phys. Lett. 87, 031903-1 (2005).
 64 A. V. Latyshev, A. L. Aseev, A. B. Krasilnikov, S. I. Stenin, Surf. Sci. 213, 157 (1989).
- 65 Y.-N. Yang, E. Fuy, E. Williams, Surf. Sci. 356, 101 (1996).
- ⁶⁶ E. Tutuc, J. Appenzeller, M. C. Reuter, and S. Guha, Nano Lett. 6, 2070 (2006).

- ⁶⁷ T. Jung, R. Schlittler, J. K. Gimzewski, and F. J. Himpsel, Appl. Phys. A: Mater. Sci. Process. 61, 467 (1995).
- ⁶⁸ F. J. Himpsel, T. Jung, and J. E. Ortega, Surf. Rev. Lett. 4, 371 (1997).
- ⁶⁹ F. J. Himpsel, T. Jung, A. Kirakosian, J.-L. Lin, D. Y. Petrovykh, H. Rauscher, and J. Viernow, MRS Bull. 24, 20 (1999).
- ⁷⁰ J. Viernow, D. Y. Petrovykh, F. K. Men, J.-L. Lin, and F. J. Himpsel, Appl. Phys. Lett. 74, 2125 (1999).
- 71 M. Kawamura, N. Paul, V. Cherepanov, and B. Voigtländer, Phys. Rev. Lett. 91, 096102 (2003).
- ⁷² A. Kirakosian, R. Bennewitz, J. N. Crain, Th. Fauster, J.-L. Lin, D. Y. Petrovykh, and F. J. Himpsel, Appl. Phys. Lett. 79, 1608 (2001).
- ⁷³ J. L. McChesney, A. Kirakosian, R. Bennewitz, J. N. Crain, J-L. Lin, and F. J. Himpsel, Nanotechnology 13, 545 (2002).
- ⁷⁴ T. Sekiguchi, S. Yoshida, and K. M. Itoh, Phys. Rev. Lett. 95, 106101 (2005).
- ⁷⁵ T. Sekiguchi, S. Yoshida, K. M. Itoh, J. Mysliveček, and B. Voigtländer, Appl. Phys. Lett. 90, 013108 (2007).
- ⁷⁶ M. Nakaya, T. Nakayama, Yu. Kuwahara, and M. Aono, Surf. Sci. 600, 2810 (2006).
- ⁷⁷ A. V. Latyshev, A. L. Aseev, A. B. Krasilnikov, S. I. Stenin, Surf. Sci. 213, 157 (1989).
- ⁷⁸ K. J. Wan, T. Guo, W. K. Ford, and J. C. Hermanson, Phys. Rev. B. 44, 3471 (1991).
- ⁷⁹ N. Paul, H. Asaoka, J. Mysliveček, and B. Voigtländer, Phys. Rev. B 69, 193402 (2004).
- ⁸⁰ N. Paul, H. Asaoka, and B. Voigtländer, Surf. Sci. 564, 187 (2004).
- ⁸¹ R. Z. Bakhtizin, Ch. Park, T. Hashizume, and T. Sakurai, J. Vac. Sci. Technol. B 12, L290 (1990). ⁸² T. Schmidt, J. Falta, and G. Materlik, Appl. Phys. Lett. 74, 1391 (1999).
- 83 S. Hasegawa, R. G. Ryland, and E. D. Williams, Appl. Phys. Lett. 65, 2609 (1994).
- 84 C. Cheng, K. Kunc, Phys. Rev. B. 56, 10283 (1997).
- 85 T. Schmidt, J. Falta, and G. Materlik, Appl. Surf. Sci. 166, 399 (2000).
- ⁸⁶ N. Paul and B. Voigtländer, Surf. Sci. 551, 80 (2004).
- ⁸⁷ M. Copel, M. C. Reuter, E. Kaxiras, and R. M. Tromp, Phys. Rev. Lett. 63, 632 (1989).
- ⁸⁸ M. Horn-von Hoegen, F. K. LeGoues, M. Copel, M. C. Reuter, and R. M. Tromp, *ibid*. 67, 1130 (1991).
- ⁸⁹ M. Copel, M. C. Reuter, M. Horn von Hoegen, and R. M. Tromp, Phys. Rev. B 42, 11682 (1990). ⁹⁰ G. Meyer, B. Voigtländer, and N. M. Amer, Surf. Sci. Lett. 274, L541 (1992).
- ⁹¹ V. Cherepanov, S. Filimonov, J. Mysliveček, and B. Voigtländer, Phys. Rev. B 70, 085401
- (2004). ⁹² I. Štich, M. C. Payne, R. D. King-Smith, J. S. Lin, and L. J. Clarke, Phys. Rev. Lett. 68,
- 93 M. Fonin, J. M. Choi, U. May, J. O. Hauch, U. Rüdiger, and G. Güntherodt, Surf. Sci. 511. 312 (2002).
- ⁹⁴ A. A. Chernov, *Modern Crystallography 3—Crystal Growth* (Springer, Berlin, 1984).
- 95 Y.-W. Mo, D. E. Savage, B. S. Swartzentruber, and M. G. Lagally, Phys. Rev. Lett. 65, 1020 (1990).
- ⁹⁶ J. Nogami, Sang-il Park, and C. F. Quate, Phys. Rev. B 36, 6221 (1987).
- ⁹⁷ A. A. Baski, J. Nogami, and C. F. Quate, Phys. Rev. B 41, 10 247 (1990).

- 98 H. Minoda, Y. Tanishiro, N. Yamamoto, and K. Yagi, Surf. Rev. Lett. 2, 1 (1995).
- ⁹⁹ M. Horn-von Hoegen, Appl. Phys. A **59**, 503 (1994).
- R. Shioda, A. Kawazu, A. A. Baski, C. F. Quate, and J. Nogami, Phys. Rev. B 48, 4895 (1993).

 101 F. Bechstedt, *Principles of Surface Physics* (Springer, Heidelberg, 2003).
- The occurrence of three different domains of arrowshaped or rhomb-shaped islands observed in the STM experiment (Fig. 1) can be explained by three (120° rotated) domains of the $(\sqrt{3} \times \sqrt{3})$ reconstruction on the islands.
- 103 M.C. Bartelt and J.W. Evans, Phys. Rev. B. 46, 12675 (1992).
- 104 C. Ratsch, A. Zangwill, P. Šmilauer, and D.D. Vvedensky, Phys. Rev. Lett. 72, 3194 (1994).
- 105 C. Ratsch, P. Šmilauer, A. Zangwill, and D.D. Vvedensky, Surf. Sci. 329, L599 (1995).
- ¹⁰⁶ J. Amar and F. Family, Phys. Rev. Lett. 74, 2066 (1995).
- ¹⁰⁷ J.A. Stroscio and D.T. Pierce, Phys. Rev. B. 49, R8522 (1994).
- H. Brune, G.S. Bales, J. Jacobsen, C. Boragno, and K. Kern, Phys. Rev. B. 60, 5991 (1999).
- ¹⁰⁹ B. Müller, L. Nedelmann, B. Fischer, H. Brune, and K. Kern, Phys. Rev. B. 54, 17858 (1996).

 110 D.D. Chambliss and K.E. Johnson, Phys. Rev. B. 50, 5012 (1994).
- ¹¹¹ A. Zangwill and E. Kaxiras, Surf. Sci. 326, L483 (1995).
- ¹¹² B.A. Joyce, D.D. Vvedensky, A.R. Avery, J.G. Belk, H.T. Dobbs, and T.S. Jones, Appl. Surf. Sci. 98, 357 (1998).
- 113 L. Andersohn, Th. Berke, U. Köhler, and B. Voigtländer, J. Vac. Sci. Technol. A 14, 312 (1996).
- 114 D. Kandel, Phys. Rev. Lett. 78, 499 (1997).
- B. Voigtländer, M. Kästner, and P. Šmilauer, Phys. Rev. Lett. 81, 858 (1998).
- ¹¹⁶ P. Jensen, H. Larralde, and A. Pimpinelli, Phys. Rev. B 55, 2556 (1997).
- ¹¹⁷ P.A. Mulheran and D.A. Robbie, Philos. Mag. B 80, 1299 (2000).
- ¹¹⁸ M. Horn-von Hoegen, F.K. LeGoues, M. Copel, M.C. Reuter, and R.M. Tromp, Phys. Rev. Lett. 67, 1130 (1991).
- 119 B. Voigtländer and A. Zinner, J. Vac. Sci. Technol. A 12, 1932 (1994).
- ¹²⁰ I.-S. Hwang, T.-C. Chang, and T.T. Tsong, Phys. Rev. Lett. 80, 4229 (1998).
- ¹²¹ I. Markov, Surf. Sci. 429, 102 (1999).
- 122 T. A. Witten, and L. M. Sander, Phys. Rev. Lett., 47, 1400 (1981).
- ¹²³ M.S.Leite, A. Malachias, S.W. Kycia, et al. Phys. Rev. Lett. 100, 226101 (2008).
- ¹²⁴ A. Rastelli, M. Stoffel, A. Malachias et al. Nano Lett. 8, 1404 (2008).
- ¹²⁵ U. Denker, A. Rastelli, M. Stoffel et al. Phys. Rev. Lett. 94, 216103 (2005).
- ¹²⁶ G. Medeiros-Ribeiro, R.S. Williams, Nano Lett. 7, 223 (2007).
- J.B. Hannon, M. Copel, R. Stumpf, M.C. Reuter, and R.M. Tromp, Phys. Rev. Lett. 92, 216104 (2004).
- ¹²⁸ F. Bechstedt and W. A. Harrison, Phys. Rev. B 39, 5041 (1989).
- ¹²⁹ H. Efstathiadis and F. W. Smith, Philosophical Magazine B 70, 547 (1994).
- ¹³⁰ P. Dorner, Philosoph. Mag. 49, 557 (1984).
- 131 H.Ibach, Physics of Surfaces and interfaces, Springer-Verlag Berlin Heidelberg (2006).
- ¹³² P.C. Kelires, J. Tersoff, Phys. Rev. Lett. 63, 1164 (1989).

- ¹³³ J.E. Bernard, A. Zunger, Phys. Rev. B 44, 1663 (1991).
- ¹³⁴ R. M. Tromp, and J. B. Hannon, Surf. Rev. Lett. 9, 1565 (2002).
- ¹³⁵ A. V. Latyshev, A. L. Aseev, A. B. Krasilnikov and S. I. Stenin, Surf. Sci. 227, 24 (1990).
- ¹³⁶ P. Zahl, P. Kury, M. Horn von Hoegen, Appl. Phys. A 69, 481 (1999).
- ¹³⁷ R. E. Martinez, W. M. Augustyniak, and J. A. Golovchenko, Phys. Rev. Lett. 64, 1035 (1990).
- 138 R. D. Meadle, and Vanderbilt D, Phys. Rev. B. 40, 3905 (1989).
- ¹³⁹ Y. Eckstein, A. W. Lawson, and D. H. Reneker, J. of Appl. Phys. 31, 1534 (1960).
- ¹⁴⁰ A. de Bretteville, Jr., E. R. Cohen, A. D. Ballato and I. N. Greenberg, S. Epstein, Phys. Rev. 148, 575 (1966).
- ¹⁴¹ N. G. Pace, G. A. Saunders, and Z. Sumengen, J. Phys. Chem. Solids, 31, 1467 (1970).
- ¹⁴² M. Saito, T. Ohno, T. Miyazaki, Appl. Surf. Sci. 237, 80 (2004).
- ¹⁴³ M. Saito, A. Oshiyama, Phys. Rev. B. 48, 11804 (1993).
- ¹⁴⁴ S. Nakatani, T. Takahashi, Y. Kuwahara, M. Aono, Phys. Rev. B. 52, 8711 (1995).
- ¹⁴⁵ T. Takahashi, K. Izumi, T. Ishikawa, S. Kikuta, Surf. Sci. Lett. 183, 302 (1987).
- ¹⁴⁶ T. Takahashi, S. Nakatani, T. Ishikawa, S. Kikuta, Surf. Sci. Lett. 191, 825 (1987).
- ¹⁴⁷ Ch. Kittel, "Introduction to Solid State Physics" (Seven edition, 1996).
- ¹⁴⁸ J. Tersoff, Phys. Rev. B 39, 5566 (1989).
- ¹⁴⁹ S. M. Lee, E. Kim, Y. H. Lee, N. Kim, Journal of the Korean Physical Society, Vol. 33 684 (1998).
- 150 G. B. Stringfellow, J. Phys. Chem. Solids, 34, 1749 (1973).
- ¹⁵¹ G. B. Stringfellow, and P. E. Greene, J. Electrochem. Soc. 117, 1075 (1970).
- ¹⁵² S. Kodiyalam, K. E. Khor, N. C. Bartelt, E. D. Williams, S. D. Sarma, Phys. Rev. B 51, 5200 (1995).
- 153 H.-Ch. Jeong, E. D. Williams, Surf. Sci. Rep. 34, 171-294 (1999).
- ¹⁵⁴ E. D. Williams, R. J. Phaneuf, J. Wei, N. C. Bartelt, T. L. Einstein, Surf. Sci. 310, 451 (1994).
- 155 A. Antons, R. Berger, K. Schroeder, and B. Voigtlander, Phys. Rev. B. 125327-173 (2006).
- ¹⁵⁶ L. D. Landau and E. M. Lifshitz, Theory of Elasticity, Butterworth Heinemann, Oxford, 1997.
- ¹⁵⁷ O. L. Alerhand, D. Vanderbilt, R. D. Meade, J. D. Joannopoulos, Phys. Rev. Lett. 61, 1973 (1988).
- 158 L. D. Landau and E. M. Lifshitz, Statistical Physics, Part 1.

Curriculum Vitae

1980 - 1990

Name: Date of birth: Nationality	Konstantin Romanyuk 13.01.1973 in Petrovka, Russian Federation Russian
Oktober 2009	PhD thesis at RWTH in Aachen, Germany
2005 – 2009	PhD student at RWTH Aachen under the supervision of Prof. Dr. Bert Voigtländer
2002 – 2005	Researcher of the Institute of Semiconductor Physics, Siberian Branch Academy of Science
2000 - 2002	Master degree in Microelectronics and Semiconductor Physics Science at Novosibirsk State University, Russian Federation. Title of Master thesis: "STM investigation of forming and self-organization of Ge nano-wires on vicinal surfaces Si(111)"
1995 - 2000	Novosibirsk State University, Physics Department, Major: Semiconductor Physics. Title of Bachelor thesis: "Study of atomic smoothing of GaAs surface by SPALEED method"
1990 - 1995	Novosibirsk State Technical University, Instrumentation Department, graduated with BS degree

High School in T-Mihailovka, Russian Federation